Laser Processing and Modelling of Multiple Memory Shape Memory Alloys

by

Andrew Michael

A thesis

presented to the University of Waterloo

in fulfillment of the

thesis requirement for the degree of

Doctor of Philosophy

in

Mechanical and Mechatronics Engineering

Waterloo, Ontario, Canada, 2018

Examining Committee Membership

The following served on the examining Committee for this thesis. The decision of the examining committee is by majority vote.

External Examiner	Professor Ian Richardson, Materials Science & Engineering, Delft University of Technology, The Netherlands
Supervisor	Professor Norman Y. Zhou, Mechanical & Mechatronics Engineering, University of Waterloo, Canada
Co-Supervisor	Professor Mustafa Yavuz, Mechanical & Mechatronics Engineering, University of Waterloo, Canada
Internal Member	Professor Behrad Khamesee, Mechanical & Mechatronics Engineering, University of Waterloo, Canada
Internal Member	Professor Kevin Musselman, Mechanical & Mechatronics Engineering, University of Waterloo, Canada
Internal-external Member	Professor Robert Gorbet, Electrical & Computer Engineering, University of Waterloo, Canada

Author's Declaration

I hereby declare that I am the sole author of this thesis. This is a true copy of the thesis, including any required final revisions, as accepted by my examiners.

I understand that my thesis may be made electronically available to the public.

Abstract

Laser processing of NiTi shape memory alloys (SMA) has been identified as having great potential in surface treatment, welding, and novel performance requirement applications. However, no models have been developed to predict the amount of Ni vaporized based on various laser processing parameters. Additionally, no models have been developed to accurately predict the performance of these novel materials after laser processing. This is a cause for concern regarding efficient development and functional reliability of the laser processed SMAs. Prior to full scale implementation, a better understanding of Ni vaporization rates and the resulting mechanical performance of these materials is required.

The first part of this study is concerned with a systematic investigation of the preferential vaporization of Ni during laser processing. The effect of duration and peak power of the laser pulse on the transformation temperature is studied. It was observed that the cooling rate causes segregation of compositions for compositions on the Ti-rich side of the congruency point. Deconvolution of overlapping transformation peaks allowed for approximations of overall bulk composition and Ni loss. A novel model was developed to predict the change in Ni concentration based on laser pulse duration and peak power.

In the second part of this study, a novel 1D model is presented for NiTi SMAs with multiple pseudoelastic plateaus. The model is scalable for any number of plateaus present in the material. It can also be adjusted to include residual strain present after unloading the stress. The model was validated by comparing it the experimental data from Multiple Memory Material (MMM). The new model was found to closely match the experimental results. Part of this study relates to accurately characterizing the tensile properties of SMAs.

The third part of this study is concerned with 2-D deformation mechanisms. The effect of texture on the bending properties of NiTi is examined. It was successfully demonstrated that the preferred bending curvature of the stress induced martensite can be predicted from the orientation of the crystallographic planes. Part of this work also relates to advancing the understanding surrounding the anisotropic and incompressible behavior of the austenite to R-phase transformation.

Acknowledgements

I would like to thank my supervisors Prof. Norman Y. Zhou and Prof. Mustafa Yavuz for invaluable career and life lessons as well as the autonomy to pursue my research and academic goals. My accomplishments in this part of my life would not have been possible without their mentorship and guidance.

I would also like to acknowledge Boyd Panton for his guidance and knowledge of NiTi microstructure, texture and thermomechanical treatments; as well as his and Matt Daly's work on sample preparation and EBSD analysis. Also, I would like to acknowledge Apratim Chakraborty for assisting with wire drawing and shape setting springs and Greg Seviora for assisting with DSC analysis and laser processing samples.

I would also like to acknowledge all of Smarter Alloys, Inc. for their relentless support, data resources, practical industrial experience and seemingly endless usage of test equipment.

Finally, I would like to thank my family for their continued love and support throughout my graduate studies.

This work has been supported by the Natural Sciences and Engineering Research Council of Canada (NSERC).

Dedication

To my amazing sons

Beatum & Caelum

Table of Contents

List of Figures

List of Tables

List of Equations

List of Abbreviations

1-D	One dimension
2-D	Two dimension
A1	Alternate composition one
A2	Alternate composition two
A_f	Austenite finish temperature
A_p	Austenite peak temperature
A_s	Austenite start temperature
ASTM	American Society for Testing and Materials
AW	Annealed wire
BM	Base material
BMS	Base material sheet
DC	Direct current
DIC	Digital imaging correlation
DSC	Differential scanning calorimetry
DTA	Differential thermal analysis
E-beam	Electron beam
GR	Grain reoriented
IMC	Intermetallic compound
LP	Laser processed
M_d	Martensite deformation temperature
M_f	Martensite finish temperature
MM	Multiple memory
M_p	Martensite peak temperature
M_s	Martensite start temperature
Nd:YAG	Neodymium: yttrium aluminum garnet
P1	Processed one
P2	Processed two
PE	Pseudoelasticity
PS	Processed sheet
PW	Processed wire
RVE	Representative volume equivalent
R_f	R-phase finish temperature
R_p	R-phase peak temperature

R_s	R-phase start temperature
SIM	Stressed induced martensite
SMA	Shape memory alloy
SME	Shape memory effect
TBM	Treated base material
TLP	Treated laser processed
TTT	Time-temperature-transformation
UP	Unprocessed
VAR	Vacuum arc re-melting
VIM	Vacuum induced melting

List of Symbols

a_i	Activity of element *i*
A	Cross-sectional area
A_{adj}	Adjustment factor
A_c	Dimensionless parameter for determining vaporization rate
A_z	Zener anisotropy
B	Bulk modulus
B_{adj}	Adjustment factor
c	Distance from the center of specimen to outer fibers
c'	Elastic constant of a single crystal associated with diagonal shearing
c_{11}	Elastic constant of a single crystal that relates deformation in the x-direction to stress in the x-direction
c_{12}	Elastic constant of a single crystal that relates deformation in the y-direction to stress in the x-direction
c_{44}	Elastic constant that is associated with the stretching of a single crystal in the <111> direction
c_{Ni}	Atomic concentration of Ni
d	Wire diameter
d_A	Goldschmidt atomic diameter of material *A*
D	Spring diameter
D_{AB}	Diffusion of solute *A* in solvent *B*
D_i	Diffusivity of element *i*
$D_{i,Ar}$	Diffusivity of vaporizing element *i* in argon
D_0	Diffusion pre-factor
E	Young's modulus/elastic modulus
$E_{<111>}$	Elastic modulus in the <111> direction
E_A	Activation energy
E_{Ai}	Elastic modulus of the austenite phase for region *i*
E_{Mi}	Elastic modulus of the martensite phase for region *i*
E_n	Effective elastic modulus of the *n*th elastic section of the stress/strain curve
F	Force
F_{ai}	Force of active region *i*
F_p	Force of the passive region

G	Shear modulus
I	Moment of inertia
J_i	Vaporization rate of element *i*
$J_{c,i}$	Vaporization rate due to the concentration gradient of element *i*
$J_{p,i}$	Vaporization rate due to the pressure gradient of element *i*
k	Scaling factor
k_B	The Boltzmann constant
$K_{g,i}$	Mass transfer coefficient of element *i*
l	arc length
ℓ_i	Length fraction for region *i*
L	Span length
m	Exponent controlling function curvature at the crest of the transformation peak
M	Maximum bending moment
M_{Ar}	Molecular weight of argon
M_i	Molecular weight of element *i*
M_v	The mean molecular weight of all alloying elements on the melt pool surface
n	Exponent controlling function curvature at the base of the transformation peak
N	Total number of data points
o	Offset of the neutral axis from the sample centerline
p	Transformation peak temperature
p_D	Laser pulse duration
p_L	Laser pulse power
p_P	Change in laser pulse power from the critical power that first forms a keyhole
P_i	Partial pressure of element *i*
P_i^o	Equilibrium pressure of element *i*
P_L	Summation of the equilibrium vapor pressure of all alloying elements on the melt pool surface
q^*	Heat flow
r	Radius
R	Gas constant
R_c	Radius of curvature
R_{crit}	Critical bending radius for SIM to form
R_m	Bending radius of SIM

R_R	Bending radius of the R-phase
Re	Reynolds number
s	Distance from the neutral axis to the outer fibers
s_0	Internal configuration entropy
Sc	Schmidt number
t	Tangent slope
t_e	Tangent slope at the sample end point
t_m	Tangent slope at the interface between SIM and austenite
T	Temperature
T_0	Equilibrium temperature of transformation
u_0	Internal configuration energy
x	X-coordinate
X_i	Mole fraction of element *i*
y	Y-coordinate
Y	True experimental value
Y'	Value predicted by the estimating equation
δ	Displacement
δ_{ai}	Displacement of active region *i*
δ_p	Displacement of passive region
ΔH	Latent heat of transformation
Δl	Elongation
Δs^*	Change in the internal entropy from the austenite to martensite phase
ΔT	Thermal hysteresis between A_p and M_p
Δu^*	Change in the internal energy from the austenite to martensite phase
ε	Strain
$\dot{\varepsilon}$	Strain rate
ϵ_{Ar}	Intermolecular force parameter for argon
ε_{crit}	Critical strain for SIM to form
ϵ_i	Intermolecular force parameter for alloy element *i*
$\epsilon_{i,Ar}$	Effect intermolecular force parameter for alloy element *i* in argon
ε_o	Normalized transformation strain
ε_{on}	Normalized transformation strain for the *n*th pseudoelastic region
ε_t	Transformation strain

ε_r	Residual strain
ε_x	Strain in the x-direction
ε_y	Strain in the y-direction
ε_z	Strain in the z-direction
θ	Angle in radians
κ	Scaling factor that converts diffusivity to Ni concentration
ν	Poisson's ratio
ξ	Volume fraction of the martensite phase
$\dot{\xi}_{A\to M}$	Rate of change in the martensite volume fraction for the austenite to martensite transformation
$\dot{\xi}_{M\to \mathrm{A}}$	Rate of change in the martensite volume fraction for the martensite to austenite transformation
Ξ	Scaling factor to adjust for turbulence
π	The number pi
π^f	Thermodynamic driving force associated with the phase transformation
π_0^{f}	Thermodynamic driving force associated with the stress-free state
ρ	Density
ς	Spread of transformation peak at 1/3 of maximum height
σ	Stress
σ_{Ar}	Collision diameter of argon
σ^{AMi}	Plateau stress for the austenite to martensite transformation for region *i*
σ_{est}	Standard error of estimation
σ_i	Collision diameter of alloy element *i*
$\sigma_{i,Ar}$	Effective collision diameter of alloy element *i* and argon
σ^{MAi}	Plateau stress for the martensite to austenite transformation for region *i*
σ_{SIM}	Critical stress to induce SIM
ϕ_{it}	Internal configuration energy
χ	Conversion factor between laser pulse power and temperature
$\Omega_{D,i}$	Collision integral for alloy element *i*

Chapter 1: Introduction

1.1 Background

The unique shape memory effect (SME) and pseudoelasticity (PE) properties of shape memory alloys (SMAs) have made them valuable engineering materials [1, 2] with the potential to be used as dampers and actuators [3-6]. The industries interested in applying SMAs range from biomedical to automotive and aerospace to microelectronics. As the applications for SMAs become increasingly complex, researchers have attempted to increase functionality by locally embedding additional memories in monolithic components using various processing techniques, including direct electric resistance heat treatment [7, 8], direct hot air heat treatment [7], gradient annealing [9, 10], short time annealing [11, 12], powder metallurgy [13-16], doping with third elements [17], welding/joining [18, 19] and more recently laser-induced vaporization [20-23].

These technologies take advantage of changes in microstructure and/or chemical composition to alter the pseudoelastic and shape memory properties of NiTi SMAs. However, a systematic investigation of how laser parameters alter the chemical composition has never been performed. Some research has been done on how multiple pulses of a certain laser pulse profile removes a set amount of Ni with each pulse [22]. However, the effect of peak power or pulse duration on the Ni vaporization rate for NiTi has not been investigated. Nor has the effect of the nominal spot size or the specimen geometry. Understanding these relationships and developing a model to predict the Ni vaporization rate (and resulting chemical composition) is crucial for advancing shorter development times for laser modified NiTi SMA devices because of the relationship between Ni concentration and physical properties (such as transformation temperatures).

Another hindrance to accelerated development of multiple memory SMAs is the ability to model their mechanical functionality. In recent decades, a substantial amount of work has been applied towards establishing phenomenological constitutive models that accurately describe the macroscopic thermomechanical response of SMAs [24-27]. Many of these models use a thermodynamic structure and select the martensitic volume fraction as an internal variable to account for the effect of the changing microstructure. Improvements to the accuracy of modelling SMAs were achieved by using different transformation functions to distinguish the asymmetric

response demonstrated by SMAs in tension and compression [28-30]. While these models are sufficient for homogeneous materials they do not account for functionally graded materials, that is materials with spatially varying material properties. Detailed studies on modeling the mechanical performance of laser processed NiTi materials are presented in this report.

1.2 Objectives

The motivation behind this work was to develop models for multiple memory SMAs that encompass the tuning of the local composition and the prediction of mechanical performance, which is directly related to industry needs that must be satisfied before the benefits of multifunctional NiTi SMAs can be fully realized. Currently, only limited studies have been performed on laser processing of NiTi, and none on modelling multiple memories in a monolithic material. Therefore, a comprehensive analysis of a pulsed Nd:YAG laser process was undertaken, pertaining to the following crucial objectives:

1. Modeling of the relative rates of Ni and Ti vaporization during laser processing to facilitate predetermination of laser parameters for precise composition tuning.
2. Develop new models capable of predicting multiple pseudoelastic responses from a monolithic material.
3. Build an understanding of the effects of the texture on the material response of as-processed NiTi wires.
4. Apply multiple memory SMAs to new mechanical designs.

1.3 Thesis Organization

This thesis is divided into nine chapters, though the major research results can be further subdivided into four major aspects, as shown in Table 1.1. Improving the analysis and characterization methods are a necessary starting point to ensure the accuracy of the material properties being captured. Enhancing the basic understanding of the materials nature and behavior is vital in developing models that are both useful and meaningful. The final two categories are the novel models and design applications that were developed from this work. A detailed overview of each chapter is given below.

Table 1.1: Table depicting the break-down of each major research area.

	Improved Analysis/ Characterization Methods	Enhanced Knowledge of Material Properties	Novel Models for Design, Fabrication and Performance	Novel Design Applications
Chapter 4	Deconvolution of Overlapping DSC Peaks	Effect of Surface Oxide on Alloy Element Vaporization	Model Change in Ni concentration after Laser Processing	
Chapter 5	Implemented Usage of Visual Extensometer		1-D Model of Multiple Pseudoelastic Plateaus in Tension	
Chapter 6	Extraction of Compressive Behavior from Three-point-bend Tests	Effect of Microstructure on Bending Properties Incompressible Behavior of Phase Transformations	Bending Model Based on Grain Orientation	"Zebra" Wire Capable of Controlling Bending Curvature
Chapter 7			Model for Predicting Stroke Displacement of Self-Biasing Spring Actuators	One-Stage and Two-Stage Self-Biasing Spring Actuators
Used by Industrial Partner	Implemented Usage of Visual Extensometer		1-D Model Applied to SmartArch™ Orthodontic Arch Wires	Functionally Gradient Medical Devices
	Implemented Usage of Cantilever Bend Tests			Functionally Gradient Sporting Goods

Chapter 2 details a thorough and relevant literature review of the physical metallurgy, phase dynamics, material properties, laser processing methods and current modeling methods. In this chapter, the limitations of current material models as well as our understanding of transformation thermodynamics are identified. The novel localized laser processing technology is explained along with the motivation behind this work.

In Chapter 3 the experimental materials, methods and conditions used in this comprehensive study are described in detail.

Chapter 4 reports on the changes in composition observed after laser processing. Detailed thermal analysis along with a novel method for deconvolving overlapping DSC peaks are presented. A model for determining the relative rates of vaporization of Ni and Ti (and thus determining the change in composition) was also developed.

Chapter 5 details the results achieved with respect to the development of a novel one-dimensional model for multiple pseudoelastic plateaus. It also presents the findings obtained concerning the newly developed analysis techniques proposed by the study.

In Chapter 6, the effects of grain orientation on the mechanical performance of as-processed NiTi wires is investigated. Also, the anisotropic and incompressible behavior of the austenite to R-phase transformation is examined.

Chapter 7 looks at the design and fabrication of a self-biasing spring actuator implementing the multiple memory SMA. A novel method for predicting the stroke displacement of the self-biasing actuator is presented.

The main conclusions of this research and proposed areas for future research are documented in Chapter 8.

Finally, Chapter 9 lists the significant contributions to research and development by the author.

Chapter 2: Literature Review

2.1 NiTi Shape Memory Alloy

The study of modelling laser processed SMAs requires a fundamental understanding of the crystallography and microstructure, phase transformation kinetics, various manufacturing methodologies, and the effect all of these have on the material properties. As well, an in-depth understanding of the current modeling methods is essential. The following literature review attempts to summarize the immense amounts of knowledge in all afore mentioned areas.

2.1.1 Physical Metallurgy

NiTi SMAs are considered to be a stoichiometric intermetallic compound (IMC) [31]. Figure 2.1 shows the Ti-Ni phase diagram. With compositions close to 50 at.% Ni, NiTi SMAs are bound by the Ti_2Ni and $TiNi_3$ phases (see Figure 2.1b). Ti_2Ni IMC formation is undesirable due to its brittleness, which can lead to cracking of Ti-rich welds [32] and will occur when the melt pool composition is on the Ti-rich side (left side in Figure 2.1b) of the congruency point.

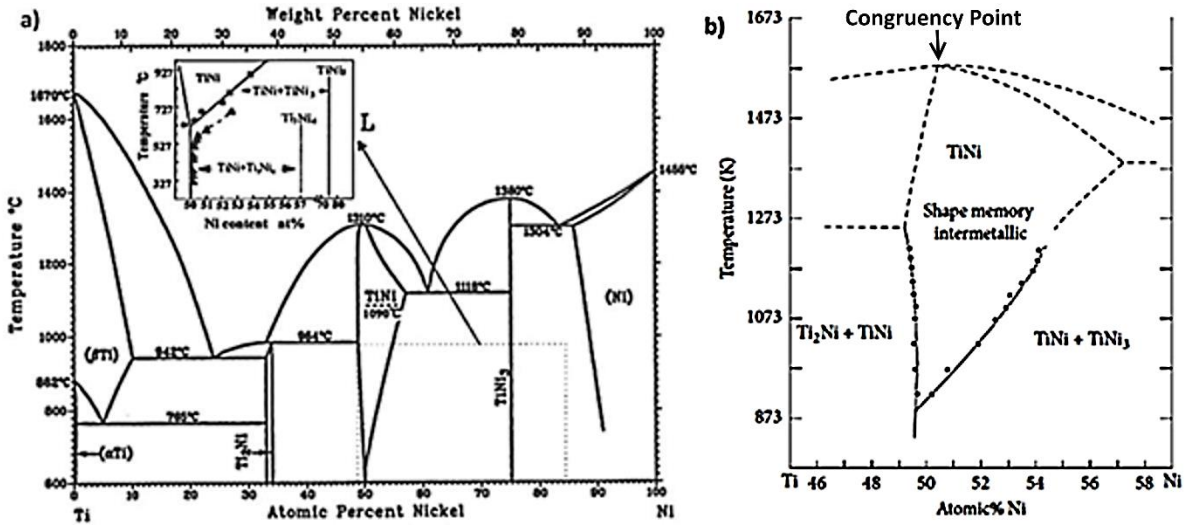

Figure 2.1: a) Binary Ti-Ni phase diagram, inset shows the metastable Ni-rich TiNi IMCs. Reprinted from Ref. [33] with permission from Elsevier. b) close-up of metastable TiNi IMC. Reproduced from Ref [34] open access article distributed under the Creative Commons Attribution License.

The constituent species are immiscible at room temperature; however, short heat treatment times at temperatures ranging from 300 °C to 600 °C can form Ni-rich metastable IMCs consisting of

Ti_3Ni_4 and Ti_2Ni_3 [31, 33, 35], as indicated by the insert in Figure 2.1a. The solubility of Ni increases significantly above 650 °C, permitting the formation of Ni-rich SMAs through quenching [33]. NiTi is presently the only IMC known to possess SMA properties, but precipitation of the other Ni-rich IMCs into the NiTi matrix can be used to modify the properties of the NiTi SMA [31].

2.1.2 Reversible Phase Transformation

The remarkable shape memory properties of NiTi SMAs are due to a reversible solid-state phase transformation from martensite to austenite that transpires when the material is exposed to an external stimulus, such as a change in temperature or applied stress. This martensitic transformation occurs between the parent B2 austenite phase and the B19' martensite phase [34, 36, 37]. The austenite phase has a simple cubic CsCl-type ordered structure with a lattice parameter of 0.3015 nm [38], shown in Figure 2.2c. The martensite phase has a monoclinic structure with lattice parameters a = 0.2889, b = 0.4120 and c = 0.4622 nm with a monoclinic angle β = 96.8° [39], shown in Figure 2.2a.

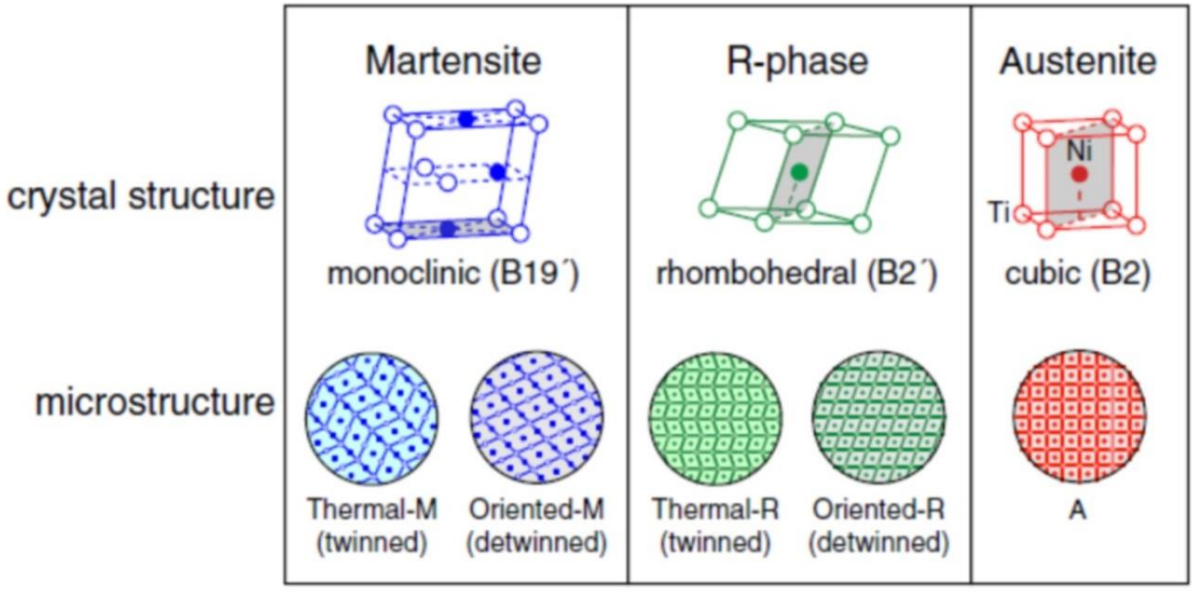

Figure 2.2: a) Monoclinic B19' martensite phase, b) rhombohedral B2' R-phase and c) cubic B2 austenite phase. Reprinted with permission from Springer Nature: [40].

This transformation does not involve any diffusional atomic migration, and therefore occurs very rapidly [41]. The maximum strain accommodated by the structure without plastic deformation can be restricted by the presence of precipitates or heavy cold working [42, 43]. This results in an

intermediate transformation to a rhombohedral (R-phase) structure (see Figure 2.2b), which competes with the B19' martensite phase [44, 45]. The R-phase will be preferred over the B19' martensite phase because R-phase has a significantly smaller lattice deformation [33, 46, 47]. This in turn leads to only a small amount of strain accommodation when austenite transforms to R-phase [43, 48].

The term 'martensite' was first used to define quench hardened steel microstructures; however, it is now used to describe several materials that have varying crystallographic properties and growth kinetics [49]. During thermally-induced martensitic transformation in steel alloys, atomic movement is accommodated by permanent dislocation motions. The crystallographic lattice undergoes an irreversible shearing distortion, which alters the volume and shape of the material at a macroscopic level [50].

In contrast, NiTi undergoes a reversible martensitic transformation. Twinning of the crystal lattice allows for a change in shape, but no change in volume occurs [36-39, 51, 52]. Twinned martensitic transformations of NiTi SMAs are considered to be reversible since the microstructures of the austenite and martensite phases can be cyclically restored with almost no buildup of lattice defects [50, 53]. In order for this transformation to be fully reversible, twinning must be the prevailing accommodation process, as is the case for NiTi SMAs [36]; whereas for steel alloys, twinning can occur but slipping is dominant mechanism.

The difference between slipping and twinning during a martensitic transformation is shown in Figure 2.3. During slip, atomic planes slide past one another and form permanent dislocations in the crystal lattice. Conversely, twinning is the formation of a mirrored structure due to atomic displacement across a particular atomic plane [41]. Twinning occurs in NiTi SMAs due to a lack of symmetry and available slip-systems, which increases the driving force for producing twins after the martensitic phase transformation. Furthermore, the twinned lattice can accommodate an externally applied stress by undergoing a recoverable detwinning process wherein the twinned lattices reorient themselves in response to the applied stress [31, 54]. This is possible because there are no bonds broken during the twinning process and thus the twins have low energy and are highly mobile. Additionally, the reversible phase transformation is achieved by there being only one low energy state for the parent phase B2 austenite while multiple low energy product phases for B19' martensite can form [55].

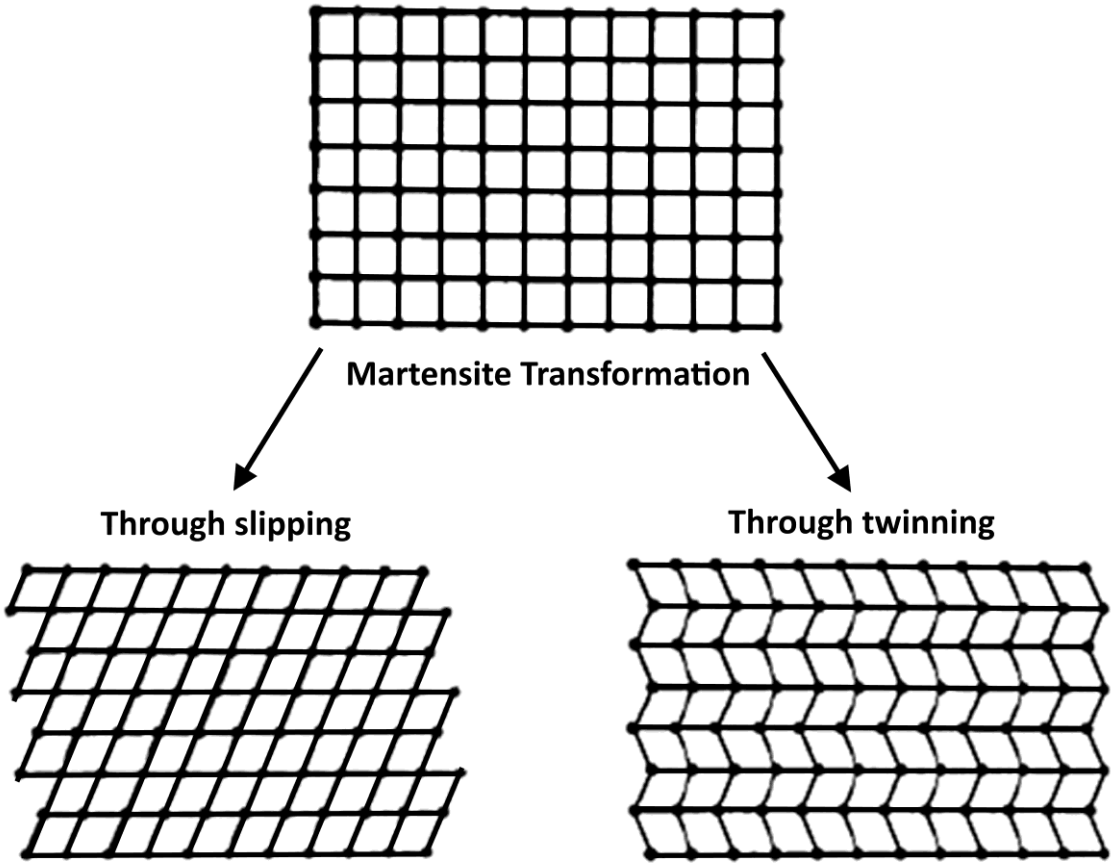

Figure 2.3: Schematic representation of the atomic movements associated with martensitic transformation by a) slipping and b) twinning.

2.1.3 The Shape Memory Effect

When twinned, martensite facilitates a large amount of strain and detwins, a biased distribution of martensite variants, or in the extreme case, a single variant form [41]. Heating above the transformation temperature causes austenite to form. Austenite is symmetrical with a single variant; thus, it recovers the original shape if unloaded [41]. This property of thermally induced phase transformation is referred to as the shape memory effect (SME), as illustrated in Figure 2.4. Shapes can be programmed into the NiTi SMA by way of a shape-setting technique where the material is fixed in a specific shape during a heat treatment procedure at a temperature range of 325-525 °C for 5-30 min, followed by a water quench [56].

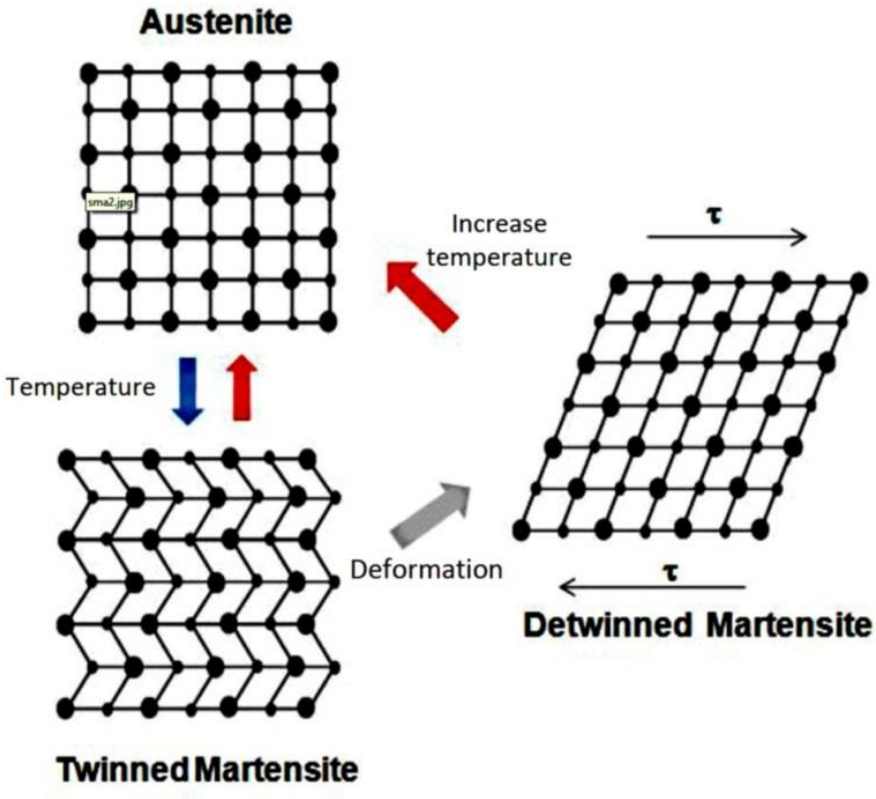

Figure 2.4: Crystallography of the SME. From Ref. [57] Copyright © Billy Tam. Reproduced with permission. All rights reserved.

Cooling below the transformation temperature allows twinned martensite to be formed once again. This two-way phase transformation occurs in different temperature ranges between -100 °C and 100 °C, depending on the composition of the NiTi SMA. The transformation is characterized by four temperatures: austenite start (A_s), austenite finish (A_f), martensite start (M_s), and martensite finish (M_f), which can be measured through Differential Scanning Calorimetry (DSC) analysis according to ASTM F2004-05(2010) standard [58]. These are the temperatures at which the martensite-to-austenite transformation and the reverse transformation begin and end. A typical DSC curve of NiTi SMA is shown in Figure 2.5.

A hysteresis is observed between the heating and cooling transformation, which is due to the frictional forces encountered during the lattice movement across interfaces and defects [41]. The magnitude of hysteresis is generally 10 °C to 50 °C, depending on the composition, processing history and stress state of the material [60-62]. However, there is limited plastic deformation during transformation, which maintains coherency between phases and enables them to grow and shrink depending on the thermodynamics of the system [49, 63]. In contrast, the martensite

formation in carbon steel is not reversible in part because of the large volume change between phases (see Table 2.1), which produces large plastic strains [64].

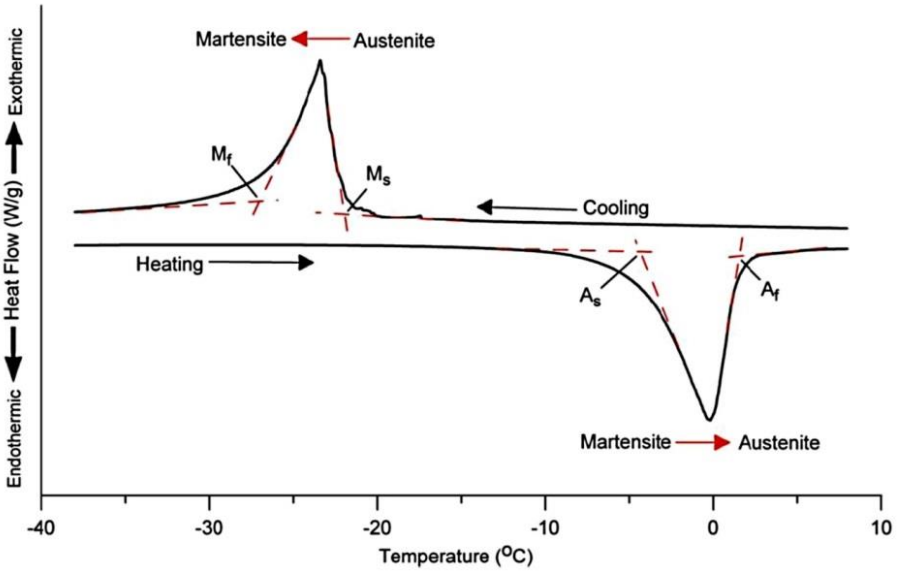

Figure 2.5: A Typical DSC curve of NiTi SMA. From Ref. [59] Copyright © Andrew Pequegnat. Reproduced with permission. All rights reserved.

Table 2.1: Percent volume change between austenite and martensite [63].

Alloy	NiTi	CuAlNi	FeNiC Alloy
%vol. change	0.023	0.297	-2.586

2.1.4 Pseudoelasticity

When NiTi SMAs are in the austenite phase, it is possible for them to be transformed into martensite by way of an applied stress. When stress (not temperature) is the stabilizer, the martensite formed is known as stress-induced martensite (SIM). This transformation process is called pseudoelasticity (PE), and the mechanical response is similar to detwinning. The principal action varies slightly and is divided into three regions, as shown in Figure 2.6a. In region (1) the austenite is deformed elastically in accordance with Hooke's Law. At a critical stress (σ_{SIM}), SIM is gradually formed at the expenditure of the parent austenite phase until all of the parent phase is consumed. The result of this transformation is the plateau in region (2). Further straining results in the elastic (and then plastic) deformation of the detwinned martensite in region (3), which is again

obeying Hooke's Law. If stress is removed in region (2), a reverse transformation takes place at a lower stress (σ_r) due to a transformational hysteresis [58], shown in Figure 2.6b. This stress hysteresis is similar to the thermal hysteresis associated with SME.

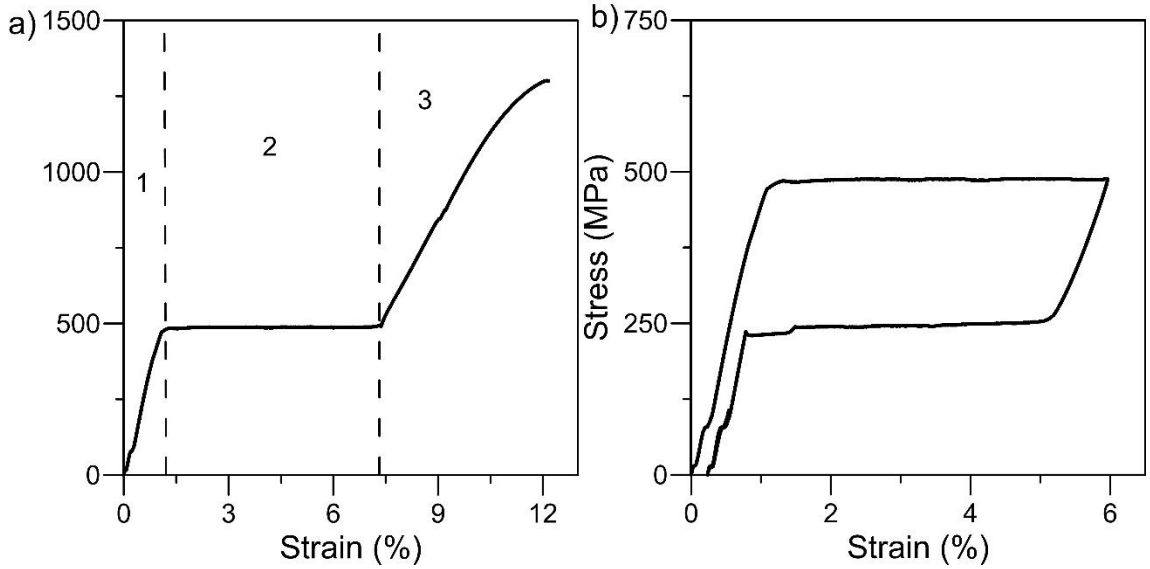

Figure 2.6: a) Stress-strain curve of pseudoelastic NiTi exhibiting the following regions: 1) elastic response of austenite, 2) pseudoelastic plateau caused by stress-induced transformation and 3) elastic and plastic deformation of martensite. b) Stress-strain curve of NiTi when the load is released in region 2).

The stable phase at the working temperature determines which functional property is active. Below M_f, the principal functional property is SME, while PE is observed above A_f but below the martensite deformation temperature (M_d), which is the highest temperature that martensite can form from austenite as a result of an applied stress. As the temperature of NiTi increases above A_f, the thermodynamic stability of the austenite phase also increases, which causes a parallel increase in the stress needed to form SIM. This stress increase has been observed to vary linearly with temperature, as shown in Figure 2.7 and follows a Clausius-Clapeyron relation [65-68]. The Clausius-Clapeyron relationship is provided in Equation (2.1) below [66]:

$$\frac{d\sigma}{dT} = \frac{-\rho \Delta H}{T_0 \varepsilon_t} \qquad \textbf{(Equation 2.1)}$$

where $d\sigma$ is the change in σ_{SIM}, dT is the change in test temperature, ρ is the material density, ΔH is the latent heat of transformation, ε_t is the transformation strain and T_0 is the equilibrium temperature of transformation, which is defined as [66]:

$$T_0 = \frac{M_s + A_f}{2} \qquad \textbf{(Equation 2.2)}$$

The left side of Equation (2.1) is the stress rate, which varies from 3 to 20 MPa/°C, depending on the processing history of the material [67]. At temperatures above M_d, the specimen begins to fail before the onset of PE. Figure 2.8 illustrates the stress-temperature conditions for SME and PE in NiTi. At temperatures between M_s and M_f or A_s and A_f the two phases will co-exist because the transformation is incomplete.

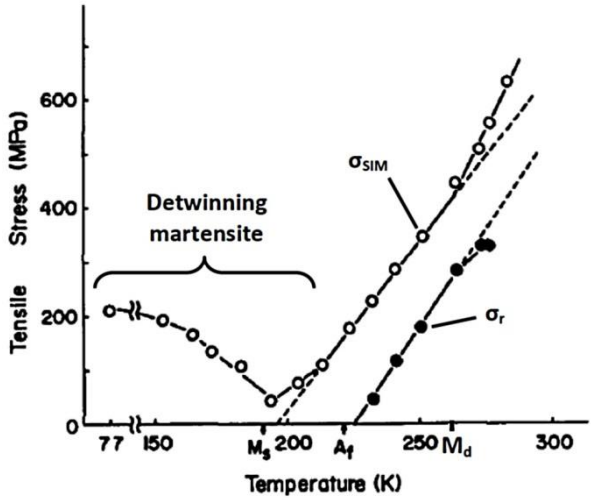

Figure 2.7: Plateau stress versus temperature plot. Dashed lines represent the linear Clausius-Clapeyron relation between σ_{SIM} (empty circles) and σ_r (solid circles) and temperature. Martensite detwinning occurs below A_f and plastic deformation of austenite occurs above M_d causing deviations from the Clausius-Clapeyron relationship. Reprinted from Ref. [65] with permission from Elsevier.

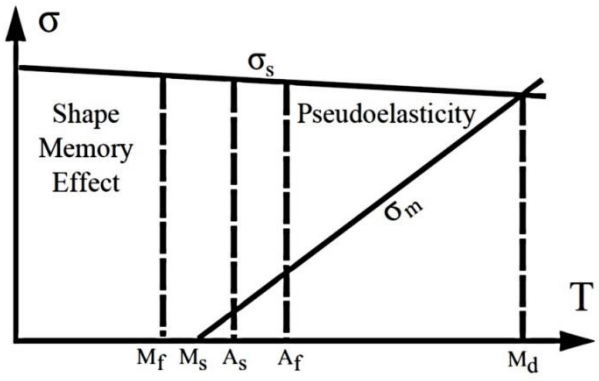

Figure 2.8: Stress-temperature conditions for NiTi SMAs exhibiting SME and PE. Reused with permission from Taylor & Francis: [69].

2.1.5 Effects of Composition

The functional properties of NiTi SMA are exceptionally sensitive to alloy composition. The transformation temperatures are very sensitive to the mole fraction of Ni for concentrations above 50 at.%. However, for Ni concentrations below 50 at.%, the transformation temperature remains almost constant at approximately 65 °C due to the insolubility of Ti below 50 at.% (Figure 2.1). The relationship between composition and transformation temperature is shown in Figure 2.9. In addition to shifting the transformation temperature, changes in composition indirectly control the amount of stress required to form SIM, since a lower A_f is linked with a more stable austenite phase [70]. Precise control over the final composition of the NiTi is critical to obtain the desired mechanical properties. Typically, commercial NiTi components require ±5 °C which means a composition tolerance of 0.05 at. % is necessary [71].

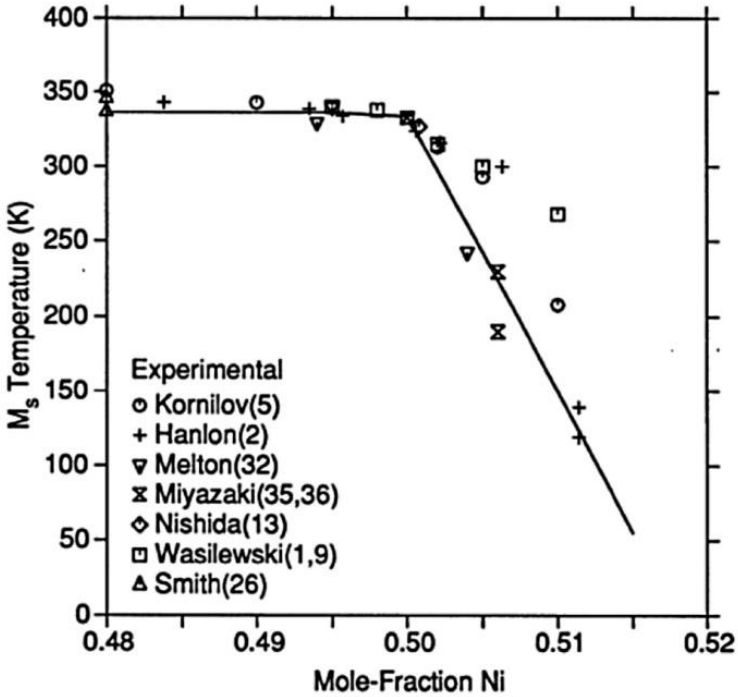

Figure 2.9: Relationship between mole-fraction of Ni and the M_s temperature in binary NiTi SMAs. Reprinted with permission from Springer Nature: [72].

2.1.6 Heat Treatments

As mentioned in Section 2.1.1 Physical Metallurgy, the formation of Ni-rich precipitates through post-process heat treatment is used to alter the functional properties of the NiTi SMA. These precipitates deplete the NiTi matrix of Ni, causing significant increases in transformation

temperatures. Increasing the transformation temperature by this method leads to a decrease in the σ_{SIM} due to a reduction in the stability of austenite [70]. A time-temperature-transformation diagram developed by Pelton *et al.* [67] is shown in Figure 2.10 illustrating the relationship between heat treatment time and transformation temperature.

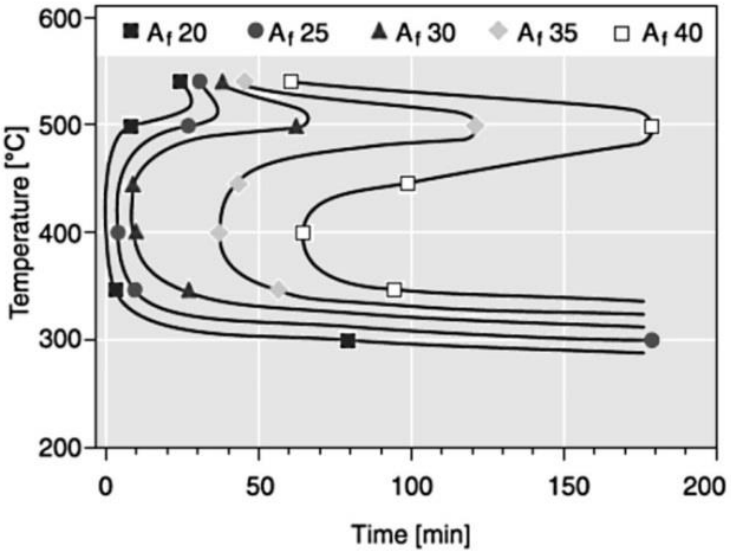

Figure 2.10: Time-temperature-transformation (TTT) diagram showing the relationship between heat treatment temperature, time, and A_f transformation temperatures. Reused with permission from Taylor & Francis: [67].

The combination of percent cold work, heating temperature and time dictate the final microstructure [67, 71]. At intermediate temperatures (350-475 °C) the nucleation and diffusion processes are optimized for maximum, coherent fine precipitate formation [67]. Heat treatment temperatures around 400 °C for approximately 1 hour have been determined to provide the most stable properties for both Ni-rich and Ti-rich NiTi [33, 56, 73, 74]. Quenching after heat treatment is required to avoid the formation of Ni_3Ti [75].

The Differential Thermal Analysis (DTA) can be used to show the effects of cold work followed by different annealing temperatures. Deformation introduces dislocations into the NiTi matrix, decreasing and broadening the phase transformation temperatures and peaks [76, 77], introducing R-phase (see Section 2.1.2 Reversible Phase Transformation), and can even suppress the martensite phase transformation from occurring all together, reducing the heat of transformation [77]. Subsequent heat treatments narrow the transformation peaks and shift them higher.

Depending on the heat treatment temperatures R-phase may also remain as identified by the presence of two phase transformation peaks.

2.1.7 Texture Dependence of Deformation

Single crystals of NiTi have anisotropic properties with different moduli of elasticity, amount of recoverable strain, and hysteresis of stress plateaus when loaded in different crystallographic directions [78]. This is due in part to the fact that the austenite phase has only the <100>{011} slip mode as a deformation pathway [33]. The unidirectional nature of shear strain on the habit planes contributes to this anisotropic, asymmetric deformation [79]. This causes the recoverable tensile strain to range from 3% in the <100> direction to 10.5% in the <111> direction (Figure 2.11) [80].

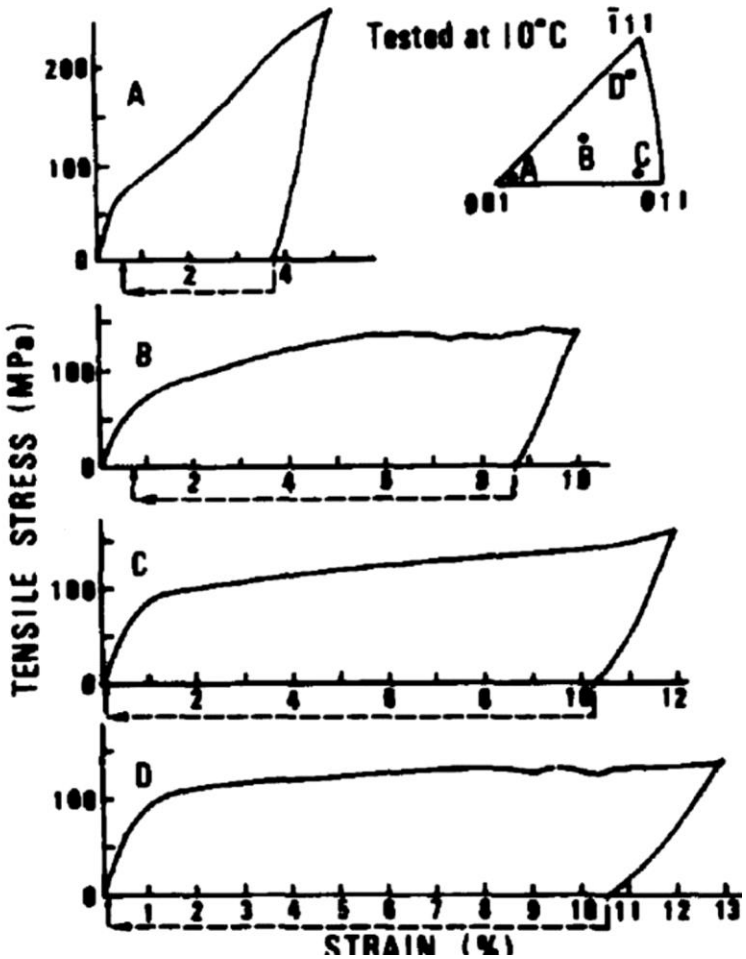

Figure 2.11: Grain orientation dependence of recoverable strain of a single crystal. Reprinted from Ref. [80] with permission from Elsevier.

In a polycrystalline material, grains are connected at the grain boundaries and need to move together while sustaining a continuous displacement across the grain boundaries [63]. When the boundary is parallel to the tensile load it is similar to single crystal deformation; however, when it is perpendicular to the tensile load it exhibits a complex deformation that is brittle [81, 82]. Triple junctions are more complicated and require the creation of complex microstructures to accommodate the strain, thus restricting the deformation in these regions, which can lead to localized plasticity even at macroscopically low stresses [63, 83].

The anisotropic properties of a single NiTi crystal make the deformation properties of polycrystalline NiTi extremely dependent on the texture. Material properties, such as the elastic modulus, yield stress, ductility, work hardening, transformation stresses and hysteresis, transformation strains and recoverable strain can all change depending on the texture and relative direction of the load [84-87]. An example of this anisotropy is the difference of martensite deformation in tension and compression seen in Figure 2.12. The grains in this example were oriented such that they provided more recoverable modes of deformation in tension than compression, where the tensile specimens has PE recovery and the compressive had almost perfect elastic recovery because they were plastically deformed [88-90].

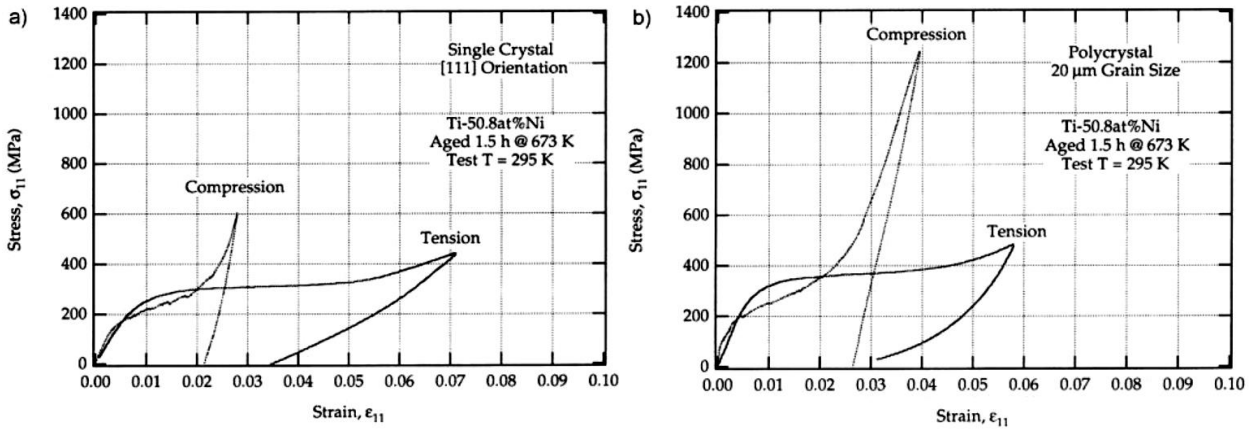

Figure 2.12: Tension and compression data for a) single crystal [111] and b) polycrystal with <111> texture. Reprinted from Ref. [89] with permission from Elsevier.

2.2 Manufacturing Methods for NiTi SMAs

2.2.1 Traditional Casting Methods

Traditionally NiTi SMAs are fabricated using vacuum induction melting (VIM) or vacuum arc re-melting (VAR) technologies which produce ingots with inclusion sizes and densities lower than the ASTM F2063 standard [98]. Typically, commercial NiTi components require ±5 °C which means a composition tolerance of 0.05 at.% is necessary[56, 71, 100, 101]. The VIM process uses an induction coil heated graphite crucible, which contaminates the melt with carbon, although the ingots produced have excellent homogeneity since mixing is assisted by eddy currents [71]. This carbon contamination can be reduced either by coating the graphite crucible with the Ti bars/disk to create a TiC diffusion barrier, or by reducing the time the ingot is molten, or by running consecutive ingots [102, 103]. The VAR process uses a DC current to melt compacted Ni and Ti electrodes into a water-cooled copper crucible, which results in significantly less contamination since the melted region is never in direct contact with the crucible [56]. However, lack of complete melting of the ingot creates inhomogeneity that can rectified by flipping the ingot, or by cutting it up and re-melting it several times, although but this adds time, cost and the risk of atmospheric contamination [71]. A combination of the two processes, or the VIM/VAR process, produces a higher purity VAR ingot in the initial melt and gains the homogeneity of the VIM process after the second melt [71].

There is a push by the robotics, automotive and medical industries for smaller cross-sectional components and very fine wires with fast actuation capabilities [104-106]. The ASTM F2063 standard for inclusion size is no longer relevant for the size scale of these desired components because the defects consume a much larger percentage of the cross-sectional area. Higher purity ingots are necessary to meet this requirement [106], so high purity VIM and VAR methods have been established to help with this demand [107]. Additionally, E-beam vacuum melting has been developed to prepare higher purity NiTi alloys; however, the current production size is limited to 2 kg [108-110]. Obstacles in the application of this technique include difficulty in controlling the composition due to Ni evaporation during E-beam melting.

In the as-cast state NiTi SMAs have a random crystal texture, low yield stress, poor ductility, limited SMA properties and poor fracture resistance properties [31, 56, 106, 111]. As was shown

in Figure 2.8, a particular yield stress is required to prevent dislocation motion, thus allowing for ideal SME and PE properties (i.e. no build-up of residual strain) [69]. Further processing is required for acceptable stability, and fatigue. NiTi alloys can be strengthened through several different mechanisms, which include: grain refinement [112], strain-hardening [70], and precipitation hardening (i.e. Ni_4Ti_3 precipitates) [67]. Combinations of hot working, cold working and heat treatments are applied during manufacturing [33]. This results in superior SME and PE properties, a wider range of temperatures at which PE occurs [33], and a more stable low-cycle performance [113].

2.2.2 Novel Manufacturing Methods

Traditional SMA casting methods can be functionally limiting as they only produce monolithic components with a single set of phase transformation characteristics. Novel material processing protocols are therefore required to overcome these challenges to enable further innovation and application. Several methods have been developed to locally control the properties of NiTi based components, improving functionality and increasing design flexibility.

Some methods involve using localized heat treatments to alter the microstructure in a specific region. These methods include direct electric resistance heat treatment [7, 8], direct hot air heat treatment [7], gradient annealing [9, 10] and short-time annealing [11, 12]. These techniques have been used to make NiTi materials containing both PE and SME properties [10, 114, 115]. However, these local heat treatment methods can only be easily applied to simple geometries, they are time intensive, and don't offer high resolution in functional properties [7-10].

Powder metallurgy combines powders of pre-alloyed or elemental Ni and Ti through blending, pressing and sintering [13-16]. Compared with the traditional casting methods, powder metallurgy provides better control over transformation temperatures as it does not involve a melting process which causes composition inaccuracy [56]. This method has been successfully used to make proof-of-concept multi-phase actuators [116]; however, they have exhibited issues with porosity, poor surface finish and composition inhomogeneity that leads to undesirable IMC formations [14-16].

The joining of multiple NiTi alloys has shown to be somewhat effective for simple devices [18, 19, 117]. The challenges associated with joining, such as joining dissimilar SMAs, IMC formation,

large freezing ranges and more complex joint geometries, have limited the application of this method [71].

Laser processing technologies that locally modify the bulk composition and/or microstructure [10, 20-23] offer promising solutions to monolithic NiTi devices with improved functionality. These processes have high spatial resolution, high manufacturing speeds, low heat input, high cooling rates, and the high quality inherent of laser processes, which makes them ideal methods for modifying SMAs. Laser processing is the basis of creating the multiple memory shape memory alloys in this study and will be discussed in greater detail in the following sections.

2.2.3 Wire Drawing SMAs

NiTi SMAs require thin film dry lubricants, such as MoS_2 [91]. If the frictional work raises the temperature of the wire too high, it will result in the transformation from the preferred marforming to the undesired ausforming [92]. Final cold work percentages between 20-50 % have been identified as being suitable for good physical properties, transformation stability and fatigue life [56, 67, 93-95]. The most complete work on NiTi wire manufacturing is by Grossmann *et al.*, but it leaves the last proprietary cold work steps unmentioned [96]. The number of passes between equivalent reductions can affect the uniformity of hardness across the cross section [91]. Multiple passes around the M_s temperature result in the lowest critical stress for deformation, reducing the drawing stress and maximizing the number of passes possible between annealing stages. Drawing in R-phase results in an even lower stress because it has the lowest critical stress for deformation [97]. After wire drawing, the texture of the material is in the <111> direction, which is the direction with the largest recoverable strain (see section 2.1.7 Texture Dependence of Deformation) [98].

2.3 Laser Fundamentals

The term laser originated as an acronym for “light amplification by stimulated emission of radiation” (LASER). The light that is emitted from a laser is spatially and temporally coherent with a very low diffraction, and transmittance optics can be used to focus the high intensity beam into a single spot with a high energy density [118, 119]. A laser system is comprised of three main components: an amplifying medium, a means of stimulating the medium to its amplifying state (pump source) and an optical resonator [119]. The amplifying medium consists of a special

material that produces energy-carrying photons when excited. The pump source is determined by the type of active medium being used. The optical resonator is composed of two parallel mirrors, one that is completely reflective and the other that is partially reflective. They are positioned around the active medium to filter and transmit photons that fulfill the specific requirements for oscillation [119].

When activated, atoms are energized from the ground state to the excited state by pumping. Incoherent photons are then released when the atoms relax back to the ground state. Photons that do not travel parallel to the optical axis of the laser are lost in the resonator; however, photons that travel parallel to the optical axis are oscillated in the resonator with the possibility of inducing stimulated emission, which in turn produces coherent photons [119]. By increasing the population of unidirectional photons, a high energy laser beam is created.

When the number of photons being amplified per unit time exceeds the number being absorbed, it is referred to as a population inversion, which is required to amplify the quantity of light [120]. When this occurs in the cavity, the laser interacts with the excited atoms and lowers the energy level, simultaneously releasing additional quanta of light [121]. If this does not occur, the energy is absorbed from the laser to energize the electrons, thus reducing the energy of the laser beam. After amplification, the beam is released through a partially reflective mirror in the cavity.

2.3.1 Pulsed Nd:YAG Laser Processing

Each type of laser available generates light with a unique wavelength, which depends on the material used to make the semiconductor. They range from 0.1 μm to 10 μm, with Nd:YAG producing one of the shorter wavelengths available. The energy emitted by an Nd:YAG laser can be more efficiently absorbed by most materials making it more efficient at melting a specific volume of material compared to other lasers. Commercially available Nd:YAG lasers are generally rated with average output powers from 0.3 kW to 3 kW, which is ideal for small scale use [119].

The cavity assembly is composed of an active medium, pumping source, and resonator. When excited, an yttrium aluminum garnet (YAG) crystal doped with neodymium (Nd) atoms produces photons with a wavelength of 1064 nm [119]. Historically, the pump source for an Nd:YAG laser was a flash lamp [119]; however, modern Nd:YAG lasers are diode pumped. The laser output is

transmitted through the input coupling optics and into an optical fiber connected to the working head before being delivered to the workpiece. The capability of delivering photons via fiber optics is advantageous for fabrication of complex components.

2.3.2 Processing Parameters

Several key parameters characterize the laser pulses produced by a Nd:YAG laser, including pulse width, peak power, frequency, travel speed and defocus distance. Figure 2.13 shows a schematic of a temporal profile of laser pulses produced with the Nd:YAG laser process. Peak power is the maximum power of the laser pulse and pulse width is the duration of the laser pulse, which typically varies from 0.2 to 20 ms. Pulse energy is determined by the area under each laser pulse. The average power transferred to the workpiece is a function of pulse energy and frequency. However, substantial energy losses can occur due to factors such as reflection, making it difficult to exactly quantify the energy absorbed by the workpiece [123].

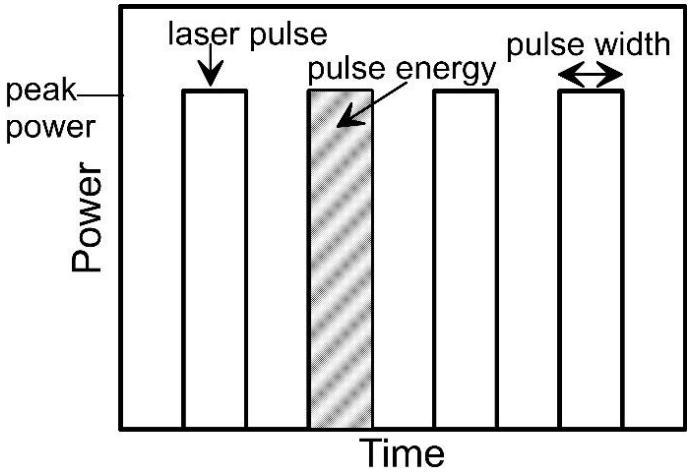

Figure 2.13: Schematic of a pulsed Nd:YAG output.

The advantage of laser processing is the ability to achieve a high energy density and maximize penetration of the workpiece. This is achieved by focusing the light to a minimum beam waist diameter [119], as shown in Figure 2.14. As the beam exits the lens, it converges down to the minimum beam waist diameter. A laser operating in this convergence range has the highest energy efficiency. An offset from the focal length results in a reduction in the power density as the beam begins to diverge from the minimum beam waist diameter. Focus spot size depends on the combined effects of optics, laser characteristics and welding parameters. The focus position

relative to the workpiece depends on the welding mode (see Section 2.3.4 Laser Beam Modes) and geometry [119]. The general rule for welding is to focus at a distance where the maximum penetration depth is attained through experimental verification.

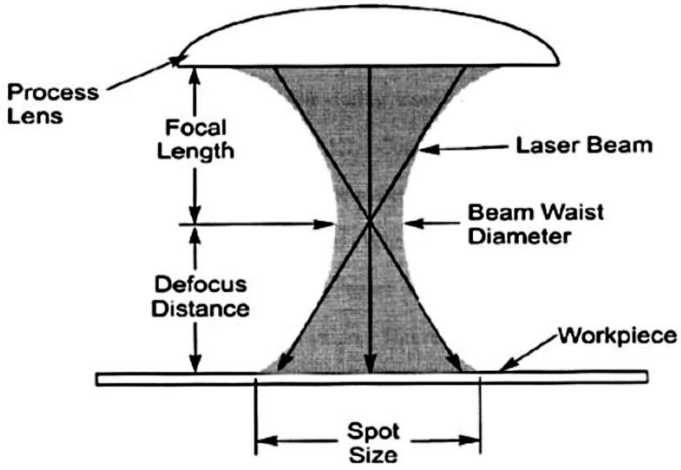

Figure 2.14: Schematic of the propagation and convergence of a laser beam. From Ref. [122] Copyright © Elliot Biro. Reproduced with permission. All rights reserved.

2.3.3 Shielding Gas

Since most metals oxidize at high temperatures, a shielding gas of argon or helium is generally used to prevent a reaction of oxygen or nitrogen with the molten weld pool. Oxide inclusions are most often detrimental to the material properties [118, 119]. Shielding is tremendously important for NiTi SMAs, which have a high affinity for oxygen and, to a lesser extent, nitrogen. Selection of the proper shielding gas has also been shown to enhance the transmission of the incident laser beam for absorption by the workpiece [120].

2.3.4 Laser Beam Modes

The incident laser beam is absorbed in one of two modes during laser welding – conduction and keyhole, as shown in Figure 2.15. During conduction mode, the laser intensity is only adequate enough to melt the workpiece. The pool first forms at the surface and grows due to conduction in all directions, which results in a semi-elliptical shape [123]. Since the laser energy is only absorbed by the top surface of the material, surface reflection can greatly reduce the amount of energy absorbed by the workpiece. The keyhole mode occurs when the peak temperature at the surface is high enough to vaporize the workpiece material. A keyhole depression in the molten pool is

produced by the pressure of vaporization [123]. This is a more efficient method of transmitting energy into the workpiece since the keyhole traps the laser energy and the internal reflectivity within the keyhole acts as a blackbody.

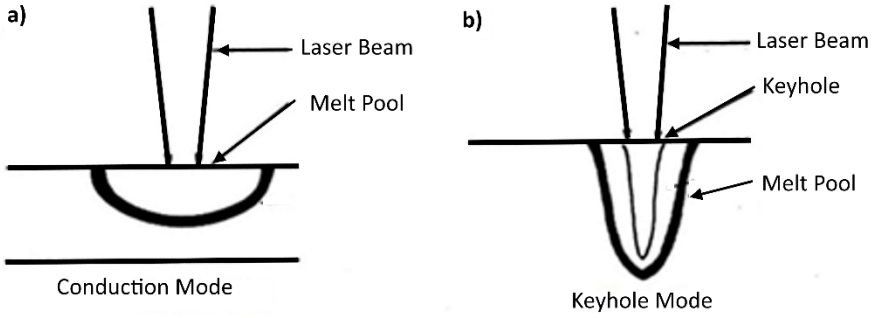

Figure 2.15: Comparison of a) conduction and b) keyhole welding modes.

2.3.5 Laser Induced Vaporization

The vaporization of alloying elements that occurs during conduction welding with a laser (see section 2.3.4 Laser Beam Modes) is a well-known phenomenon that holds particular importance in the welding of stainless steels where the loss of chromium negatively impacts the corrosion properties of the weld [124-127]. The change in composition that occurs during laser processing is due to the difference in vaporization rates of the alloy elements [124-131]. The pressure gradient has been shown to have the most significant effect on the vaporization rate of each element, as shown in Equation 2.3 [127]:

$$J_{p,i} = \frac{A_c P_i}{\sqrt{2\pi M_i R T}} \qquad \textbf{(Equation 2.3)}$$

where $J_{p,i}$ is the vaporization rate due to the pressure gradient in kg-moles/m^{2}s, A_c is a dimensionless parameter, P_i is the partial pressure of element *i* in N/m^2, M_i is the molecular weight of element *i* in kg/kg-moles, $\boldsymbol{R}$ is the gas constant in kg m^2/(s^2 kg-mole K) and $\boldsymbol{T}$ is the temperature in K. The relative rate of vaporization is given by the following dimensionless ratio [127]:

$$\frac{J_{p,i}}{J_{p,j}} = \frac{P_i}{P_j}\sqrt{\frac{M_j}{M_i}} \qquad \textbf{(Equation 2.4)}$$

The partial pressure of each element can be calculated by multiplying the mole fraction of each element by the equilibrium pressure of that element, as shown in Equation 2.5 [128, 129]:

$$P_i = X_i P_i^{\,o} \qquad \textbf{(Equation 2.5)}$$

The equilibrium pressure, $P_i^{\,o}$, is dependent on the temperature [132]:

$$log(P_i^{\,o}) = A + B/T + C\,log(T) + D/T^3 \qquad \textbf{(Equation 2.6)}$$

where ***A***, ***B***, ***C*** and ***D*** are material specific coefficients; those corresponding to Ni and Ti are shown in Table 2.2.

Table 2.2: Equilibrium pressure coefficients for Ni and Ti [132].

Element	A	B	C	D
Ni (liquid)	6.666	-20765	0	0
Ti (liquid)	6.358	-22747	0	0

The vaporization rates are clearly dependent on temperature, since the equilibrium pressures are dependent on temperature. Additionally, it has been found that once the temperature in the weld pool exceeds the boiling temperature of the alloy, then keyhole (see section 2.3.4 Laser Beam Modes) vaporization will also occur [128, 129]. Furthermore, the larger the surface area of the melt pool, the more material lost from vaporization [127], as shown in Figure 2.16.

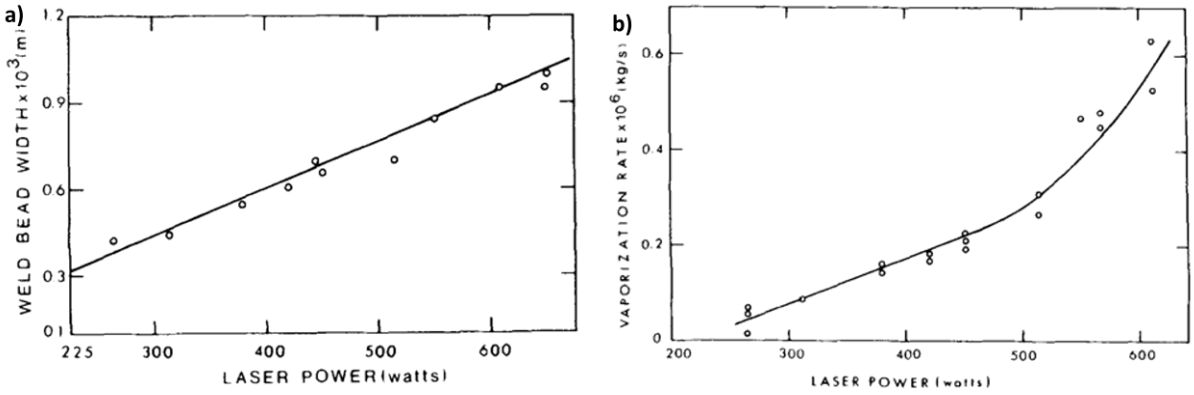

Figure 2.16: a) weld bead width vs laser power and b) vaporization vs laser power. Reprinted with permission from Springer Nature: [127].

There are several other factors that can contribute to the vaporization rates. Firstly, it is important to consider the atmosphere in which the laser processing is being performed. Initial theoretical calculations for vaporization rates (see Equations 2.3) were assuming a low-pressure/vacuum

environment [127], which can over-estimate the vaporization rates [133]. It is also important to note that when laser processing is performed in an argon atmosphere, an argon plasma can form, creating ionized and excited atoms, as shown in Figure 2.17. The surface of the weld pool can become negatively charged due to electrons striking at a higher flux than the ions [133], resulting in an attraction between the positive ions of the vaporized alloy elements and the negative charge built up on the weld pool surface. This attraction could lead to condensation of the vaporized alloy elements back into the weld pool, reducing the net vaporization rate.

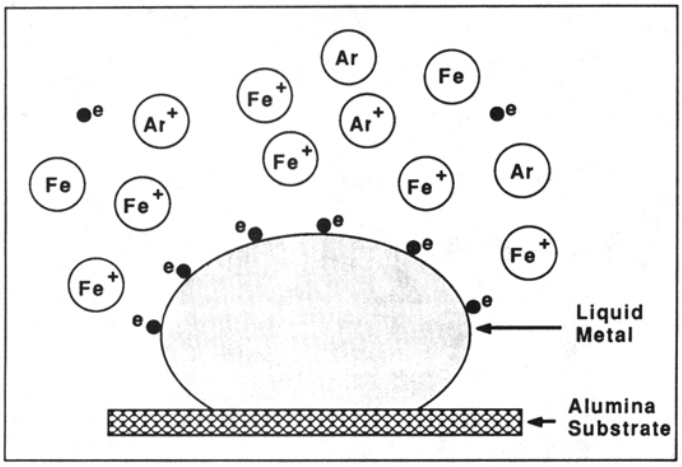

Figure 2.17: A schematic representation of the ion charge phenomenon. Reprinted with permission from Springer Nature: [133].

A newer vaporization rate takes into account condensation of the vapor elements back to the melt pool surface and the transport of vaporized elements into the atmosphere through diffusion [134].

$$J_i = J_{p,i} + J_{c,i} \qquad \textbf{(Equation 2.7)}$$

where $J_{p,i}$ is the vaporization flux due to the pressure gradient at the melt pool surface, as shown in Equation 2.8, and $J_{c,i}$ is the vaporization flux due to concentration gradient in the argon atmosphere, as shown in Equation 2.9 [134, 135].

$$\mathbf{J_{p,i} = a_i \frac{P_i^o M_i}{P_L M_v} J_p} \qquad \textbf{(Equation 2.8)}$$

$$\mathbf{J_{c,i} = K_{g,i} M_i \frac{a_i P_i^o}{RT}} \qquad \textbf{(Equation 2.9)}$$

where a_i is the activity of element i (mole fraction), P_L is the summation of equilibrium vapor pressures of all alloying elements on the surface, M_v is the mean molecular weight of all vaporized

species, J_p is the total vaporization flux caused by the pressure gradient and $K_{g,i}$ is the mass transfer coefficient of element *i* given by [136]:

$$K_{g,i} = \frac{2Sc^{0.42}Re^{0.5}D_i}{d}\left(1+\frac{Re^{0.55}}{200}\right)^{0.5}\left[0.483-0.108\frac{r}{d}+7.71\times10^{-3}\left\{\frac{r}{d}\right\}^2\right] \quad \textbf{(Equation 2.10)}$$

where *Sc* is the Schmidt number, *Re* is the Reynolds number at the nozzle exit, D_i is the diffusivity of element *i* in the shielding gas, *r* is the radial distance on the melt pool surface and *d* is the diameter of the nozzle of the shielding gas.

The overall relative rate of vaporization (2.11) can be estimated as an average of the relative rate of vaporization due to the pressure gradient (Equation 2.12) and the relative rate of vaporization due to condensation (Equation 2.13):

$$\frac{J_i}{J_j} = \frac{J_{p,i}/J_{p,j} + J_{c,i}/J_{c,j}}{2} \quad \textbf{(Equation 2.11)}$$

$$\frac{J_{p,i}}{J_{p,j}} = \frac{a_i P_i^{\,o} M_i}{a_j P_j^{\,o} M_j} \quad \textbf{(Equation 2.12)}$$

$$\frac{J_{c,i}}{J_{c,j}} = \frac{D_i M_i a_i P_i^{\,o}}{D_j M_j a_j P_j^{\,o}} \quad \textbf{(Equation 2.13)}$$

The ratio of mass transfer coefficients can be reduced to the ratio of diffusivities in the shielding gas. So, even though the presence of argon shielding reduces the total vaporization flux, it appears to have a negligible effect on the relative rates of vaporization.

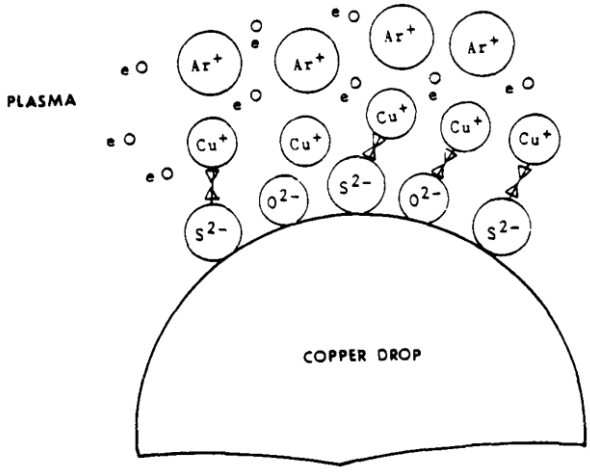

Figure 2.18: A schematic representation of the electrical interaction between the positively charged plasma cloud and the negatively charged oxygen. Reprinted with permission from Springer Nature: [125].

Another factor that can play a role in the vaporization rates is the presence of a surface oxide. The oxygen is negatively charged and would be attracted towards the surface due to the positive charge of the plasma cloud [125]. This can form electromagnetically driven eddies near the surface that create turbulence and destabilize the surface tension [137]. This results in an increase in the effective surface area, and thus raises the vaporization rates [133]. However, if too much oxygen covers the surface it can reduce the vaporization rate by occupying surface sites from where alloy elements can vaporize [125], as shown in Figure 2.18.

2.3.6 Laser Processing of SMA

Ni has a higher equilibrium vapor pressure than Ti, as shown in Figure 2.19, thus it experiences preferential vaporization during laser processing [22]. This results in a decrease in Ni concentration of the bulk matrix, which in turn translates into an increase in the phase transformation temperatures (see Section 2.1.5 Effects of Composition) [72, 138-141]. Previous studies have been able to confirm this change through DSC analysis [22, 23], as shown in Figure 2.20. Initial research into the effects of laser parameters on relative rates of vaporization have only looked at the change in NiTi composition from a single laser pulse profile with additional pulses per spot [23]. This method offers only rigid steps by which the composition can be changed and little insight into how to apply this method to other materials or other laser sources.

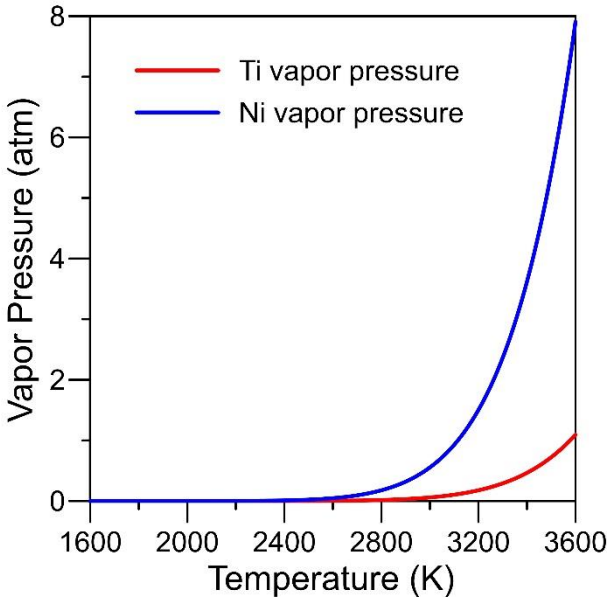

Figure 2.19: Nickel and Titanium equilibrium vapor pressures.

From welding of stainless steel, it is known that pulse power and duration play a critical role in determining the temperature of the weld pool, and thus how much of each element is vaporized [128, 129]. A similar understanding is needed for NiTi. Developing laser processing methods for improving the performance or enhancing the functionality of traditional SMA materials has recently gained a lot of momentum, with many proof-of-concepts having been recently developed [5, 17, 21-23, 142]. The ability to locally modify the microstructure and/or composition along with the speed, precision, and quality inherent in laser processes make them an excellent means for processing SMAs. This in turn allows for the creation of monolithic NiTi components with spatially varying properties.

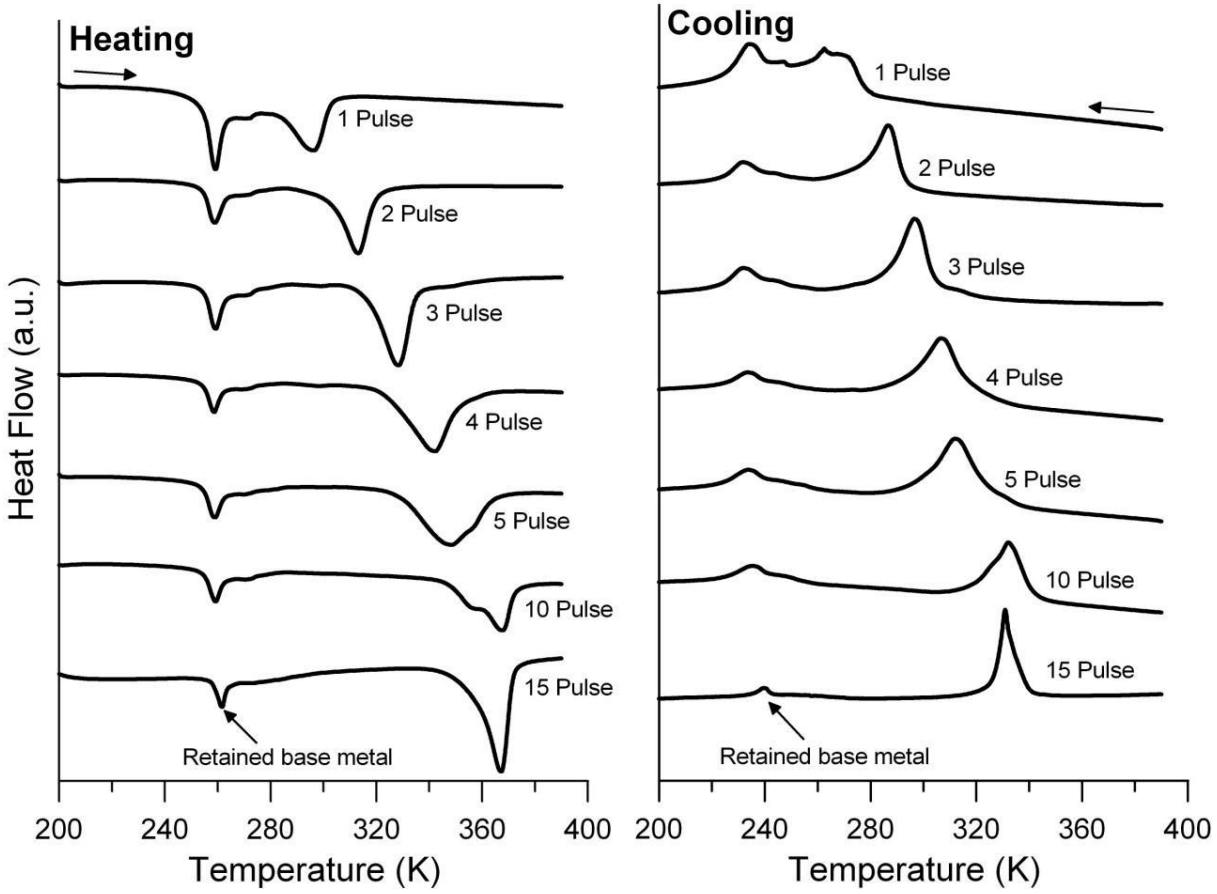

Figure 2.20: DSC analysis of laser processed Ti-50.7 at.% Ni with 0.6 kW peak power and 30 ms pulse duration. Shift in second peak due to preferential vaporization if Ni. From Ref. [22] Copyright © 2013 WILEY-VCH Verlag GmbH & Co. KGaA, Weinheim. Reproduced with permission. All rights reserved.

2.4 Modelling

2.4.1 Determining Material Properties

The Young's modulus, E, of a material can be determined from the bulk properties of that material, according to the Voigt-Reuss-Hill approximation for isotropic materials [143]:

$$\boldsymbol{E = \frac{9BG}{3B + G}} \qquad \textbf{(Equation 2.14)}$$

where B is the bulk modulus and G is the shear modulus. The bulk and shear moduli can be determined from the elastic constants of a single-crystal by [143]:

$$\boldsymbol{B = \frac{1}{3}(c_{11} + 2c_{12})} \qquad \textbf{(Equation 2.15)}$$

$$\boldsymbol{G = \frac{(c_{11} - c_{12}) + 3c_{44}}{5}} \qquad \textbf{(Equation 2.16)}$$

where c_{11}, c_{12} and c_{44} are all elastic constants of a single-crystal. The elastic constant c_{11} is the relationship between deformation in the x-direction and a stress applied in the x-direction, whereas the c_{12} elastic constant describes the deformation in the y-direction associated with a stress in the x-direction. The c_{44} elastic constant is associated with a rhombohedral shear or stretching of the single-crystal along a <111> direction while maintaining a constant volume [144]. Due to the symmetry of a cubic crystal structure, such as the austenite phase of NiTi, there are only three independent elastic constants. However, for a monoclinic crystal structure, such as the martensite phase of NiTi, there are thirteen elastic constants as shown in Figure 2.21.

$$\boldsymbol{a)}\begin{vmatrix} C_{11} & C_{12} & C_{12} & 0 & 0 & 0 \\ C_{12} & C_{11} & C_{12} & 0 & 0 & 0 \\ C_{12} & C_{12} & C_{11} & 0 & 0 & 0 \\ 0 & 0 & 0 & C_{44} & 0 & 0 \\ 0 & 0 & 0 & 0 & C_{44} & 0 \\ 0 & 0 & 0 & 0 & 0 & C_{44} \end{vmatrix} \qquad \boldsymbol{b)}\begin{vmatrix} C_{11} & C_{12} & C_{13} & 0 & C_{15} & 0 \\ C_{12} & C_{22} & C_{23} & 0 & C_{25} & 0 \\ C_{13} & C_{23} & C_{33} & 0 & C_{35} & 0 \\ 0 & 0 & 0 & C_{44} & 0 & C_{46} \\ C_{15} & C_{25} & C_{35} & 0 & C_{55} & 0 \\ 0 & 0 & 0 & C_{46} & 0 & C_{66} \end{vmatrix}$$

Figure 2.21: Elastic constants of a single-crystal a) cubic structure and b) monoclinic structure.

2.4.2 Elastic Properties of NiTi SMAs

Modelling of the pseudoelastic properties of NiTi SMAs requires an understanding of the elastic moduli of both the austenite and martensite phases. Recorded values for the Young's modulus for austenite range from 41 GPa to 75 GPa; for martensite the range is from 28 GPa to 41 GPa [146].

Part of the discrepancy in results may be due to inconsistencies in mechanical testing. Standard test methods like the ASTM F2516-14 specifies the use of either a contact extensometer or a minimum gauge length of 150 mm for testing thin NiTi wires [147]. Both of these procedures are highly susceptible to slipping within the grips/extensometer when testing thin NiTi wires due to the small diameters of the wires and therefore low surface contact area.

The use of digital image correlation (DIC) has become increasingly popular and looks to replace traditional methods of global strain measurements by providing localized strain values. However, commercially available DIC systems are often limited to analyzing wires ~700 µm in diameter during tensile testing. Recently it has been shown that custom DIC set-ups are capable of analyzing wires as thin as 381 µm [148]. The speckle pattern produced by Reedlunn *et al.* creates speckles that are approximately 50 µm in diameter [148]; for analyzing a 100 µm wire, this speckle is not fine enough. A lithographic method would most likely need to be employed to fabricate a pattern with small enough speckles [149]. Thus, using a visual extensometer is more time efficient and cost effective than using a DIC set-up to analyze ultra-fine (~100 µm diameter) NiTi wires.

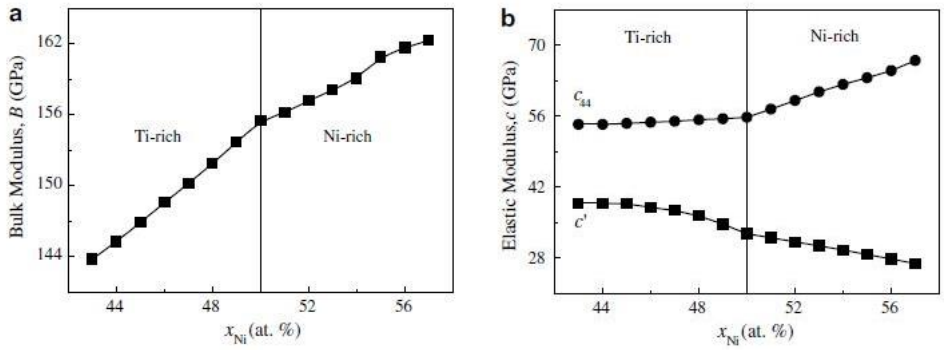

Figure 2.22: Theoretical a) bulk modulus and b) elastic constants as a function of Ni composition. Reprinted from Ref. [150] with permission from Elsevier.

Some of this variance in elastic properties reported in literature is also due to the variations in composition, thermomechanical history and test temperature. It has been shown experimentally by Lu *et al.* that as the alloy becomes more Ni rich the value of c_{44} increases [150], as shown in Figure 2.22. Simultaneously, the value for c' decreases, where c' is defined as:

$$c' = \frac{1}{2}(c_{11} - c_{12}) \qquad \textbf{(Equation 2.17)}$$

This results in both an increase in the bulk modulus and a slight increase in the Zener anisotropy as the material becomes more Ni rich. Zener anisotropy is defined as:

$$A_z = \frac{c_{44}}{c'} \qquad \textbf{(Equation 2.18)}$$

For a perfectly isotropic material, the Zener anisotropy value would be 1.

The test temperature has less of an effect on the material properties than the composition does. It was shown by Ren *et al.* that the bulk modulus does not change with temperature [46]. However, for NiTi SMAs, c' softens as temperature decreases towards M_s, as shown in Figure 2.23. Interestingly, c_{44} also decreases as temperature approaches M_s, which results in a relatively low Zener anisotropy factor compared to other SMAs (i.e. Cu-based alloys) [46]. This results in a change in the Young's modulus that is contrary to what might be expected, i.e. the Young's modulus of the austenite phase increases with temperature.

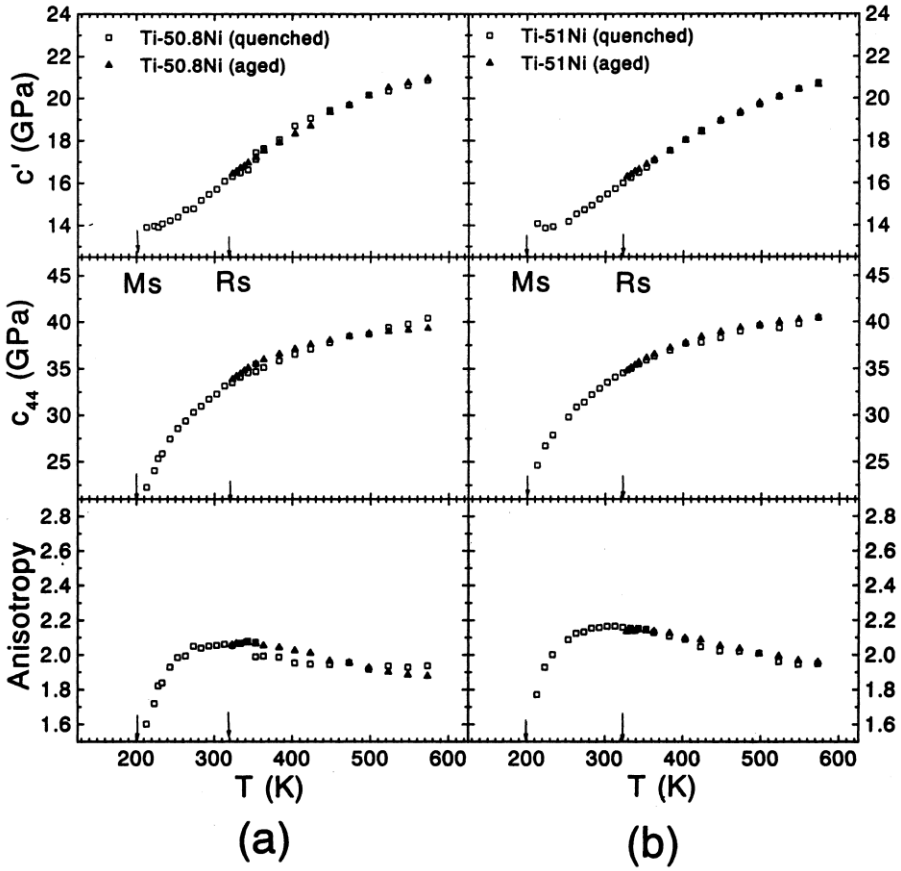

Figure 2.23: Experimental values for c' and c_{44} for a) Ti-50.8Ni and b) Ti-51Ni as a function of temperature. Reprinted from Ref. [46] with permission from Elsevier.

Further complicating the determination of the elastic moduli is the thermomechanical history of the material. Heat treatments ranging from 310 °C to 560 °C have been shown to facilitate an austenite to R-phase to martensite transformation pathway [151]. The activity of the R-phase

cannot always be easily distinguished from a stress/strain curve since it may be almost linear, and may result in much lower experimental values for the austenite elastic modulus than the theoretical values calculated from first principles [146]. In recent years, there has been some agreement that the austenite elastic modulus based on first principles is approximately 70 GPa [146, 152].

The texture of the material is also a critical factor in determining the elastic properties. Suresh *et al.* found that for mixed texture materials, the elastic modulus is not uniform throughout the material [153]. The local elastic modulus of the austenite phase varies depending on the grain orientation (due to anisotropy) and internal stresses. The local elastic modulus of the martensite phase also varies due to grain orientation attributing to different twin mobilities. However, wires have a preferential grain orientation, not a mixed texture (see Section 2.2.3 Wire Drawing SMAs). Therefore, it may be prudent to use direction-dependent elastic moduli, such as:

$$E_{<111>} = \frac{4(c_{11} - c_{12})(c_{11} + 2c_{12})c_{44}}{c_{11}^2 + c_{11}c_{12} - 2c_{12}^2 + 2c_{11}c_{44}} \qquad \textbf{(Equation 2.19)}$$

Due to this preferential orientation and the extreme anisotropy of the martensite phase, unusually low values for the martensitic elastic modulus have been found experimentally. This is due to the fact that the $<111>_A$ direction aligns with the $<10\bar{1}>_M$ direction which has an elastic modulus as low as 33.2 GPa [146]. It has also been shown that the elastic modulus of the martensite phase decreases with increased temperature [154], which may account for martensitic elastic modulus values observed experimentally to be as low as 20 GPa [146].

2.4.3 Modelling Pseudoelasticity of SMAs

In recent years, constitutive modeling of SMAs has been significantly advanced by numerous research groups. The majority of the models developed to represent PE in SMAs can be divided into two major groups: micromechanics-based models and phenomenological models [155, 156]. Both methodologies are reviewed in detail.

Micromechanical models try to predict the response of the SMA by taking into account the microstructure. If the microstructure is well-known, understanding of the single crystal behavior can be used to solve boundary value problems in a polycrystalline material, as was demonstrated by Anand and Gurtin [157]. It is essential to use homogenization techniques in order to achieve

representative thermomechanical properties. Several homogenization techniques have been developed for elastic and elastoplastic methods [158-163], which make use of a Representative Volume Element (RVE). These homogenization methods presume the effective response of a composite is attainable by accounting for a solitary inhomogeneity embedded within an infinite matrix. Most micromechanical models for SMAs use a self-consistent type of averaging to account for interactions between grains [164-169]. That is, the interactions between grains can be accounted for by associating properties of the matrix with effective properties of the composite, or by embedding the grain into a representative medium [158-160]. An alternative approach, known as the Mori-Tanaka method, accounts for the interactions between grains by modifying the average stress in the matrix from the applied stress [161, 170, 171].

Some micromechanics models are capable of capturing all of the different mechanical responses of an SMA, such as PE, SME and a rubber-like behavior [172, 173]. They take into consideration the evolution of the total transformation strain of each grain, then progression of the martensitic volume fraction is attained through a balancing of the internal dissipation due to phase transformation with the external output of energy. The model presented by Gao *et al*. [169] takes into account the evolution of each martensitic variant.

These micromechanics models effectively predict material behavior based only on crystal lattice parameters and information about the martensitic transformation and provide valuable insight into the micro-scale phase transformation process. However, it is not practical to have an exact representation of the micro-structure, nor is it possible to solve numerically for the number of grains that would be present in a realistic 3-D boundary value problem [155]. Additionally, the complexity of the micro-to-macro transition has limited the use of micro-scale modelling of SMA responses [156].

The phenomenological models often use continuum thermomechanics with internal variables to represent the changes in the microstructure due to the phase change. These models implement a macroscopic energy function that depends on the state and the internal variables used to define the degree of phase transformation [155]. They apply a thermodynamic structure and choose the martensitic volume fraction as the internal state variable, which accounts for the influences of the microstructure.

The benefit of phenomenological models is that they can be more easily implemented into a finite element method. The draw-back is that since they are not based on the microstructure and are phenomenological in nature, they are individually customized to suit a specific need. This results in frequent instances of "curve fitting" to data sets and not the development of a generalized model. Early models have a common thermomechanical framework, but differences arise due to the varying choices for the transformation hardening function [24-27]. A more recent work by Qidwai and Lagoudas [29] presented a more general thermodynamic model where the transformation function can be tuned to capture transformation effects, such as pressure dependence and volumetric strain. Different transformation functions have also been used to simulate the asymmetric response of SMAs in tension and compression [28-30]. This asymmetric response is extremely important when modelling the bending behavior of SMAs, as consideration must be given for the neutral axis offset [174, 175]. Figure 2.24 shows the several schematics of bending strain profiles.

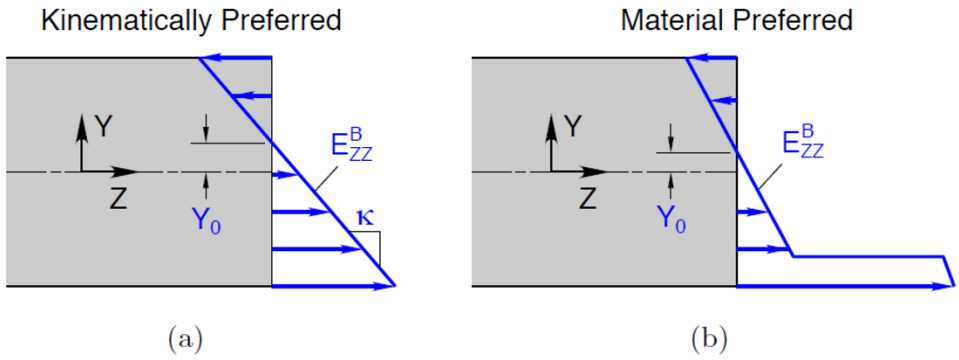

Figure 2.24: Schematics showing theoretical bending strain profiles. Reprinted from Ref. [174] with permission from Elsevier.

While the majority of these models are only capable of modelling PE, some models decompose the martensite volume fraction into self-accommodated (twinned) and detwinned components, allowing for the modelling of SME and thermal responses as well as PE [26, 176]. Figure 2.25 shows the four distinct regions associated with phase transformation as defined by this type of model.

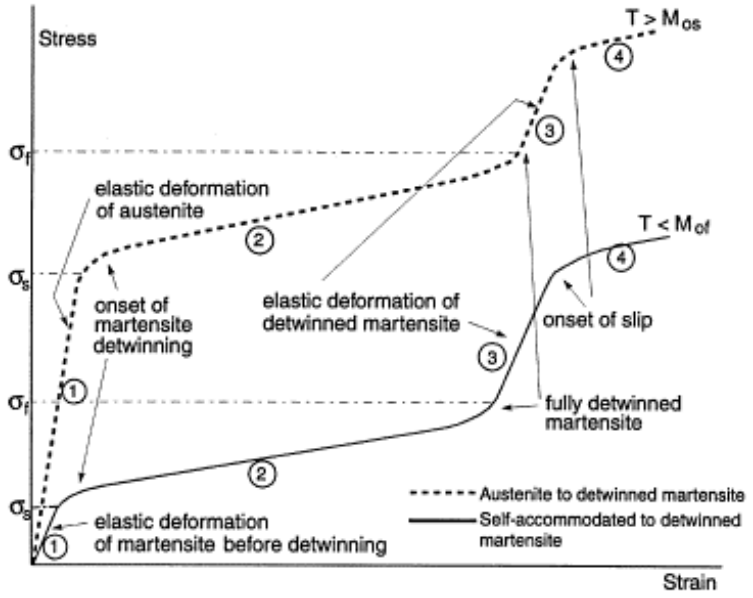

Figure 2.25: Schematic of stress/strain response showing four distinct regions associated with phase transformation. Reprinted from Ref. [176] with permission from Elsevier.

These thermodynamic models are analogous to elastoplasticity regarding the hysteretic response of the SMA [28, 177-180]. They essentially are assuming that the phase transformation is similar to plastic flow. Transformation-induced plasticity models have been developed to predict the evolution of the hysteresis loop's size and shape during repeated cycling [156, 181, 182]. This evolution of the transformation hysteresis loop is also of great importance. Earlier models were developed based on experimental observations [183-185]. More recent developments have led to better cyclic/fatigue modelling of pseudoelastic loading and unloading [186-188]. This has been brought about primarily by a better understanding of the nucleation and propagation of the austenite to martensite transformation, which has been achieved in part by discerning the effects of heat transfer during the phase transformation [187, 188] and also by determining the effects of grain size [189, 190].

Alternatives to these thermomechanical models are domain wall models, free energy models [25, 190] and Preisach models [192-194], which are analogous to magnetic domain wall transitions. These models are entirely phenomenological in nature and typically are not based on thermodynamics. However, they are capable of modeling internal hysteresis loops and other complex phenomena in a simplified manner [194]. The classical Preisach model represents hysteresis through an assembly of a number of hysterons (basic hysteretic elements), which are connected in series [195]. Each hysteron is essentially a non-ideal switch (see Figure 2.26) that

turns on when an input is increased beyond a specific threshold, giving a certain output, then turns off again when the input is decreased below a different threshold. The Preisach triangle (see Figure 2.27) is a geometric construal for organizing the hysterons [195]. In the context of modelling SMA PE, the thresholds for the hysterons are the forces required to cause phase transformation, and the output is the volume fraction of martensite.

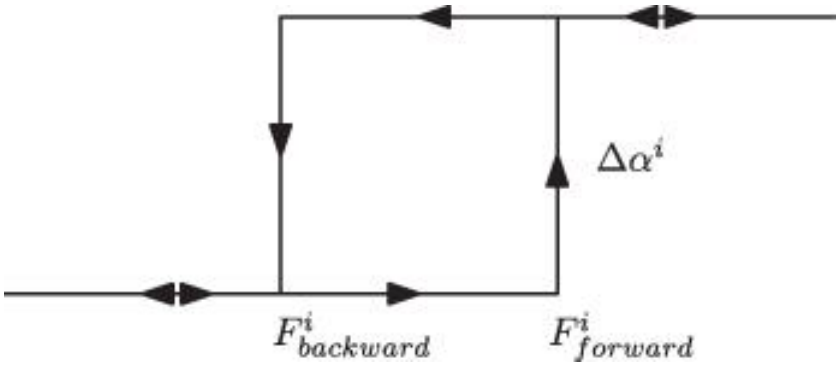

Figure 2.26: The hysteron used in the Preisach model. The directions of allowed phase transformation are indicated by the arrows on the hysteron. From Ref. [194] Copyright © IOP Publishing. Reproduced with permission. All rights reserved.

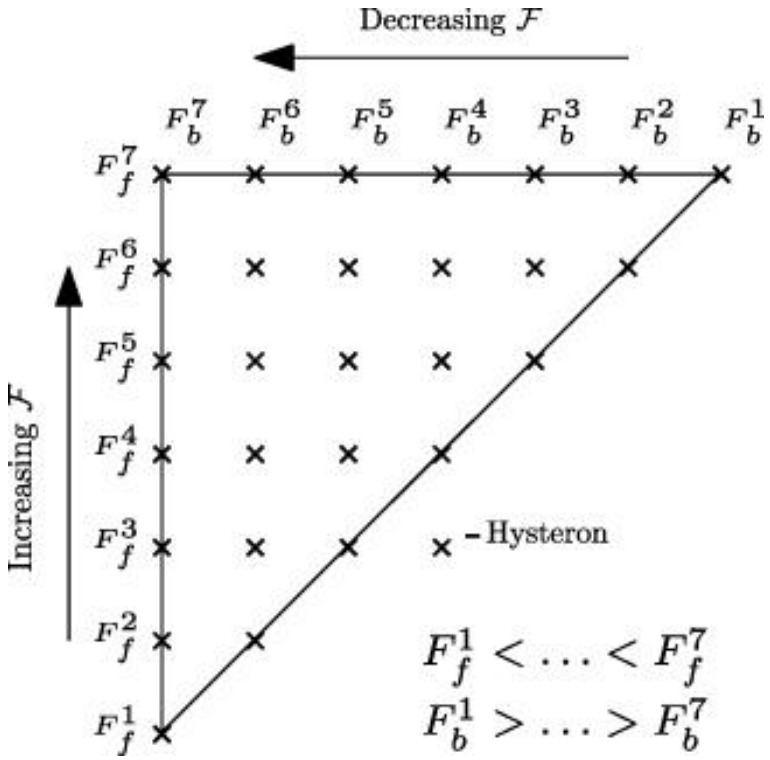

Figure 2.27: The Preisach triangle is a useful method for designating hysterons with their parameters to allow orderly on/off switching. The directions for the loading and unloading forces are indicated on the figure. From Ref. [194] Copyright © IOP Publishing. Reproduced with permission. All rights reserved.

2.5 Summary and Concluding Remarks

This extensive review of literature underscores the complexity of comprehending NiTi: its phase transformation characteristics, its manufacturing/processing methods and how it is modeled. Traditional manufacturing techniques are performance limiting because each component has only one set of thermomechanical properties. Newer methods, such as localized heat treatments, powder metallurgy, dissimilar joining and laser processing, have been investigated to locally modify functionality. Laser processing has more recently shown great potential in attaining local modification to functional properties. While there are several studies exploring the use of laser processing to modify NiTi SMAs [5, 20-23], it is still a young art and much more research is required before they can be fully integrated successfully in industrial applications. The primary knowledge gaps related to the science of laser-processed multiple memory SMAs identified herein include:

1. The existence of preferential alloy element vaporization is known and has even been exploited in the case of NiTi SMAs. However, only limited studies have looked into the relationship between laser parameters and the resulting change in the bulk composition (see 2.3.6 Laser Processing of SMA). More work in this area is essential in being able to successfully predict compositional change and aid in the precise manufacturing of tailored tunable SMAs.
2. Although there has been extensive work done to develop mechanical deformation models for NiTi SMAs (see Section 2.4.3 Modelling Pseudoelasticity of SMAs) this work has never been extended to SMAs exhibiting multiple pseudoelastic responses. This makes applying multiple memory SMAs in complex mechanical devices a difficult task at best, since the performance cannot be fully modelled and must be tested through trial and error methods.
3. There have been studies exploring the tension/compression asymmetry of NiTi SMAs and how texture effects the functionality (see 2.4.3 Modelling Pseudoelasticity of SMAs). However, there have not been any studies that examine the macroscale effect of localized texture modifications to the two-dimensional bending deformation. Nor has there been enough work done towards understanding the incompressible behavior of the austenite to R-phase transformation.

4. There has been previous work done to implement laser processed NiTi SMAs into novel design applications [5, 20]. However, there are always new ways to take advantage of this improved functionality.

The above findings regarding laser processed multiple memory SMAs directly reflect the objectives of this research study (presented in Section 1.2 Objectives) and will therefore be addressed in the coming chapters.

Chapter 3: Experimental Methods

3.1 Material Selection

Two different NiTi wires were investigated in this study. The most frequently used material was a 700 µm diameter NiTi wire (NT-E9) manufactured by Furukawa Electric Co. Ltd. It was thermomechanically treated by the manufacturer to exhibit pseudoelastic properties at room temperature with an A_f temperature of 25 °C. This material will be referred to as base material 700 µm (BM7) for the remainder of this study. In this study, all laser processing of NiTi wires was performed on this material.

The second wire investigated had a 400 µm diameter (N15516B) and was manufactured by Memry Corporation. This wire was also thermomechanically treated by the manufacturer to be pseudoelastic at room temperature with an A_f temperature of 8 °C. This material will be referred to as base material 400 µm (BM4) for the remainder of this study.

A NiTi sheet from Memry with a thickness of 2.5 mm, a composition of 50.8 at.% Ni and pseudoelastic properties at room temperature was also used for this study. This material will be referred to as base material sheet (BMS) for the remainder of this study. This material was only used to study the deconvolution of overlapping DSC peaks (see Section 4.3 Deconvolution of Overlapping Peaks), not for mechanical characterization. One of the sheet samples was processed with a laser to modify and control the composition in part of the sheet. The laser used for processing the sheets was a Miyachi Unitek LW15 pulsed Nd:YAG laser with a wavelength of 1064 nm. This material will be referred to as processed sheet (PS).

3.2 Laser Processing Equipment and Parameters

Laser processing of the BMS material was performed on a LW15 pulsed Nd:YAG laser with a wavelength of 1064 nm and 150 µm nominal spot diameter. During laser processing, the sheets were shielded with argon gas in order to prevent oxidation. The gas flowed gently across the material surface at a rate of 4.7 L/min (10 CFH). Prior to laser processing, the sheets were etched in a 7.5 vol. % HF, 20 vol. % HNO_3, bal. H_2O solution for 2 minutes, flipping half way, to remove the thick black oxide layer that forms during manufacturing. After etching, the sheets were cleaned

with acetone, ethanol and de-ionized water to remove any potential contaminants. A square pulsed laser protocol was utilized having a peak power of 3.35 kW and an energy output of 15.7 J. This material will be referred to a processed sheet (PS) for the remainder of this study.

Laser processing of wires was performed only on the BM7 wires. A LW50A Miyachi Unitek pulsed Nd:YAG laser system with a 1.06 µm wavelength, 600 µm nominal spot diameter was used for laser processing. During laser processing, the wires were shielded with argon gas using a flow rate of 9.4 L/min (20 CFH) in order to avoid oxidation. The laser processing setup, including fixtures, is shown in Figure 3.1. This setup was developed by previous researchers [59, 196]. The wires were cleaned with acetone, ethanol and de-ionized water prior to laser processing to remove any potential contaminants.

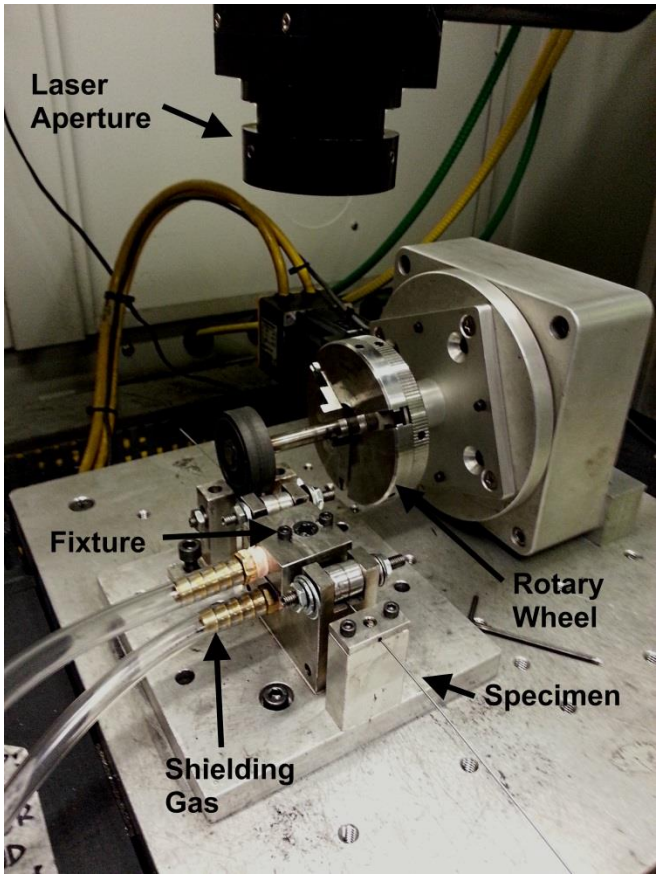

Figure 3.1: Laser processing setup. NiTi wire was fed through the fixture with Ar gas shielding the top and bottom to prevent oxidation. A rotary wheel was used to advance the wire during processing.

3.2.1 Laser Profiles for Vaporization Study

For the study of relative vaporization rates numerous square pulse profiles were used and will be discussed in more detail later (see Section 4.1 Laser Parameters). Within that study, work to deconvolute overlapping DSC was also conducted, presenting very specific processed wires. All laser processed wires were processed such that sequential pulses were overlapped 60% to ensure complete compositional change. Four different square pulse profile were employed, as shown in Figure 3.2. Each wire fabricated with these profiles will be referred to as processed wires (i.e. PW1, PW2, PW3 and PW4, respectively). A fifth laser pulse profile was utilized, as shown in Figure 3.3. This wire will be referred to as processed wire (PW). Finally, some BM7 wires were annealed at 600 ˚C for 1 hour, which resulted in a narrower DSC peak. It has been shown that extended annealing increases the relative intensity of the transformation peak [197], which is due in part to an increase in the homogeneity of the microstructure [31]. This material will be referred to as annealed wire (AW) for the remainder of this study.

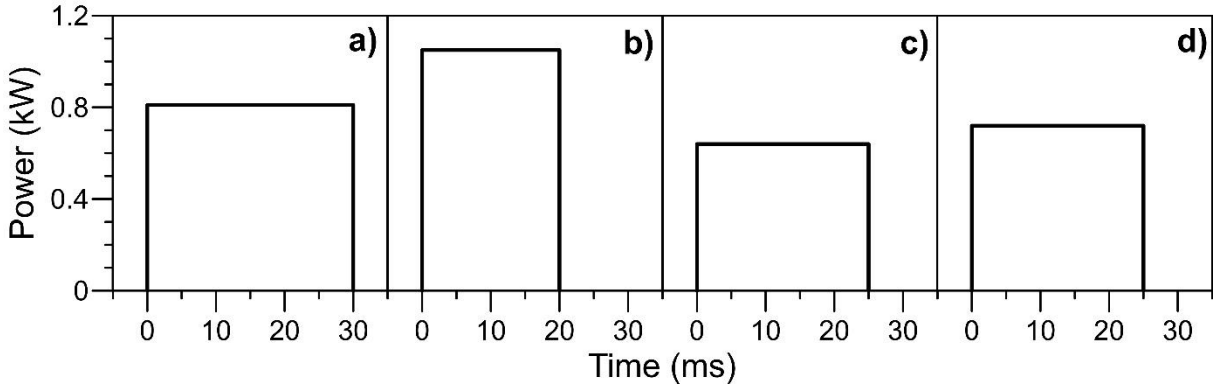

Figure 3.2: Laser processing schedules for a) PW1, b) PW2, c) PW3 and d) PW4.

3.2.2 Laser Profiles for 1-D Model Validation

For the manufacturing of the multiple memory material used to validate the 1-D model, a pulsed laser protocol was utilized having a peak power of 1.5 kW and an energy output of 13.1 J; the pulse schedule is shown in Figure 3.3. The laser spots were overlapped by 60 % to ensure that the whole bulk of the wire was processed. The laser processing was performed to achieve a compositional change to the bulk material, similar to previous work [22, 23]. This material will be referred to as laser processed (LP).

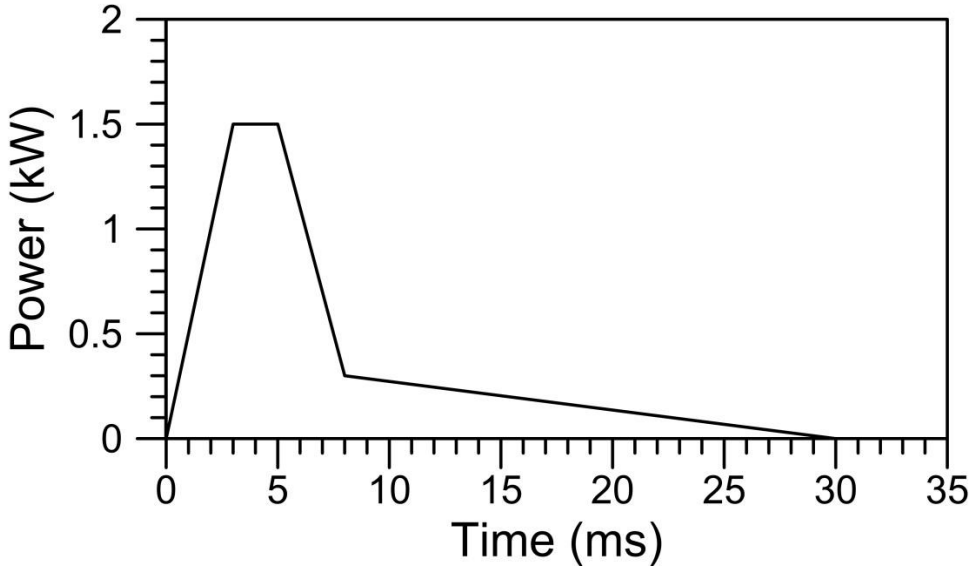

Figure 3.3: Laser processing schedule for the 1-D model validation.

3.2.3 Laser Profiles for Bending Model Development

For the fabrication of laser processed wires used to determine the effects of grain orientation on bending properties (see Section 6.2 Effect of Grain Orientation on Bending Geometries) a square pulsed profile was used. The peak power was 0.52 kW with a duration of 30 ms. This profile was picked to reduce the alteration of Ni composition due to vaporization during processing so as to isolate the effect of microstructure change from the effects of composition change. The laser pulses were overlapped 60 % to ensure processing of the entire bulk of the wire. This material will be referred to as grain reoriented (GR). Additional samples were made utilizing the same laser pulse profile, but instead of overlapping, the pulses were spread out with gaps equivalent to one pulse in between each laser spot. This material will be referred to as “zebra” during this study.

3.2.4 Laser Profiles for Fabricating Self-Biasing Springs

For the manufacturing of the multiple memory self-biasing spring, a pulsed laser protocol was utilized having a peak power of 2.0 kW and an energy output of 15.0 J; the pulse shape is similar to that shown in Figure 3.3. The laser was pulsed either once per spot (1LP) or twice per spot (2LP), with each spot being overlapped by 60 % to ensure a homogeneous composition through the thickness of the wire in the processed region. This laser processing method was performed similar to previous work [22, 23].

3.3 Post-Process Thermomechanical Treatment

The PW, LP, BM, 1LP and 2LP wires were solutionized at 1000 °C for 1 hour in an argon atmosphere then immediately water quenched to homogenize the microstructure for stable wire-drawing. Several wire drawing and inter-annealing stages were performed until the diameter of the samples was reduced to 500 µm, in line with previous work [196]. Figure 3.4 outlines the different thermomechanical treatments that were performed on the wires. The PW, LP and BM samples followed the left track and underwent 35.0 % total cold-working. The BM, 1LP and 2LP samples follow the right tract and ended up with a total cold-working of 42.6 %. The purpose of these cold-working procedures was to homogenize the structure across the entire length of wire when both as-received and laser modified materials are in one monolithic specimen and to increase dislocation density in the laser processed region [198, 199].

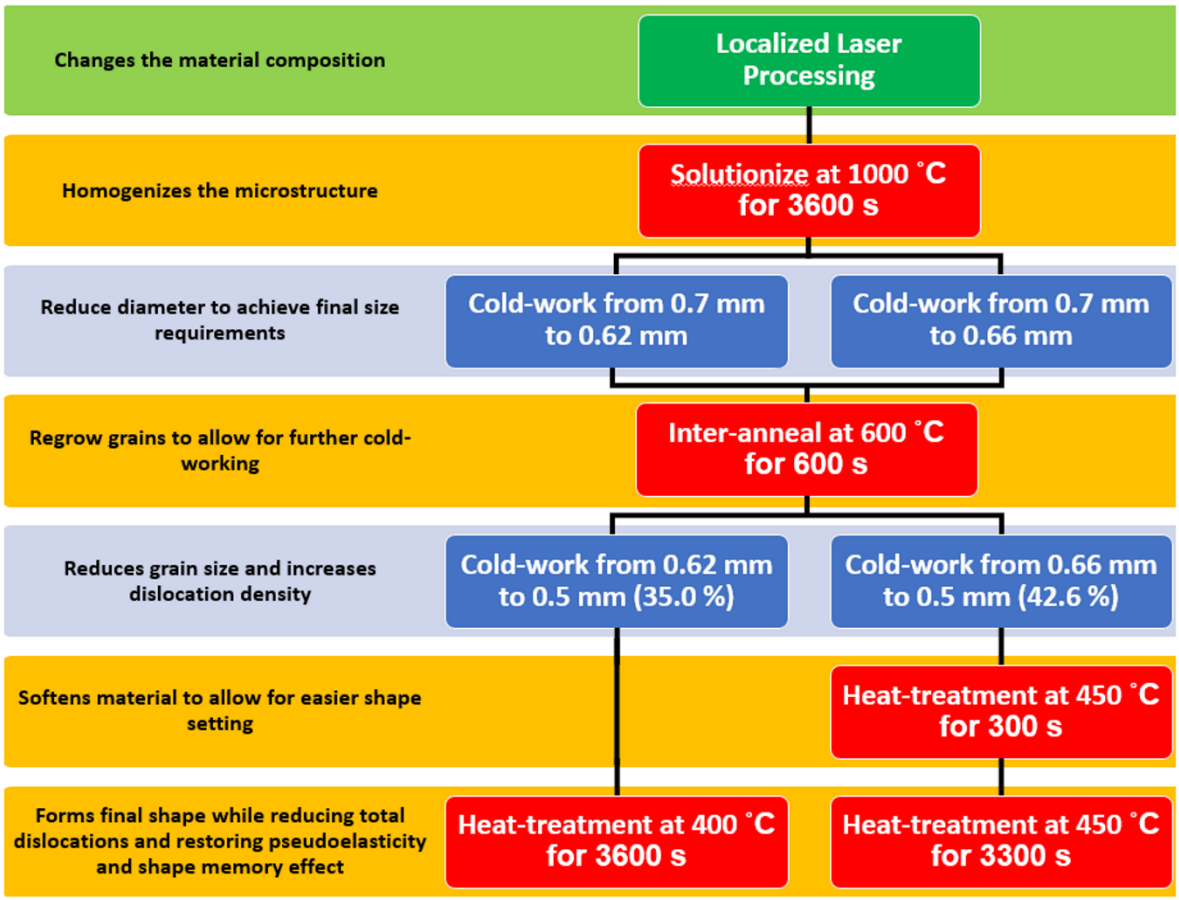

Figure 3.4: Flow chart outlining the manufacturing processes.

3.3.1 Heat Treatment for Multiple Memory Wires

A final heat treatment of 400 °C for 60 minutes in air followed by a water quench was used to restore pseudoelastic properties. During the annealing process, the wires were fixed at both ends to a flat metal plate to ensure the wire maintained a straight, non-curve shape. Annealing at 400 °C reduces the overall number of dislocations present in the material [112]. A temperature of 400 °C was chosen since it has been shown to provide stable properties for both Ni-rich (i.e. BM) and Ti-rich (i.e. LP) NiTi [33, 56, 73, 74]. The PW material after solutionizing, cold working and final heat treatment will be referred to as treated processed wire (TPW). The BM material after solutionizing, cold working and final heat treatment will be referred to as treated base material (TBM) for the remainder of this study. The LP material after solutionizing, cold working and final heat treatment will be referred to as treated laser processed (TLP) for the remainder of this study. The monolithic wire containing both TBM and TLP regions (see Figure 3.5) will be referred to as multiple memory (MM) for the remainder of this study.

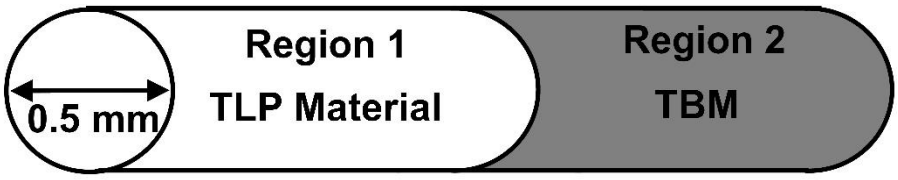

Figure 3.5: Schematic illustration of MM sample containing both TLP and TBM regions.

3.3.2 Heat Treatment for Self-Biasing Springs

The cold-worked wires were softened before shape-setting by heat-treating at 450 °C for 5 minutes. This was done to restore some ductility and prevented wire breakage during shape-setting due to work-hardening. The spring samples were manufactured by fixing the wire into a custom fixture (shown in Figure 3.7) and annealing at 450 °C for 55 minutes followed by water quenching. This procedure served to shape-set the wire while simultaneously restoring the pseudoelastic and shape memory properties. A temperature of 450 °C was chosen because it has been shown to provide a better separation of transformation peaks from region to region, facilitating multi-stage actuation [200] while remaining within the temperature range for optimal coherent, fine precipitate formation [67].

The BM material after solutionizing, cold working and final heat treatment will be referred to as Unprocessed (UP) for the remainder of this study. The LP1 and LP2 material after solutionizing, cold working and final heat treatment will be referred to as Processed 1 (P1) and Processed 2 (P2), respectively, for the remainder of this study. The monolithic springs containing both processed and unprocessed regions (see Figure 3.6) will be referred to as multiple memory 1 (MM1) and multiple memory 2 (MM2) for the remainder of this study.

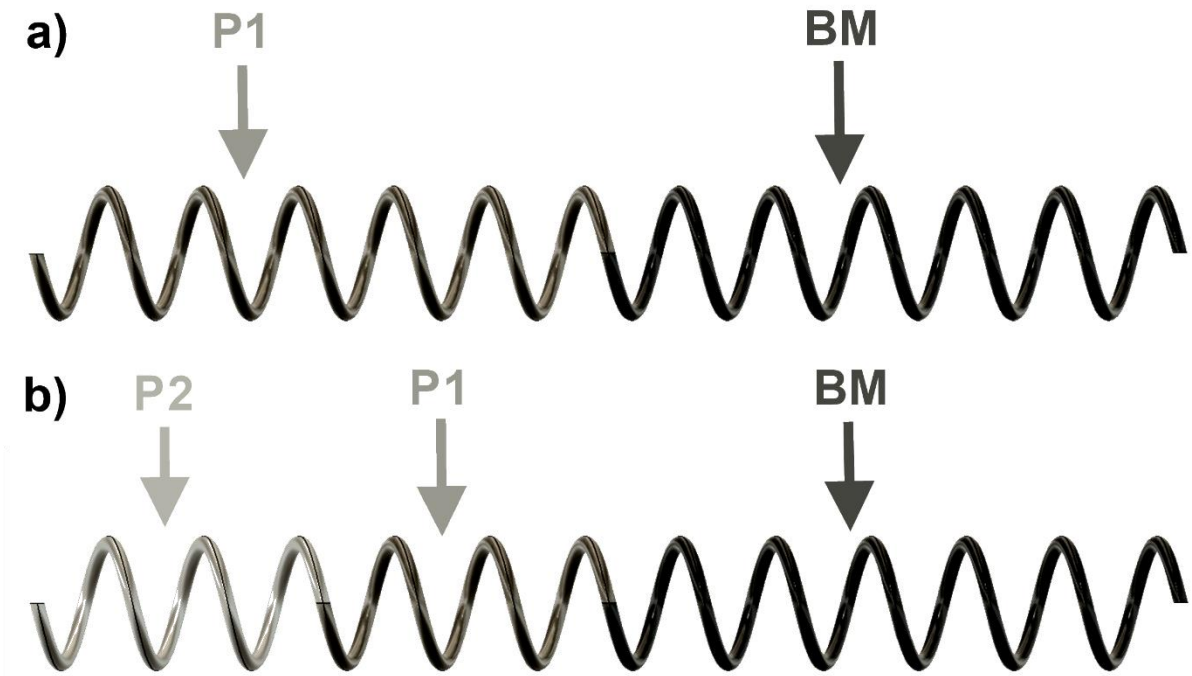

Figure 3.6: Schematics for a) MM1 spring containing both UP and P1 regions and b) MM2 spring containing UP, P1 and P2 regions.

3.4 Shape-setting Springs

Previous attempts at manufacturing helical NiTi compression springs have been able to achieve springs with constant diameters [201, 202]. However, these methods do not have the ability to accurately control and maintain a consistent spring pitch. Therefore, a unique universal custom spring fixture (see Figure 3.6) was developed to fabricate helical compression springs with a constant pitch and diameter [200]. The threaded rod in the center produces a constant pitch throughout the length of the spring; it is interchangeable to allow for any desired pitch or diameter. The MM1 and MM2 springs described in the previous section were created with a pitch of 3.175 mm and a mean diameter of ~4 cm.

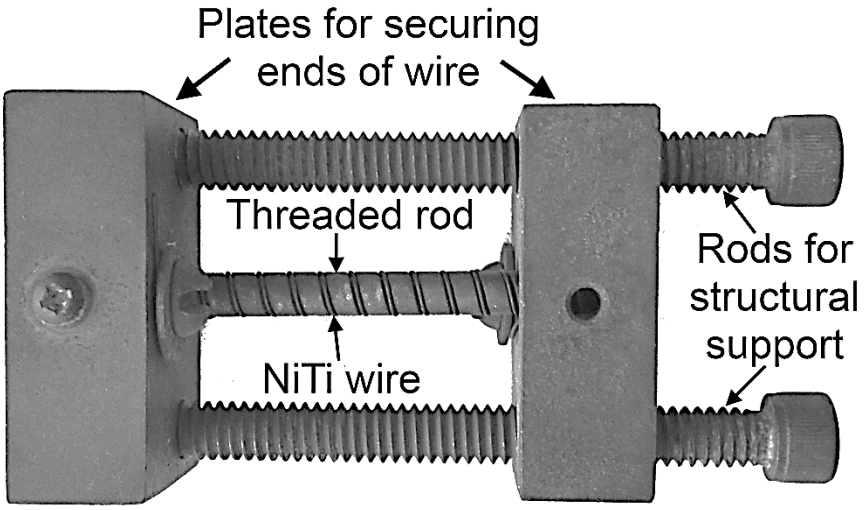

Figure 3.7: Spring shape-setting fixture.

3.5 Phase Analysis

The thermoanalytical properties of the NiTi materials were characterized by differential scanning calorimetry (DSC) analysis using a TA Discovery DSC system equipped with refrigerated cooling. DSC curves were recorded from -75 °C to 120 °C using a controlled heating/cooling rate of 5 °C/min. The M_s, M_f, A_s, and A_f phase transformation temperatures were measured using the TA Instruments Trios software v3.2 following the ASTM F2004-05(2010) standard [58].

3.6 Mechanical Analysis of NiTi Wires

3.6.1 Preliminary Tensile Test Method

Preliminary tensile testing was done using an Instron 5548 micro-tensile tester with a ±0.5 µm measurement accuracy equipped with a temperature chamber. A crosshead speed of 0.04 mm/min was used. A gauge length of 50 mm was used for all samples tested, due to the size constraints of the temperature chamber. The result was a strain rate of 1.5×10^{-5} s^{-1}, which is slow enough to avoid thermal effects and thermomechanical coupling [203, 204]. Cyclic tests were pulled to maximum strains of 11 % before unloading to zero stress. The test temperatures for cyclic testing were determined by DSC analysis such that they were at least 10 °C above the A_f temperature of the sample being tested.

3.6.2 Improved Tensile Test Methods

Additional tensile testing was conducted using an Instron 5548 micro-tensile tester equipped with a contact extensometer. The contact extensometer required elastics, springs and thermal glue to attach it to the thin samples with minimal slipping during testing. Thermal glue was used to facilitate the removal of the sample from the contact extensometer after testing. Additionally, the contact extensometer was loosely wedged into the corner of the environmental chamber to reduce the amount of non-axial stress applied to the wire by the weight of the extensometer. This test set-up is portrayed in Figure 3.8.

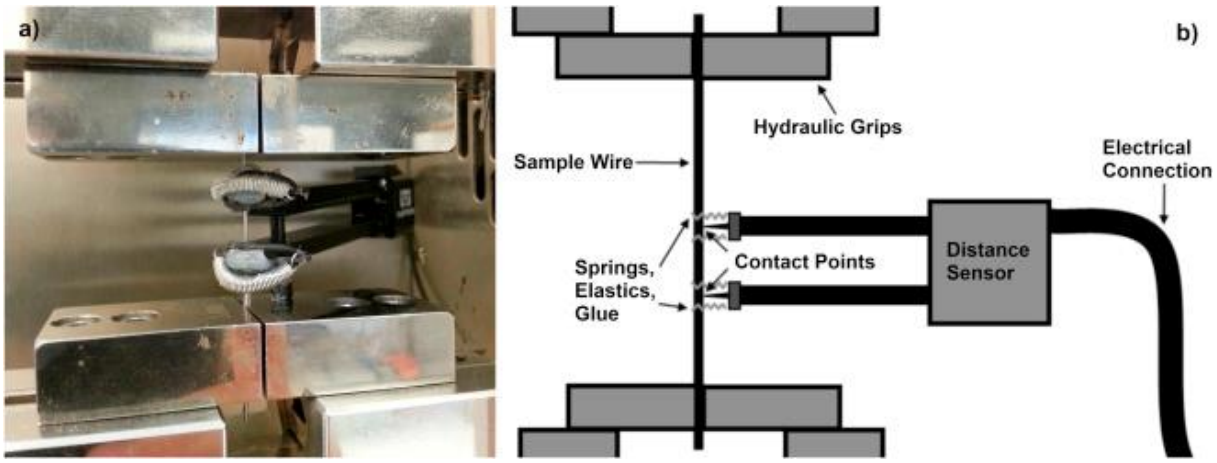

Figure 3.8 a) Photograph showing test set-up using contact extensometer attached to a sample and b) schematic depicting the contact extensometer set-up.

The visual extensometer tests were conducted on an Instron 5565 table-top tester. Typically, white circles are painted to the surface of standard ASTM "dog bone" shaped coupons that act as data points being tracked by the visual extensometer during each test. However, the dimensions of fine wires prevent white circles from being drawn on the surface. In lieu of painted circles, Styrofoam balls were glued to the sample as markers and tracked during the test. This was achieved by first skewering the Styrofoam balls with the sample wire, as shown in Figure 3.9a. To fix the white Styrofoam balls in place, a two-part epoxy was used since the Styrofoam balls do not need to be removed after testing is completed. This ensured that no slipping would occur during the test. The entire test set-up is portrayed in Figure 3.9.

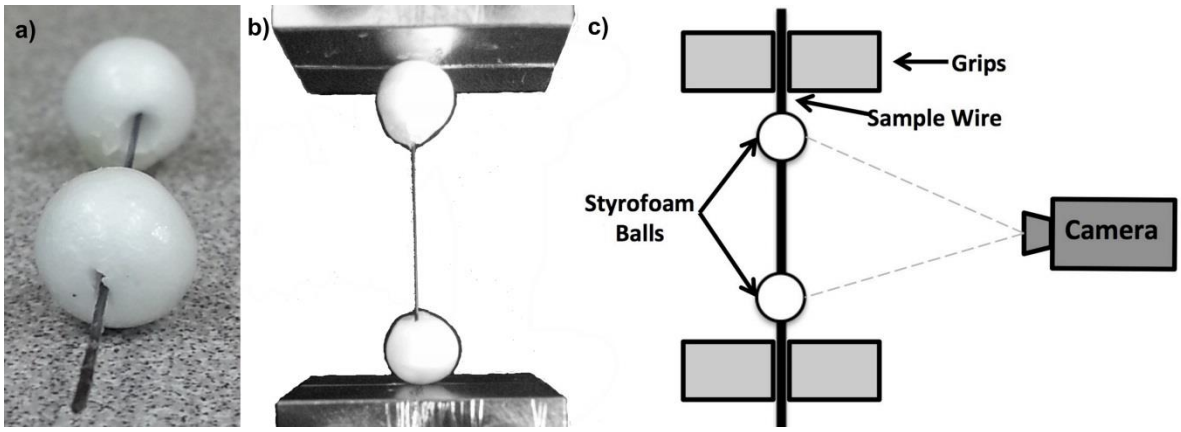

Figure 3.9 Photographs showing a) Styrofoam balls attached to wire sample, b) wire sample loaded in grips with white balls attached and c) schematic depicting the visual extensometer set-up.

Both Instron testers were equipped with environmental chambers. Pre-cycles were pulled to a strain of 6% before unloading to zero stress. The sample gauge length varied depending on the mode of strain measurement. A gauge length of 12.5 mm was used with the contact extensometer and 25 mm was used with the visual extensometer. A gauge length of 150 mm was used for samples tested by crosshead motion, in accordance with ASTM F2516-14 standard [147]. Crosshead motion data was collected using the table-top Instron. The BM4 wire was tested at room temperature, which was approximately 12 °C above the A_f. The BM7 was tested at 40 °C to ensure it was also around 15 °C above the A_f temperature. Each test condition was tested in triplicate to verify results.

3.6.3 Three-point-bend Test Method

Three-point-bend testing was done using an Instron 5548 micro-tensile tester with a ±0.5 µm measurement accuracy, see Figure 3.10. To ensure negligible shearing effects the span length was 40 times the wire diameter, which and is consistent with previous studies [205]. The crosshead speed was one tenth of the wire radius per second, which gives an approximate strain rate of 1.2×10^{-4} s^{-1} on the outer edge of the sample. Photographs were taken at the maximum deflection to determine the bending curvature of the transformed region. All tests were run at room temperature because the test set-up with camera did not fit in the environmental chamber. At least three samples were tested for each wire type.

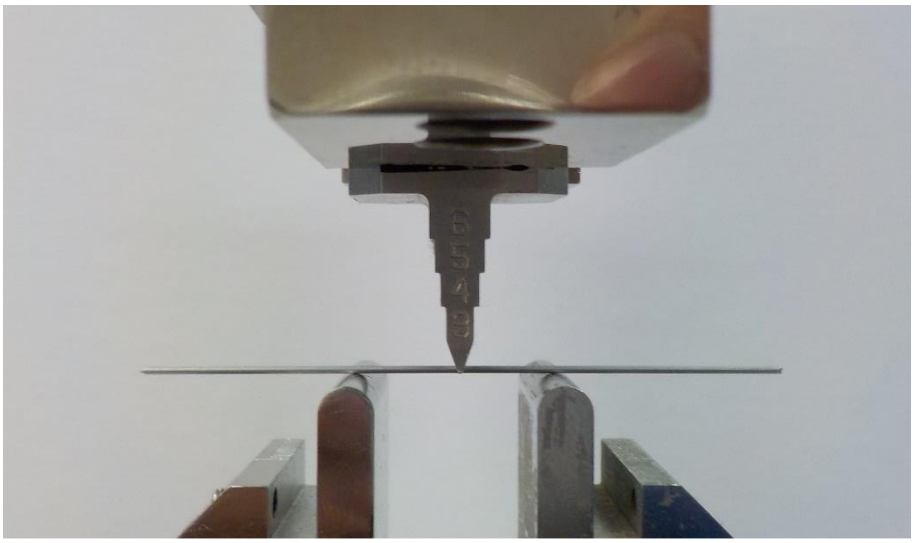

Figure 3.10 Photograph showing the three-point-bend test set-up.

3.6.4 Torsional Shear Test Method

Torsion testing was conducted using a customized set-up provided by Smarter Alloys, Inc. The test specimens had a gauge length of 10 mm, which is in line with previous studies [206]. A MTT03-10Z torque sensor from Mark-10 Corp. was attached to one end of the specimen. A programmable stepping motor rotated the opposite end of the specimen at a speed of 1 RPM. The BM4 wires were tested at room temperature, which was approximately 12 °C above the A_f. The BM7 wires were tested at 37 °C, which was the thermal limit of the torque sensor, and was also around 12 °C above the A_f temperature. At least three samples were tested for each sample type.

3.7 Microstructure Analysis of NiTi Wires

The microstructure of laser processed NiTi wires was analysed using two different methods. Optical microscopy was performed using an Olympus BX51M optical microscope. Electron backscatter diffraction (EBSD) analysis was performed using a Hitachi SU 3500 scanning electron microscope (SEM) operating at 20 keV. A conservative spline filtering algorithm was utilized to interpolate orientation information for non-indexed intragranular measurement points, which had a negligible impact on the orientation distribution of the collected dataset.

3.8 Mechanical Analysis of NiTi Springs

3.8.1 Spring Compression Test

Spring compression testing was done using an Instron 5548 micro-tensile tester with a ±0.5 μm measurement accuracy equipped with a temperature chamber. The spring ends were ground flat and the springs were compressed between two parallel plates to ensure uniform compression. A spring length of 10 mm was used for all samples tested. A crosshead speed of 4 mm/min was used. Samples were compressed to a maximum displacement of 2 mm before unloading to zero stress. Each spring type was tested in triplicate to verify results.

3.8.2 Self-Biasing Spring Test

To prevent buckling, the self-biasing springs were preloaded on a rod. The springs were compressed with enough force to compress the laser processed region(s), but not the unprocessed region. The ends were held in place to maintain a constant total length during testing. The samples were thermally heated until the laser processed region(s) transformed into austenite. The motion of the interface between laser processed and unprocessed regions was observed visually with a camera and reported as the actuation displacement.

Chapter 4: Modelling Compositional Changes of Laser Processed NiTi

4.1 Laser Parameters

In order to optimize the development of new MM SMA devices, the effect of laser processing parameters on Ni vaporization must be better understood. Until now, no in-depth investigation has been performed to fully understand and model relative vaporization rates for NiTi based on laser parameters. The material used for this study was BM7 wire. Laser pulses were overlapped ~60 % in order to remove the centerline solidification, which is necessary for post-process wire drawing [196]. Square pulse profiles, as shown in Figure 4.1, were investigated.

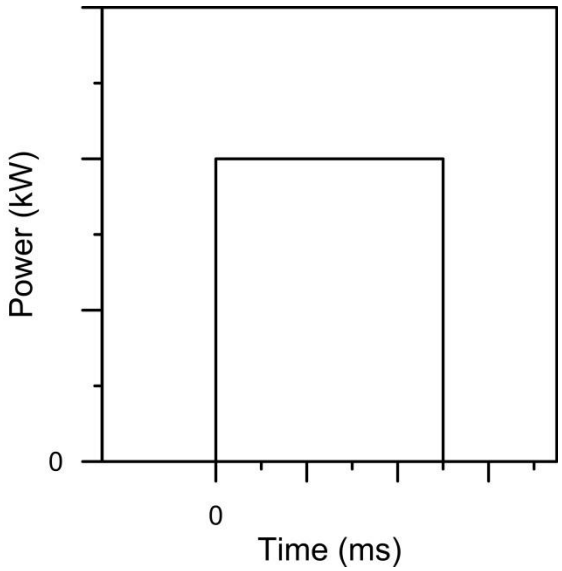

Figure 4.1 Generic square laser pulse profile.

Only pulse profiles that achieved full penetration of the specimen thickness without compromising the structural integrity of the specimen were used. Full penetration is defined such that no un-melted base material is observed between the laser spots on the underside of the specimen, see Figure 4.2b. Samples were examined with an optical microscope to verify the completeness of melting on the underside of wire. The structural integrity was considered to be compromised if the wire broke during laser processing or if there was significant bulging and distortion to the circularity of the cross section of the specimen wire. A map of all usable laser profiles is shown in

Figure 4.3. Note that the maximum power output of the laser is 5 kW and the maximum time duration of the laser is 30 ms. For pulse durations of 2 ms, the specimen is compromised as soon as full penetration is achieved due to significant expulsion of material, as indicated by the upper left portion of Figure 4.3. Therefore, 3 ms pulse durations were the shortest that could be examined in the study.

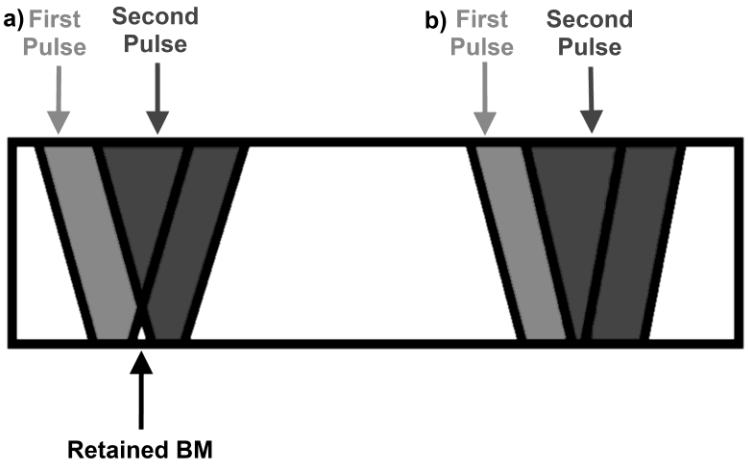

Figure 4.2 Schematic showing cross section view of laser processed wire depicting a) full melting with retained base material between laser processed spots and b) full melting with no retained base material between spots.

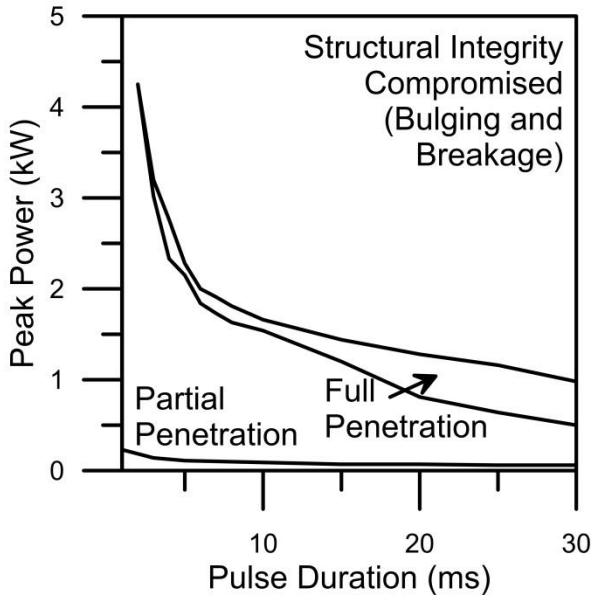

Figure 4.3 Laser pulse profile map showing which power and time combinations result in full penetration without compromising the specimen.

4.2 Changes in Transformation Temperature

A correlation between the M_s temperature and the mole fraction of Ni has been previously shown [72]. The M_s temperature is quite sensitive to the mole fraction of Ni. This means that small changes in the Ni mole fraction result in large changes in the M_s temperature. Conversely, large deviations in the measured M_s temperature would result in a minor error of the estimated Ni mole fraction (assuming a reliable conversion between the two can be developed). An error of ~5 % in the measurement of the M_s temperature (approximately 10-15 K) would result in an error of only about 0.1-0.15 % in the prediction of the Ni mole fraction (approximately 0.0005-0.0008, or 0.05-0.08 at. % Ni), as shown in Figure 4.4.

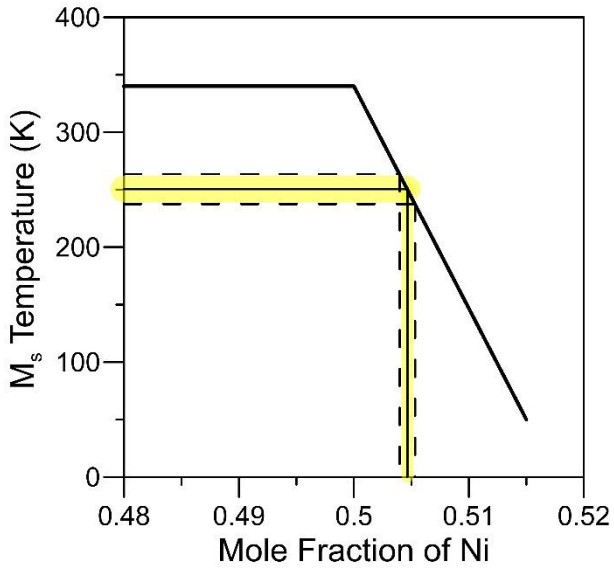

Figure 4.4 Relationship of error in M_s temperature carried over to error mole-fraction determination, based on Figure 2.9.

Therefore, the Ni composition after laser processing can be estimated from the M_s temperature observed by DSC analysis. From this data, a model can be developed to predict change in Ni composition for any square pulse profile that meets the requirements specified in the previous section. However, for some of the laser pulse profiles tested, the DSC data shows two transformation peaks, see Figure 4.5. This phenomenon has been observed before [22, 196] and suggests that there is a segregation of compositions occurring during the re-solidification of these specimens.

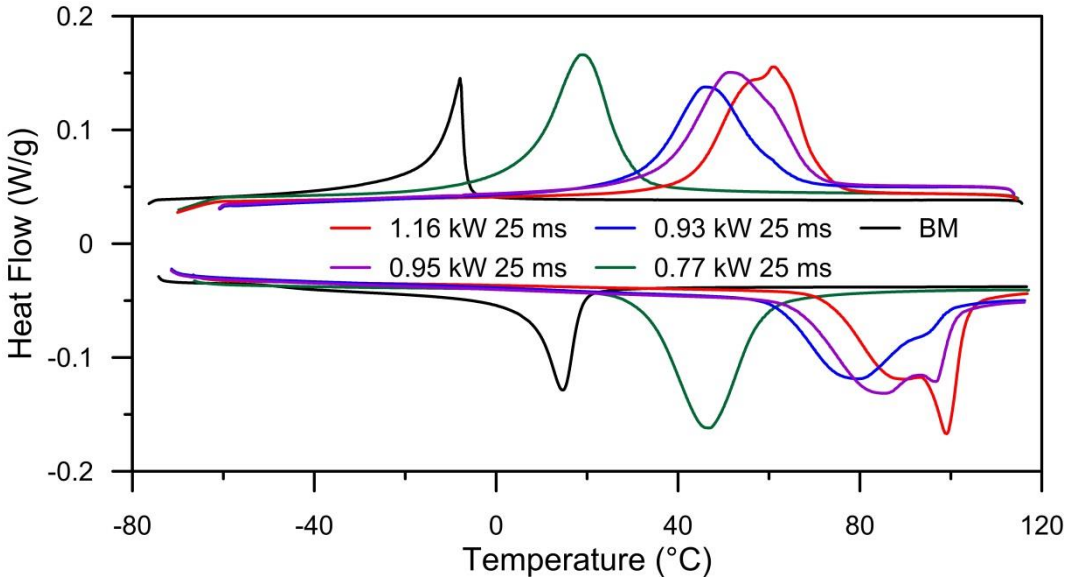

Figure 4.5 DSC data for BM compared with different laser pulse profiles.

Figure 4.6 shows the relationship between the peak power of the laser pulse and the austenite transformation peak. It can be seen that the composition segregation is independent of pulse duration, as pulse durations ranging from 30 to 20 ms show no segregation at low power, while segregation does occur at higher power. It should also be noted that for 3 ms pulses, there is only one transformation observed. This suggests that the composition segregation is not dependent on peak power either. All the samples that displayed dual transformation peaks were within a specific temperature range, i.e. ~66 to 101 ˚C. This implies that the composition segregation is occurring due to the resulting composition, not the laser parameters.

It has been shown that there is a very small difference between the solidus and liquidus on the Ni-rich side of the NiTi intermetallic congruency point and a much larger difference on the Ti-rich side of the congruency point (see Section 2.1.1 Physical Metallurgy) [34]. This means that for Ni-rich compositions, the cooling rate is fast enough to avoid significant segregation. However, on the Ti-rich side there is a steep drop-off in the solidus temperature (see Figure 2.1b) and solidification does not occur rapidly enough. Laser processing with a ramp down, similar to the profile in Figure 3.3, also results in two observable transformation peaks; however, thermomechanical post-processing sufficiently homogenizes the composition [207].

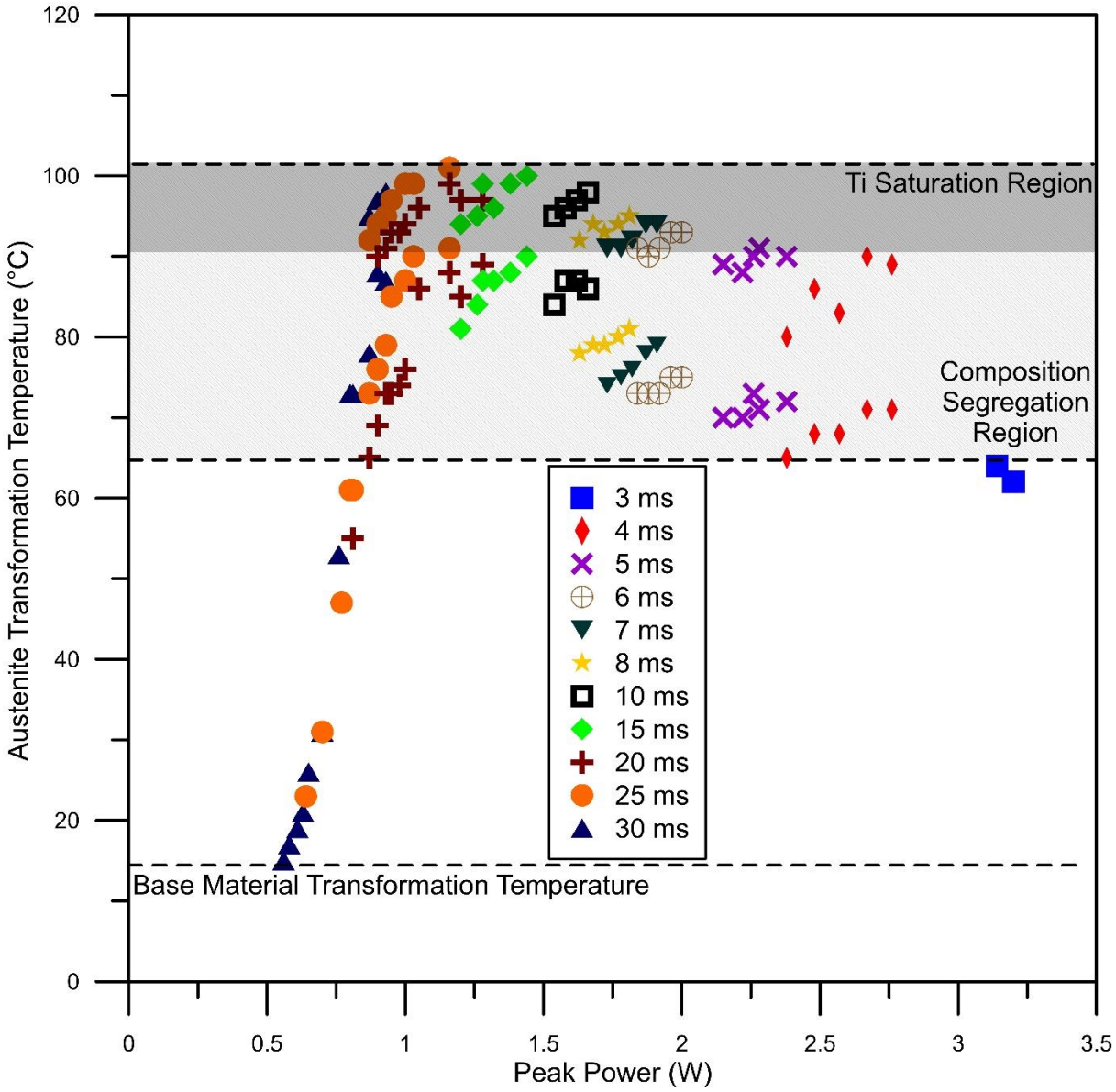

Figure 4.6 Austenite transformation temperature versus peak power for various pulse durations.

4.3 Deconvolution of Overlapping Peaks

In order to determine the amount of Ni lost during laser processing for the samples that experience compositional segregation, the overlapping DSC peaks must be deconvoluted. When the peaks are deconvoluted, the ratio of area under each peak can be used to approximate the volume ratio of each composition. This in turn can be used to determine the overall composition of the laser processed material.

Deconvoluting overlapping peaks is a common occurrence for many spectral analysis techniques. However, these techniques are typically looking for specific elements or compounds that behave in a predictable manor. The maximum peak height will be in a known location (plus or minus a known amount) and the peak height-to-width ratio will also be known in advance. This foreknowledge of the exact shape and location of the peak makes isolation of an individual peak from a group of overlapping peaks relatively easy.

Modelling and deconvolution of DSC peaks, while more complex than spectral analysis, has also been performed on generic DSC data; however, this technique requires some knowledge of the reaction kinetics that will occur, or the mathematics becomes extremely complicated [208]. Simpler methods rely on standard distribution models; however, these methods may not be suitable for curve fitting NiTi transformation peaks. The transformation kinetics for NiTi are not easily predetermined and the peak shapes are non-uniform. The thermomechanical history [42, 151, 209, 210] as well as changes in composition [42, 72, 211] will result in different shapes and locations for the transformation peaks. The numerous combinations of composition, grain size, precipitate size/density, etc. make developing a complete correlation between microstructure and transformation kinetics an unfathomable undertaking. This is further complicated when multiple compositions are contained in a monolithic material [22]. This study sets out to develop an adaptive function that can be fit to any shape of peak for NiTi DSC data. An algorithm will be put forth to separate overlapping DSC peaks and determine the individual peak characteristics.

4.3.1 Curve Fitting a Single Peak

Prior to curve fitting the data, a simple baseline subtraction is performed. Regression analysis is done on several data points not contained within the transformation peak. The function that best fits these data points is subtracted from the data, as shown in Figure 4.7. The baseline subtraction is performed first to simplify the process of curve fitting the NiTi DSC phase transformation peak(s).

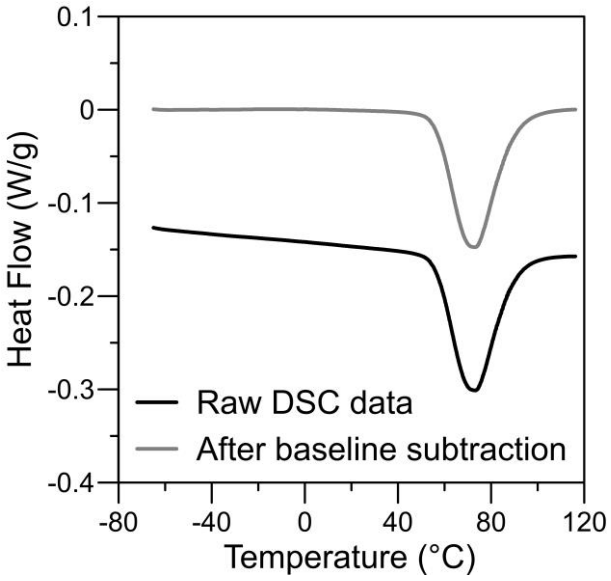

Figure 4.7. Depiction of a NiTi DSC transformation peak before and after a baseline subtraction is performed.

Due to the variability of peak shapes, an adaptive function was necessary. The function developed for this study was:

$$q^* = \frac{k}{1 + \left(\frac{abs(p-T)}{\varsigma}\right)^n + \left(\frac{abs(p-T)}{\varsigma}\right)^m} \quad \textbf{(Equation 4.1)}$$

where *k* is a scaling factor, *p* is the peak temperature, and ς is the peak width at 1/3 the peak height. The exponent *n* controls the curvature of the function and the base of the peak and the exponent *m* controls the curvature at the crest of the peak. At this time, the equation is purely a mathematical expression that best represents the transformation curve and currently does not have any physical relationship to the actual phase transformation kinetics. A program was created in Matlab™ to solve for *n* and *m*. Due to the skewness of the transformation peak, the function is split into two piecewise functions, one for the onset (Equation 4.2) and one for the endset (Equation 4.3) of the transformation:

$$if\ T \leq p, q^* = \frac{k_1}{1 + \left(\frac{p-T}{\varsigma_1}\right)^{n_1} + \left(\frac{p-T}{\varsigma_1}\right)^{m_1}} \quad \textbf{(Equation 4.2)}$$

$$if\ T > p, q^* = \frac{k_2}{1 + \left(\frac{T-p}{\varsigma_2}\right)^{n_2} + \left(\frac{T-p}{\varsigma_2}\right)^{m_2}} \quad \textbf{(Equation 4.3)}$$

Each equation is solved independently to best fit the skewness of the transformation peak. This function allows for curve fitting of any peak shape, regardless of the height to width ratio or the asymmetry of the peak.

Figure 4.8 shows how well the function fits the individual peaks of two different NiTi samples. Also, a comparison with a standard Fraser-Suzuki asymmetric Gaussian model and a Cauchy model are shown. The DSC peak of the AW sample has a skewed distribution, with the onset being more gradual and the endset being more abrupt. This is borne out in the parameters used to model the peak. The σ value for the onset is larger than for the endset, indicating a skewed distribution. Additionally, the n and m values for the onset are smaller than the endset values, indicating a steeper curve for the endset. The residual error for this new method is significantly lower than the two standard methods examined. The Fraser-Suzuki method can account for the skewness relatively well, but it cannot not account for the base of the AW peak being relatively wide. The Cauchy method does well matching the top to bottom distribution but is unable to account for the large asymmetry present in the AW peak.

The asymmetry of the PW1 sample is less apparent. Both the onset and endset have comparable σ values because the peak is more evenly distributed; however, the n and m values of the onset are larger than then endset because the endset has a more gradual transition. The peak for PW1 is broader than the peak for AW, which is reflected by much larger σ values for PW1 than AW. The Fraser-Suzuki method does appear to match the PW1 curve well; however, it still has a larger residual error than the newly proposed method. Overall, the new method does a much better job at curve fitting the data, as the standard methods do not have enough parameters to account for the non-uniformity of the NiTi transformation peaks. All of the relevant parameters for the new model are shown in Table 4.1.

Table 4.1. List of function parameters and transformation characteristics for single peak NiTi samples.

	Onset			**Endset**			**Derivative Method**			**Trios Software**		
	ς	**n**	**m**	**ς**	**n**	**m**	**A_s (˚C)**	**A_f (˚C)**	**Area J/g**	**A_s (˚C)**	**A_f (˚C)**	**Area J/g**
AW	4.457	2.1	1.4	3.093	3.3	2.4	8.9	18.2	12.7	8.9	18.3	13.1
PW1	13.131	6.1	2.3	13.101	4.4	1.5	55.9	91.4	20.0	55.7	89.8	20.2

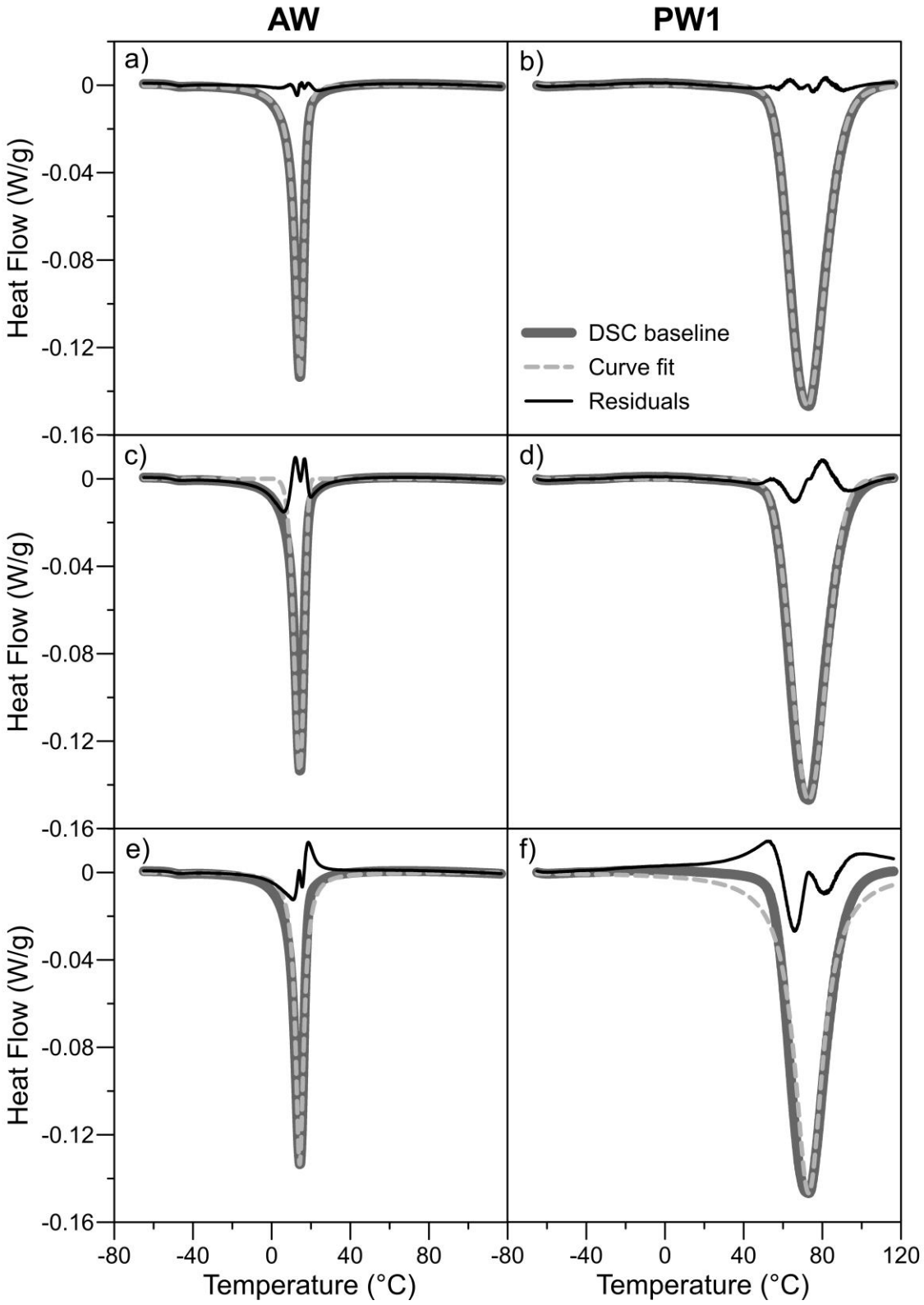

Figure 4.8. Depiction of curves fitting the DSC data for AW and PW1 samples using a-b) the proposed new model, c-d) a Fraser-Suzuki asymmetric Gaussian model and e-f) a Cauchy model.

Furthermore, calculating the A_s and A_f temperatures becomes a simple matter. These characteristic temperatures are determined by the intersection of the peak baseline and a tangent line running through the inflection point [58]. This inflection point is where the second derivative of the equation is equal to zero. The A_s and A_f temperatures for the single peaks were determined in this manner and compared with analysis performed using Trios software v3.2 (see Table 4.1), which is available from TA Instruments. The two methods showed comparable characteristic temperatures for both samples. These results validate this method as a means for fitting the DSC phase transformation peak and properly characterizing any NiTi sample with a single-phase transition.

4.3.2 Overlapping NiTi Transformation Peaks

4.3.2.1 Multiple Phase Transformations

Many NiTi SMAs have an intermediary R-phase transformation that reduces the amount of kinetic energy required to transition from martensite to austenite [212, 213]. Oftentimes, the DSC phase transformations peaks overlap, obscuring the endset of the first peak with the onset of the second peak. Occasionally, the peaks are so close together it is difficult to even determine what the R-phase peak (R_p) temperature is. Additionally, some NiTi alloys experience multi-stage martensite to austenite transformation due to precipitate formations. In these cases, the bulk material transforms first, while the material immediately surrounding the precipitates transforms later due to internal stresses or compositional gradients that arise near the precipitate formations [214-216]. This may also result in overlapping transformation peaks that create difficulty in properly characterizing the material.

The first step in deconvoluting the peaks is to estimate the shape of the taller of the two peaks. The initial value for σ_1 must be estimated, since it cannot be determined accurately from the data. The values for n_1 and m_1 are initially set to 1. Once the shape of the taller peak has been estimated, it is subtracted from the data, as shown in Figure 4.9. After this subtraction, one major peak remains in the data, representing the other phase transition. This peak is approximated as best as possible by the method previously described for single peaks. This peak is then subtracted from the original data set to better determine the shape of the first peak. This process is iterated several times to achieve the best curve fit for both peaks.

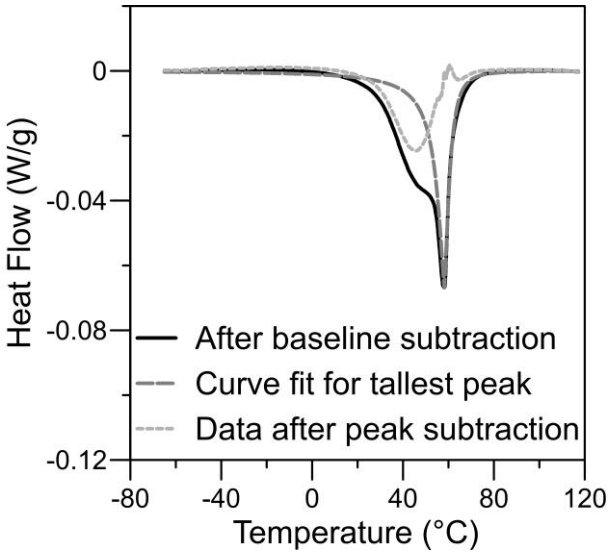

Figure 4.9. Depiction of first iteration of curve fitting the taller peak and subtracting it from the data.

Figure 4.10 shows how well this process fits two overlapping NiTi DSC transformation peaks. Comparison of the characteristic transformation temperatures before and after deconvolution is presented in Table 4.2 and Table 4.3. All of the characteristic temperatures determined by the deconvolution method are in good agreement with the temperatures that were ascertained from the raw data (within 1.5 ˚C). The only exception is the R-phase start (R_s) for the BMS sample, which was off by almost 5 ˚C. This discrepancy is most likely due to the inaccuracy of determining the inflection point of this shoulder peak, which is overlapped such that it is difficult for the untrained eye to even detect its presence; it appears slightly more prominently in Figure 4.11. It should be noted that the R_p and R-phase finish (R_f) temperatures cannot be determined without performing a deconvolution of the peaks, which is the added benefit of performing this analysis.

Table 4.2. Transformation characteristics determined from standard analysis.

	R_s (˚C)	R_p (˚C)	R_f (˚C)	A_s (˚C)	A_p (˚C)	A_f (˚C)	Peak 1 Area J/g	Peak 2 Area J/g	Total Area J/g
TPW	27.7	-	-	49.3	58.2	62.0	-	-	14.7
SBM	-21.4	-	-	-2.4	6.3	14.1	-	-	13.3

Table 4.3. Transformation characteristics determined after deconvolution.

	R_s (˚C)	R_p (˚C)	R_f (˚C)	A_s (˚C)	A_p (˚C)	A_f (˚C)	Peak 1 Area J/g	Peak 2 Area J/g	Total Area J/g
TPW	26.3	44.5	54.0	48.6	58.2	62.4	8.3	5.8	14.1
SBM	-26.1	-2.8	8.0	-3.9	6.3	13.6	9.2	3.8	13.0

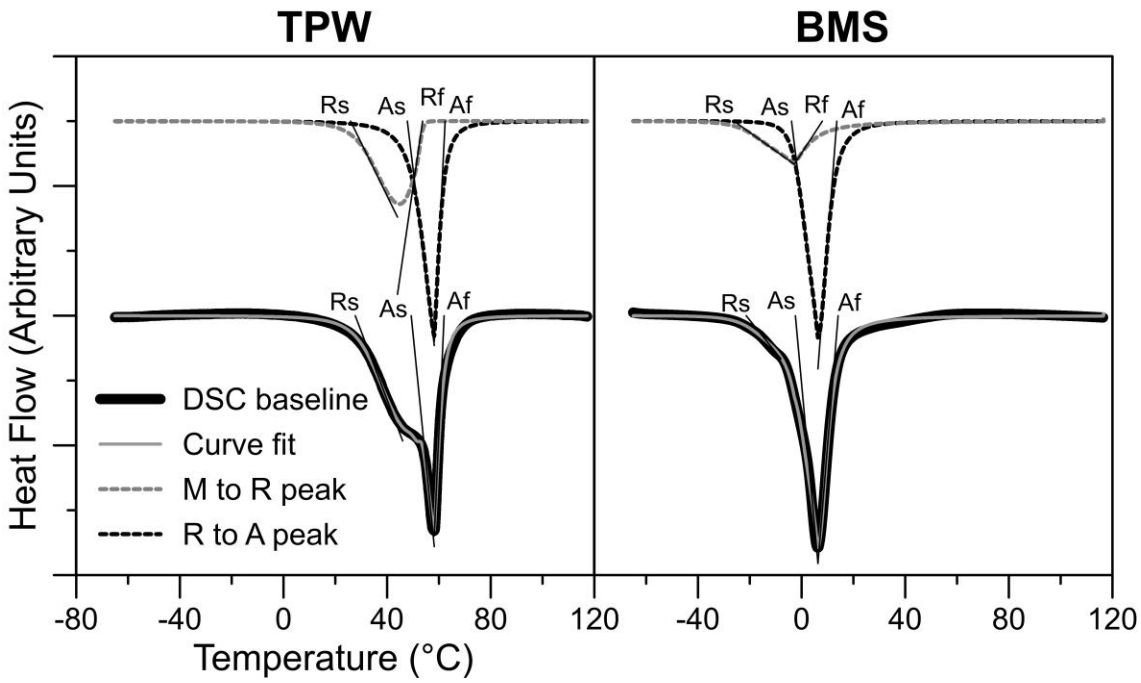

Figure 4.10. Depiction of curve fitting the DSC data for the TPW and BMS samples.

The DSC analysis can become even more complicated when the material has been partially treated with a laser. Figure 4.11a shows a cross-section of a NiTi sheet that has been partly re-melted by a laser pulse. The re-melted region experienced Ni depletion during laser processing, which changed the local composition and thus the phase transformation temperature in the region [22]. If the base material undergoes an intermediate R-phase transformation and the laser treated region has a slightly shifted transformation temperature, then it is possible to have three overlapping transformation peaks, as shown in Figure 4.11b.

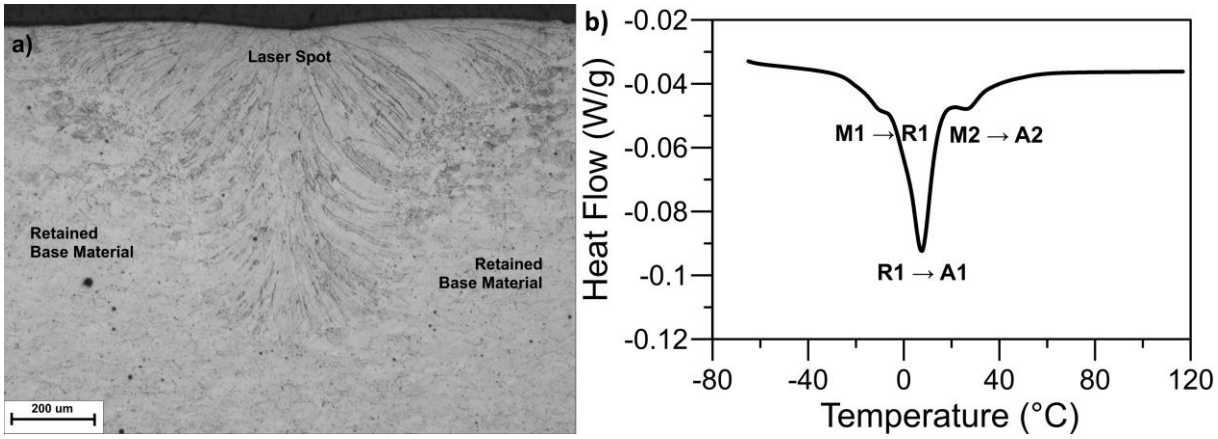

Figure 4.11. a) Cross section showing the partially laser processed PS sample, and b) DSC heating curve of the PS material showing the overlapping phase transformations.

Deconvolution of three overlapping peaks proceeds in a similar manner as for two overlapping peaks. The shape of the tallest peak is estimated then subtracted, followed by the second tallest, then the shortest. Figure 4.12 demonstrates the ability of this method to deconvolute three overlapping NiTi DSC transformation peaks. By this method, it would be possible to deconvolute any number of peaks for a complex nonhomogeneous NiTi SMA.

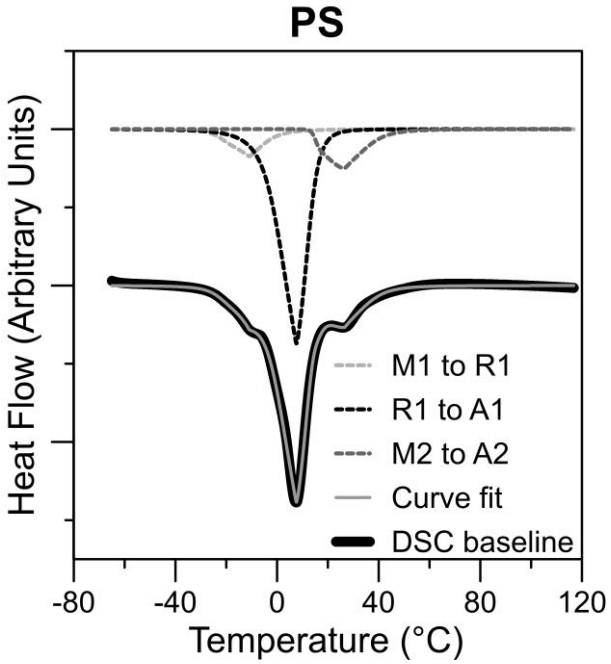

Figure 4.12. Depiction of curve fitting the DSC data for the PS sample with three overlapping peaks.

4.3.2.2 Single Phase Transformations with Mixed Compositions

When laser welding to join NiTi or laser treating to modify the composition, it is possible to get compositional segregation during solidification [22, 207], as shown in Figure 4.13. It is known that both phase transformations are martensite to austenite due to the hysteresis between the heating and cooling peaks. The first transformation has a hysteresis of 36 ˚C and the second transformation has a hysteresis of approximately 37 ˚C. These are typical for a martensite to austenite transformation [60]; however, the R-phase to austenite transformation has a much smaller hysteresis, typically only a few degrees [44, 43]. Therefore, the material must be experiencing two separate martensite to austenite phase transformations due to the presence of two different compositions.

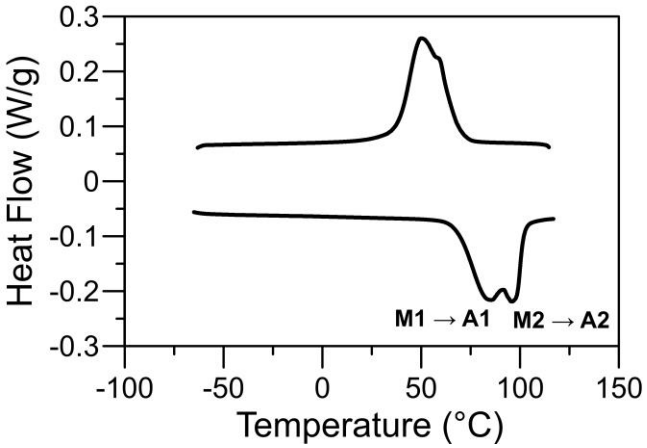

Figure 4.13. DSC heating/cooling curves of the PW2 showing the overlapping transformation peaks of two segregated compositions.

Even though the DSC peaks are overlapping, they can be deconvoluted by the method described previously. In addition to determining the transformation properties of each composition, the areas under the individual curves can be used to approximate the volume fraction of each composition and determine the overall bulk composition, as shown in Figure 4.14. Since both compositions have similar transformation pathways (i.e. martensite directly to austenite with no intermediate phases), the ratio of the amount of energy required for each phase transformation should be approximately proportional to the ratio of the volume of each composition. In this case, the first transformation volume is 55.8 % of the total volume and the second transformation volume is 44.5 % of the total volume.

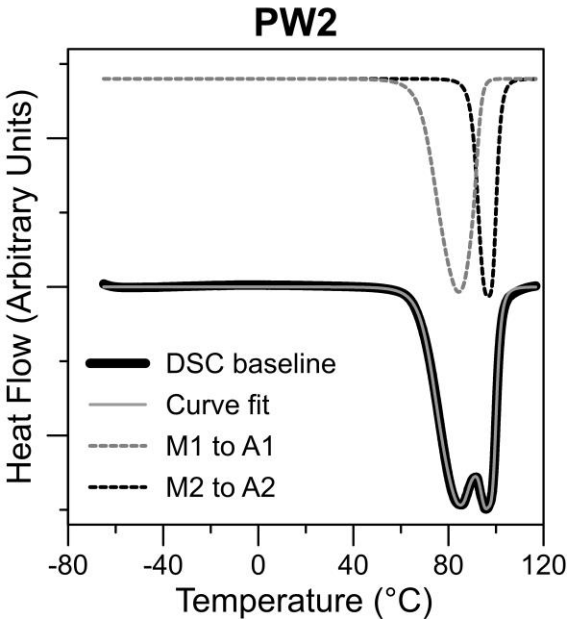

Figure 4.14. Depiction of curve fitting of sample PW2 with mixed composition.

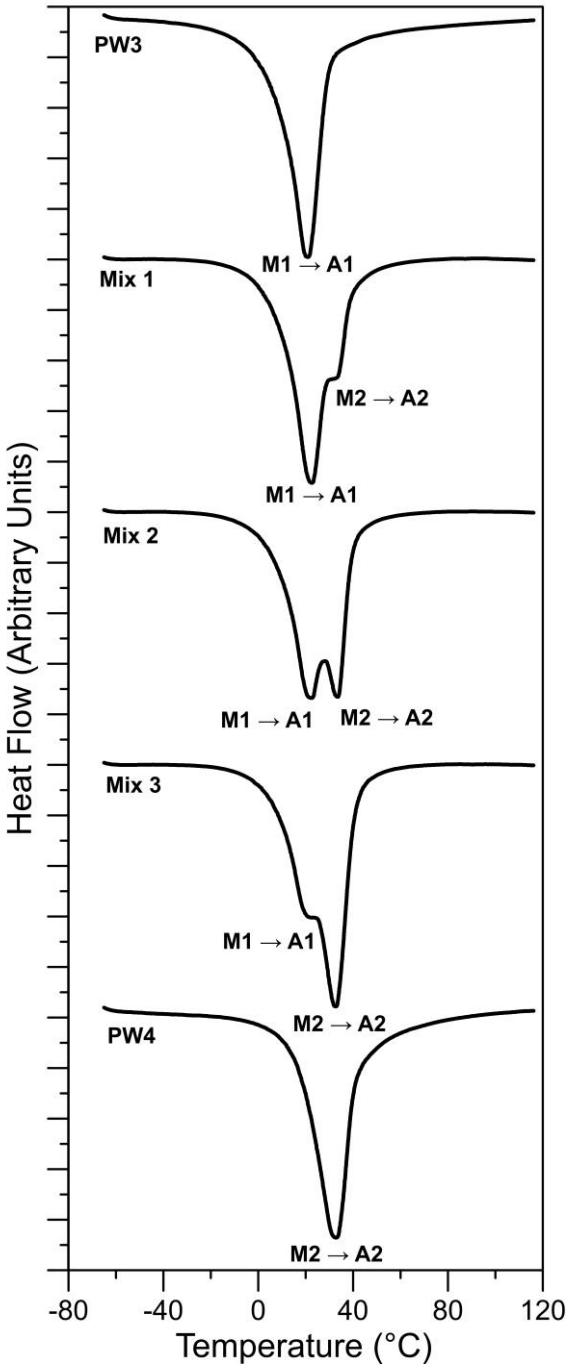

Figure 4.15. DSC heating curves for PW3, PW4 and mixed samples.

In order to verify this method, two materials (PW3 and PW4) with known compositions and only a single transformation peak each were placed together in known quantities and analyzed by DSC in three different ratios, as shown in Figure 4.15. The individual peaks for PW3 and PW4 were found to have areas of 19.1 J/g and 19.5 J/g, respectively. Since both materials have similar thermomechanical histories and transformation kinetics, the ratio of the areas of the deconvoluted

peaks can be analyzed and compared to the actual ratio of volumes for each material present. In all cases, the calculated volume percentage was in close agreement with the actual volume percentage (see Table 4.4). Additionally, the transformation temperatures of Mix, Mix 2 and Mix 3, which were determined through the new deconvolution method, are in good agreement with the transformation temperatures of PW3 and PW4, which were determined using the Trios software. This indicates that this method is a reasonable approximation for determining the relative volumes present for a sample with mixed compositions when both compositions have a similar microstructure and phase transformation pathway.

Table 4.4. List of physical volume percentages, calculated volume percentages and transformation peaks.

	Actual Volume (%)		**Calculated Volume (%)**		**1st peak (˚C)**	**2nd peak (˚C)**
PW3	100	0	100	0	20.9	N/A
Mix 1	65.8	34.2	67.8	32.2	21.7	33.7
Mix 2	51.9	48.1	53.0	47.0	20.6	33.8
Mix 3	36.9	63.1	35.1	64.9	19.8	32.7
PW4	0	100	0	100	N/A	32.7

4.4 Changes in Ni Concentration

Since the heating DSC curves showed more separation between overlapping peaks when composition segregation occurred, they allowed for easier and more accurate deconvolution of peaks. Therefore, the austenite peak temperature (A_p) was used to determine the change in Ni concentration after laser processing. Figure 4.16 shows the relationship between A_p and pulse peak power after deconvoluting the peaks. After deconvoluting the peaks, it can be seen that for each pulse duration, the transformation temperature trends higher as peak power increases.

To determine the Ni composition, a relationship between the A_p and Ni atomic concentration must be established. Khalil-Allafi *et al.* [215] have already established a relationship between Ni concentration and the martensite peak temperature (M_p):

$$M_p(c_{Ni}) = (2027077588.5 - 205968221.1 \times c_{Ni} + 8370845.646 \times {c_{Ni}}^2 - 170093.5974 \times {c_{Ni}}^3 + 1728.050544 \times {c_{Ni}}^4 - 7.022069029 \times {c_{Ni}}^5)K \quad \textbf{(Equation 4.4)}$$

where c_{Ni} is the atomic concentration of Ni in a binary NiTi alloy. Furthermore, Frenzel *et al.* [211] have established a piecewise relationship between Ni concentration and the hysteresis between the M_p and A_p:

$$\begin{cases} if\ c_{Ni} > 49.8\ at.\%, & \Delta T = (-17.5 \times c_{Ni} + 920.5)K \\ if\ c_{Ni} \leq 49.8\ at.\%, & \Delta T = 49K \end{cases} \quad \textbf{(Equation 4.5)}$$

Thus, it is possible to determine what the A_p temperature should be for any given Ni concentration by replacing ΔT with (A_p – M_p) and substituting in Equation 4.4 for M_p. A list of A_p values for several Ni concentrations can be found in Appendix I: Tabulated Transformations Peaks Relative to Ni Concentration.

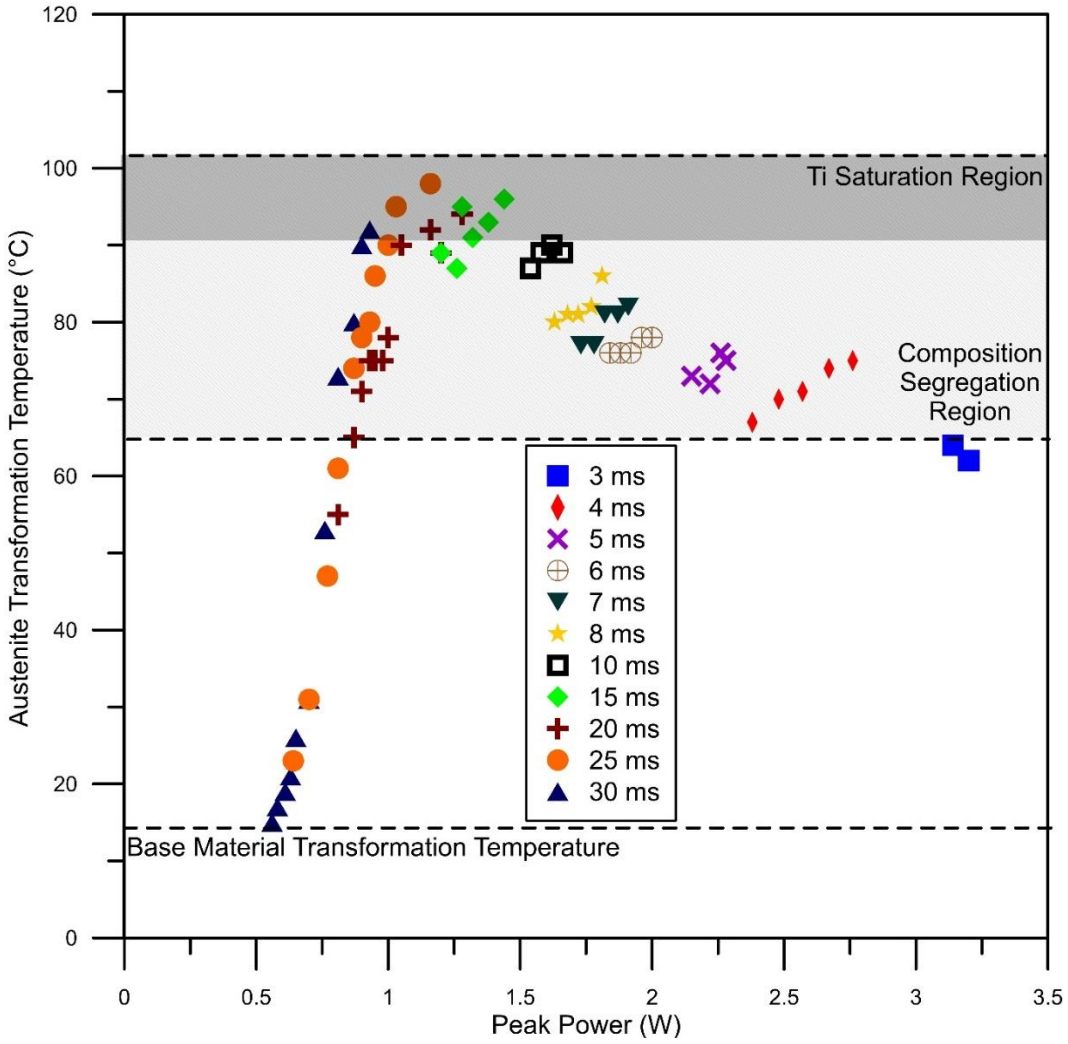

Figure 4.16 Average austenite transformation temperature after deconvolution of overlapping peaks versus laser pulse peak power for various pulse durations.

This relationship was found to be in good agreement with previous experimental results. Pequegnat [59] used micro-PIXE analysis to determine the Ni concentration of a NiTi sheet after laser processing with an error of ±0.21 at.%. It was shown that for a sample with an A_p of ~34.9 ˚C the Ni concentration was 50.46 ±0.15 at.% and for a sample with an A_p of ~65.2 ˚C the Ni concentration was 50.16 ±0.15 at.%. Using the relationship above it was determined that a material with an A_p of 34.9 ˚C would have a Ni concentration of ~50.57 at.%, which is within the standard deviation of the micro-PIXE results. Additionally, the above relationship can be used to find that for a material with an A_p of 65.2 ˚C has a Ni concentration of ~50.20 at.%. These results validate this relationship for determining Ni concentrations via the DSC transformation peaks.

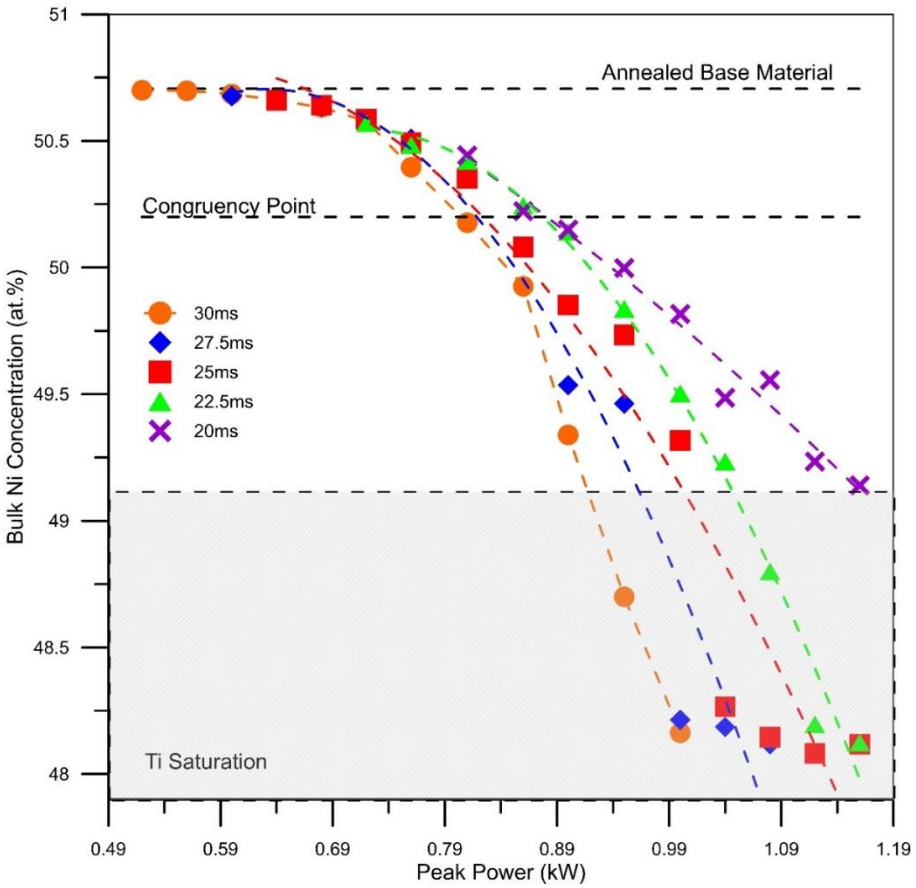

Figure 4.17 Bulk Ni concentration versus laser pulse peak power for various pulse durations.

Figure 4.17 shows Ni concentrations relative to peak power for various pulse durations. Pulse durations from 20 ms to 30 ms were examined since they showed the widest range of usability based on the range of transformation temperatures achievable while maintaining wire integrity (see Figure 4.3). When too much Ni is removed, the material becomes saturated with Ti and Ti_2Ni

precipitates form as the composition is moving outside the range where the equiatomic NiTi intermetallic is stable [211] (see Section 2.1.1 Physical Metallurgy). It is important to note that the composition in the Ti Saturation region (see Figure 4.17) may not properly represent the amount of Ni lost due to the likely formation of these Ti-rich precipitates during solidification; however, these compositions would be undesirable to manufacture by the method of laser processing, since Ti_2Ni precipitates are brittle [32].

4.5 Modelling the Change in Ni Composition

Looking closely at Figure 4.17 reveals there are two different vaporization mechanisms at play. At lower pulse powers (< 0.72 kW), the change in Ni concentration appears to be independent of the pulse duration. This most likely indicates conduction mode vaporization, where the alloy elements vaporize from the melt pool surface. Once the atmosphere immediately surrounding the melt pool surface becomes saturated with alloy element ions, the vaporization reaches a steady state, thus longer pulses have no effect on further changing the relative composition. At higher powers (> 0.72 kW), the change in pulse duration has a significant effect on the resultant Ni concentration. This most likely indicates that keyhole vaporization is occurring. As the pulse duration becomes longer, the heat builds up and the keyhole continues to grow [217]. The more the keyhole grows, the more alloy elements are removed.

This transition from conduction mode to keyhole mode can be observed through examination of the melt pool geometry, as shown in Figure 4.18. It can be seen that at 0.60 kW, the melt pool has a wide “bowl” shape (see Figure 4.18a). Meanwhile, at 0.76 kW the melt pool volume is smaller and has a more triangular shape that is typical of transition keyhole melt pool formations. There is a wide “bowl” shape at the top, since the pulse starts in conduction mode, and a narrower “vase” shape at the bottom, which is formed once the keyhole is generated (see Figure 4.18b). These results are in line with previous studies using similar pulse powers and energy densities [217]. It should be noted that this change in melt pool shape occurs due to the change in the flow pattern of the liquid within the melt pool. This change may be brought about by a change in the surface tension that may not necessarily result in the formation of a keyhole; however, there is currently no good understanding of how the surface tension of NiTi changes with temperature.

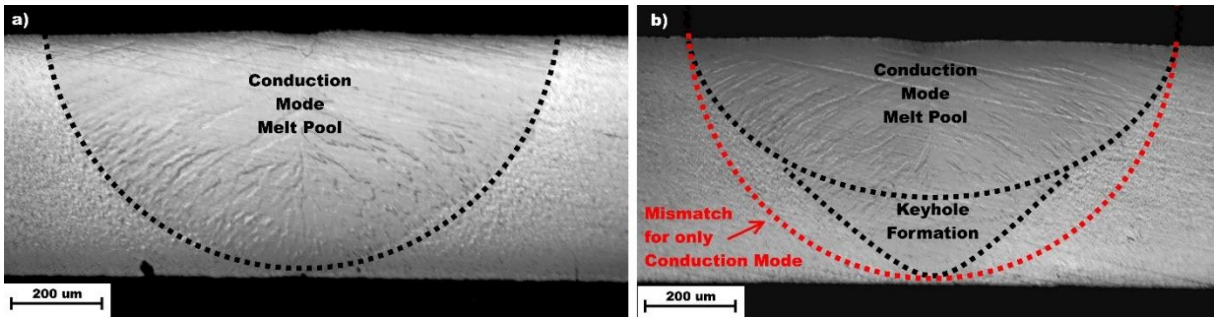

Figure 4.18 Melt pool cross sections for a) 0.60 kW and b) 0.76 kW.

Focusing in on just the conduction mode vaporization reveals even more insights. As the peak power increases, the amount of Ni lost increases. This suggests that the vaporization rate of Ni increases relative to that of Ti as temperature increases, which would seem to be in agreement with how the equilibrium vapor pressure of Ni increases relative to Ti, as shown in Figure 2.19. However, plotting the partial pressures on a log scale reveals something different. There is little change between the magnitudes of the Ni partial pressure and the Ti partial pressure as temperature increases, as shown in Figure 4.19a. Furthermore, plotting the theoretical flux ratio J_{Ti}/J_{Ni} shows a slight increase with temperature (see Figure 4.19b), which would result in a decrease in Ni loss relative to Ti as the temperature increases. Though this decrease would be slight, it is contrary to the experimental results, which show an increase in the Ni vaporization rate even before the onset of keyhole vaporization.

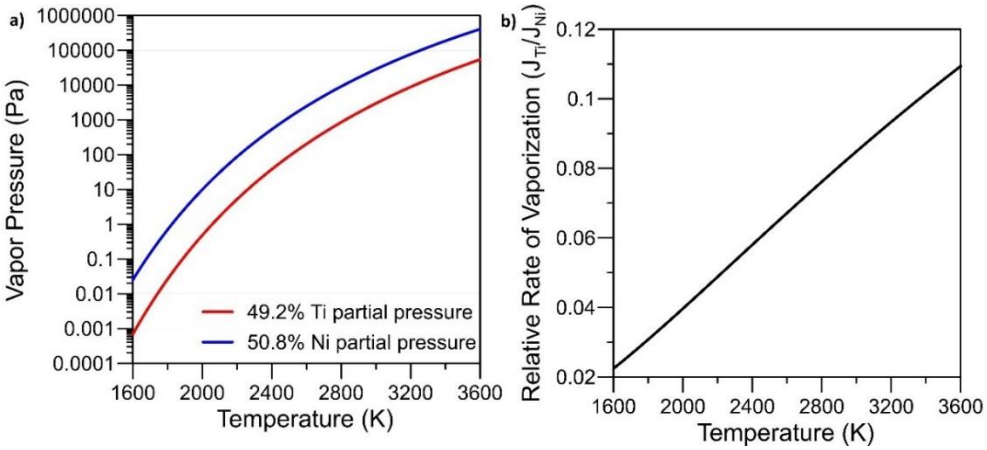

Figure 4.19 a) Partial pressures of Ni and Ti plot on a log scale and b) relative rates of vaporization for Ti/Ni.

The ratio of fluxes was calculated using Equations 2.11 to 2.13, where the diffusivities of the vaporizing elements in the argon shielding gas is given by [134, 135]:

$$D_{i,Ar} = \frac{1.8583 \times 10^{-7} \sqrt{\left(\frac{1}{M_i} + \frac{1}{M_{Ar}}\right) T^3}}{{\sigma_{i,Ar}}^2 \Omega_{D,i} T^*} \quad \textbf{(Equation 4.6)}$$

where M_i is the molecular weight of element *i*, M_{Ar} is the molecular weight of argon, $\boldsymbol{T}$ is the absolute temperature, $\Omega_{D,i}$ is a collision integral (values were obtained from J.O. Hirschfielder *et al.* [218]) that is a function of the dimensionless parameter $k_B T/\epsilon_{i,Ar}$. The values for $\epsilon_{i,Ar}$, $\sigma_{i,Ar}$ and T^* are determined by Equations 4.7, 4.8 and 4.9, respectively [134, 135].

$$\epsilon_{i,Ar} = \sqrt{\epsilon_i \epsilon_{Ar}} \quad \textbf{(Equation 4.7)}$$

$$\sigma_{i,Ar} = \frac{\sigma_i + \sigma_{Ar}}{2} \quad \textbf{(Equation 4.8)}$$

$$T^* = \frac{k_B T}{\epsilon_{Ar}} \quad \textbf{(Equation 4.9)}$$

where $\epsilon_{i,Ar}$ is the effective intermolecular force parameter, ϵ_i is the intermolecular force parameter of alloy element *i*, $\epsilon_{i,Ar}$ is the intermolecular force parameter of argon, $\sigma_{i,Ar}$ is the effective collision diameter, σ_i is the collision diameter of alloy element *i*, σ_{Ar} is the collision diameter of argon and k_B is the Boltzmann constant. The values of each parameter for Ni, Ti and Ar are presented in Table 4.5.

Table 4.5. Data used to for calculating gas diffusivity [134, 135].

Parameter	Ni	Ti	Ar
M	58.693	47.867	39.948
σ	2.38	2.76	3.418
ϵ/k_B	3641.5	3894.83	124.0

To attempt a determination of the total amount of material vaporized, samples were weighed before and after laser processing to assess how much material was lost due to vaporization, as was done in previous studies [127]. Sample weights per unit length are shown in Figure 4.20, while the weight change per unit length is tabulated in Table 4.6. It was found that for laser pulse powers less than 0.8 kW there was a slight increase in sample weight after laser processing. This is most likely due to oxygen entrapment during laser-processing [207] and/or immediately after laser processing due to re-passivation of the surface oxide [219]. Typically, titanium oxide formation is preferred over nickel oxide [220]; however, it has been shown that after laser processing, nickel oxides are also present [221]. In addition to forming surface oxides, the oxygen may also get mixed into the bulk material and form oxide inclusions [207]. For Ni-rich alloys, Ti_4Ni_2O is the most

commonly formed inclusion, while $Ti_2Ni(O)$ is frequently found in Ti-rich compositions [222]. The sudden increase in weight loss that occurs above 0.8 kW most likely corresponds with the formation of keyholes, as this phenomenon results in significant material loss.

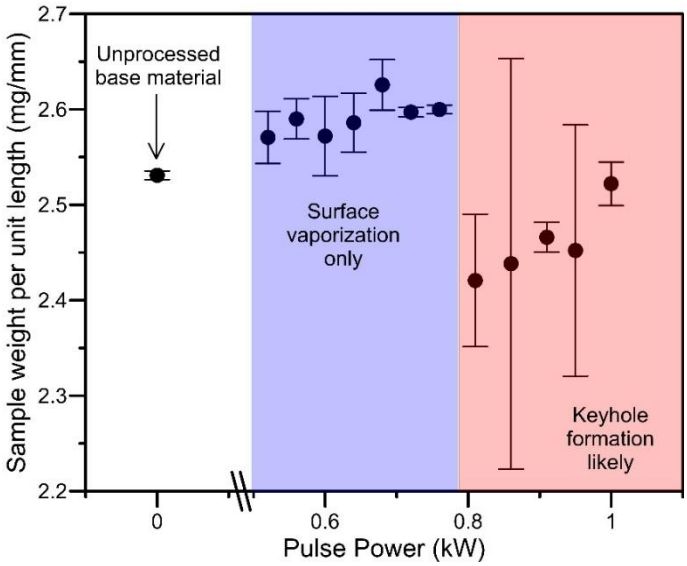

Figure 4.20 Sample weight per unit length for 30 ms pulse durations. Each sample condition was tested five times.

Table 4.6. Weight change per unit length after laser processing (30 ms pulse durations). Each sample condition was tested five times.

Peak Power (kW)	Weight Change (mg/mm)
0.52	+0.0396
0.56	+0.0591
0.60	+0.0123
0.64	+0.0551
0.68	+0.0948
0.72	+0.0662
0.76	+0.0690
0.81	-0.1101
0.85	-0.0926
0.90	-0.0649
0.95	-0.0788
1.00	-0.0088

An alternative method to determine weight loss (or total vaporization rate) through the collection of element vapor would be difficult to implement. NiTi requires argon shielding to prevent excessive oxidation and any collection device would have to be sufficiently far enough from the surface so as not to prevent proper shielding, which would reduce the effectiveness of the collection method. Additionally, since the entire cross section of the wire melts during laser processing, it is very possible the alloys elements vaporize from the entire melt pool surface around the entire circumference of the wire. Since the temperature of the melt pool surface will be cooler on the underside of the wire, the vaporization rates in that area would be different than those on top of the wire. So, without collecting all of the vapor that is produced, the vaporization rates may be misrepresented. The trouble with collecting the vapor during processing becomes doubly fruitless due to the inevitable presence of oxide inclusions, surface oxide formations and precipitate formations. The relative rates of vaporization would not completely account for the change in the bulk composition. For these reasons, a model was developed to predict the change in composition, not the relative vaporization rate, since a model relating laser parameters to the final bulk composition is what is truly needed.

4.5.1 Conduction Mode Vaporization

In conduction mode, vaporization occurs entirely at the melt pool surface, therefore it is necessary to understand what is happening at the surface. It was already shown that the change in Ni concentration is independent of pulse duration due to saturation of the surrounding atmosphere. This suggests that transport away from the surface is not the limiting factor for relative rates of vaporization. Additionally, it has been shown that after laser processing, NiTi has a homogeneous composition [59]. This suggests that bulk mixing is also not the limiting factor in determining the relative rates of vaporization, since no composition gradient is formed.

NiTi is self-passivating and Ti_2O is the preferred oxide, which means that the surface oxide layer is usually nickel depleted [220]. The Ti:Ni ratio can range from 6:1 to 10:1 for acid etched surfaces (surface condition before laser processing) [221]. Acid etching is a common practice to remove the thick oxide layer that forms during the manufacturing process, and it was the surface condition prior to laser processing in this study. Since the flux of Ni is ten times higher than that of Ti and the surface concentration of Ni may be ten times lower than Ti, any Ni on the surface will most

certainly vaporize and further vaporization can only occur if more Ni can reach the surface. While previous studies have shown that bulk mixing is sufficient to prevent any compositional gradient across the melt pool, characterizations of the surface of NiTi after laser processing have shown that the Ti-rich surface skin is preserved during laser processing and even expanded slightly [221]. The presence of Ti oxides on the surface may result in the formation of micro-eddies and surface turbulence [125], which may prevent complete mixing with the bulk (see Section 2.3.5 Laser Induced Vaporization), as shown in Figure 4.21. Thus, the observed rise in the relative rate of Ni vaporization as the temperature increases may be ascribed to the increase in the diffusivity rate of Ni through the Ti-rich surface layer.

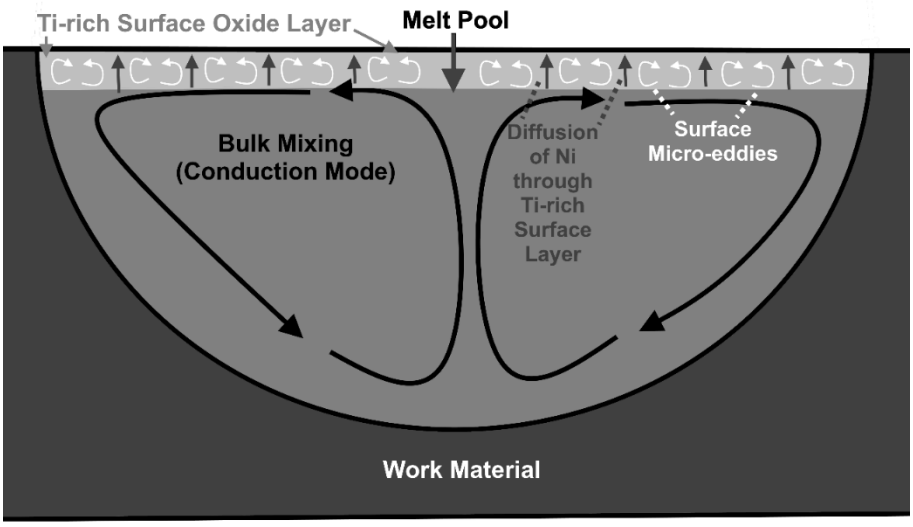

Figure 4.21 Schematic showing bulk mixing of a conduction mode melt pool with surface micro-eddies. Nickel must diffuse through the surface layer before it can vaporize. Not drawn to scale.

A look at the diffusion properties of Ni and Ti reveals that the self-diffusion of both metals has an Arrhenius-type dependence on temperature [223]:

$$D = D_0 e^{\left(-E_A/k_B T\right)} \qquad \textbf{(Equation 4.10)}$$

where D is the diffusion coefficient, D_0 is a pre-factor, E_A is an activation energy, k_B is the Boltzmann constant and T is the temperature. A first approximation for diffusion of a solute A into a solvent B assumes that the size of flow is proportional to the Goldschmidt atomic diameter of the metals in question [224]:

$$D_{AB} = \frac{d_B}{d_A} D_{BB} \quad \textbf{(Equation 4.11)}$$

Substituting Equation 4.10 into Equation 4.11 gives:

$$D_{Ni,Ti} = \frac{d_{Ti}}{d_{Ni}} D_{Ti} e^{\left(-E_A/k_B T\right)} \quad \textbf{(Equation 4.12)}$$

where d_{Ti} and d_{Ni} are the Goldschmidt atomic diameters of Ti and Ni, D_{Ti} is the self-diffusion pre-factor for Ti, E_A is an activation energy for self-diffusion of Ti, and k_B is the Boltzmann constant. The specimen temperature was not measured directly in this study, but it is dependent on the power of the laser pulse. Therefore, a conversion from laser pulse power to temperature was introduced:

$$T = \chi p_L \quad \textbf{(Equation 4.13)}$$

where χ is the conversion factor that translates laser power into temperature and p_L is the power of the laser pulse. The value for χ was chosen by assuming the melt pool reached the boiling point for NiTi (~3277 K) at 0.76 kW (i.e. the first laser power to experience a jump in the amount of Ni lost).

Additionally, the Ti-rich surface layer is not static. Turbulence and mixing are occurring. Thus, a scaling factor Ξ is added to adjust for this phenomenon. So, Equation 4.12 becomes:

$$D_{Ni,Ti} = \frac{d_{Ti}}{d_{Ni}} D_{Ti} e^{\left(\Xi E_A/k_B \chi p_L\right)} \quad \textbf{(Equation 4.14)}$$

Finally, the resultant concentration of Ni is dependent on the initial concentration, the area through which the Ni diffuses, and the time it takes to reach a steady state condition. Since these are all scalers, they were condensed into a single scaling factor, κ. Then Equation 4.14 becomes:

$$\Delta C_{Ni} = \kappa \frac{d_{Ti}}{d_{Ni}} D_{Ti} e^{\left(\Xi E_A/k_B \chi p_L\right)} \quad \textbf{(Equation 4.15)}$$

where ΔC_{Ni} is the change in Ni concentration. The Goldschmidt atomic diameters were found in Smithells' Metals Reference Book [40], the diffusion properties of Ti were determined from previous research [41], and the scaling/conversion factors were determined experimentally. All of the values used are shown in Table 4.7.

Table 4.7. Coefficients used to model the change in Ni concentration through surface evaporation.

κ (at. % s/m^2)	d_{Ti}	d_{Ni}	D_0 (m^2/s)	Ξ	E_A (eV)	k_B (eV/K)	χ (K/kW)
1×10^{10}	2.94	2.50	1.15×10^{-7}	4.68	0.53	8.61733×10^{-5}	4312

Figure 4.22 shows this new relationship compared with the changes in Ni concentration for laser powers from 0.52 kW to 0.9 kW. There is a good correlation between the experimental results and the proposed model up to 0.76 kW. Above 0.76 kW the experimental data begins to scatter, because this is when keyhole formation is first observed. At first glance, one might think this should only lead to an increase above the diffusion-only model for the change in the Ni concentration. However, the onset of keyhole formation coincides with the material reaching its boiling point. This means that temperature of the liquid is no longer increasing because it is beginning to boil. Therefore, there would be no change to the diffusivity or resulting vaporization rates since the liquid temperature would not be increasing. This would result in a maximum amount of Ni loss achievable through surface vaporization with some Ni vaporization occurring due to the keyhole formation, as shown in Figure 4.22.

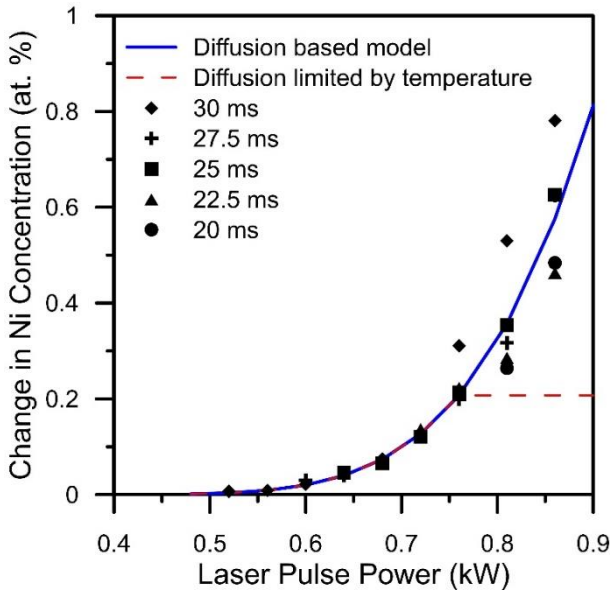

Figure 4.22 Comparison between experimental data and diffusion-based models for change in Ni concentration.

4.5.2 Keyhole Mode Vaporization

During keyhole vaporization, the formation of the actual keyhole most likely does not contribute to any significant change in composition. Rather it allows the bulk Ni to circumvent the Ti-rich surface layer and vaporize directly. To analyze the effects of the keyhole formation, the change in Ni concentration due to surface vaporization is subtracted from the total change in Ni concentration for all powers greater than 0.76 kW. This was done because the surface vaporization will occur

and finish before the keyhole even forms due to the long duration of the laser pulse profiles. In keyhole mode, both the pulse power and duration do have an effect on how large the keyhole becomes [126]. Therefore, a first approximation was chosen such that:

$$\Delta C_{Ni} = C {p_D}^a {p_p}^b \qquad \textbf{(Equation 4.16)}$$

where *C*, *a* and *b* are constants, p_D is the duration of the laser pulse and p_p is the change in power of the laser pulse. The change in pulse power is relative to the power where no keyhole vaporization occurred. A large shift in Ni concentration was observed at 0.76 kW after 30 ms, see Figure 4.22. Thus, it was assumed that at 0.72 kW there may have either been small unobservable/unstable keyhole formations or there were disturbances in the surface oxide (due changes in surface tension) that exposed the bulk material to direct vaporization, so a peak power of 0.68 kW was set as the reference power where no keyhole vaporization occurs. The values for *C*, *a* and *b* where determined by reducing the error of the function. The standard error of estimation was calculated by:

$$\sigma_{est} = \sqrt{\frac{\sum (Y - Y')^2}{N}} \qquad \textbf{(Equation 4.17)}$$

where σ_{est} is the standard error of the estimation, *Y* is the true experimental value, *Y'* is the value estimated by the equation and *N* is the number of data points.

It was determined from the experimental results that the pulse duration had a larger influence on the change in Ni concentration than the peak power. The values determined for the three constants are given in Table 4.8, and Figure 4.23 shows a plot of the model compared with data for each pulse duration. A good correlation between the model and the data was found, with an overall standard error of 0.098. It is important to note that this relationship is not applicable below 0.72 kW because keyhole vaporization is not occurring. Also, it does not hold up when the material becomes Ti-saturated.

Table 4.8. Coefficients used to model the change in Ni concentration by keyhole formation.

C (at. %)	a	b
1.45×10^{-3}	3	2.5

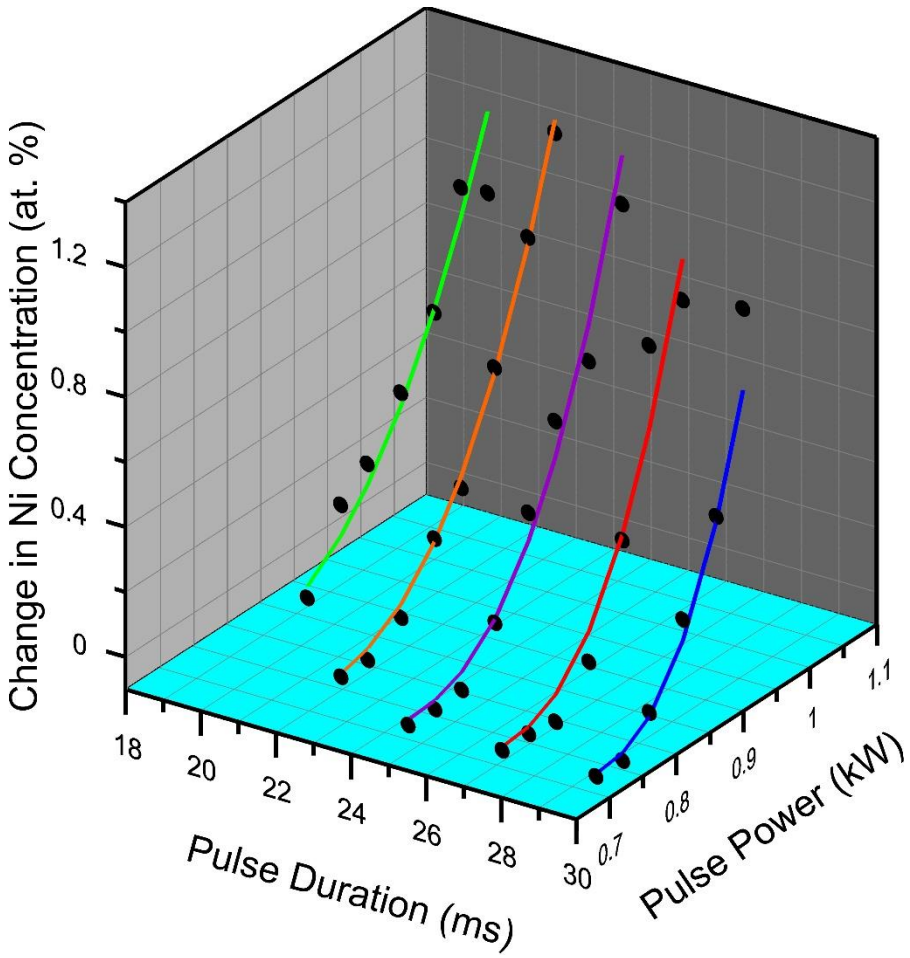

Figure 4.23 Comparison between experimental data and keyhole-size models for change in Ni concentration.

4.5.3 Verification of Model

The full comprehensive model for change in Ni composition is piecewise and dependent on which vaporization mechanisms present and how they are changing:

$$\begin{cases} if\ p_L < 0.68\ kW, & \Delta C_{Ni} = (1{,}352.4)e^{(-6.6/p_L)} \\ if\ 0.68 \le p_L \le 0.76\ kW, & \Delta C_{Ni} = (1{,}352.4)e^{(-6.6/p_L)} + (1.45 \times 10^{-3}){p_D}^3(p_L - 0.68)^{2.5} \\ if\ p_L > 0.76\ kW, & \Delta C_{Ni} = 0.2277 + (1.45 \times 10^{-3}){p_D}^3(p_L - 0.68)^{2.5} \end{cases}$$ **(Equation 4.18)**

For powers peak powers less than 0.68 kW the composition change is dependent only on diffusion of Ni to the surface. For powers that are between 0.68 kW and 0.76 kW, inclusive, the change in composition is determined by the diffusion of Ni to the surface and the growth of the keyhole. Above 0.76 kW, the change in composition is primarily determined by the size of the keyhole with a constant contribution from surface vaporization. The overlap of increasing diffusion rate and the

growth of the keyhole present in the second part of the model may be explained by the fact that the pool melt can exceed the boiling point of the alloy. Zhao and DebRoy found that the melt pool temperature can surpass the boiling temperature of the molten metal resulting in a positive pressure and keyhole initiation [227]. Therefore, small keyhole formations may be present before the surface diffusion reaches its maximum diffusion rate.

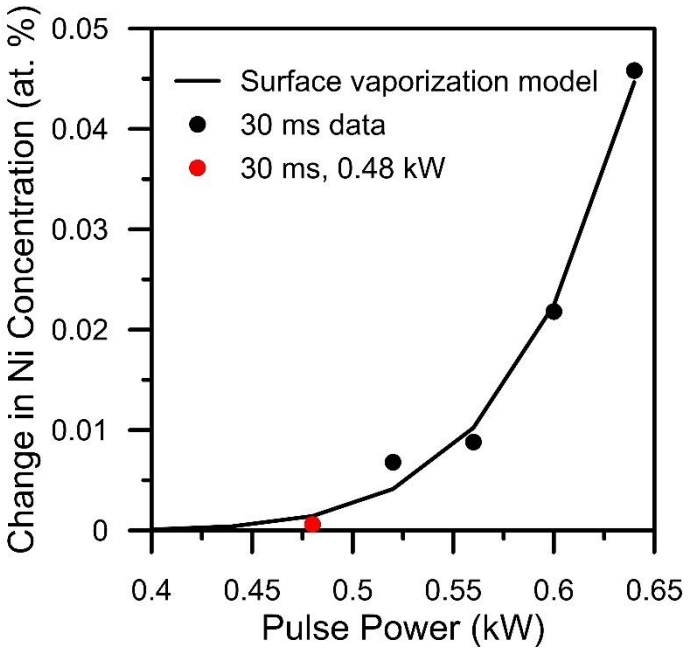

Figure 4.24 Comparison between experimental data for 30 ms pulse durations and the surface vaporization model.

To verify the surface vaporization mechanism (< 0.68 kW), a lower laser power was tested. A peak power of 0.48 kW was used to determine how accurate the surface vaporization model is. This power was chosen because it was previously untested, and it is the minimum power capable of fully melting the wire specimen size chosen for this study. It was important to avoid testing partial penetration profiles at this time, since any change of less than 1 ˚C in the transformation temperature would be undetectable by DSC if any base material was retained. After laser processing with a pulse profile of 0.48 kW and 30 ms, hardly any change in the Ni concentration was detected. A change of only 0.6×10^{-3} at. % was observed, which is in good agreement with the surface vaporization model, as shown in Figure 4.24. Using this pulse profile will have a negligible effect on the bulk composition and transformation properties.

To verify the keyhole growth portion of the model (> 0.76 kW), shorter pulses with higher peak powers were examined (see Figure 4.16). Only compositions below Ti-saturation could be tested

since the model is not valid in the Ti-saturation range. Only two data points fit this criteria for the 15 ms pulse durations; however, these two data points do show good correlation with the proposed model. There is also a reasonable correlation for the profiles using 10, 8, 7, 6, 5 and 4 ms pulse durations, see Figure 4.25. Predictions for 12.5 and 9 ms pulse durations are also shown, though there is no corresponding experimental data for these pulse profiles.

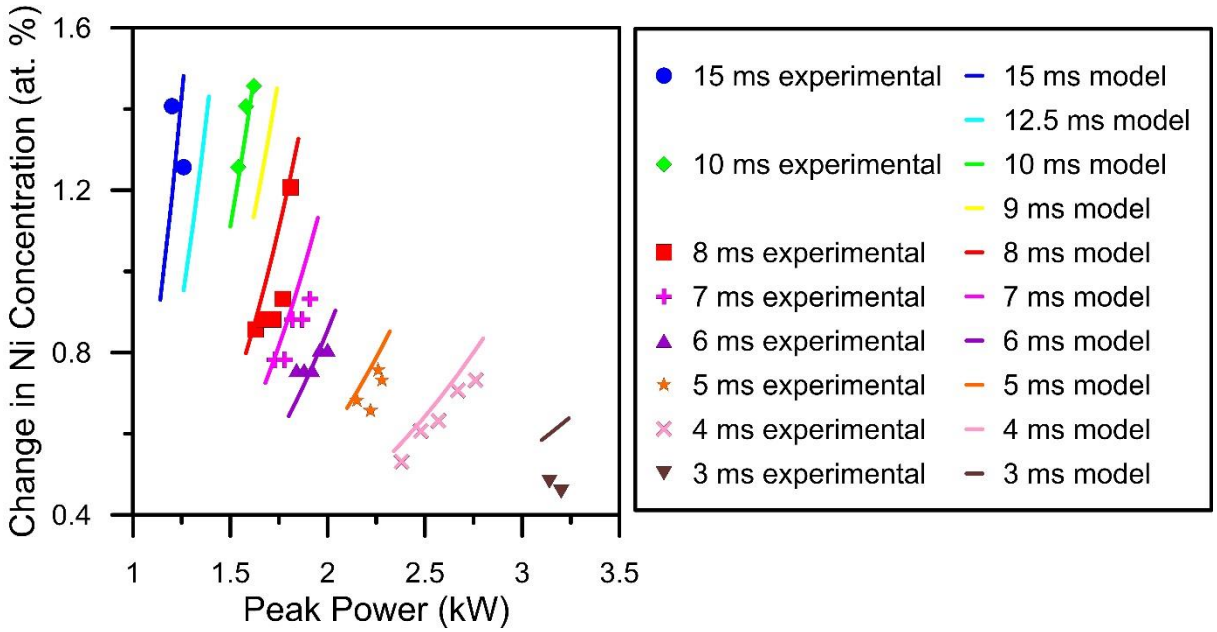

Figure 4.25 Comparison between experimental data and keyhole growth models for high power short duration laser pulse profiles.

The experimental results for 3 ms pulse durations are significantly lower than the values predicted by the model. This could be due to insufficient time for Ni to diffuse to the surface. For long pulse durations, surface vaporization reaches a steady-state before the pulse ends and appears to be independent of pulse duration. However, 3 ms may not be enough time for the surface vaporization to reach steady-state. It has been shown that the vaporization rates change significantly over the first three milliseconds of a laser pulse as the melt pool gets hotter [129]. Since the vaporization mechanism and the diffusion rate of Ni to the surface are determined by temperature, insufficient time to reach a thermal steady-state on the surface could result in a higher ratio of Ti vaporizing during the laser pulse. This may account for the over estimation of the change in Ni composition for the 3 ms pulse profiles. Further work will need to be done to determine how much time is needed for Ni diffusion and surface vaporization to reach a steady-state.

Additionally, this overestimation may be due to extreme instability of the keyhole during laser processing. The keyhole has been found to be unstable even in stationary conditions (such as pulsed laser processing) due to an oscillating motion along the keyhole wall that creates a protrusion, which causes the keyhole to collapse in on itself [217]. If the keyhole collapses prematurely (before the laser pulse terminates), then less material will be vaporized during that pulse as keyhole growth will be impeded. Further work will need to assess the effect of keyhole stability on compositional changes.

It was already mentioned earlier that the data seems to show more scatter when keyhole vaporization has been induced compared to conduction mode vaporization (see Section 4.5.1 Conduction Mode Vaporization). This is probably due in part to keyhole instability generating more variance from pulse to pulse and sample to sample. Therefore, for manufacturing processes involving full penetration of laser processed of NiTi wires, conduction mode vaporization seems to be a better option, as it has been shown to be more predictable and more tuneable (smaller increments of change). Increasing the pulse overlap or the number of pulses per spot can be used to expand the range of compositional change without using keyhole vaporization. Additionally, lower pulse powers are effective at reducing the amount of Ni loss during laser processing. This would be beneficial for laser joining methods to mitigate the effect of embrittlement due to the formation of Ti-rich precipitates.

4.6 Chapter Summary

In this chapter, a systematic investigation into the effect of laser pulse duration and peak power on the compositional change of a binary NiTi alloy was undertaken. A good correlation between laser parameters and transformation temperature was observed. However, when the composition moved to the Ti-rich side of the NiTi intermetallic congruency point, compositional segregation obfuscated the total amount of Ni removed.

A function capable of fitting the DSC transformation curve of any shape for NiTi alloys was developed. A method was successfully demonstrated to be able to deconvolute overlapping DSC peaks for NiTi alloys that exhibit complex phase transformation pathways. A good correlation between the newly proposed methodology and the currently used analysis techniques was

established. This sets the groundwork for enhanced material characterization of complex and non-homogeneous multi-phase NiTi SMAs that implement gradient compositions or microstructures.

Deconvolution of the overlapping DSC peaks allowed for the Ni concentration to be determined through previously established relationships. This in turn allowed for a better understanding of how the bulk composition changes with respect to laser pulse parameters. It was found that there are two different mechanisms for vaporization: surface vaporization and keyhole growth. A comprehensive model was developed to predict the change in Ni composition due to laser pulse parameters. A good correlation was found between experimental data and the proposed model for peak powers ranging from 0.48 kW to 2.75 kW and for pulse durations ranging from 30 ms to 4 ms. It was also observed that conduction mode vaporization appears to be a better choice for reliable manufacturing of laser processed NiTi SMAs.

Chapter 5: One-Dimensional Model for Monolithic SMAs with Multiple Pseudoelastic Plateaus

5.1 Thermodynamics of Pseudoelasticity in Multiple Memory Material

For 1-dimensional modelling, the use of an expression with thermodynamic potential and yield functions for the forward and reverse phase transformations was employed. This type of model is capable of striking a balance between the overly complex micromechanics models and over-simplified models, as it integrates some inherent material properties that can be predetermined from in-depth DSC analysis. The model initiated by Raniecki *et al.* [28] has been recalled. The stress/strain relationship is given by:

$$\boldsymbol{\sigma = \frac{3E}{2(1+\nu)}(\varepsilon - \varepsilon_t \xi)} \qquad \textbf{(Equation 5.1)}$$

Where *E* is the elastic modulus, ν is Poisson's ratio, ε_t is the transformation strain and ξ is the volume fraction of the martensite phase.

The value of ξ is determined iteratively by calculating the change in ξ at each time step as defined by Thiebaud et al [228]:

$$\boldsymbol{\dot{\xi}_{A\to M} = \frac{3\varepsilon_t E \dot{\varepsilon}}{2\rho(1+\nu)\left(\frac{A_1}{1-\xi} - 2\phi_{it}(T)\right) + 3{\varepsilon_t}^2 E}} \qquad \textbf{(Equation 5.2)}$$

$$\boldsymbol{\dot{\xi}_{M\to A} = \frac{3\varepsilon_t E \dot{\varepsilon}}{2\rho(1+\nu)\left(\frac{A_2}{\xi} - 2\phi_{it}(T)\right) + 3{\varepsilon_t}^2 E}} \qquad \textbf{(Equation 5.3)}$$

where

$$\boldsymbol{\phi_{it} = u_0 - Ts_0} \qquad \textbf{(Equation 5.4)}$$

and u_0 and s_0 are the internal configurational energy and entropy and T is the temperature of the material. Thiebaud et al [228] derived A_1 and A_2 to be:

$$\mathbf{A_1} = -\frac{\boldsymbol{\pi^f}}{\mathbf{ln(1-\xi)}} \qquad \textbf{(Equation 5.5)}$$

$$\mathbf{A_2} = \frac{\boldsymbol{\pi^f}}{\mathbf{ln(\xi)}} \qquad \textbf{(Equation 5.6)}$$

where π^f is the thermodynamic driving force associated with progression of the phase transformation, given as [228]:

$$\boldsymbol{\pi^f} = \frac{\mathbf{3\varepsilon_t E\varepsilon}}{\mathbf{2\rho(1+\nu)}} + \boldsymbol{\pi_0^f}\mathbf{(T)} - \mathbf{(1-2\xi)}\boldsymbol{\phi_{it}}\mathbf{(T)} - \frac{\mathbf{3{\varepsilon_t}^2 E\xi}}{\mathbf{2\rho(1+\nu)}} \qquad \textbf{(Equation 5.7)}$$

and π_0^f is the thermodynamic driving force in the stress-free state:

$$\boldsymbol{\pi_0^f} = \mathbf{\Delta u^*} - \mathbf{T\Delta s^*} \qquad \textbf{(Equation 5.8)}$$

where Δu^* and Δs^* are the differences between the internal energy and entropy of the austenite and martensite phases.

These models make the assumption that the austenite and martensite phases have the same elastic modulus. For the multiple memory material, there are three distinct elastic responses and the assumption that all three have the same elastic modulus is not valid. To account for the different elastic responses, the effective elastic modulus is used instead, as demonstrated by Maletta at el [229]:

$$\mathbf{E} = \mathbf{1} \Big/ \left(\frac{\mathbf{1-\xi}}{\mathbf{E_A}} + \frac{\boldsymbol{\xi}}{\mathbf{E_M}}\right) \qquad \textbf{(Equation 5.9)}$$

where E_M and E_A are the elastic moduli for martensite and austenite, respectively. For this study, this equation has been modified to include an additional elastic response that occurs in between the two pseudoelastic plateaus:

$$\mathbf{E} = \mathbf{1} \Big/ \left(\frac{\mathbf{1-\xi_1}}{\mathbf{E_1}} + \frac{\boldsymbol{\xi_1-\xi_2}}{\mathbf{E_2}} + \frac{\boldsymbol{\xi_2}}{\mathbf{E_3}}\right) \qquad \textbf{(Equation 5.10)}$$

where ξ_1 is the volume fraction of martensite for the first material region, ξ_2 is the volume fraction of martensite for the second material region, E_1 is the effective elastic modulus of the first elastic response (where both sections are in austenite phase), E_2 is the effective elastic modulus of the second elastic response (where one section is still in the austenite phase while the other has transformed into martensite), and E_3 is the effective elastic modulus of the third elastic response

(where both sections are in the martensite phase). These new effective elastic moduli are defined as:

$$\mathbf{E_1} = \mathbf{1} \Big/ \left(\frac{\boldsymbol{\ell_1}}{\mathbf{E_{A1}}} + \frac{\mathbf{1} - \boldsymbol{\ell_1}}{\mathbf{E_{A2}}} \right) \qquad \textbf{(Equation 5.11)}$$

$$\mathbf{E_2} = \mathbf{1} \Big/ \left(\frac{\boldsymbol{\ell_1}}{\mathbf{E_{M1}}} + \frac{\mathbf{1} - \boldsymbol{\ell_1}}{\mathbf{E_{A2}}} \right) \qquad \textbf{(Equation 5.12)}$$

$$\mathbf{E_3} = \mathbf{1} \Big/ \left(\frac{\boldsymbol{\ell_1}}{\mathbf{E_{M1}}} + \frac{\mathbf{1} - \boldsymbol{\ell_1}}{\mathbf{E_{M2}}} \right) \qquad \textbf{(Equation 5.13)}$$

where E_{A1} and E_{M1} are the elastic moduli for the austenite and martensite phases of the first material region, E_{A2} and E_{M2} are the elastic moduli for the austenite and martensite phases of the second material region, and ℓ_1 is the length fraction of the first material region ($\ell_1 \neq 0$). If E_{A1} is equivalent to E_{A2}, then E_1 reduces to be E_A by:

$$\textbf{If } \mathbf{E_{A1} = E_{A2} = E_A}$$

$$\textbf{then } \mathbf{E_1} = \mathbf{1} \Big/ \left(\frac{\boldsymbol{\ell_1}}{\mathbf{E_A}} + \frac{\mathbf{1} - \boldsymbol{\ell_1}}{\mathbf{E_A}} \right) = \mathbf{1} \Big/ \left(\frac{\boldsymbol{\ell_1} + \mathbf{1} - \boldsymbol{\ell_1}}{\mathbf{E_A}} \right) = \mathbf{1} \Big/ \frac{\mathbf{1}}{\mathbf{E_A}} = \mathbf{E_A} \qquad \textbf{(Equation 5.14)}$$

The same is true for E_3 reducing to E_M if E_{M1} and E_{M2} are equivalent. Additionally, if there is only one distinct material region not two, then ℓ_1 would be 1 thus E_1 reduces to be E_A and E_2 reduces to be E_M, and ξ_2 would always be zero. Therefore, with only one uniform region, Equation 5.10 is equivalent to Equation 5.9.

With the new modifications to the elastic modulus, the use of transformation strain ε_t is no longer valid. Instead, a normalized transformation strain ε_o must be used, as was validated by Liu and Yang [230]:

$$\boldsymbol{\varepsilon_o} = \frac{\boldsymbol{\sigma^{AM}}}{\mathbf{E_A}} + \boldsymbol{\varepsilon_t} - \frac{\boldsymbol{\sigma^{AM}}}{\mathbf{E_M}} \qquad \textbf{(Equation 5.15)}$$

where σ^{AM} is the plateau stress for the austenite to martensite transformation, and ε_o is shown in the schematic in Figure 5.1a. For use with multiple plateau stresses, a new equation was developed for the second transformation plateau:

$$\boldsymbol{\varepsilon_{o1}} = \frac{\boldsymbol{\sigma^{AM1}}}{\mathbf{E_1}} + \boldsymbol{\varepsilon_{t1}} - \frac{\boldsymbol{\sigma^{AM1}}}{\mathbf{E_2}} \qquad \textbf{(Equation 5.16)}$$

$$\boldsymbol{\varepsilon_{o2} = \frac{\sigma^{AM1}}{E_1} + \varepsilon_{t1} + \frac{\sigma^{AM2} - \sigma^{AM1}}{E_2} + \varepsilon_{t2} - \frac{\sigma^{AM2}}{E_3}} \qquad \textbf{(Equation 5.17)}$$

where σ^{AM1} and σ^{AM2} are the plateau stresses for the austenite to martensite transformations of the first and second material regions, respectively, and ε_{t1} and ε_{t2} are the transformation strains for the first and second material regions, respectively. The transformation strain, ε_{t1}, is defined to be:

$$\boldsymbol{\varepsilon_{t1} = \ell_1 \varepsilon_t} \qquad \textbf{(Equation 5.18)}$$

where ℓ_1 is the length fraction of the first region and ε_t is the transformation strain of that individual material from Equation 5.1. The same relationship is also valid for the second material region. In this way, any length ratio between the first and second material regions can be predicted. Additionally, if there is only one material region and ℓ_1 is 1, then Equation 5.16 is equivalent to Equation 5.15. These modifications result in the following new stress/strain relationship for a material with two pseudoelastic plateaus:

$$\boldsymbol{\sigma = \frac{3E}{2(1+\nu)}(\varepsilon - \varepsilon_{o1}(\xi_1 - \xi_2) - \varepsilon_{o2}\xi_2)} \qquad \textbf{(Equation 5.19)}$$

where E is calculated using Equation 5.10 and ξ_1 and ξ_2 are both calculated using Equations 5.2 and 5.3, ε_{o1} and ε_{o2} are calculated using Equations 5.16 and 5.17, and ε is the total strain.

Since the same moduli are not used for the austenite and martensite phases, the reverse plateaus will have a shorter transformation strains than the forward plateaus (see Figure 5.1). This is already accounted for with the use of ε_{o1} and ε_{o2}.

$$\boldsymbol{\varepsilon_{o1} = \frac{\sigma^{AM1}}{E_1} + \varepsilon_{t1f} - \frac{\sigma^{AM1}}{E_2} = \frac{\sigma^{MA1}}{E_1} + \varepsilon_{t1r} - \frac{\sigma^{MA1}}{E_2}} \qquad \textbf{(Equation 5.20)}$$

$$\boldsymbol{\varepsilon_{o2} = \frac{\sigma^{AM1}}{E_1} + \varepsilon_{t1f} + \frac{\sigma^{AM2} - \sigma^{AM1}}{E_2} + \varepsilon_{t2f} - \frac{\sigma^{AM2}}{E_3}} = \boldsymbol{\frac{\sigma^{MA1}}{E_1} + \varepsilon_{t1r} + \frac{\sigma^{MA2} - \sigma^{MA1}}{E_2} + \varepsilon_{t2r} - \frac{\sigma^{MA2}}{E_3}} \qquad \textbf{(Equation 5.21)}$$

where σ^{MA1} and σ^{MA2} are the plateau stresses for the martensite to austenite transformation of the first and second material regions, respectively, ε_{t1f} and ε_{t2f} are the forward transformation strains for the first and second material regions, respectively, and ε_{t1r} and ε_{t2r} are the reverse transformation strains for the first and second material regions, respectively.

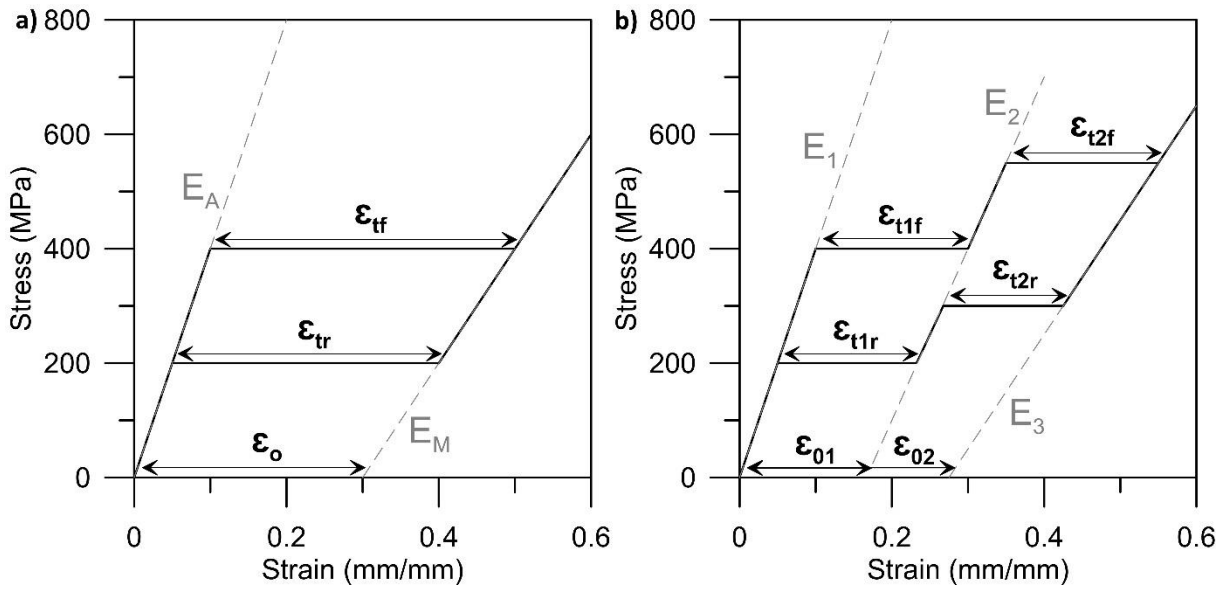

Figure 5.1: Schematics showing the elastic moduli and transformation strains for a) single plateau and b) double plateaus.

This novel equation can be expanded to model any number of plateaus, as shown in Figure 5.2. Equation 5.10 becomes:

$$\boldsymbol{E = 1 \Big/ \left(\frac{1}{E_1} + \sum_{n=1}^{j} \left(-\frac{\xi_n}{E_n} + \frac{\xi_n}{E_{n+1}} \right) \right)} \qquad \textbf{(Equation 5.22)}$$

where *j* is the total number of pseudoelastic regions, ξ_n is the martensite volume fraction for the *n*th pseudoelastic region, and E_n is the effective elastic modulus for the *n*th elastic response, calculated by:

$$\boldsymbol{E_n = 1 \Big/ \left(\sum_{i=n, when\ n<j+1}^{j} \frac{\ell_i}{E_{Ai}} + \sum_{i=1, when\ n>1}^{n-1} \frac{\ell_i}{E_{Mi}} \right)} \qquad \textbf{(Equation 5.23)}$$

where ℓ_i is the length fraction of the *i*th material region, E_{Ai} is the austenite elastic modulus for the *i*th material region and E_{Mi} is martensite elastic modulus for the *i*th material region. The first summation is never used for the last elastic region (i.e. when $E_n = E_{j+1}$ all elastic moduli are martensitic) and the second summation is never used in the first response (i.e. when $E_n = E_1$ all elastic moduli are austenitic). It is important to note that if there are *n* pseudoelastic plateaus, there will be *n*+1 elastic responses, as shown in Figure 5.2. This leads to the following stress strain relationship:

$$\sigma = \frac{3E}{2(1+\nu)}\left(\varepsilon - \varepsilon_{o1}\xi_1 + \sum_{n=2}^{j}\left(\xi_n\left(\varepsilon_{o(n-1)} - \varepsilon_{on}\right)\right)\right) \qquad \textbf{(Equation 5.24)}$$

where E is calculated using Equation 5.22 and ε_{on} is the normalized transformation strain for the *n*th pseudoelastic region.

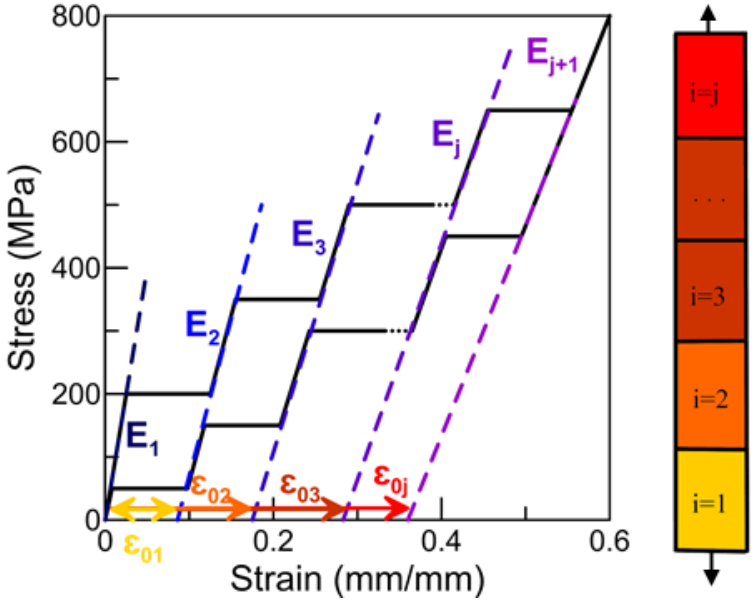

Figure 5.2 Schematic showing the elastic moduli and transformation strains for a material containing *j* distinctly different material regions.

Residual strain can also be represented in the unloading curve by subtracting it from the total strain:

$$\sigma_L = \frac{3E}{2(1+\nu)}(\varepsilon - \varepsilon_{o1L}(\xi_1 - \xi_2) - \varepsilon_{o2L}\xi_2) \qquad \textbf{(Equation 5.25)}$$

$$\sigma_U = \frac{3E}{2(1+\nu)}(\varepsilon - \varepsilon_{o1U}(\xi_1 - \xi_2) - \varepsilon_{o2U}\xi_2 - \varepsilon_r) \qquad \textbf{(Equation 5.26)}$$

where σ_L is the loading stress, σ_U is the unloading stress, ε_r is the residual strain, ε_{o1L} and ε_{o2L} are the normalized transformation strains for loading, and ε_{o1U} and ε_{o2U} are the normalized transformation strains for unloading, as shown in Figure 5.3 and defined as:

$$\varepsilon_{o1U} = \varepsilon_{o1L} - \varepsilon_r \qquad \textbf{(Equation 5.27)}$$

$$\varepsilon_{o2U} = \varepsilon_{o2L} - \varepsilon_r \qquad \textbf{(Equation 5.28)}$$

It is important to note that this model does not predict how much residual strain there will be, rather it only accounts for residual strain occurring. The amount of residual strain is a material

property that must be entered manually before the simulation is performed. Also, since the residual strain is represented by a constant, this equation would only be valid for one cycle since residual strain can accumulate during additional cycles. However, it may be possible to replace the residual strain constant with a residual strain function for multiple cycles, but this has not been attempted yet.

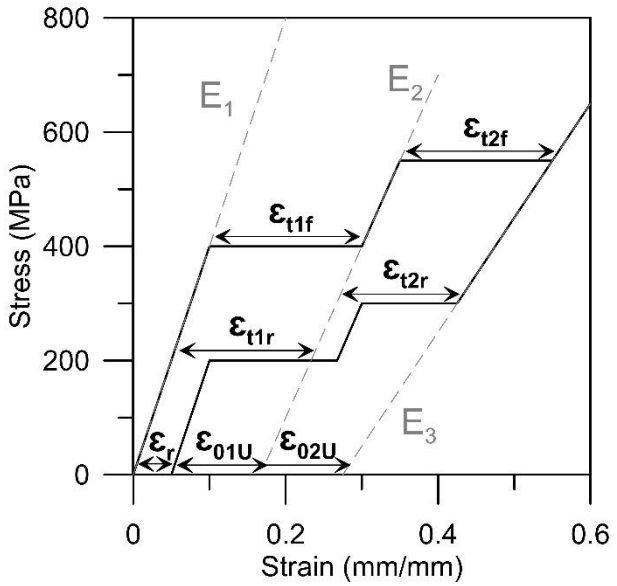

Figure 5.3: Schematic showing the elastic moduli and transformation strains for double plateaus with residual strain.

5.2 Modelling Tensile Loading of Multiple Memory Material

5.2.1 Material Characterization

From the DSC results shown in Figure 5.4, it was observed that after laser processing the austenite transformation peak is shifted to a higher temperature. This shift in transformation temperature is due to Ni depletion, as was investigated in previous studies [22, 23] and in Chapter 4. The martensite transformation temperature of the TBM cannot be observed by DSC, which is a common occurrence after heat treatments at 400 °C [151]. Due to atomic rearrangement, the martensite transformation is suppressed and occurs over a very wide temperature range making it "invisible" to the DSC technique [151]. R-phase transformation occurs because the internal stresses are high due to formation of Ti_3Ni_4 precipitates (see Section 2.1.2 Reversible Phase Transformation) [42, 43]. While the austenite to R-phase transformation strain is very low (~1 %) [43, 48], the R-phase to martensite transformation is still capable of achieving large recoverable

transformation strain (~10 %) [43]. The deconvolution method described in Section 4.3 Deconvolution of Overlapping Peaks was used to separate the overlapping R-phase peaks; all phase transformation temperatures are provided in Table 5.1. In binary NiTi alloys, it is typical to have a large hysteresis upon heating and cooling of the B2 austenite to B19' martensite transformation; however, the austenite to R-phase transformation hysteresis is typically much smaller [42].

Table 5.1: Transformation temperatures from DSC analysis
***TBM M_s determined from pseudoelastic plateaus**

	Heating				Cooling			
	R_s (°C)	R_f (°C)	A_s (°C)	A_f (°C)	R_s (°C)	R_f (°C)	M_s (°C)	M_f (°C)
TBM	-3.7	36.7	21.7	61.2	58.7	18.8	-31.7*	UNDET
TLP	1.3	53.1	31.8	62.9	59.0	46.3	-15.7	-65.8

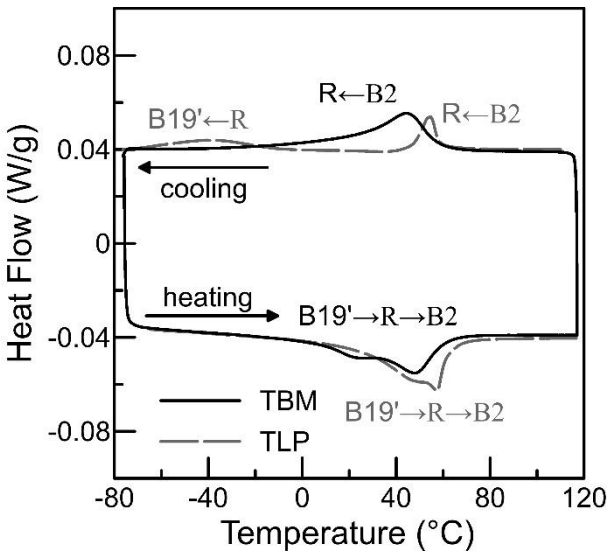

Figure 5.4: DSC results for laser processed NiTi wires and base material using a 5 °C heating/cooling rate.

Since M_s temperature of the TBM could not be determined through DSC analysis, several tensile tests were performed to determine the pseudoelastic plateaus at varying temperatures, as shown in Figure 5.5. The relationship between change in pseudoelastic plateau and change in temperature was used to estimate the temperature at which the pseudoelastic plateau is zero (i.e. the M_s

temperature), since this relationship follows a Clausius-Clapeyron relation (see Equation 2.1). This analysis produced a stress rate of 7.35 MPa/°C and an approximate M_s temperature of -31.7 °C for the TBM.

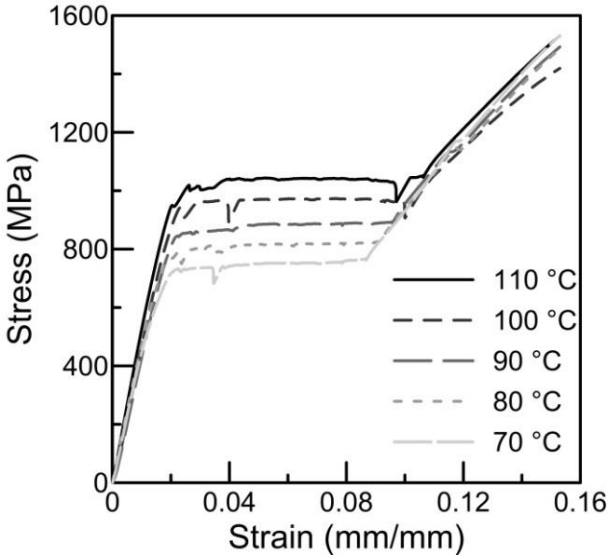

Figure 5.5: Tensile results for TBM at incremental temperatures above A_f.

Since the TLP material underwent the same thermomechanical treatment, this stress rate can be used to predict its pseudoelastic stress at any temperature. Since the material will be modelled at 90 °C:

$$\frac{d\sigma}{dT} = \frac{\sigma - 0}{90 - (-15.7)} = 7.35 \rightarrow \sigma = 7.35 \times 105.7 = 769\ MPa \qquad \textbf{(Equation 5.29)}$$

Cyclic tensile tests were performed at 90 °C using the preliminary tensile test method (see Section 3.6.1 Preliminary Tensile Test Method) to characterize the reverse pseudoelastic plateaus of both TLP and TBM above the A_f temperature for both materials, as shown in Figure 5.6. This is due to the fact that the unloading plateau has a different pseudoelastic stress rate than the loading plateau [65]. It can be seen that the pseudoelastic plateaus of the TLP sample has been shifted to a lower stress due to Ni vaporization and there is a larger stress hysteresis for the TLP sample compared with the TBM sample. This increase in hysteresis may be due to insufficient grain refinement during the cold-working procedure, as it is known that larger grain sizes increase the stress hysteresis [189, 231]. Additionally, the transformation strain of the TLP sample is larger than the TBM sample. All relevant material properties necessary for modelling are summarized in Table 5.2.

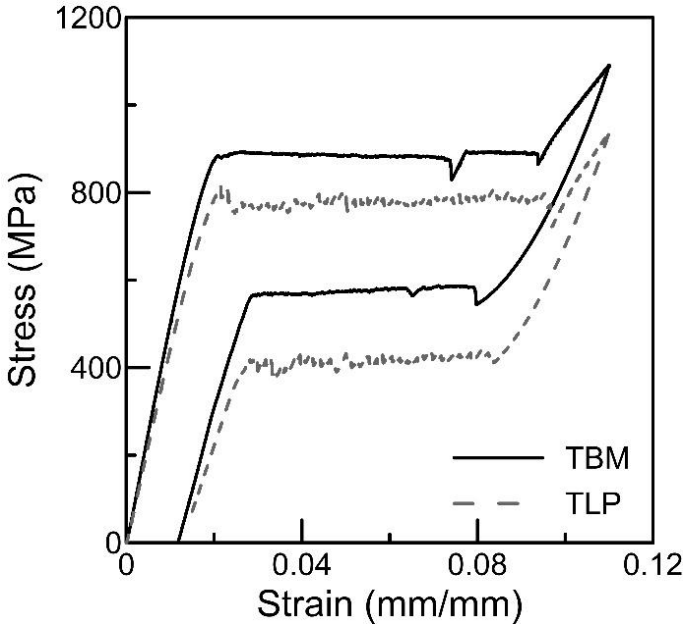

Figure 5.6: Cyclic tensile data for BM and LP samples at 90 °C.

Table 5.2: Material properties necessary for modelling.

	TBM	**TLP**
T	90 °C	90 °C
ρ	6450 kg/m^3	6450 kg/m^3
ν	0.3	0.3
M_s	-31.7 °C	-15.7 °C
A_s	21.7 °C	47.5 °C
E_A	42 GPa	39 GPa
E_M	16 GPa	17 GPa
σ^{AM}	888 MPa	769 MPa
σ^{MA}	580 MPa	398 MPa
ε_t	0.0810 mm/mm	0.0850 mm/mm
ε_o	0.0502 mm/mm	0.0621 mm/mm
ε_r	0.007 mm/mm	0.007 mm/mm

5.2.2 Model Implementation for Multiple Memory Material

One-dimensional numerical modelling can be developed using available commercial software packages. This study used *Matlab*^{TM} to implement the modelling of the stress/strain relationship. The newly modified model was compared with the old unmodified model put forth by Raniecki *et al.* (see Equation 5.1) and the experimental data for both the TBM and TLP samples, as shown in Figure 5.7. The use of an effective modulus and accounting for the residual strain enables the new model to better match experimental data when compared to the original model.

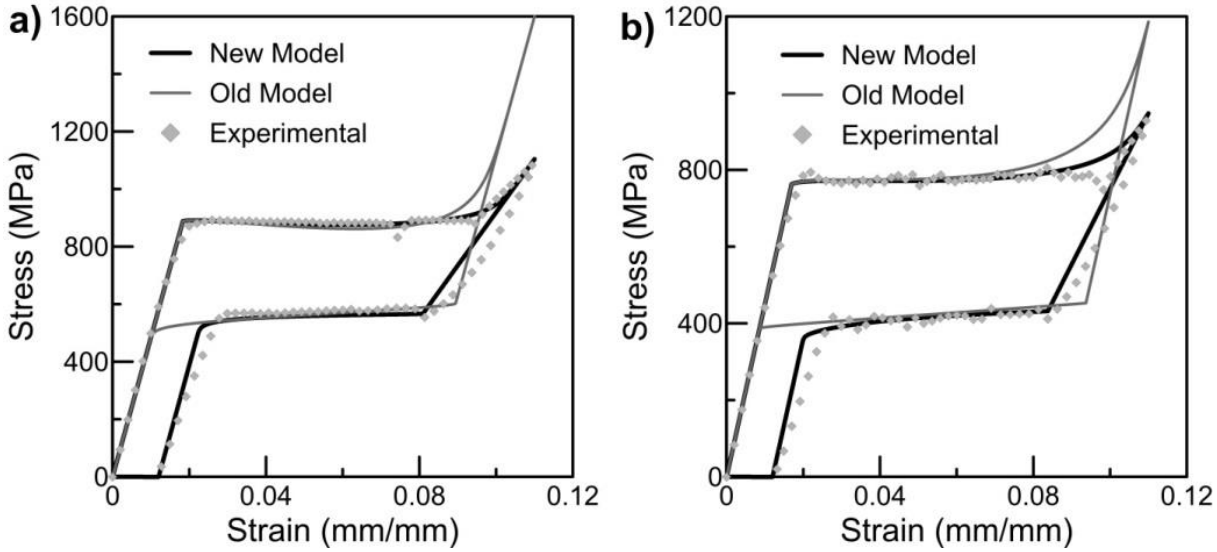

Figure 5.7: Comparison of the newly proposed model to the original unmodified model and the experimental data for a) TBM and b) TLP.

Since the new model provides better matching for the homogeneous materials, the same parameters were used to model a monolithic material containing two pseudoelastic plateaus (referred to as the MM model). The results of the simulated stress/strain curves are shown in Figure 5.8. It can be verified that the model exhibits all the necessary responses: 1) elastic behavior of the austenite phase, 2) first forward transformation from austenite to martensite, 3) elastic behavior of the austenite/martensite mixed phases, 4) second forward transformation from austenite to martensite, 5) elastic behavior of the martensite phase, and 6) both reverse transformations. It can be seen that the two different sections of the MM model match closely to the original models of the TLP and TBM, respectively.

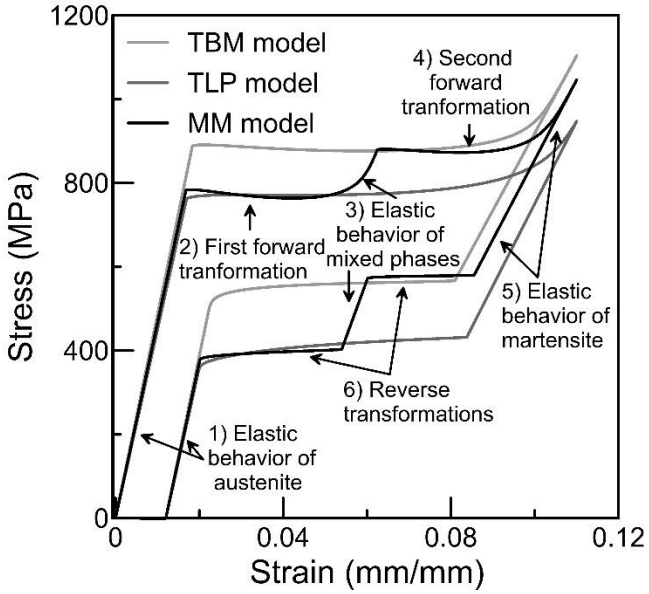

Figure 5.8: Simulated stress/strain curves for TBM, TLP and MM materials.

In order to further validate the accuracy of the MM model, the simulated results are compared with experimental data, as shown in Figure 5.9. Three different sets of samples were tested. The first, shown in Figure 5.9a, was 33 % TLP and 67 % TBM. The second, shown in Figure 5.9b, was 50 % TLP and 50 % TBM. The third, shown in Figure 5.9c, was 67% TLP and 33% TBM. The newly developed MM model matches closely with the experimental data for the MM samples. The greatest discrepancy is in the unloading elastic responses. This is due to the fact that these responses were assumed to be linear and with the same slope as the loading elastic responses, which is not accurate. This nonlinear elastic behavior observed in this region may be the result of inelastic deformation, such as twin boundary movement [232-234].

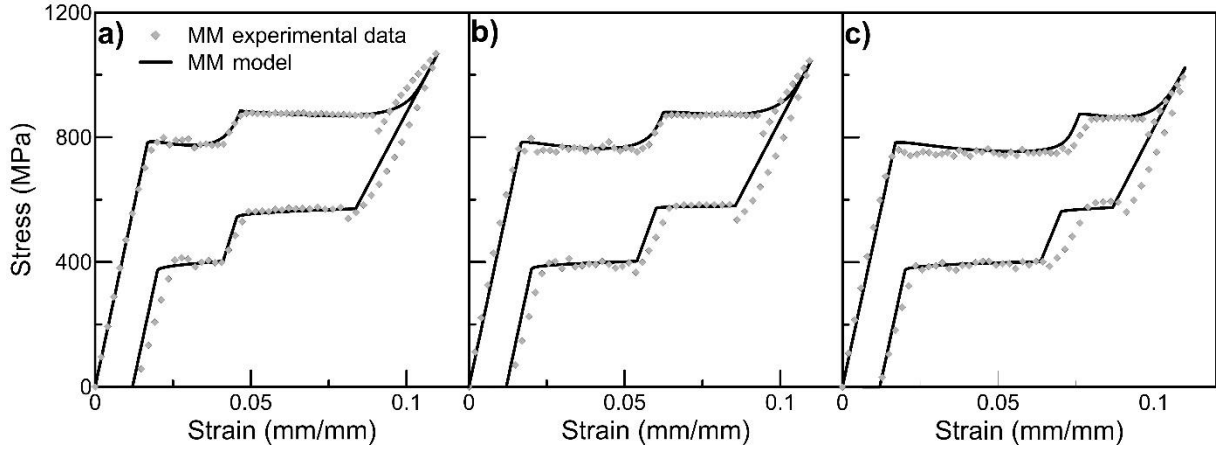

Figure 5.9: MM model compared with experimental data for a) 33% TLP and 67 % TBM, b) 50 % TLP and 50 % TBM, and c) 67 % TLP and 33 % TBM.

5.3 Improving Mechanical Characterization

This investigation presents an experimental analysis of different global strain measurement techniques used on very thin pseudoelastic NiTi wires. Both crosshead motion and a standard contact extensometer are compared with an unconventional method of using a visual extensometer. The visual extensometer is a contactless measuring device so no slippage of the sample can occur relative to the instrument, resulting in more accurate measurements.

Figure 5.10a shows tensile test results for the BM7 wire using all three measurement techniques. Quantified properties extrapolated from the data are presented in Table 5.3. The visual and contact extensometers both exhibited similar elastic moduli consistent with theoretical first principles calculations [146]. Both also experienced negligible amounts of residual strain (<0.05 % after one cycle). This validates the visual extensometer test method for NiTi wires. In contrast, the crosshead motion method experienced some residual strain (~0.25 %) and relatively reduced elastic moduli, which is typical for samples experiencing grip slippage during testing.

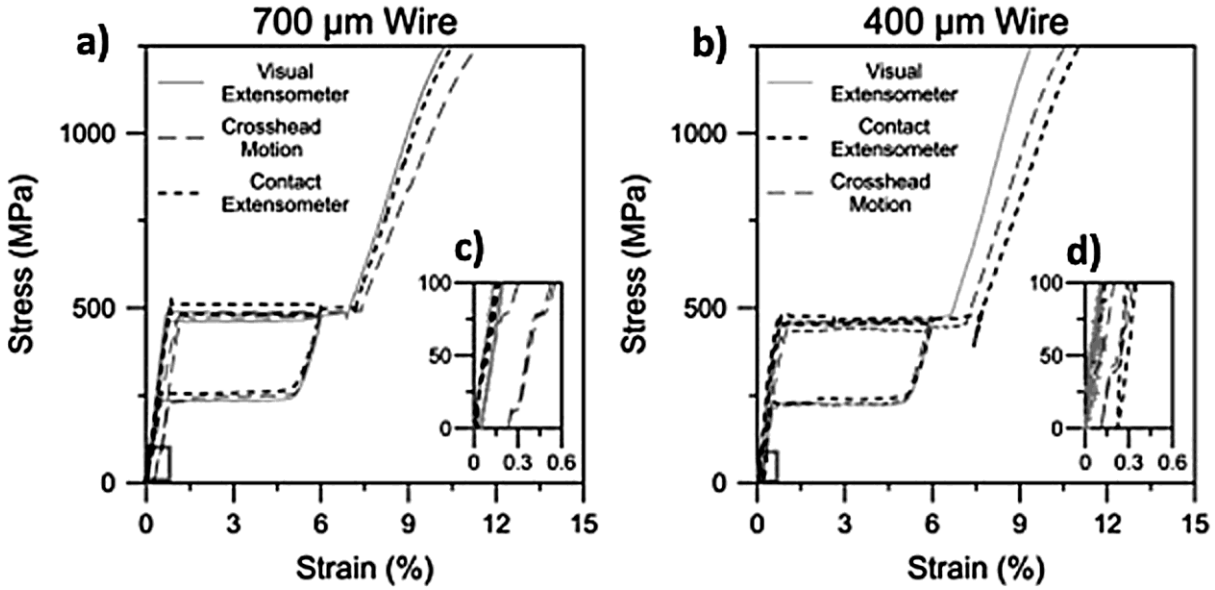

Figure 5.10 Tensile test results for a) BM7 and b) BM4 wires comparing the visual extensometer with the contact extensometer and cross head motion. Close-ups to observe residual strain after one cycle for the c) BM7 and d) BM4.

Figure 5.10b shows the tensile test results for the BM4 using all three measurement techniques. The visual and contact extensometers again agreed on the elastic modulus for the austenite phase. However, the contact extensometer experienced significant "residual strain" (~0.22%), which may

be indicative of the sample slipping relative to the contact points during unloading. Slipping at the contact point can alter the gauge length, which may account for the overestimation of the transformation strain and underestimation of the martensitic elastic modulus. The crosshead motion also experienced some slippage due to the difficulty of gripping such thin wires, as was evidenced by a small amount of "residual strain" (~0.1%) observed after one cycle.

Table 5.3: Comparison of all three test methods for each wire.

	Properties	Crosshead Motion	Contact Extensometer	Visual Extensometer
BM7	Austenite Elastic Modulus (GPa)	57	70	70
	Plateau Completion Strain (%)	7.35	7.15	6.9
	Martensite Elastic Modulus (GPa)	22	25	25
	Residual Strain (%)	0.25	< 0.05	< 0.05
BM4	Austenite Elastic Modulus (GPa)	61	71	71
	Plateau Completion Strain (%)	7.25	7.6	6.5
	Martensite Elastic Modulus (GPa)	24	24	29
	Residual Strain (%)	0.1	0.22	< 0.05

From Table 5.3, it is apparent that the visual extensometer experienced less slippage than either other technique for both wire diameters since it consistently had higher elastic moduli and shorter transformation strains. The crosshead motion results gave values that were 12 % to 19 % lower than the values observed by visual extensometer for both austenite and martensite elastic moduli. The contact extensometer also underestimated the elastic moduli of the BM4 wire by ~14 % and severely overestimated the transformational strain and residual strain.

5.4 Model Revalidation

After the development of a more accurate tensile test method, TBM and TLP samples were characterized using a visual extensometer. Figure 5.11 shows the stress/strain curves for both TBM and TLP. There is a drastic difference in transformation and residual strains observed when compared with the data collected by the previous method (see Figure 5.6), as well as much higher elastic moduli.

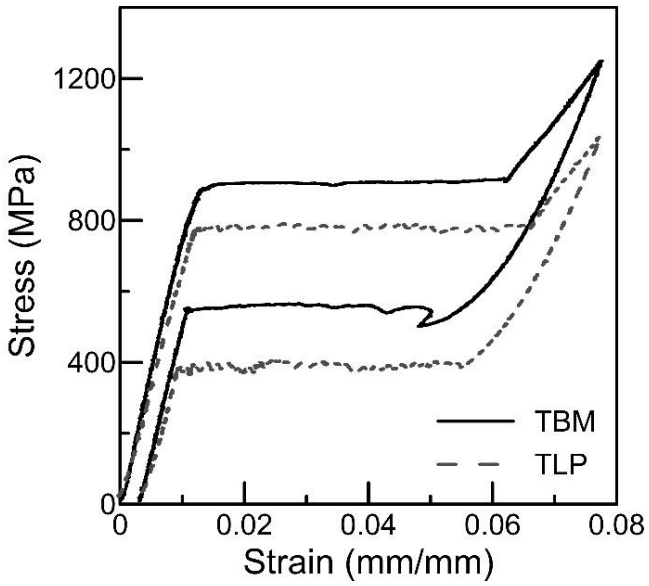

Figure 5.11: New cyclic tensile data for TBM and TLP samples at 90 °C.

With this more accurate tensile data it is now possible to clearly see the relationship between the latent heat of transformation and the transformation strain. From DSC analysis (see Figure 5.4), the latent heat of transformation can be determined by dividing the area under the transformation peak by the heating/cooling rate (in this case 5 K/min). The relevant values are shown in Table 5.4. Using the Clausius-Clapeyron relationship (Equation 2.1) gives:

$$\mathbf{7.35} = \frac{\mathbf{6.45(19.8)}}{\mathbf{312.3}\boldsymbol{\varepsilon_t}} \qquad \textbf{(Equation 5.30)}$$

Solving for ε_t gives a transformation strain of 0.0556 mm/mm, which is in good agreement with the new tensile data. However, since the martensitic transformation is suppressed during the cooling cycle for the TBM, the average latent heat of transformation for martensite cannot be determined.

Table 5.4: Relevant phase transformation properties extracted from DSC.

	M_s (K)	A_f (K)	T_0 (K)	ΔH_H (J/g)	ΔH_C (J/g)	ΔH_{ave} (J/g)
LP	**257.3**	**335.9**	**312.3**	**15.6**	**24.0**	**19.8**

In order to reaffirm the accuracy of the MM model, results simulated with the new material properties were compared with new experimental data for the MM material, as shown in Figure 5.12. The newly developed MM model still matches closely with the experimental data for the 50/50 MM samples. The new material properties used for modelling are summarized in Table 5.5.

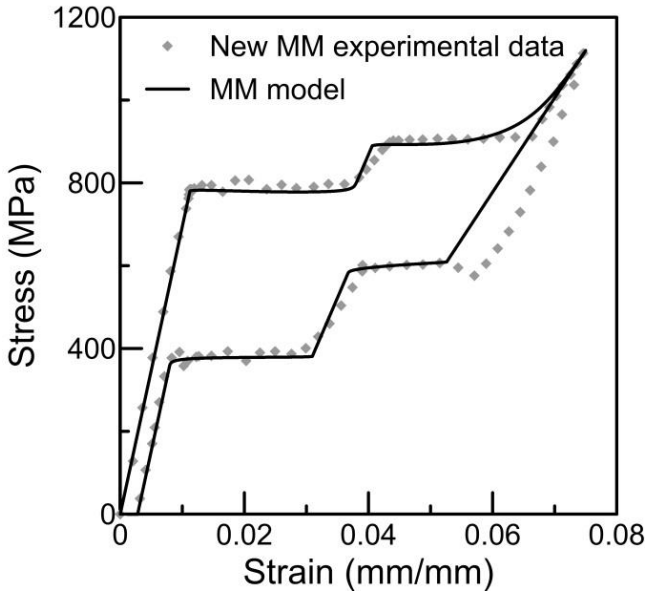

Figure 5.12: MM model compared with new data for 50 % TLP and 50 % TBM.

Table 5.5: New material properties used for modelling.
***Only the values that changed are listed in this table.**

	TBM	**TLP**
E_A	72.5 GPa	67.4 GPa
E_M	21.2 GPa	24.7 GPa
ε_t	0.0510 mm/mm	0.0556 mm/mm
ε_0	0.0210 mm/mm	0.0360 mm/mm
ε_r	0.0028 mm/mm	0.0028 mm/mm

With good correlation found between the MM model and the experimental results, this novel model was applied to the SmarthArch™ orthodontic arch wire to model its tensile response. The SmartArch™ orthodontic wire contains several regions with differing laser processing parameters to precisely tune the pseudoelastic force along the length of the wire, as shown in Figure 5.13. The laser processed orthodontic arch wire contains six different processed regions plus retained base material. For proprietary reasons, the exact laser parameters, DSC transformation characteristics and other material properties cannot be disclosed.

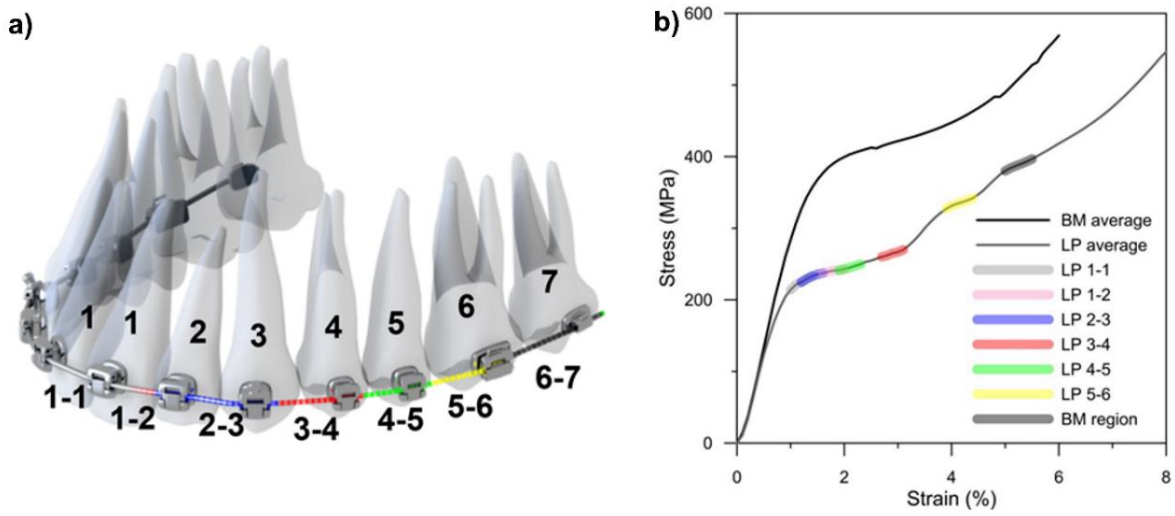

Figure 5.13: a) Schematic depicting the various regions of the orthodontic arch wire and b) tensile response of the SmarthArch™ orthodontic arch wire.

This particular material was modified for a common prescription of misaligned teeth and exhibited five different pseudoelastic responses (some laser processed regions used similar parameters but were not adjacent to each other). With known material properties, any number of pseudoelastic regions can be predicted using the novel 1-D tensile model developed in this study, as shown in Figure 5.14. All data related to the SmartArch™ orthodontic arch wire has been generously provide by Smarter Alloys, Inc.

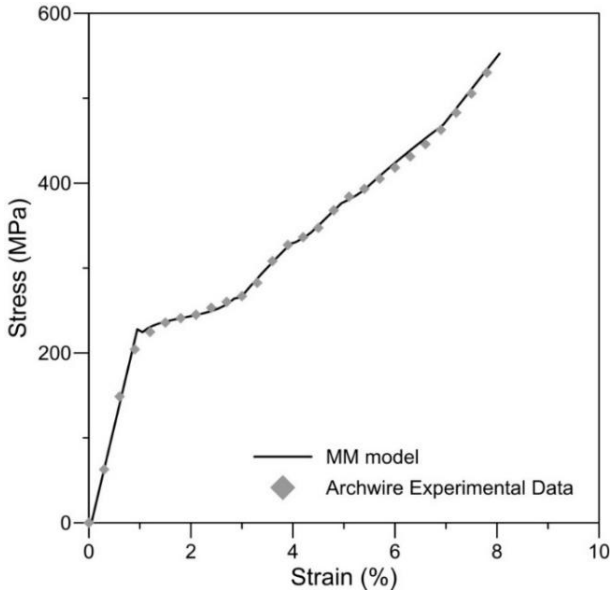

Figure 5.14: MM model compared with experimental tensile data for the SmarthArch™ orthodontic arch wire.

5.5 Chapter Summary

In this chapter, a novel thermodynamic model was presented that takes into account non-homogeneous material properties, permitting the fitting of stress/strain responses for tensile loadings in a laser-modified thin wire of NiTi SMA. The monolithic wires exhibiting multiple pseudoelastic responses were fabricated and used to validate the proposed model, and the experimental data was shown.

Several mechanical properties were successfully determined through DSC analysis; however, the suppression of the martensitic phase transformation made complete thermodynamic analysis impossible. Therefore, mechanical testing was still required to verify all of the material properties. Through a systematic investigation of three different strain measurement methods, it was determined that the visual extensometer method combined ease of sample preparation with accurate test results making it the clear choice for testing thin and ultra-thin NiTi wires.

The novel one-dimensional model was revalidated with more accurate material properties and showed excellent correlation to the experimental data. The model was then applied to the SmartArch™ orthodontic arch wire and predicted the tensile response with great success. This sets the ground work for better modelling capabilities of future devices that take advantage of functionally gradient SMAs.

Chapter 6: Two-Dimensional Deformation of NiTi Wires

6.1 Modelling Bending Deformations

When modelling bending of NiTi wires, there are three important features to keep in mind. First is the asymmetry between the tensile and compressive strains on the outer and inner edges of the bending wire [174, 175]. Second is the localization of the phase transformation, which occurs through the thickness of the wire [174, 175, 235, 236] as well as along the length of the wire [235, 236]. Third is the texture of the material, as that will determine the bending radius after transformation. Due to preferential grain orientation of NiTi wires, texture effects have not been examined closely prior to this study. Any laser processing method that results in melting of the work material will alter the material texture. Therefore, it is necessary to understand how texture affects the bending properties.

6.1.1 Elastic Strains

To be able to account for the effect of texture on the bending curvature of pseudoelastic NiTi wires, a macroscale model was initiated as a first approximation for the expected physical geometry of the deformed wire will be. A simple curve function was chosen to represent the geometric shape of the bent wire. Since this model proposes to show the connection between texture and bending curvature, the bent wires will be approximated by determining their bending radius and using the function for a circle. For simple elastic strains, if the curvature is assumed to be uniform, then the bending radius can be determined by using the intersecting chords theorem, as shown in Figure 6.1. The intersecting chords theorem states that the products of the lengths of each line segment for each chord are equal [237]. In this instance, that equates to:

$$\frac{\boldsymbol{L}}{\boldsymbol{2}} \times \frac{\boldsymbol{L}}{\boldsymbol{2}} = \boldsymbol{\delta} \times \boldsymbol{e} \qquad \textbf{(Equation 6.1)}$$

where $\boldsymbol{L}$ is the span of the of the bend, and $\boldsymbol{\delta}$ and $\boldsymbol{e}$ add up to be the diameter of the circle, since that chord bisects and is perpendicular to the other. Therefore:

$$\boldsymbol{\delta} + \boldsymbol{e} = \boldsymbol{2R_c} \qquad \textbf{(Equation 6.2)}$$

where $\boldsymbol{R_c}$ is the radius of curvature. Since $\boldsymbol{\delta}$ is a known displacement, $\boldsymbol{e}$ can be solved for:

$$\boldsymbol{e} = \boldsymbol{2R_c} - \boldsymbol{\delta} \qquad \textbf{(Equation 6.3)}$$

Substituting Equation 6.3 into Equation 6.1 gives:

$$\frac{\boldsymbol{L}}{\boldsymbol{2}} \times \frac{\boldsymbol{L}}{\boldsymbol{2}} = \boldsymbol{\delta} \times (\boldsymbol{2R_c} - \boldsymbol{\delta}) \qquad \textbf{(Equation 6.4)}$$

Rearranging to solve for $\boldsymbol{R_c}$ gives:

$$\boldsymbol{R_c} = \frac{\boldsymbol{\delta} + \frac{\boldsymbol{L^2}}{\boldsymbol{4\delta}}}{\boldsymbol{2}} \qquad \textbf{(Equation 6.5)}$$

Therefore, for any span length and displacement that results in elastic deformation, the bending curvature can be calculated, and the physical shape approximated by the equation:

$$\boldsymbol{y} = \sqrt{\boldsymbol{R_c}^{\boldsymbol{2}} - \boldsymbol{x^2}} \qquad \textbf{(Equation 6.6)}$$

where $\boldsymbol{y}$ is the y-coordinate corresponding to any x-coordinate along the bending span.

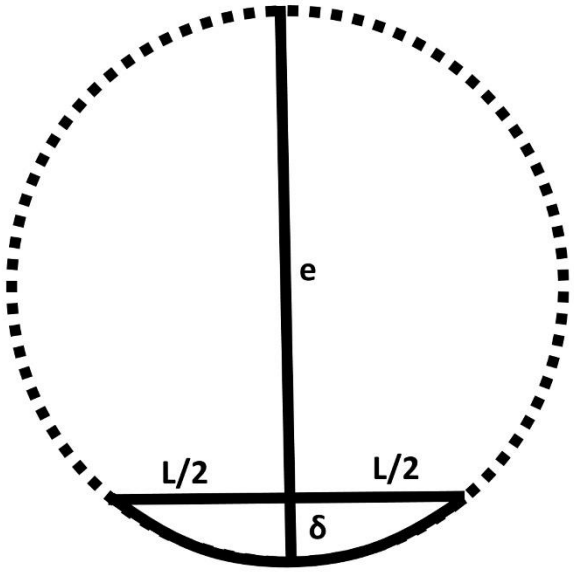

Figure 6.1: Schematic depicting the intersecting chords from a three-point-bend test.

6.1.2 Transformation Strains

This simplified bending model is only valid in the elastic region of deformation. The martensite phase transform will begin once a critical stress/strain criterion is met. The use of similar triangles can determine the bending radius for the critical strain, as shown in Figure 6.2. Triangles of different sizes with the same angles will be proportional to each other. In this case, the distance from the outer edge to the wire middle (i.e. the wire radius) is proportional to the distance from the middle of the wire to the center of the bending circle (i.e. the bending radius).

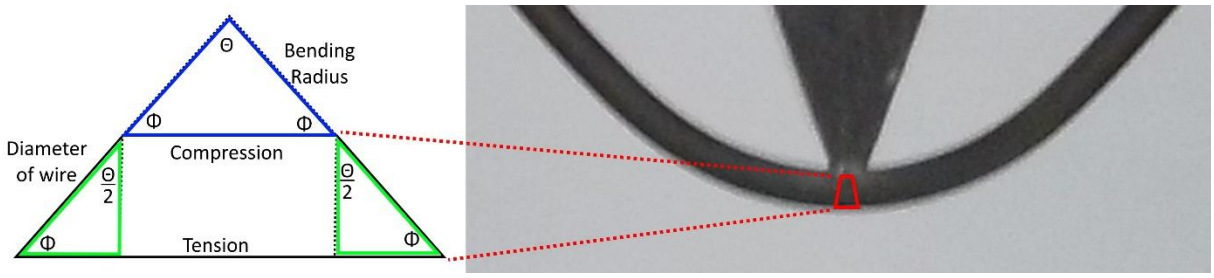

Figure 6.2: Schematic depicting the bending curvature represented as similar triangles.

Also, the elongation of a unit cell on the outer edge is proportional to the distance of the unstrained unit cell at the neutral axis.

$$\frac{r}{\Delta l} = \frac{R_c}{0.5283} \qquad \textbf{(Equation 6.7)}$$

where r is the radius of the NiTi wire, Δl is the elongation on the outer edge of the wire, and 0.5283 is the interplanar distance of an austenite unit cell in the <111> direction, see Figure 6.3.

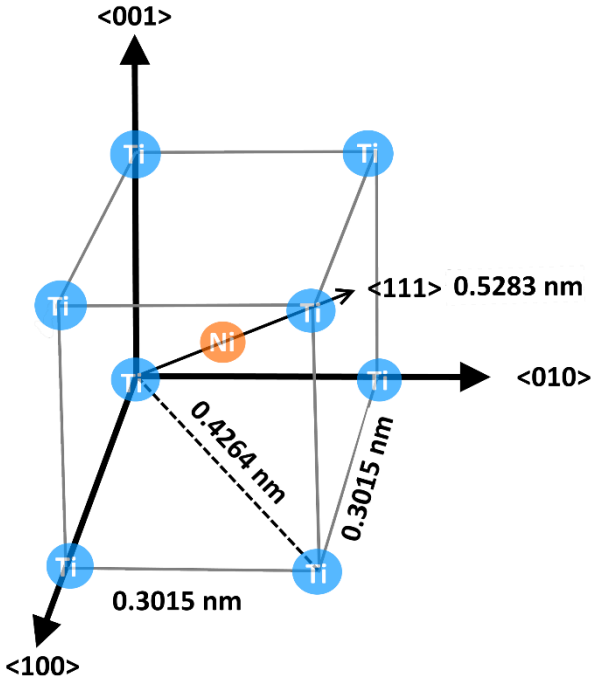

Figure 6.3: Schematic depicting the interplanar spacing of the austenite cubic unit cell.

Since the critical elongation is equivalent to the unit cell spacing multiplied by the critical strain, Equation 6.7 becomes:

$$\frac{r}{\varepsilon_{crit}} = R_{crit} \qquad \textbf{(Equation 6.8)}$$

This works out to be the standard relationship for determining strain of a bent body [238]. Once the elastic region reaches maximum strain, the bending curvature in that region can be approximated by the equation:

$$y = \sqrt{{R_{crit}}^2 - x^2} \qquad \textbf{(Equation 6.9)}$$

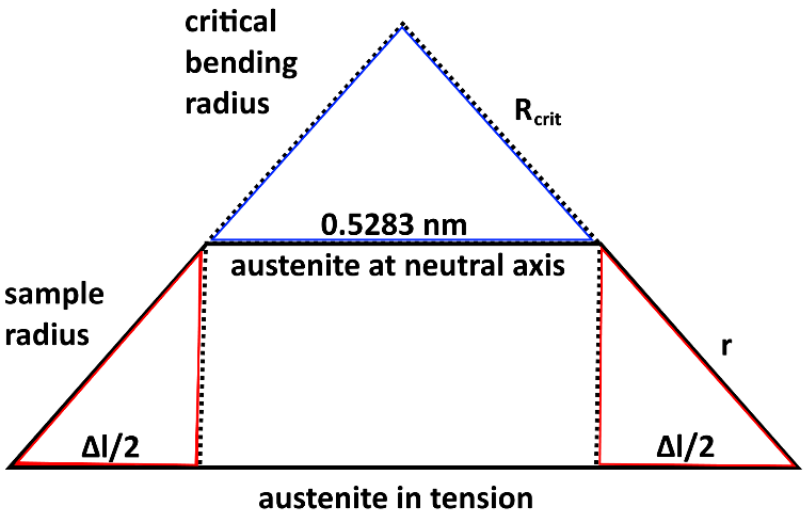

Figure 6.4: Schematic depicting the relationship of similar triangles for the critical bending radius.

Transformation to martensite changes the local curvature significantly, as shown in Figure 6.5. It has been shown the when austenite is in the <111> direction, the preferred martensite variant is the <$10\bar{1}$> direction [146]. Also, it has been shown that the preferred martensite variant in compression is the <110> direction [146]. Using similar triangles again reveals what the preferred bending radius is of the transformed material.

$$\frac{d}{(0.5759 - 0.5032)} = \frac{R_m}{0.5032} \qquad \textbf{(Equation 6.10)}$$

$$6.912 \times d = R_m \qquad \textbf{(Equation 6.11)}$$

where $\boldsymbol{d}$ is the diameter of the wire, $\boldsymbol{R_m}$ is the preferred bending radius of the transformed region, 0.5759 is the distance of a martensite unit cell in the <$10\bar{1}$> direction and 0.5032 is the distance of a martensite unit cell in the <110> direction. The bending curvature in that transformed region is fixed and can be approximated by the equation:

$$y = \sqrt{{R_m}^2 - x^2} \qquad \textbf{(Equation 6.12)}$$

Since the transformation is localized, the sample will contain both elastically strained regions and pseudoelastically strained regions. Continuity between to the two regions must be maintained. This is achieved by ensuring that the point where the function mapping the elastic curvature meets the function mapping the transformed curvature is the place where both functions have the same slope (i.e. their derivatives are equal at that point), as shown in Figure 6.6.

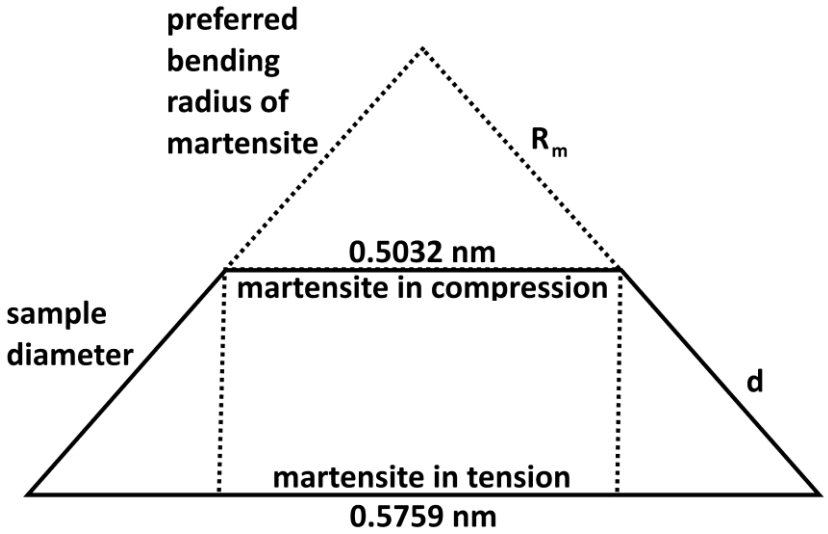

Figure 6.5: Schematic depicting the relationship of similar triangles for the transformed region.

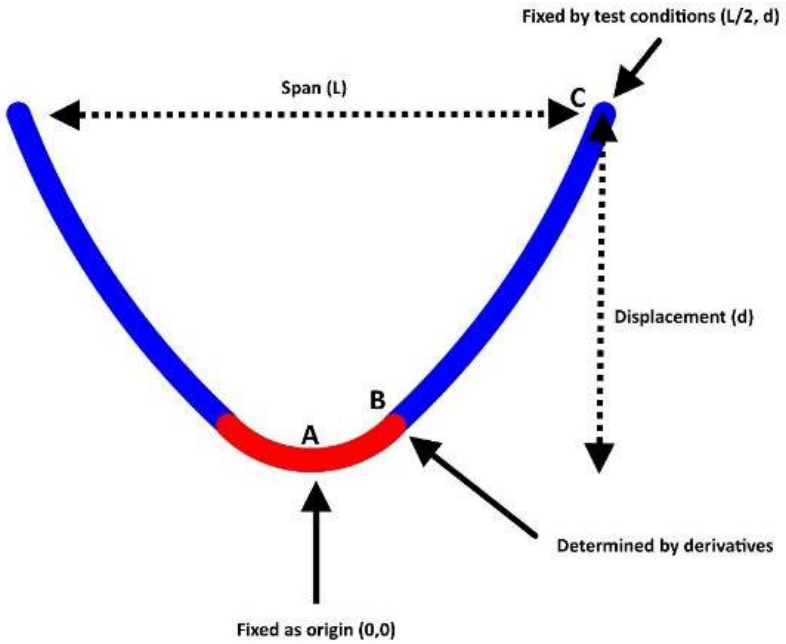

Figure 6.6: Schematic depicting the continuity between the elastic and transformed regions, as well as the physical constraints imposed on the system.

The equation that approximates the elastic region must be modified to:

$$\boldsymbol{y = A_{adj} - \sqrt{R_{crit}{}^2 - (x - B_{adj})^2}} \qquad \textbf{(Equation 6.13)}$$

where $\boldsymbol{A_{adj}}$ and $\boldsymbol{B_{adj}}$ are used to shift the function so that all constraints are successfully satisfied.

6.1.3 Length Adjustments

Typically, stress analysis for a three-point-bend test uses the following relationship [239]:

$$\boldsymbol{\sigma = \frac{Mc}{I}} \qquad \textbf{(Equation 6.14)}$$

where $\boldsymbol{c}$ is the distance from the center of the specimen to the outer fibers, $\boldsymbol{I}$ is the moment of inertia of the cross section and $\boldsymbol{M}$ is the maximum bending moment given by [239]:

$$\boldsymbol{M = \frac{FL}{4}} \qquad \textbf{(Equation 6.15)}$$

where $\boldsymbol{F}$ is force and $\boldsymbol{L}$ is the span between the two supports and is assumed to be constant. For small deflections, which are typical for most metals, this assumption is valid. However, this is not valid for the large displacements undertaken by bending NiTi wires. ASTM standard E855-08 details test procedures for analyzing bending properties. For cantilever bend tests, the specimen length is used to determine the bending moment [240]. Since the model uses simple curve functions to estimate the sample place, calculating the arc length of each region will reveal the sample length.

$$\boldsymbol{l = R_c\theta} \qquad \textbf{(Equation 6.16)}$$

where l is the arc length and θ is the angle in radians over which the arc is being measured. For elastic deformations, the angle over which the arc is being measured can be easily calculated by [241], as depicted in Figure 6.7a:

$$\boldsymbol{\frac{\theta}{2} = \tan^{-1}(t)} \qquad \textbf{(Equation 6.17)}$$

where $\boldsymbol{t}$ is equivalent to the slope of the function at the end point (due to similar triangles having proportional lengths), which can be determined from the derivative of the function.

For partially transformed regions, the angle over which the transformed region is present can be determined by Equation 6.15, using the end of the transformed region as the end point. However, the angle over which the elastic region occurs is calculated as:

$$\boldsymbol{\frac{\theta_e}{2} = \tan^{-1}(t_e) - \tan^{-1}(t_m)} \qquad \textbf{(Equation 6.18)}$$

where t_e is the derivative of the function and the sample end point and t_m is the derivative of the function at the boundary between the transformed region and the elastic region, as shown in Figure 6.7b.

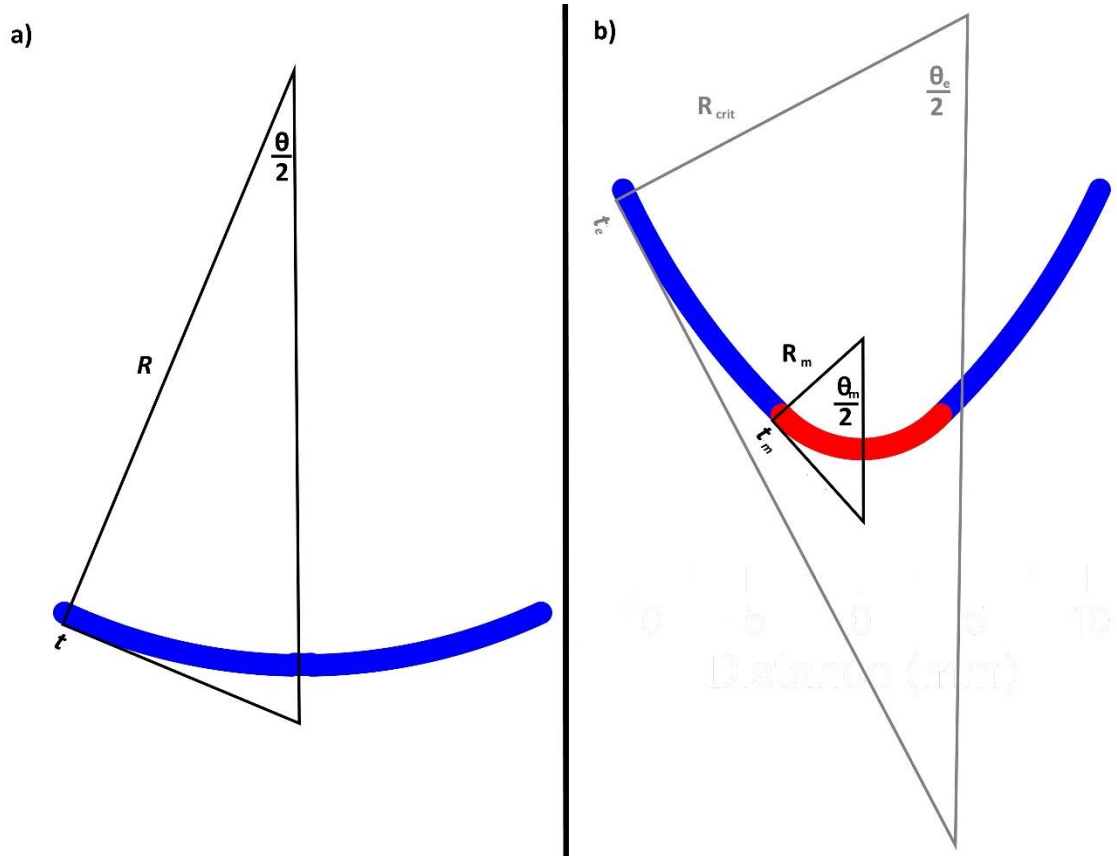

Figure 6.7: Schematic depicting the method for calculating Θ to determine arc length for a) elastic deformation only and b) pseudoelastic and elastic deformations.

In addition to the sample length increasing for large deflections, the span length and measured displacement decrease as the sample rotates to the inside edge of the bottom supports, as highlighted in Figure 6.8. The derivative, or slope, of the sample at the end point (i.e. the contact point with support) is already being calculated to update the true sample length. This knowledge can be used to determine where on the support the sample will most likely be resting based on the angle of the sample end and the shape of the support. In this way, the true contact point and true displacement (relative to the new contact point) can be updated at each time step. Figure 6.9 shows the effect of accounting for changing sample length, contact point and relative displacement. The result is a lower more level plateau stress around 750 MPa, which is comparable to previous studies [174].

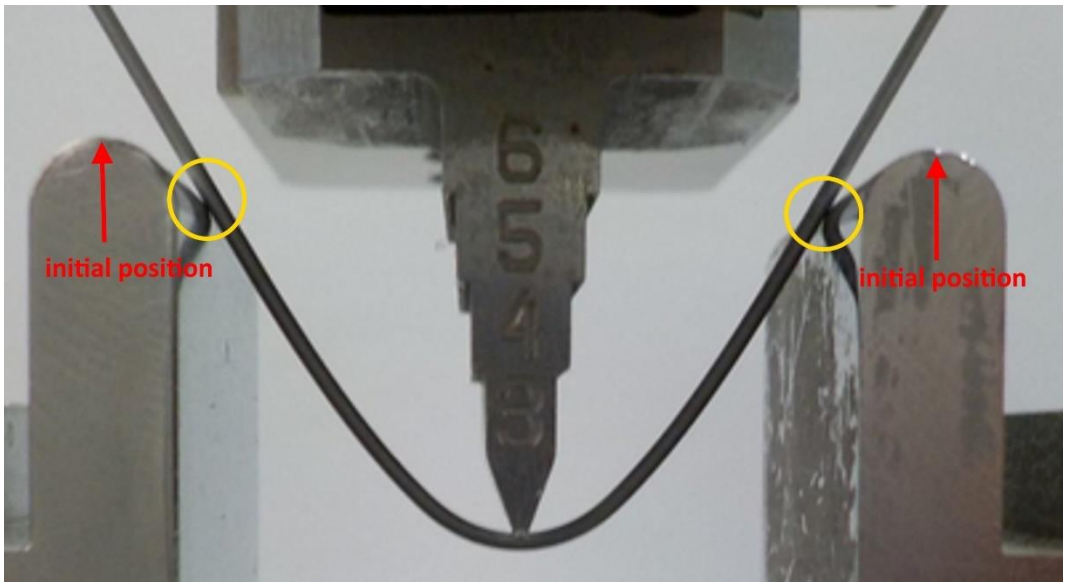

Figure 6.8: Photograph highlighting the shift of the sample to the inside of the supports during three-point-bend testing.

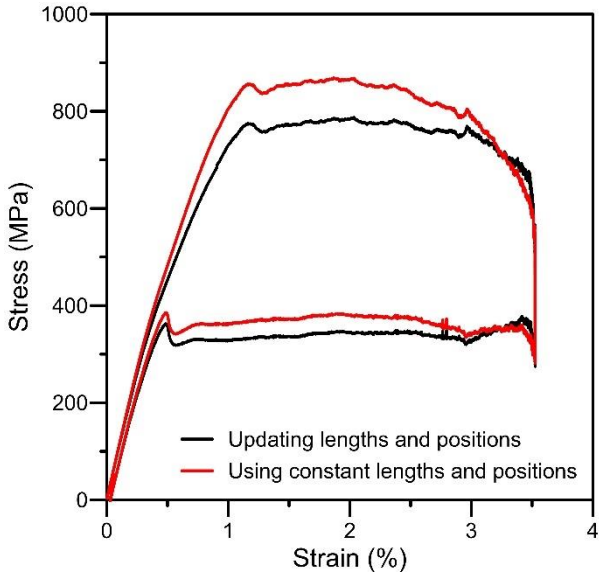

Figure 6.9: Stress/strain results with updated lengths and positions compared to using only fixed initial conditions.

6.1.4 Model Validation

To validate the accuracy of this modelling method, the prediction of transformation initiation is first examined. The elastic modulus of the BM7 wire appears to be reduced at room temperature due to the presence of the R-phase (see Figure 6.10a) and is comparable to previous studies of austenite/R-phase mixed materials [146, 242]. The simplest assumption would be this is a

softening of the material due to the presence of mixed phases, and an effective modulus could be determined through homogenization techniques that are based on the volume fraction of each phase present and their respective elastic moduli [243]. There are several homogenization methods for doing just that, including Voigt, Mori-Tanaka, Reuss, as well as others [179].

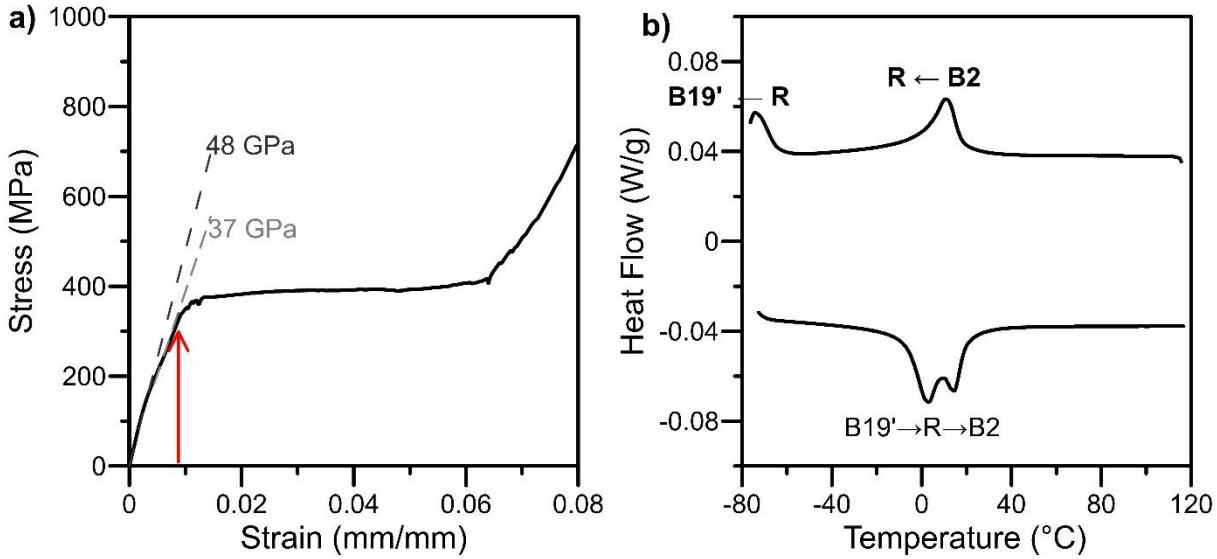

Figure 6.10: a) Tensile test data highlighting the phase martensite transformation initiation strain. b) DSC data showing R-phase stability at room temperature.

However, closer examination of the tensile results shows a clear non-linear response. There is a shift from a slope of 48 GPa to 37 GPa. This is because the BM7 is actually undergoing a gradual phase transformation from austenite to R-phase, with the initial thermally stable R-phase (see Figure 6.10b and Table 6.1) acting as a seed for this transformation. While use of an effective modulus is still appropriate during the phase transformation [179, 186, 244, 245], consideration must be made for the fact that the R-phase volume is changing [246] and how that affects more complex mechanical deformations. For this study, the bending geometries in the R-phase will be approximated as uniformly elastic. The reason for this is that the initial distribution of R-phase in the material is unknown. Also, there is currently no consensus on what the lattice parameters are for R-phase [247-250], making interplanar spacing calculations for predicting bending curvatures difficult.

Table 6.1: Transformation temperatures for the wires.

	Heating				Cooling			
	R_s	R_f	A_s	A_f	R_s	R_f	M_s	M_f
BM4	N/A	N/A	-16.2	8.5	5.5	-22.0	N/A	N/A
BM7	-8.5	13.2	10.3	20.5	18.7	1.0	-67.9	N/A

The maximum tensile strain the BM7 wire can withstand at room temperature before martensite transformation occurs is 0.9 %, as shown in Figure 6.10a. After 0.9 % strain, austenite/R-phase transforms into martensite. Therefore, when the bent wire reaches 0.9 % strain on the outer edge, phase the martensitic phase transformation will occur. The BM4 wire was also examined to verify that this method holds up for any wire diameter, and to remove the uncertainty associated with the intermediary R-phase transformation. The BM4 wire is fully pseudoelastic and austenitic at room temperature and has already been characterized (see Section 5.3 Improving Mechanical Characterization). Therefore,

$$\varepsilon_{crit} = \frac{\sigma_{SIM}}{E_A} = 0.0071\ mm/mm \qquad \textbf{(Equation 6.19)}$$

Figure 6.11a shows the model prediction for BM7 wire with a 28 mm span length at 2.1 mm displacement. This is the first displacement in which the model predicts the presence of a transformed region. This displacement can be compared with the data collected using a wire of the same diameter and span length. It can be seen from Figure 6.11b that around 2.2 mm the load begins to deviate from the linear elastic response, indicating the onset of phase transformation. Furthermore, Figure 6.11c shows the model prediction for BM4 wire with a 16 mm span length at 0.85 mm displacement (the first displacement where transformation is present). Examining the experimental data reveals the onset of transformation occurs around 0.95 mm displacement. The model predictions show good correlation with the experimental data for both wire diameters. Additional figures showing the complete evolution of the phase transformation for BM7 wire can be found in Appendix II: The Evolution of the Localized Phase Transformation during Bending.

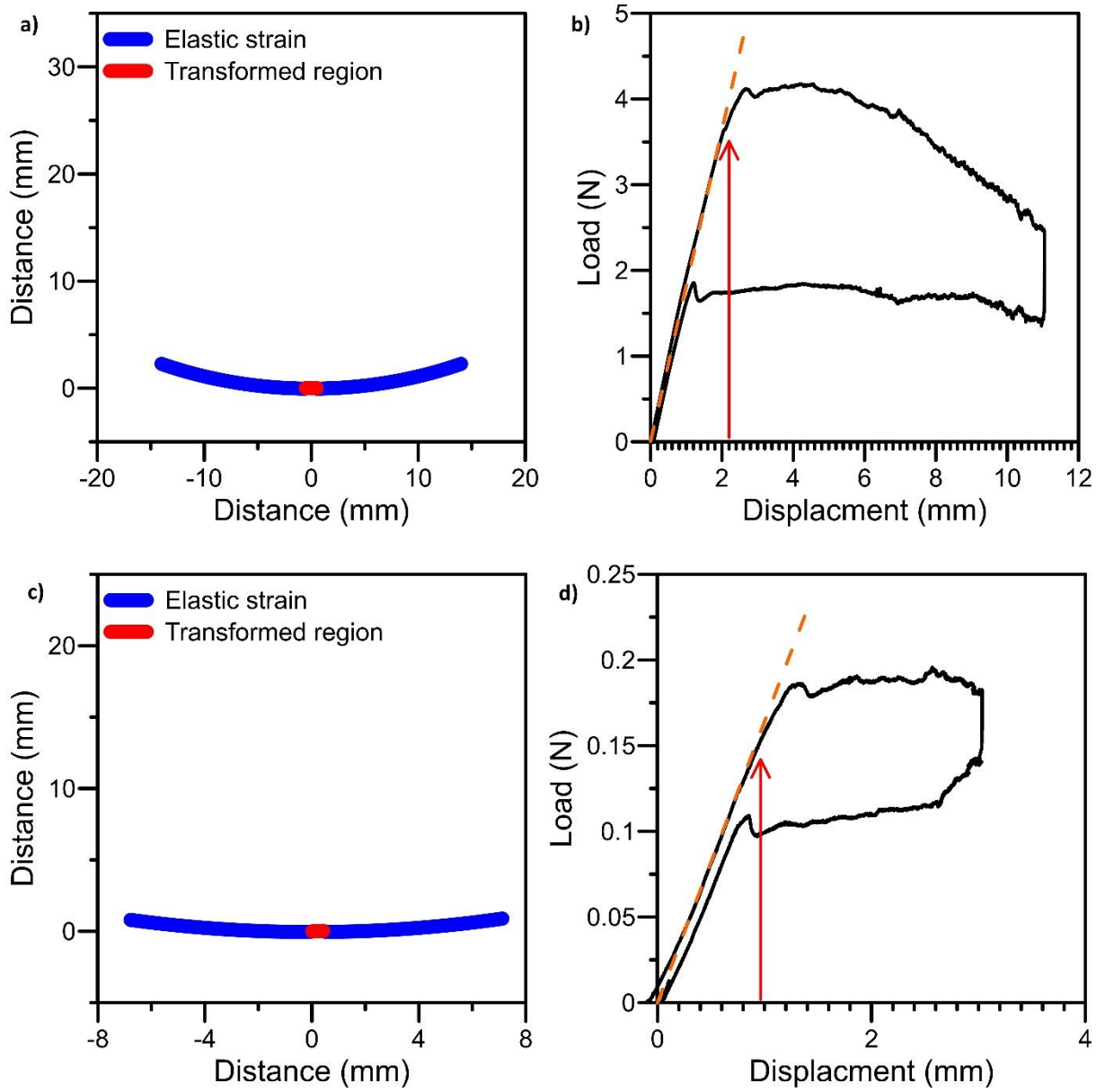

Figure 6.11: a) Model prediction of the transformation initiation and b) three-point-bend data for BM7 wire with a span of 28 mm. c) Model prediction of the transformation initiation and d) three-point-bend data for BM4 wire with a span of 16 mm.

Next, the model was used to predict the physical shape of NiTi wires at large displacements. As can be seen in Figure 6.12, the model shows good correlation to the actual physical geometries of bent wires for both the BM4 and BM7 wires. Using Equation 6.11 predicts a bending radius of 4.838 mm and 2.765 mm for the BM7 and BM4 wires, respectively. This correlates very closely to the measured values of 4.8 mm and 2.7 mm, as shown in Figure 6.12a and b. The overlays shown in Figure 6.12e and f also show good correlation to the entire bending geometry.

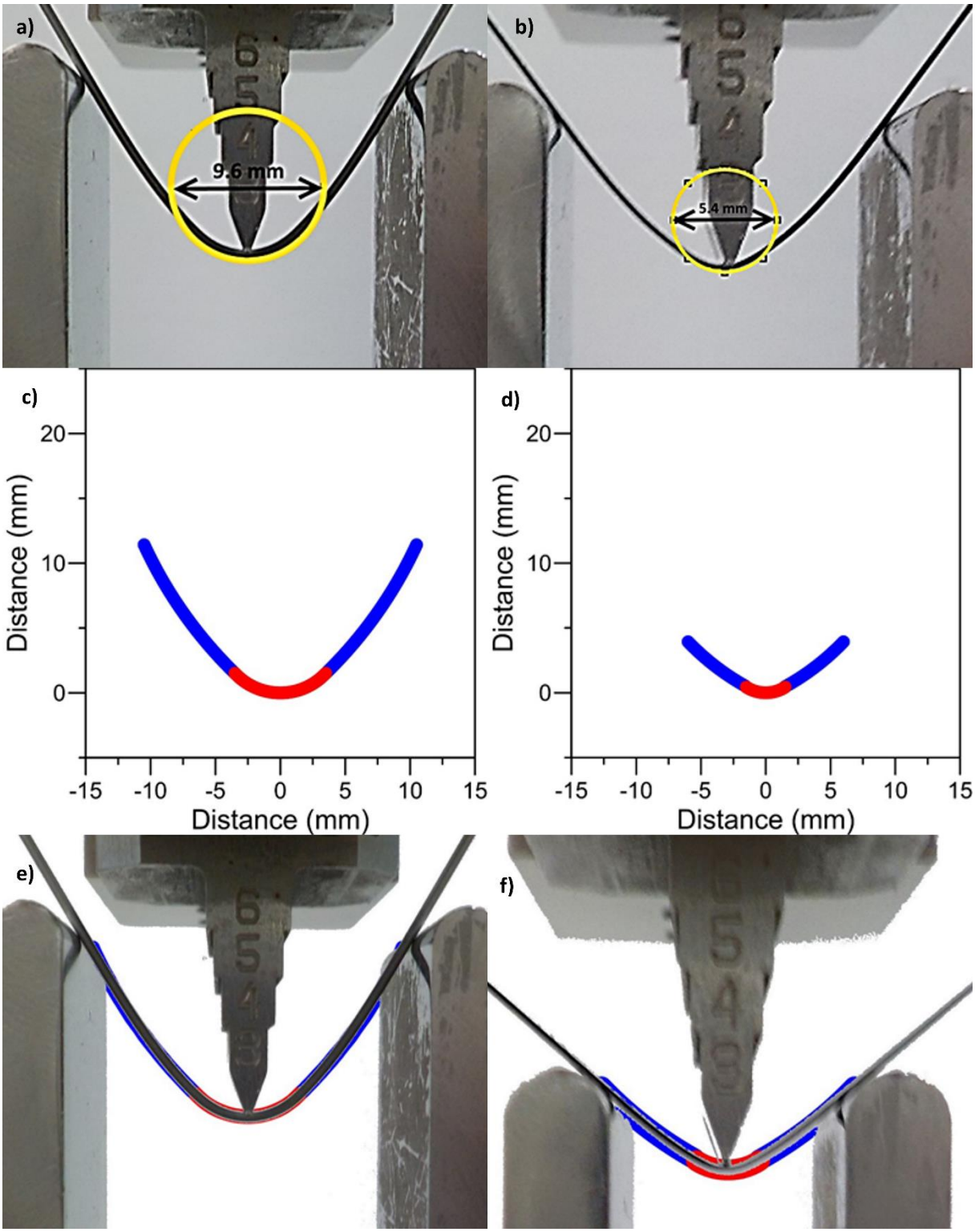

Figure 6.12: Actual bending geometries of a) BM7 wire and b) BM4 wire. Model predictions for c) BM7 wire and d) BM4 wire. Overlay of bending model and physical geometry for e) BM7 wire with 21 mm span at 11.5 mm displacement and f) BM4 wire with 12 mm span at 4 mm displacement.

6.2 Effect of Grain Orientation on Bending Geometries

NiTi wires typically have a preferential <111> orientation of grains (see Section 2.2.3 Wire Drawing SMAs). After laser processing, the texture becomes more mixed, as shown in Figure 6.13. NiTi solidifies in the parent austenite phase, which has a CsCl cubic structure (see Section 2.1.1 Physical Metallurgy). For cubic structures <100> is an easy growth direction, but the <100> direction is oriented in the direction of cooling. This results in large columnar grains with mixed orientations, as shown in Figure 6.13b.

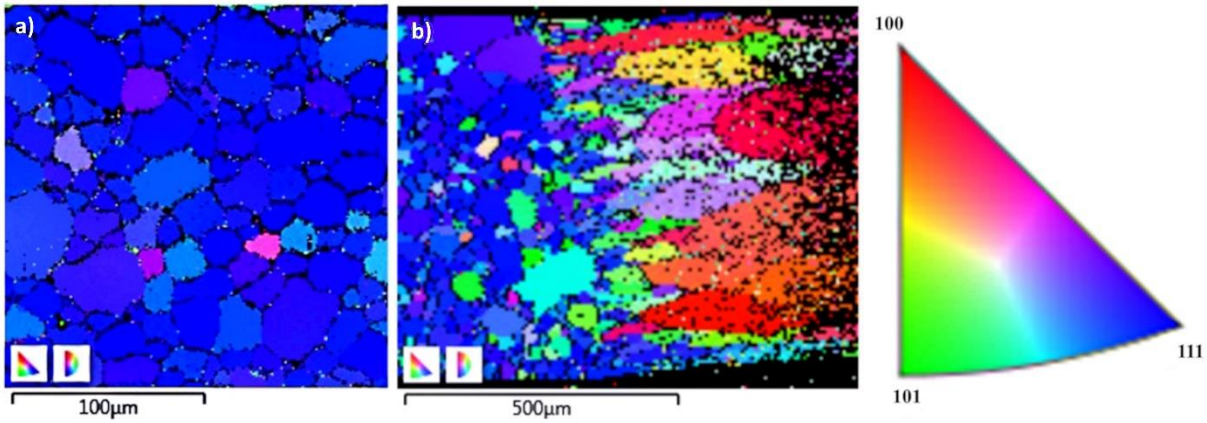

Figure 6.13: Austenite texture of a) as-received and b) laser-processed BM7 NiTi wire measured by EBSD (inverse pole figure in the axial direction).

Different austenite directions have different preferred martensite variants when they are stressed [146]. Table 6.2 summarizes the primary austenite unit cell directions, their spacing and their preferred martensite variant direction.

Table 6.2: Unit cell spacing and preferred martensite variant for each primary austenite unit cell direction.
***This is actually half the unit cell spacing since in this direction it takes two austenite unit cells to form one martensite unit cell.**

Austenite		Martensite Variant (Tension)		Martensite Variant (Compression)	
Direction	**Unit Cell Spacing**	**Direction**	**Unit Cell Spacing**	**Direction**	**Unit Cell Spacing**
<111>	0.5283	$<10\bar{1}>$	0.5759	<110>	0.5032
<110>	0.4264	$<00\bar{1}>$	0.4622	$<2\bar{1}\bar{1}>$/<211>	0.4234
<100>	0.3015	$<01\bar{1}>$	0.3096*	$<\bar{1}00>$	0.2889

mixed	0.4187	mixed	0.4492	mixed	0.4052

If the texture is randomly mixed, then it is assumed that each variant is equally likely to exist so the average unit cell spacings can be used to determine the bending radii. The transformation bending radius can again be determined from similar triangles using the average unit cell spacing for mixed texture, as shown in Figure 6.14.

$$\frac{\boldsymbol{d}}{(\mathbf{0.4492 - 0.4052})} = \frac{\boldsymbol{R_m}}{\mathbf{0.4492}} \qquad \textbf{(Equation 6.20)}$$

$$\mathbf{10.2091} \times \boldsymbol{d} = \boldsymbol{R_m} \qquad \textbf{(Equation 6.21)}$$

The mixed texture of the martensite results in a much larger bending radius in the transformed region compared with that of the preferential <111> texture found in wire-drawn wires (see Equation 6.11).

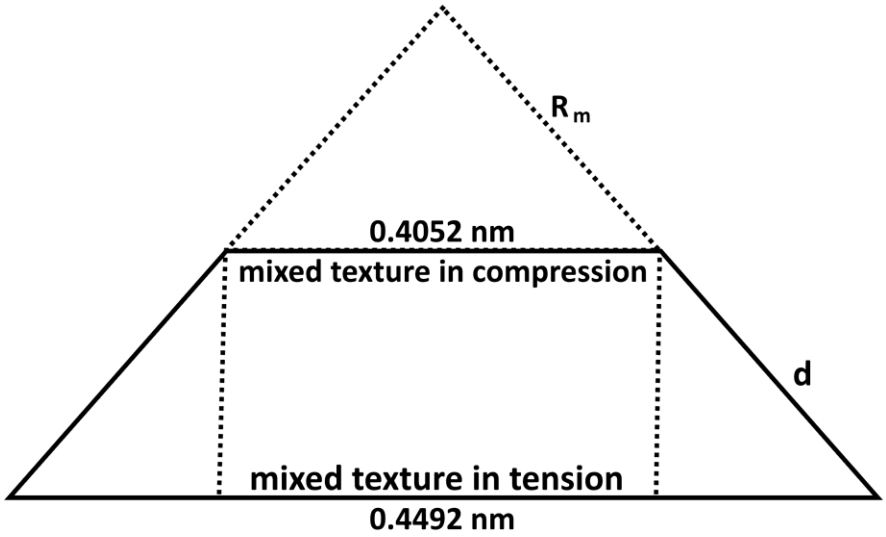

Figure 6.14: Schematic depicting the relationship of similar triangles for the transformed region with mixed texture.

Since the critical elongation to initiate transformation is determined by the critical strain, tensile tests were performed to determine the critical strain of an as-processed NiTi wire, as shown in Figure 6.15. It can be seen that the critical stress to induce martensite transformation is 0.8 % of the unit cell, so for mixed texture Equation 6.6 becomes:

$$\frac{\boldsymbol{r}}{\mathbf{0.008}} = \boldsymbol{R_{crit}} \qquad \textbf{(Equation 6.22)}$$

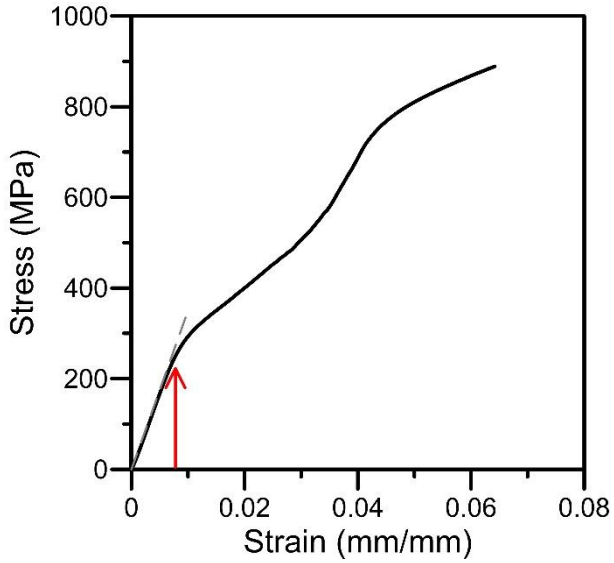

Figure 6.15: Tensile test data highlighting the critical strain for the GR wire.

6.2.1 As-Processed Bending

Figure 6.16a shows the model prediction for a GR wire with a 28 mm span length at 1.8 mm displacement. This is the first displacement at which the transformed region is observed. This displacement can be compared with the data collected from a GR wire with the same span. It can be seen from Figure 6.16b that around 1.6 mm the load begins to deviate from the linear elastic response, indicating the onset of phase transformation.

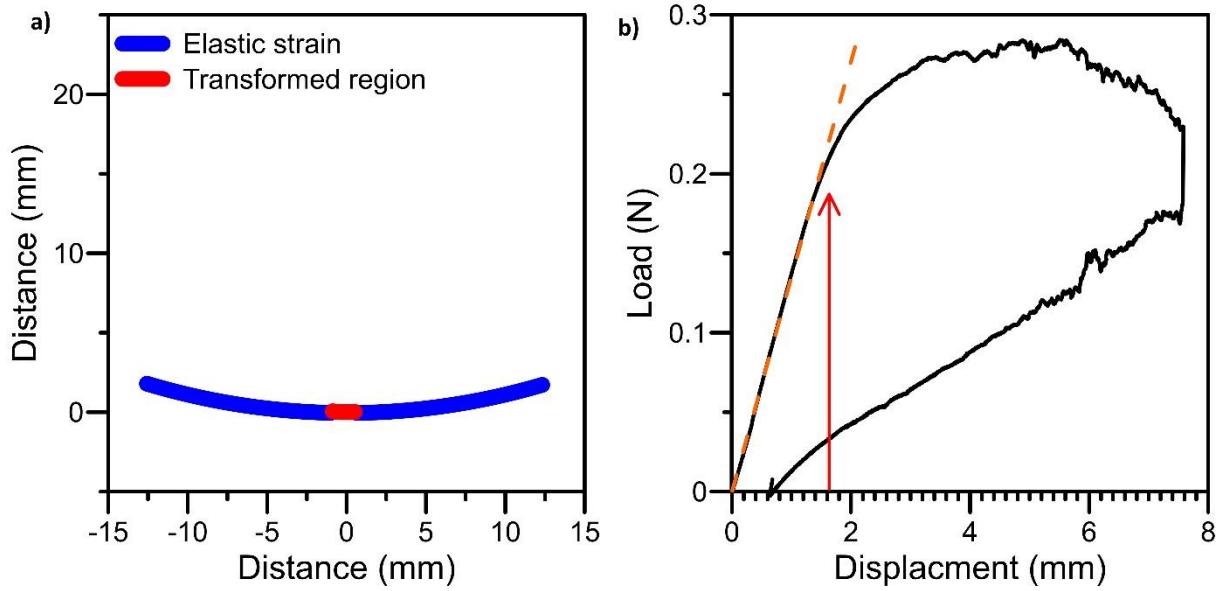

Figure 6.16: a) Model prediction of the transformation initiation and b) three-point-bend data for a GR sample with a span of 28 mm.

Next, the model was used to predict the physical shape of a GR wire at large displacements. As can be seen in Figure 6.17, the model shows a fairly good correlation to the actual physical geometry of the GR wire. Equation 6.11 predicts a bending radius of 7.1 mm for the GR wire. This is close to the measured value of 6.85 mm, as shown in Figure 6.17a. The small discrepancies observed for the GR samples compared with the as-received material may be due to the assumption of a uniform mixing of textures, when in fact there may be more or less of some grain orientations. The overlay shown in Figure 6.17c also shows a decent correlation to the entire bending geometry; however, the GR sample appears to have a non-symmetrical bending shape. Laser processing creates an uneven surface texture [196] which may have resulted in increased friction and prevented uniform sliding of the wire across the supports during bending.

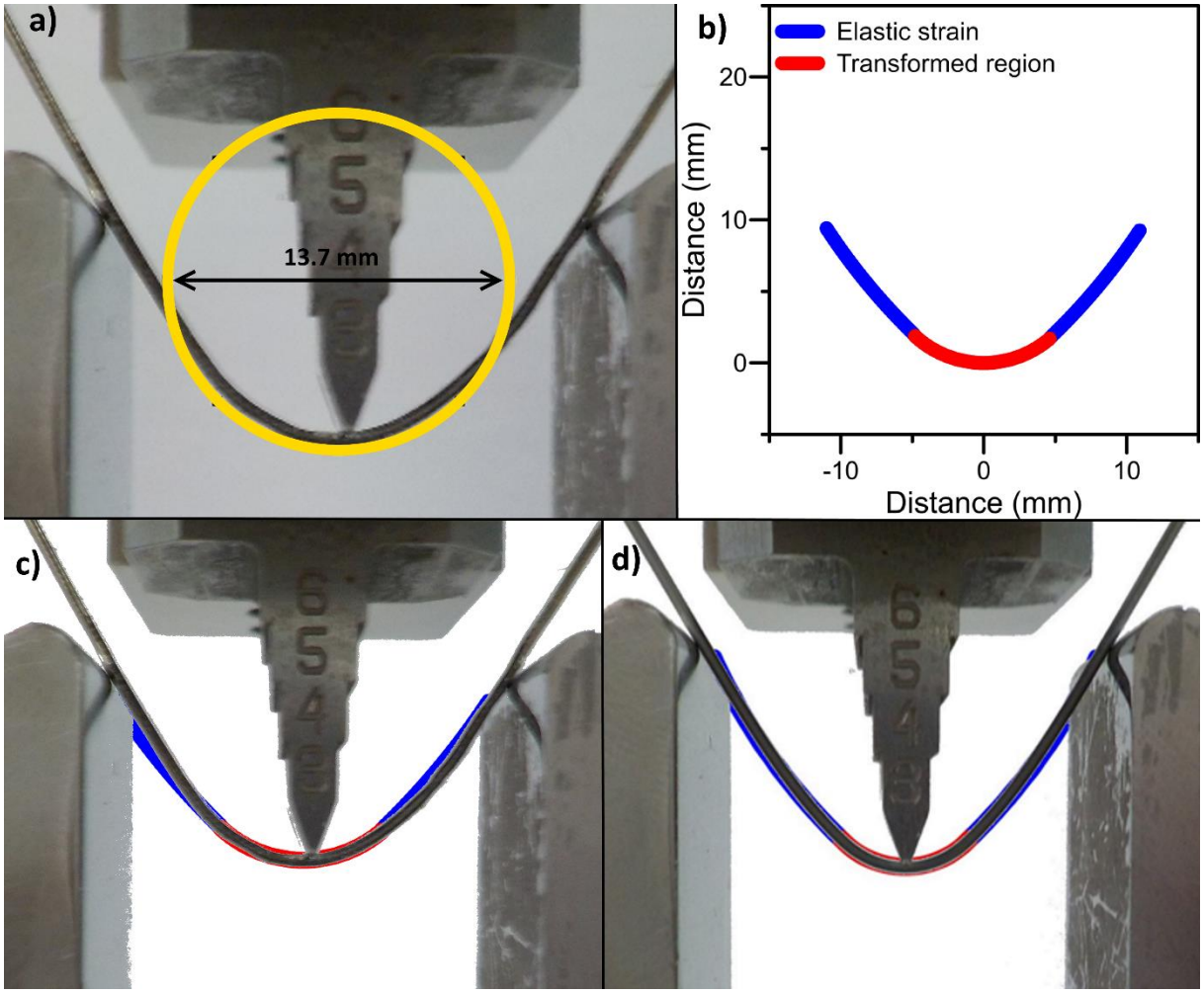

Figure 6.17: a) Actual bending geometry, b) model predictions and c) overlay of the bending model and physical geometry for the GR wire with a 28 mm span at 9.5 mm displacement. d) Overlay of the bending model and physical geometry for the BM7 base material with a 28 mm span at 11.5 mm displacement

It is also important to note that the GR sample could not be displaced as far as the BM7 base material for the same span length. At large displacements, the GR samples would spring out of the test fixture, since the wire ends are not fixed in place during a three-point-bend test. This suggests that NiTi becomes incompressible after phase transformation has occurred, because the GR samples maintained a larger bending radius after transformation compared to the base material (see Figure 6.17c and d).

6.2.2 As-Processed with Retained Base Material

The previous section showed how grain texture can alter the bending geometry of NiTi wires. To demonstrate this further, "zebra" samples were prepared containing alternating regions of retained base material and laser pulses, as show in Figure 6.18. By this method, the average bending radius along the length should be in between that of the base material and the laser processed region.

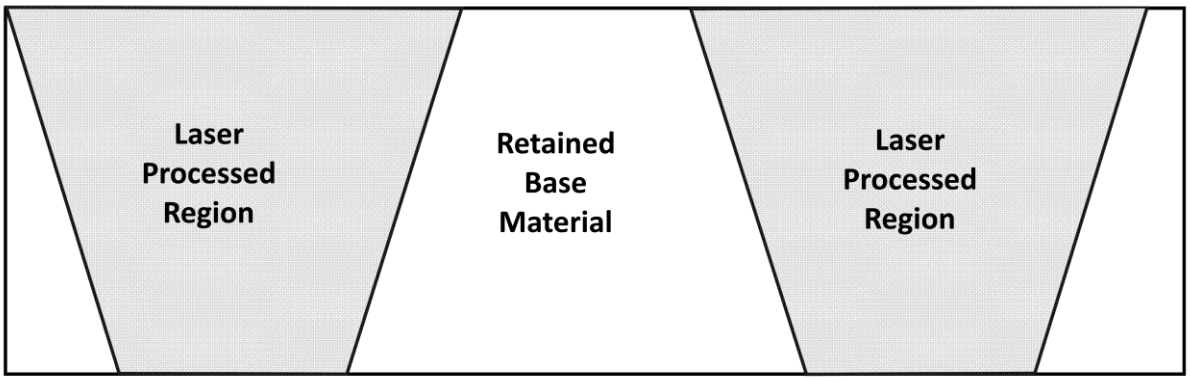

Figure 6.18: Schematic showing alternating regions of base material and laser processing.

The laser processed region will have a $\boldsymbol{\varepsilon_{crit}}$ of 0.008 mm/mm while for the base material it will be 0.009 mm/mm, so the laser processed region will transform first. Also, the laser processed region will have a $\boldsymbol{R_m}$ value of 7.1 mm while the base material is 4.8 mm. If the regions are split 50/50, this should give and average approximate $\boldsymbol{R_m}$ value of 5.95 mm. To determine if this is a reasonable estimate, the average bending radius of the "zebra" sample was measured at maximum deflection, as shown in Figure 6.19. It was found the actual average bending radius was 6.05, so this is a very good approximation.

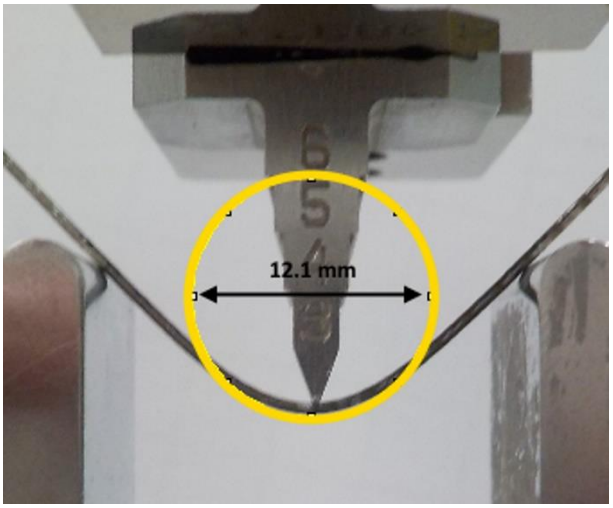

Figure 6.19: Actual bending geometry of the "zebra" sample.

The elastic region was modeled with a uniform strain equivalent to the $\boldsymbol{\varepsilon_{crit}}$ of the GR region, since it is the lower sustainable strain before onset of transformation. To simplify the shape determination process and reduce computation time, the transformed region is initially modelled with the average bending radius of 5.95 mm. It can be seen from Figure 6.20 that the average bending radius of 5.95 closely matches the shape of a curve with alternating sections of bending at 7.1 mm radius and 4.8 mm radius.

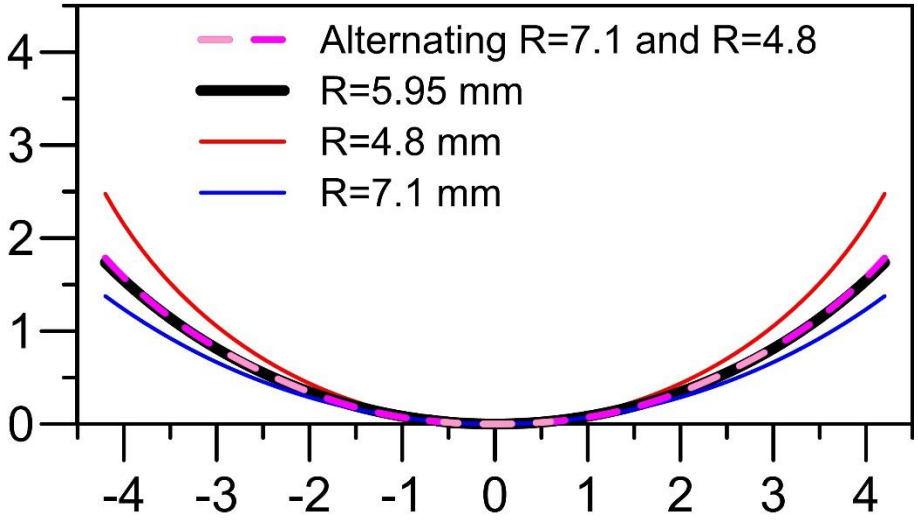

Figure 6.20: Comparison of various bending curvatures.

As can be seen in Figure 6.21, the model again shows good correlation to the actual physical geometry of the "zebra" wire. This provides further confirmation of the texture dependence on the bending properties of NiTi. By changing the ratio between laser processed regions and retained

base material, the average preferred bending radius can be adjusted between 7.1 mm and 4.8 mm. It should be noted again that the "zebra" samples could not be displaced as much as the BM7 base material samples without springing out of the test fixture, and the incompressibility of NiTi needs to be investigated further.

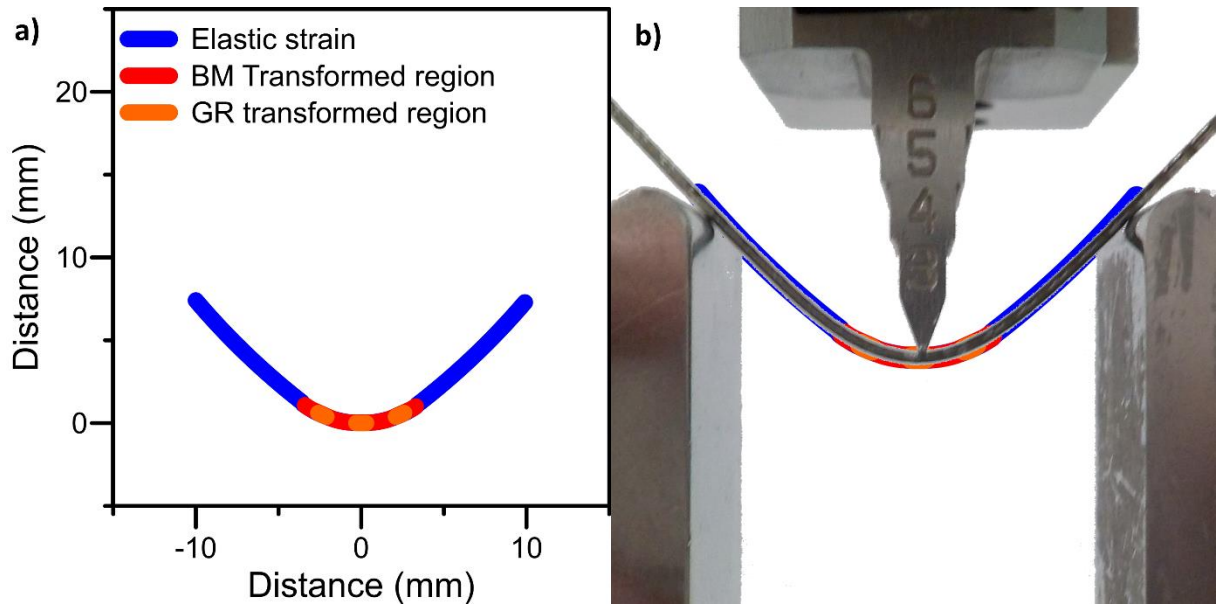

Figure 6.21: a) Model predictions and b) overlay of the bending model and physical geometry for the "zebra" wire with a 28 mm span at 8.5 mm displacement.

6.3 Extracting Compressive Response from Bending Behavior

6.3.1 Maximum Tensile Response

It has been shown previously that NiTi experiences asymmetry between the tensile and compressive responses [146, 174, 175]. This can be predicted easily by comparing the interplanar spacings of martensite in tension, martensite in compression and unstrained austenite, as shown in Figure 6.22. Similar triangles can be used to approximate where the neutral axis will reside, assuming that the strain changes linearly through the sample diameter, using the following relationship:

$$\frac{\boldsymbol{d}}{(\mathbf{0.5759-0.5032})}=\frac{\boldsymbol{s}}{(\mathbf{0.5759-0.5283})} \qquad \textbf{(Equation 6.23)}$$

$$\boldsymbol{s}=\mathbf{0.655}\boldsymbol{d} \qquad \textbf{(Equation 6.24)}$$

where $\boldsymbol{s}$ is the distance of the neutral axis from the outer fibers.

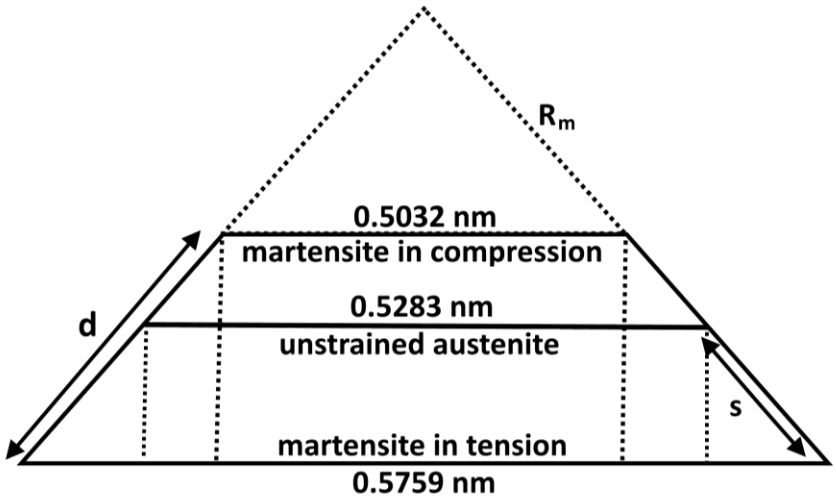

Figure 6.22: Schematic depicting the relationship of similar triangles for approximating the location of the neutral axis.

To determine the maximum tensile stress and strain during bending, the neutral axis offset must be accounted for. The new calculation for strain becomes:

$$\varepsilon_t = \frac{s}{R_{crit} - o} \qquad \textbf{(Equation 6.25)}$$

where the distance from the outer edge to the neutral axis is used in place of the sample radius and the offset, o, is given by:

$$o = s - r \qquad \textbf{(Equation 6.26)}$$

where r is the radius of the sample wire. The calculation for maximum tensile stress (see Equation 6.14) requires a new value for the moment of inertia that accounts for the offset of the neutral axis, which can be done by using the parallel axis theorem [251]:

$$I = \frac{\pi r^4}{4} + Ao^2 \qquad \textbf{(Equation 6.27)}$$

where A is the cross-sectional area of the wire. So, with the adjustment for offset, the updated equation for stress becomes:

$$\sigma = \frac{M(c - o)}{\frac{\pi r^4}{4} + Ao^2} \qquad \textbf{(Equation 6.28)}$$

The offset does not remain constant during loading, so a simplified piecewise exponential function was used to determine amount of offset that is occurring at any given strain. The piecewise function for the BM4 wire was found to be:

$$\begin{cases} if\ deformation\ is\ elastic, & o = 0.13\left(1 - e^{-150^{r}/_{R_c}}\right) \\ if\ deformation\ is\ pseudoelastic, & o = 0.07\left(1 - e^{-500^{r}/_{R_{ave}-R_{crit}}}\right) + 0.085 \end{cases} \quad \textbf{(Equation 6.29)}$$

where R_{ave} is the average bending radius of the entire sample test length. Though simplified, this function follows a similar trend to those observed experimentally in bent NiTi tubes [174]. The piecewise function for the BM7 was found to be:

$$\begin{cases} if\ deformation\ is\ elastic, & o = 0.13\left(1 - e^{-2000^{r}/_{R_c}}\right) \\ if\ deformation\ is\ in\ transition, & o = 0.005\left(1 - e^{-2000^{r}/_{R_c-R_R}}\right) + 0.13 \\ if\ deformation\ is\ pseudoelastic, & o = 0.02\left(1 - e^{-2000^{r}/_{R_{ave}-R_{crit}}}\right) + 0.135 \end{cases} \quad \textbf{(Equation 6.30)}$$

where R_R is the bending radius at which the R-phase transformation occurs. The function for the BM7 wire required an additional piece due to the presence of R-phase (see Figure 6.10) as it seems the R-phase has a different neutral axis compared to the austenite and martensite phases. It could not be verified if the predicted offset for R-phase realistically corresponds to lattice parameters, due a lack of certainty associated with this phase. Currently, there is no consensus on what the lattice parameters are for R-phase [247-250]. It has been said that the <111> direction for austenite corresponds with the <001> direction of R-phase (in a hexagonal setting) [244]; however, some reported values for the c_H lattice parameter are less than or almost equal to the atomic spacing for austenite in the <111> direction.

The predicted changes to the neutral axis offset are plotted in Figure 6.23. It is important to note that the shift in the offset for the BM4 wire began gradually until there was a sudden movement when phase transformation initiated, indicated by the number 1 in Figure 6.23a. However, the BM7 wire had much quicker shifts as the material rapidly transitioned from austenite to R-phase (number 1 in Figure 6.23b) and from R-phase to martensite (number 2 in Figure 6.23b). This demonstrates the importance of the transformation pathway on the micromechanics of bending NiTi wires.

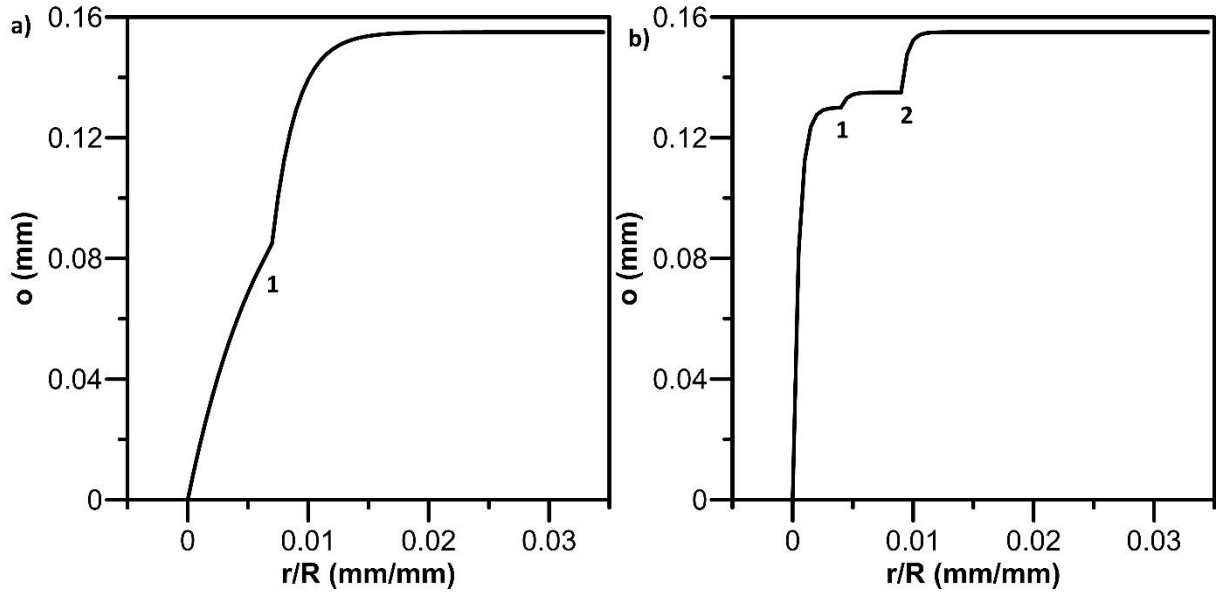

Figure 6.23: Neutral axis offset for a) BM4 and b) BM7 NiTi wires during three-point-bending.

By applying Equations 6.25 and 6.27 to the three-point-bend data for the BM7 and BM4 NiTi wires in combination with the appropriate maximum tensile stress/strain experienced during bending can be extracted (see Figure 6.24). Although the offset determination functions were tuned to fit the data, the maximum offset amount was predicted to be 0.655×d by the similar triangles method. This maximum value occurs in the pseudoelastic plateau and shows good correlation with the pseudoelastic plateau values observed during tensile testing.

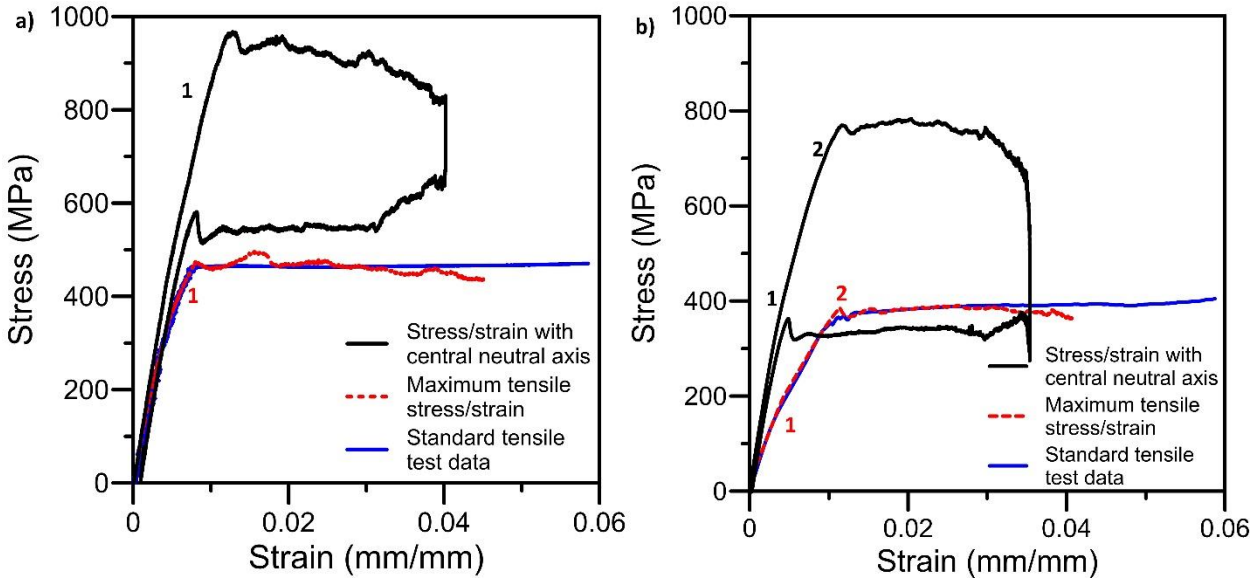

Figure 6.24: Stress/strain response of a) BM4 and b) BM7 NiTi wires during three-point-bending and uniaxial tension.

6.3.2 Compressive Behavior

Since the extraction method has been verified for the maximum tensile response, it can now be applied to the maximum compressive response. The maximum compressive strain during bending becomes:

$$\varepsilon_t = \frac{d - s}{R_{crit} - o} \qquad \textbf{(Equation 6.31)}$$

Meanwhile, the updated maximum compressive stress becomes:

$$\sigma = \frac{M(c + o)}{\frac{\pi r^4}{4} + Ao^2} \qquad \textbf{(Equation 6.32)}$$

Figure 6.25 shows the extracted maximum compressive response of the BM4 and BM7 wires. The compressive response of the BM4 wire demonstrates an initial elastic region that is similar to the tensile response and a plateau the is slightly below the value determined by a central neutral axis. This is in line with previous work that examined tensile, compressive and bending responses of NiTi tubes [174]. The BM7 wire exhibited asymmetry sooner with two different elastic responses in compression and tension. This also agrees with work that examined the effect of R-phase on the asymmetry of the tensile and compressive behavior of NiTi [252]. This is an indication of the incompressible behavior of the austenite to R-phase transformation that is occurring, as incompressible materials are significantly more rigid in compression than tension [253].

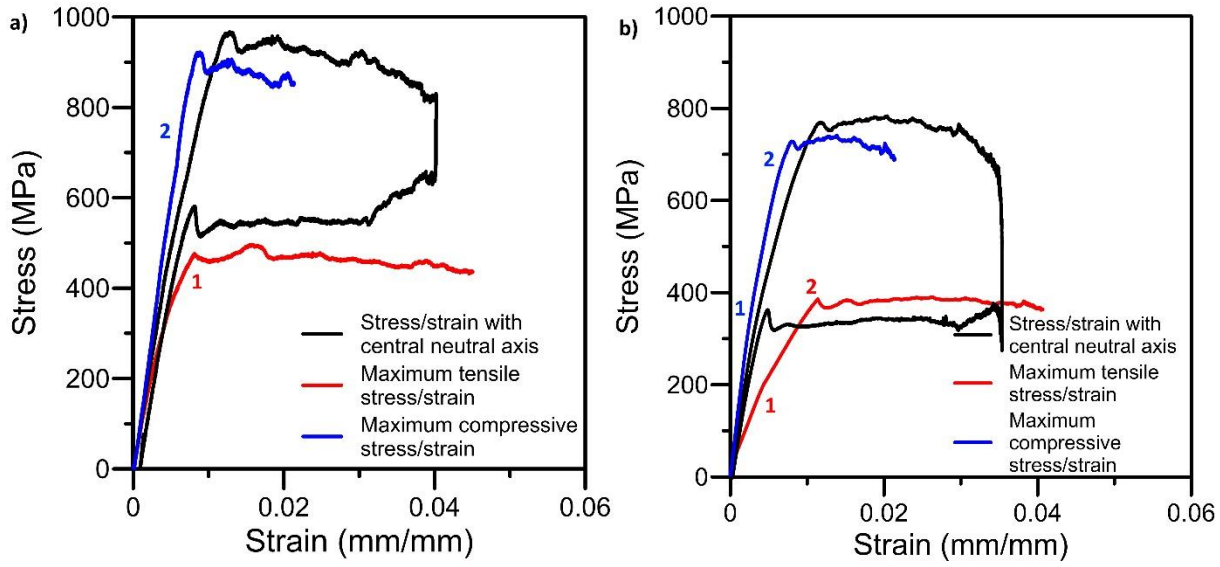

Figure 6.25: Stress/strain response of a) BM4 and b) BM7 NiTi wires during three-point-bending with maximum tensile and compressive extractions.

6.3.3 Effect of Microstructure

It has already been shown that the texture has an effect on the preferred bending radius of the martensite phase. Furthermore, it will have an effect on the location of the neutral axis, as shown in Figure 6.26. Similar triangles can again be used to approximate where the neutral axis will reside, assuming that the strain changes linearly through the sample thickness, using the following relationship:

$$\frac{\boldsymbol{d}}{(\mathbf{0.4492 - 0.4052})} = \frac{\boldsymbol{s}}{(\mathbf{0.4492 - 0.4187})} \qquad \textbf{(Equation 6.33)}$$

$$\boldsymbol{s = 0.693d} \qquad \textbf{(Equation 6.34)}$$

This suggest that there would be a larger offset of the neutral axis for the GR sample compared with the BM4 and BM7 samples.

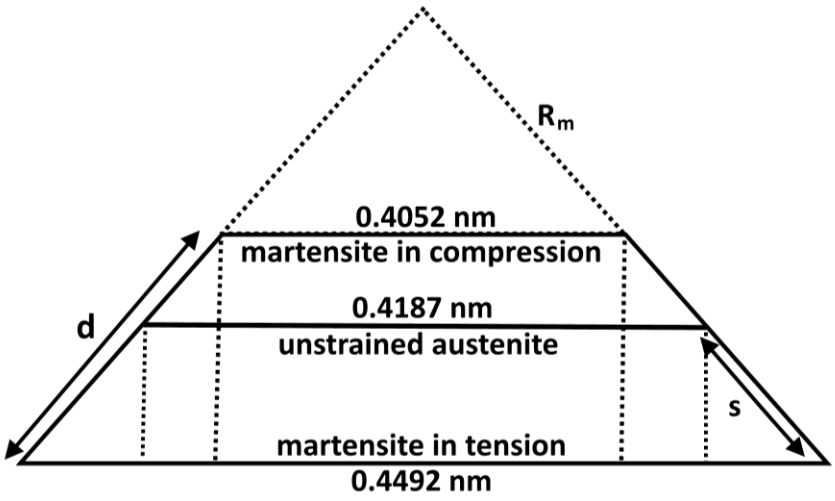

Figure 6.26: Schematic depicting the relationship of similar triangles for approximating the location of the neutral axis for a mixed texture samples.

However, the true offset of the neutral axis could not be determined solely from the three-point-bend test. This is due to the fact when the GR sample is tested in uniaxial tension, it experiences strain hardening and a flat plateau is not observable, as shown in Figure 6.27. This strain hardening is a result of the microstructure and the martensite variants that are formed [254]. During three-point-bend testing, the GR sample did not appear to experience any strain hardening. This may be the result of anisotropic strain hardening, as has been observed in aluminum alloys [255]. Also, it appears that the neutral axis did not shift as far from the central point as was predicted. This may be due in part to internal breaking and reorientation of large grains to accommodate strain.

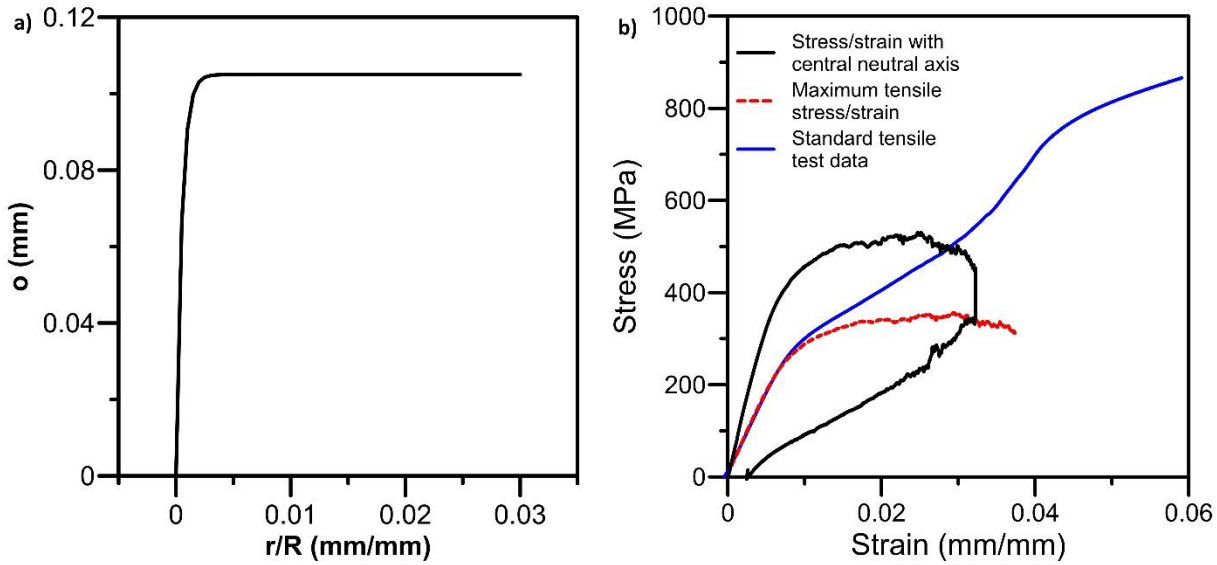

Figure 6.27: a) Neutral axis offset and b) stress/strain data for GR NiTi wire during three-point-bending and uniaxial tension.

The offset in the elastic region appears to be 0.105×d, which 54.4 % of the total transformed offset of 0.193×d. This is in line with the results from the BM4 wire, which experienced an initial offset of 0.085×d (54.8 % of the total transformed offset) in the elastic region. It is possible that, once phase transformation began, the internal grains broke up and reoriented themselves to facilitate the neutral axis remaining where it was when it accommodated the elastic strains. This internal restructuring evidenced by the much larger amount of residual strain that was observed in the GR sample after three-point-bending. Table 6.3 shows the comparison between residual strains for each material type. In order to fully understand how the GR sample is accommodating bending deformations, further extensive microstructural analysis must be conducted on the GR material before and after three-point-bending.

Table 6.3: Comparison of residual strain after three-point-bending.

NiTi wire type	**BM4**	**BM7**	**GR**	**zebra**
Residual strain (mm/mm)	**0.001**	**<0.0005**	**0.0025**	**0.003**

6.3.4 Effect of Ternary Elements

The orthodontic arch wires modelled in the previous chapter (see Section 5.4 Model Revalidation) are a ternary NiTiCu alloy. The Cu element is substituted in place of some of the Ni. This substitution causes a distortion of the crystal structures, which varies with Cu concentration [256].

These distortions to the lattice parameters will affect the bending curvature and the neutral axis offset. This can be seen in Figure 6.28, where the predicted relative neutral axis offset is only 0.09 compared with 0.155 that was seen in the binary NiTi alloys.

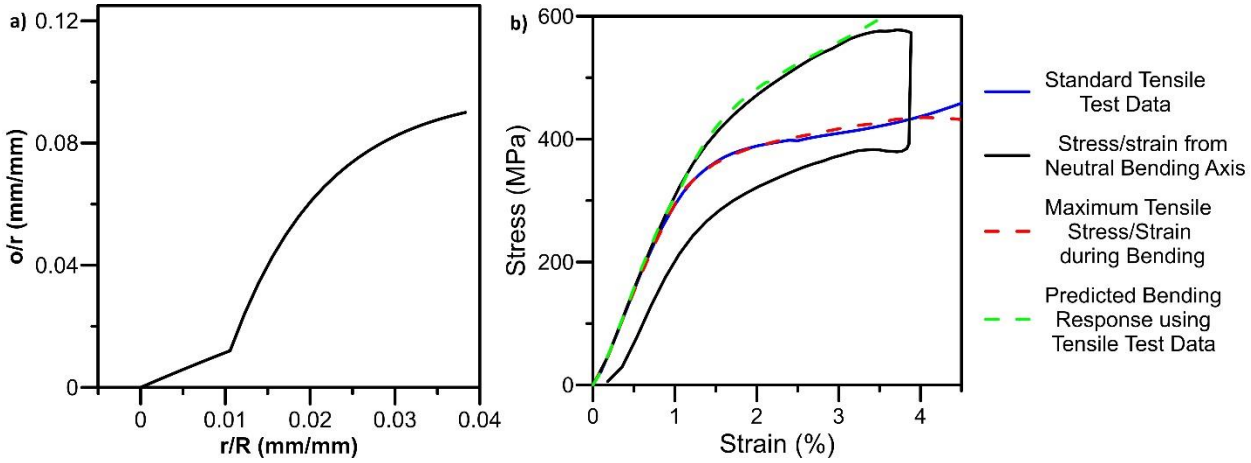

Figure 6.28: a) Relative neutral axis offset and b) stress/strain data for NiTiCu orthodontic arch wire during three-point-bending and uniaxial tension.

To be able to predict the bending response of as-processed laser modified NiTiCu would be a difficult task. The varying composition attributed to the laser processing would alter the local bending geometries, so the exact composition and lattice parameters in each compositional region would need to be known. In addition, it has already been shown in previous section that the microstructural deformation of laser processed material results in an unpredictable stress response. Much more work is required in this area to improve the predictive modelling capabilities of as-processed NiTi SMA alloys.

6.4 Shear Properties

6.4.1 Torsional Shear

The results from the three-point-bend tests discussed previously in this chapter allude to the fact that the NiTi wires behaves in an incompressible manner during phase transformation. To better understanding this phenomenon, torsional properties were investigated since compressibility can be determined by the relationship between the elastic and shear properties. For an isotropic material, incompressibility occurs when the Poisson's ratio is ~0.5 (such as is the case for some rubbers [253]). What this means is that the strain in the z-direction is twice as much as the strain

in the x-direction, and the strain in the x-direction equals the strain in the y-direction (due to material isotropy):

$$\frac{1}{2} = \frac{\varepsilon_x}{\varepsilon_z} \rightarrow \varepsilon_z = 2\varepsilon_x \rightarrow \varepsilon_z = \varepsilon_x + \varepsilon_y \quad \textbf{(Equation 6.35)}$$

This results in a conservation of volume during deformation. If the changes in strain are achieved through no change in volume, the material is said to be incompressible [257]. It is known that the phase transformation from austenite to R-phase results in very small changes in volume [33, 47]. This is one of the reasons why the phase transformation is reversible. The accommodation of strain through the reorientation of atoms into a new crystal structure undergone by NiTi during phase transformation is comparable to the uncoiling reorientation of polymer chains in rubber.

The results of the torsional shear test for the BM4 wire can be seen in Figure 6.29. It was found to that the BM4 wire has a shear modulus of 26.7 GPa. Using the following equation to determine Poisson's ratio:

$$\nu = \frac{E}{2G} - 1 \quad \textbf{(Equation 6.36)}$$

where E is the elastic modulus and G is the shear modulus, results in a Poisson's ratio of 0.33 in the elastic region and is in line with previous work [146, 152]. These results are typical for a NiTi SMA that is fully austenitic and elastically deforming before the onset of the martensite transformation.

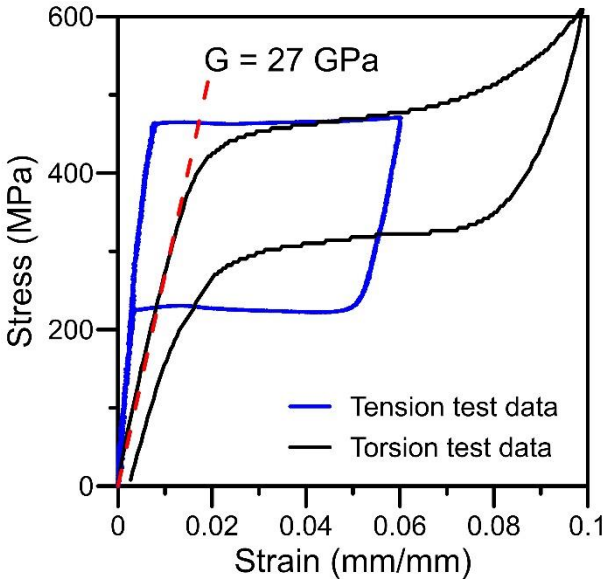

Figure 6.29: Comparison of torsion results to tension results for BM4 wires.

The torsion test results for the BM7 wire, shown in Figure 6.30, demonstrate a shear slope of 33.8 GPa, which is higher than the shear modulus of the BM4 wire. Recalling that the BM7 wire has both austenite and R-phase present at room temperature and experienced a reduced elastic modulus in tension due to the presence of R-phase, one would have expected a reduced shear modulus as well. Rearranging Equation 6.36 gives:

$$\mathbf{G} = \frac{\boldsymbol{E}}{\mathbf{2}(\boldsymbol{\nu} + \mathbf{1})} \qquad \textbf{(Equation 6.37)}$$

Using a Poisson's ratio of 0.5 (incompressible behavior) gives a predicted shear modulus of 12.3, while using a Poisson's ratio of 0.33 (standard for austenite and martensite) gives a shear modulus of 13.9. However, the use of a Poisson's ratio is only valid when austenite is being elastically deformed. The austenite phase has uniform cubic crystal structure; however, the R-phase is rhombohedral in the P3 space group, which has no center of symmetry [244]. Since the R-phase has no center of symmetry, its mechanical response is anisotropic and is dependent on the direction that the load is applied. It has already been shown that the martensite phase transformation in NiTi is not isotropic and cannot be modelled as such [245].

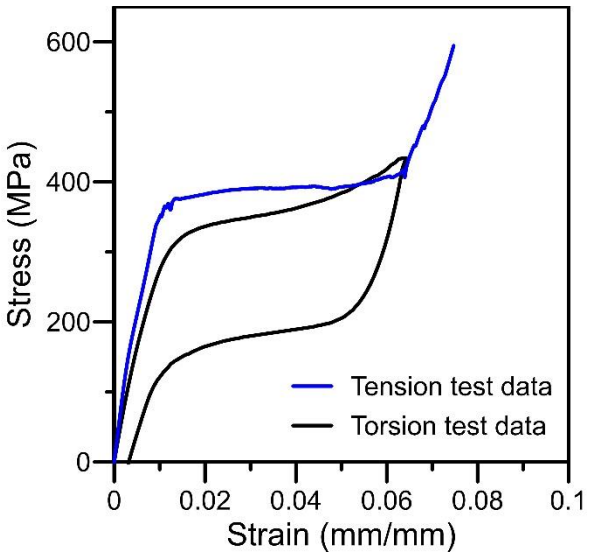

Figure 6.30: Comparison of torsion results to tension results for BM7 wires.

These results are again contradictory to the modelling results put forth by Santos *et al.* who over simplify this material response to be fully elastic [242]. They theorized that the material with mixed phases would have a reduced bending moment compared to a fully austenitic material due to the softening observed in tensile tests. They go so far as to claim that a mixed austenite/R-phase

material would be beneficial for use in endodontic files because of this theoretical reduction of the torque and bending moment [242]. However, due to the incompressible nature of the anisotropic phase transformation that occurs in place of true elastic deformation, these mixed-phase materials would be stiffer in torsion and bending and quite possibly perform worse for the proposed endodontic file applications. A comparison of actual experimental slopes to the theoretical values (assuming complete linear elastic response of an isotropic compressible material) is summarized in Table 6.4.

Table 6.4: Summary of material properties for the NiTi wires.

	Elastic Modulus	Shear Modulus	Bending Modulus
BM4	71 GPa	26.7 GPa	71 GPa
BM7 (Experimental)	48 GPa	33.8 GPa	80 GPa
BM7 (Theoretical)	37 GPa	13.9 GPa	37 GPa

6.4.2 Effect of Laser Processing

The effects of laser processed microstructure have already been shown in the bending geometry and difficulty of understanding the bending stresses. For thermo-mechanically treated wires, such as the MM wires examined in tension previously in Chapter 4, these effects are not an issue since wire drawing reorients the grains in the <111> direction. However, for wires such as the SmartArch^{TM} orthodontic arch wires this is a concern because these wires are used in the as-processed state. Also of concern for orthodontic arch wires are the torsion properties.

Figure 6.31 shows the torsion results for the GR sample. It can be seen that this sample also exhibits a higher than expected shear modulus, but a lower than expected transformation plateau that is not recoverable. This large amount of residual strain was not observed in bending and may be the result of significant transformation-induced plasticity during shearing. These results are concerning for an application such as orthodontic arch wires and necessitate a deeper investigation into the microstructural evolution during torsion.

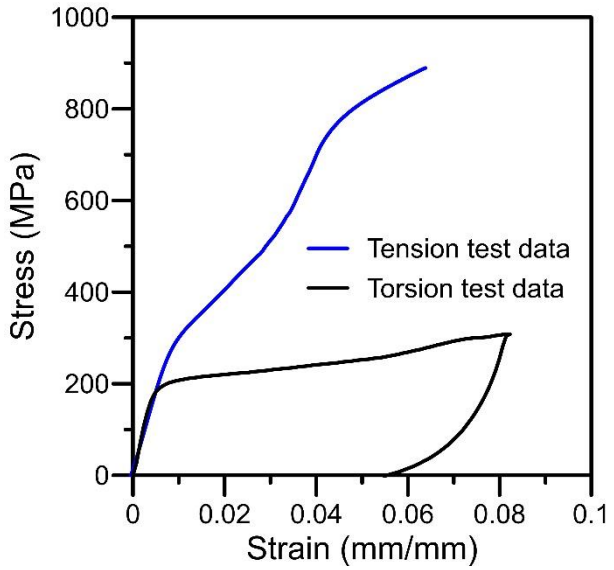

Figure 6.31: Comparison of torsion results to tension results for GR samples.

6.5 Chapter Summary

In this chapter, a macro-scale model was presented that accounts for the effect of texture on the bending properties, permitting the prediction of bending geometries of laser modified pseudoelastic NiTi wires. Monolithic wires containing multiple texture regions were fabricated and used to validate the proposed model. A good correlation between the model and the experimental data was shown. It was shown that laser processing can be successfully used to alter the preferred average bending radius of SIM in NiTi wires.

The neutral axis offset and the maximum tensile/compressive stresses/strains were successfully determined from the bending response for the as-received materials. However, the microstructure of the as-processed material experienced internal reorientation and anisotropic transformation induced plasticity during bending that made determination of the maximum tensile and compressive stresses and strains impossible without further microstructural analysis.

The incompressible and anisotropic behavior of the austenite to R-phase transformation was examined. It was shown that the material undergoing the R-phase transformation exhibits higher shearing and bending stresses than the material the is elastically deforming in the austenite phase. These results are consistent with previous results but are contrary to some current over-simplified theoretical modelling assumptions.

Chapter 7: Designing a Self-Biasing Spring Actuator

Existing actuators used in the aerospace, robotics and automotive industries are heavy and expensive [259], and they are slowly being replaced by NiTi spring actuators [260-262], which are light weight and less costly. In addition, the maximum stroke and recovery force of an SMA spring actuator is much higher than that of other linear actuators [201]. Currently, many actuator designs incorporate individual springs in series [263] or parallel [264] in order to bias the actuation of the SMA spring. This is because conventional NiTi SMAs have a uniform composition and processing history, leading to unchanging shape memory properties throughout the material; thus, they can only move in one direction.

It is possible to achieve a two-way SME that results in a change in shape from both heating and cooling of the material. This is achieved by training the SMA microstructure through the introduction of dislocations, formation of preferentially oriented precipitates, thermal cycling and constrained aging [33, 265]. This two-way SME is only capable of ~2 % actuation strain, which degrades during cycling as the microstructure evolves [33, 266]. This degradation can be more than 5 % plastic strain for stresses as low as 100 MPa; additionally, degradation can even occur during stress-free thermal cycling [266]. This susceptibility to degradation of the actuation strain severely hinders the applicability of two-way SME for use as reliable actuators.

Alternatively, laser processing can be used to locally modify the Ni concentration and create a self-biasing mechanism. Some proof-of-concept actuators have already been proposed, including actuators with two memories (i.e. two transformation temperatures) and a self-biasing linear actuator [5, 21]. However, none of them can achieve the large displacements attainable with a self-biasing spring actuator, which limits their functionality.

7.1 Determining an Appropriate Heat Treatment Temperature

After laser processing, the wires must undergo thermomechanical treatment to improve the microstructure (see Section 3.3 Post-Process Thermomechanical Treatment). The cold-worked material requires a heat treatment to restore shape memory and pseudoelastic properties. Typically, the heat treatment is performed at 400 ˚C for 1 hour, as this has been found to produce the most

stable material properties (see Section 2.1.6 Heat Treatments). Figure 7.1 shows the DSC results for the UP, P1 and P2 materials after a 400 ˚C heat treatment. It can be seen all of the materials have similar and overlapping phase transformation temperatures. This is because, even though the materials have different initial compositions, at lower heat treatment temperatures precipitates form causing the bulk composition to shift towards a similar thermally stable composition.

While this can be acceptable for passive applications where the difference in pseudoelastic plateau stresses is the desired result (see Section 5.2.1 Material Characterization), this raises difficulty for thermally active actuation applications. Overlapping transformation temperatures means that activating each active region individually would be difficult or impossible.

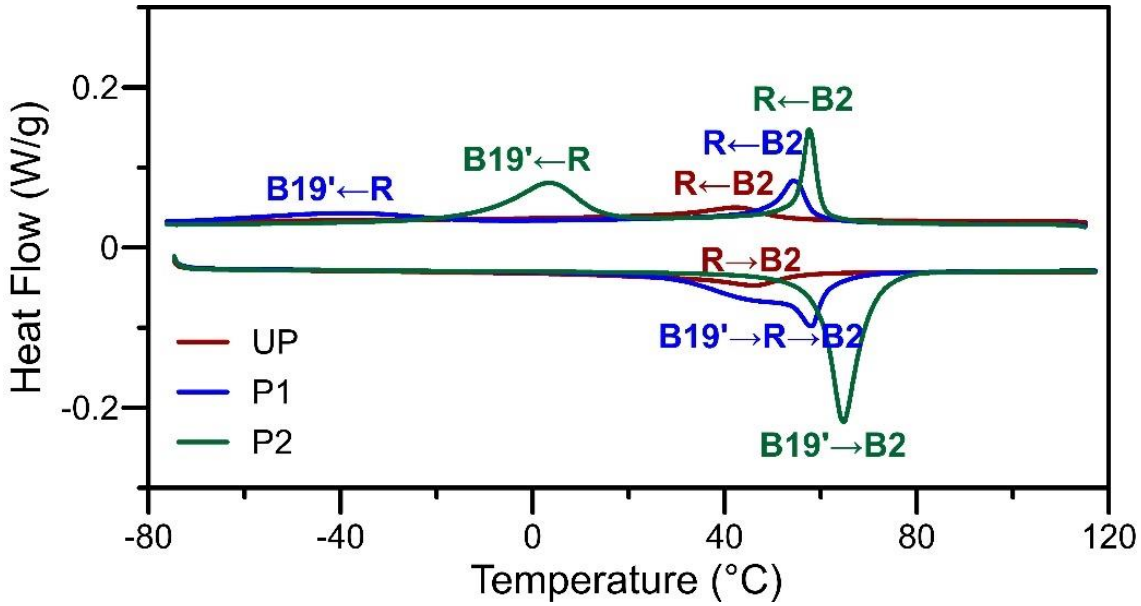

Figure 7.1: DSC results for BM, P1 and P2 materials after 400 ˚C heat treatment.

Several heat treatment temperatures were tested to determine which one gives an appropriate separation of the various transformation temperatures. Figure 7.2 shows the effect heat treatment temperature has on the A_p. All compositions appear to be converging to an A_p of ~56 ˚C at low heat treatment temperatures. As temperature is increased, the A_p temperatures spread farther apart until they stabilize at the true precipitate-free compositions. The changes in transformation temperature appear to follow logistic relationships for all of the materials tested; however, more compositions are required to develop a more robust and inclusive relationship.

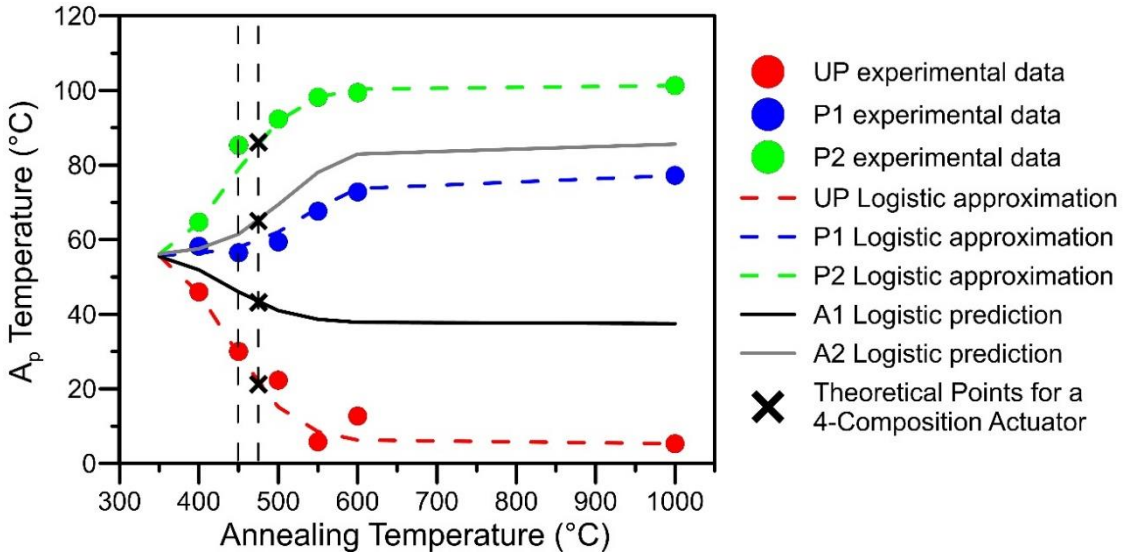

Figure 7.2: Effect of heat treatment temperature on the austenite transformation temperature. All heat treatment times were 1 hour.

For this study, a heat treatment temperature of 450 ˚C was chosen. This method gave sufficient separation of transformation peaks (~27 ˚C between A_p temperatures) while remaining within the ideal heat treatment temperature range (350-475 ˚C), as can be seen in Figure 7.3. It was observed that at 40 ˚C, the austenite transformation of the UP material is complete, but the P1 material has not yet started transforming. At a temperature of 75 ˚C, the P1 material is fully austenite while the P2 material has not yet begun transforming. Above 100 ˚C the P2 material will also be fully austenite.

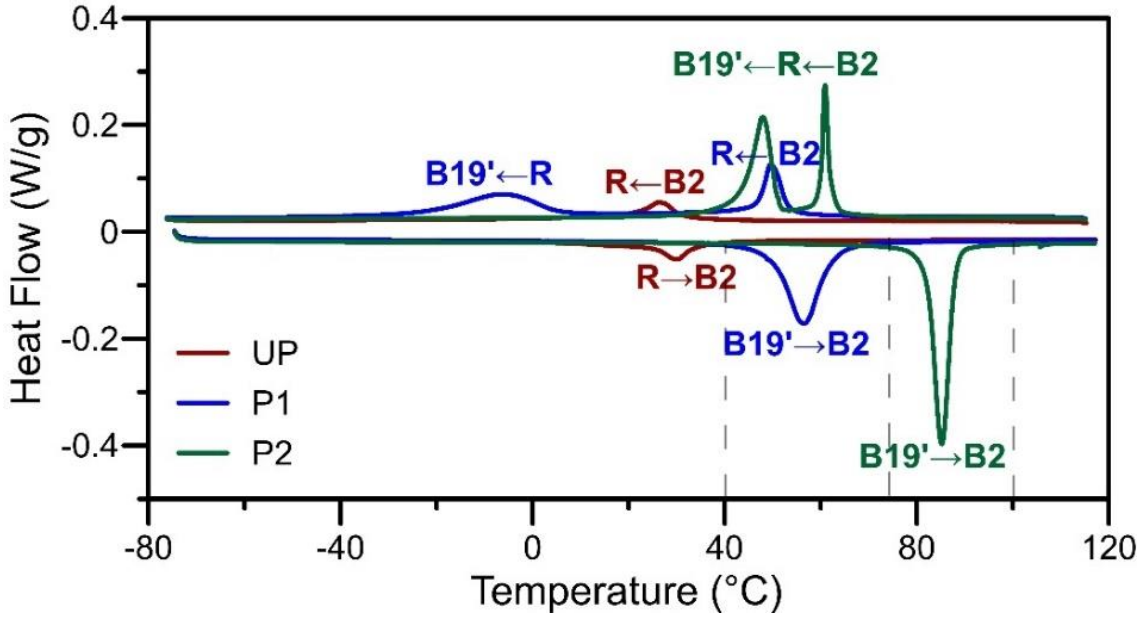

Figure 7.3: DSC results for BM, P1 and P2 materials after 450 ˚C heat treatment.

It may possible to create an actuator with four distinct transformation temperature zones. Now that precise control over the laser processed composition has been successfully demonstrated (see Section 4.5 Modelling the Change in Ni Composition), alternative compositions (A1 and A2) could be chosen that are in between the compositions of the UP and P2 samples. Using a heat treatment temperature of 475 ˚C may allow for enough separation of the transformation peaks (~22 ˚C between A_p temperatures) to allow for the fabrication of a three-stage self-biasing actuator with four distinct compositions and transformation temperature zones (see Figure 7.2). This leads to the possibility of further enhancement to the functionality of the multi-stage self-biasing actuator and should be investigated further. Increasing the annealing temperature above 475 ˚C looks to provide even better separation of peaks, allowing for more self-biasing memories to be imbedded, but the mechanical performance suffers, and it is not recommended [200].

7.2 Modelling Actuation Stroke

Constitutive, experimental and conventional spring design models have all been used to predict the thermomechanical behavior of SMA springs [267-269]. Constitutive thermomechanical models are complex and difficult to use directly for spring design, while models based on experimental characterization or conventional spring design are much simpler [270]. Conventional spring design implements a linear coil spring equation to study the spring's mechanical response at different temperatures, which does not accurately capture the non-linear response of the martensite detwinning process. Experimental characterization is done by heating SMA spring actuators to different temperatures and studying the mechanical response. For both of these methods, force-deflection plots of SMA springs in fully martensitic ($T < M_f$) and fully austenitic ($T > A_f$) states are used to determine the maximum force and deflection of the spring actuator [270].

7.2.1 Predicting Actuation for One-stage Spring Actuator

Several experiments were previously conducted to characterize the mechanical performance of NiTi springs made from UP, P1 and P2 wires at various temperatures [200]. To predict the stroke of a self-biasing spring, the number of active coils of each material composition contained within the spring must be determined. In the case of the MM1 spring (see Figure 3.6), there are six active coils for both the P1 and UP material regions. The experimental compression data can be used to

approximate the self-biasing behavior by scaling the displacement to the number of active coils, since the force exerted by the spring is proportional to the displacement per number of active coils (N_a).

$$\boldsymbol{F = \frac{Gd^4\delta}{8D^3N_a}} \qquad \textbf{(Equation 7.1)}$$

where δ is the displacement, $\boldsymbol{N_a}$ is the number of active coils, $\boldsymbol{d}$ is the wire diameter and $\boldsymbol{D}$ is the spring diameter. Additionally, when heated to the activating temperature the force of the activating spring material (laser processed) must be equal to the counter-force that is exerted by the passive spring material (base material).

$$\boldsymbol{F_a = F_p} \qquad \textbf{(Equation 7.2)}$$

Also, the activating spring material is recovering and uncompressing, so the passive spring material must compress an equivalent amount, since the self-biasing spring is a self-contained system.

$$\boldsymbol{-\delta_a = \delta_p} \qquad \textbf{(Equation 7.3)}$$

Figure 7.4 shows the force-displacement plot of the MM1 spring materials after adjusting their displacements for six active coils. At the lower temperature state (45 ˚C), the P1 material is fully compressed, denoted by the diamond symbol. The UP region must also be partially compressed in order to exert a balancing force greater than or equal to that which is required to compress the P1 region, denoted by the cross symbol. Ideally, the forces will be equal at this temperature, because over-compression of the passive region would result in reduced actuation displacement at high temperature. Upon heating to the activating temperature for the P1 material (85 ˚C), the UP material compresses an equal displacement to that which the P1 material recovers. Also, the forces exerted by each spring material must be equivalent at this temperature. This balanced state is denoted by the circle symbol. From this analysis, it can be seen that the MM1 design should achieve a stroke of ~4.1 mm.

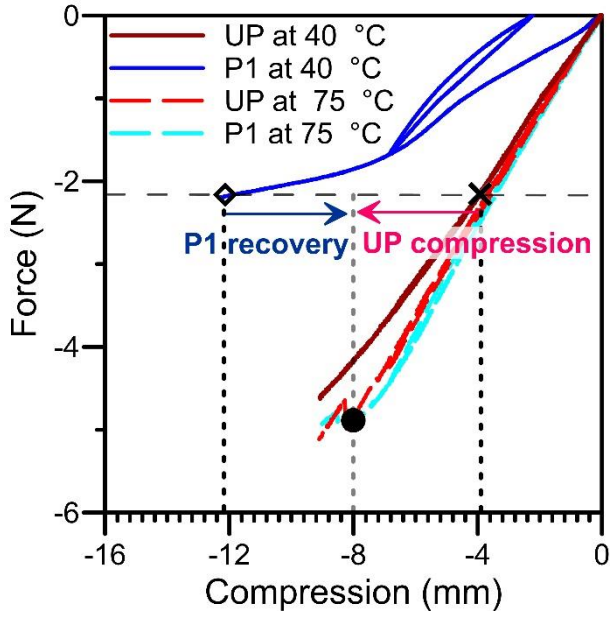

Figure 7.4: Theoretical force-deflection plots for the MM1 design used to predict stroke.

Figure 7.5 shows a prototype of the MM1 spring design that has been partially compressed in the test fixture. The total length of the spring actuator was measured to be 2.1 cm. The interface between the P1 region and the UP region was marked with white paint for easy observation of the displacement. It can be seen that at the low temperature (≤ 45 ˚C) the P1 region of the spring is compressed significantly more than the UP region. Upon heating, the interface between the P1 region and the UP region moved slightly more than 4 mm after the spring sections equalized in stiffness, as was predicted by the stroke prediction shown in Figure 7.4. This displacement is 19 % of the total length of the actuator, which is much higher than the 2-5 % of a typical SMA linear actuator [202, 270].

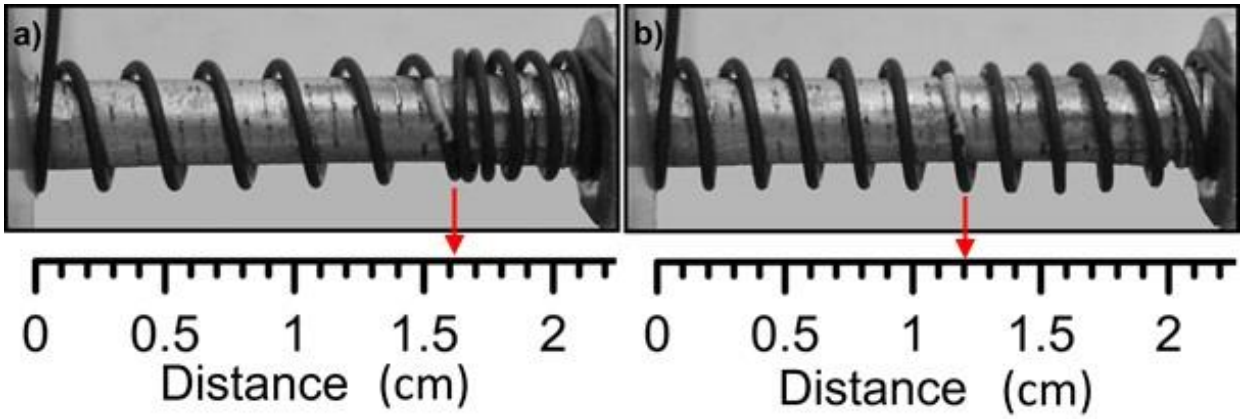

Figure 7.5: Displacement measurement set-up depicting the MM1 spring containing both UP and P1 regions at a) room temperature (≤40 °C) b) high temperature (~75 °C).

7.2.2 Predicting Actuation for Two-stage Spring Actuator

This stroke analysis can also be performed for the MM2 design; however, it is slightly more complex since there are two activating regions. At the low temperature both activating regions are fully compressed with force exertions that are less than or equal to the passive region (UP). At the intermediate temperature, only the first activating region (P1) must balance with the passive region, as it did for the MM1 design.

$$\boldsymbol{F_{a2} \leq F_{a1} = F_p} \qquad \textbf{(Equation 7.4)}$$

Also, since the P2 region has not been activated yet, only the P1 region recovers and the displacement follows Equation 7.3. However, at the high temperature all three regions must have equivalent force exertions.

$$\boldsymbol{F_{a2} = F_{a1} = F_p} \qquad \textbf{(Equation 7.5)}$$

Additionally, at the high temperature the P1 region becomes a passive region, so the displacement recovered by the second activating region (P2) must equal the compression of both the P1 and UP regions combined.

$$\boldsymbol{-\delta_{a2} = \delta_{a1} + \delta_p} \qquad \textbf{(Equation 7.6)}$$

Figure 7.6 shows the force-displacement plots for the MM2 materials after adjusting for the number of active coils in the design. The UP displacements are adjusted to six coils, but the P1 and P2 displacements are adjusted to three coils each (see Figure 3.6). At the low temperature, the P1 region is fully compressed (as in the MM1 prediction), denoted by the open diamond symbol in Figure 7.6a. The UP region is still partially compressed in order to exert a balancing force equivalent to that required to fully compress the P1 region, denoted by the cross symbol. The P2 region is also fully compressed, as shown with the triangle symbol. Upon heating, the P1 region again recovers the same displacement that the UP region compresses. Like before, the forces exerted by the P1 region and UP region are balanced. This is denoted by the circle and diamond symbols. From this analysis, it can be seen that the MM2 design should achieve a stroke of ~2.8 mm at the intermediate temperature.

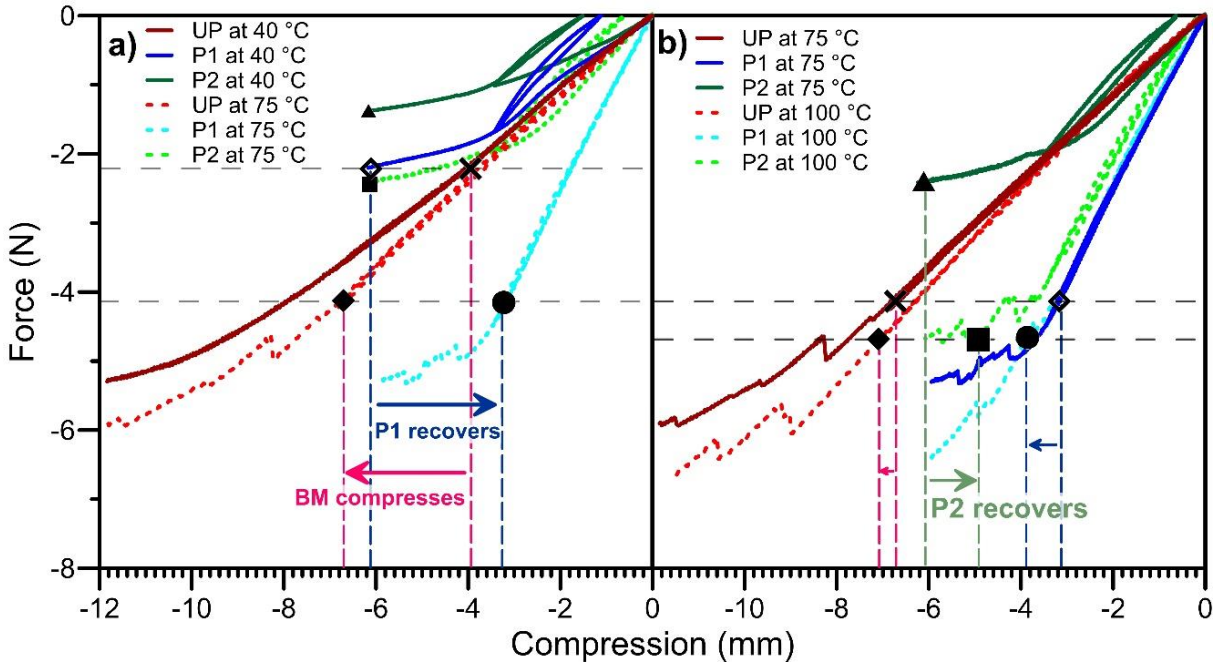

Figure 7.6. Theoretical force-deflection curves for the MM2 design used to predict the stroke for a) first actuation at 75 °C and b) second actuation at 100 °C.

Upon further heating, the P2 region must recover the same displacement (triangle to square in Figure 7.6b) that the P1 (open diamond to circle Figure 7.6b) and UP (cross to diamond in Figure 7.6b) regions are compressed, and all three regions must have balanced forces at this temperature. From this analysis, it can be seen that the MM2 design should achieve a stroke of ~1.2 mm at the P2/P1 interface at high temperature. However, the P1/BM interface only moves ~0.4 mm, due to the recompression of the P1 region. This gives a total stroke at the BM/P1 interface of 3.2 mm (2.8 mm + 0.4 mm). This is less than the total stroke of the MM1 design, but it has the increased functionality of being able to stop precisely part way through the total actuation.

Figure 7.7 shows a prototype of the MM2 spring design that has been partially compressed in the test fixture. The total length of the spring actuator was measured to be 2.4 cm. At room temperature the P1 and P2 regions of the spring are both compressed significantly more than the UP region Upon heating to the intermediate temperature (~75 °C), the interface between the P1 region and the UP region moved ~1 mm as the P1 and UP spring sections equalized forces. This is a displacement of ~4 % of the total length of the actuator. Upon further heating, the interface between the P1 and UP regions moves again by ~1.5 mm as the P2 section transforms to austenite and its stiffness increases. This is a displacement of ~6 %. The total displacement achieved from low temperature to high temperature is 10 %, with a controlled intermediate stop. This design has

a reduced total stroke compared with the MM1 design, but it is still higher than the 4-6 % achievable by linear actuators and it exhibits enhanced functionality.

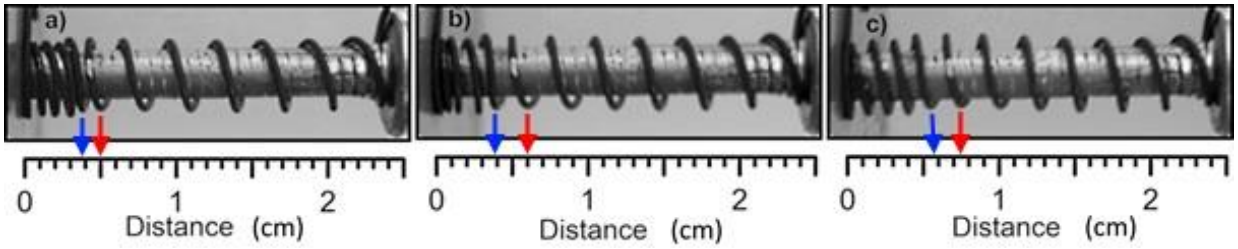

Figure 7.7. Displacement measurement set-up depicting the MM2 spring containing both BM, P1 and P2 regions at a) low temperature (≤40 °C), b) mid temperature (~75 °C) and c) high temperature (≥100 °C).

The experimental results for the prototype MM2 spring design did not agree with the theoretical stroke calculations shown in Figure 7.6. This discrepancy was because of a fabrication error in the number of active coils actually created for each region. It can be seen in Figure 7.7b that there appears to be only one active coil for the P1 region. Thus, the stroke analysis was redone using only one active coil for P1, as shown in Figure 7.8.

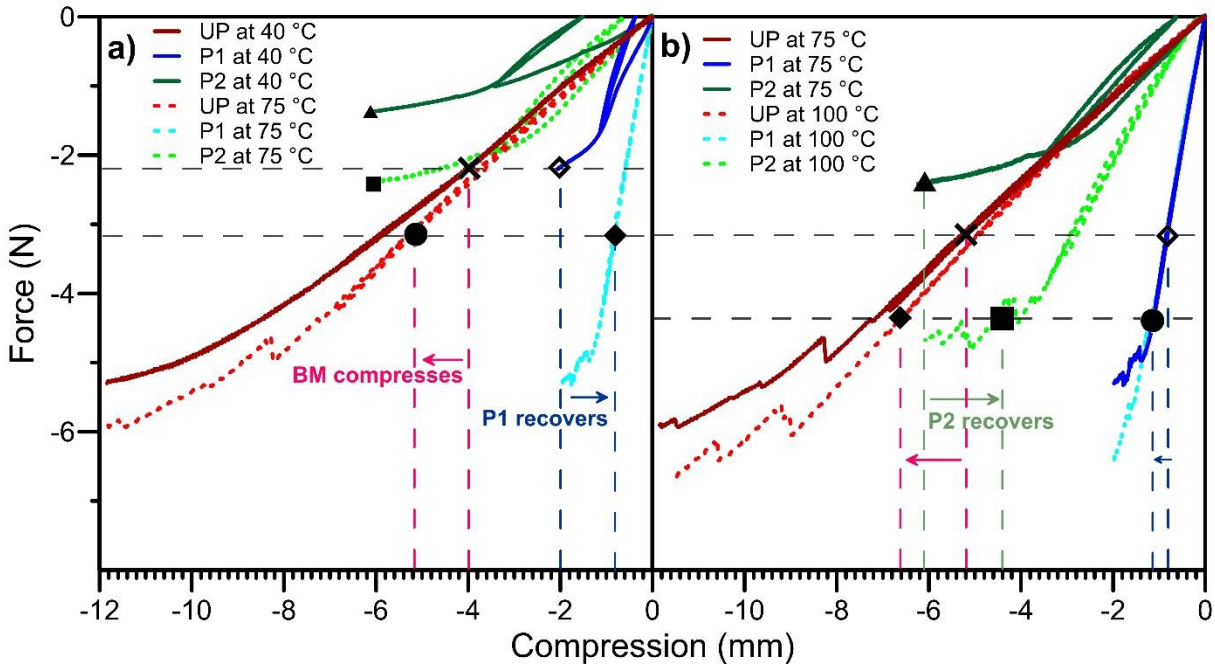

Figure 7.8. Revised theoretical force-deflection curves for the MM2 design used to calculate expected stroke for a) first actuation at 80 °C and b) second actuation at 110 °C.

It can be seen that if there is only one active coil for the P1 region, there will only be a recovery of 1.2 mm at the intermediate temperature. Additionally, it shows that the P2/P1 interface moves

1.7 mm at the high temperature, while the P1/BM interface moves only 1.4 mm due to the recompression of the P1 region. These are both in good agreement with the observed experimental strokes, and demonstrates how the ratio of active coils in each region can be used to alter the functionality of the self-biasing spring and the ability to accurately determine the stroke for any number coils.

7.3 Chapter Summary

In this chapter, design and fabrication methodologies for self-biasing springs were investigated. A rudimentary study on the effect of the final heat treatment temperature (after cold working) on the phase transformation temperature was performed. This did allow for the separation of the phase transformation temperatures for each composition while staying within the optimal heat treatment range for fatigue and actuation performance. This separation is necessary for the distinct thermal activation of each region independently from one another.

A new stroke prediction method for determining the actuation of a self-biasing spring was successfully demonstrated. Additionally, proof-of-concept self-biasing springs were successfully manufactured. A good correlation was observed between the stroke predictions and the experimental displacements. This facilitates the future designing and manufacturing of a self-biasing spring actuator with any desired stroke displacement.

Chapter 8: Conclusions and Proposed Future Research

In the current study, modeling of multiple memory SMAs was explored. Specifically, modelling of alloy element vaporization during laser processing, modelling of the one-dimensional tensile response of multiple memory SMAs, and modelling of two-dimensional torsion and bending were investigated. A fundamental understanding of the vaporization mechanism and the material properties of binary NiTi SMAs was achieved through this work. The following sections contain the major conclusions from this work and detailed recommendations for proposed future work.

8.1 Conclusions

8.1.1 Relative vaporization rates of Ni and Ti during laser processing

In this work, an in-depth investigation into the effects of laser parameters on the bulk Ni composition was performed. The use of DSC transformation temperatures allowed for quick and easy estimations of the bulk composition. The novel model developed was shown to be capable of predicting the change in the bulk Ni composition for a wide range of laser pulse profiles. The main findings were as follows:

1. The DSC analysis showed an obvious trend between laser parameters and transformation temperatures. Compositional segregation occurred on the Ti-rich side of the NiTi congruency point.
2. A new methodology was developed to deconvolve overlapping DSC transformation peaks for multi-phase NiTi. This method was validated as a means to determine the amount of each composition present in a sample that experienced compositional segregation during cooling/resolidification following a laser pulse.
3. A relationship between DSC transformation peaks and Ni composition was shown. This facilitated the use of DSC to determine Ni composition. Additionally, it was found that there are two separate vaporization mechanism that are taking place during laser processing. At low powers (conduction mode), vaporization only occurs from the surface of the melt. At high powers (keyhole mode), surface vaporization occurs in addition to

vaporization to form the keyhole. For extremely short times (≤ 3 ms), surface vaporization appears to be incomplete.

4. Models were successfully developed to predict the change in Ni composition. The diffusion of Ni through the Ti-rich surface layer was found to influence the surface vaporization. The effect of pulse duration and peak power on the keyhole growth was established. The comprehensive model was shown to successfully predict the change in Ni composition for a wide range of peak powers and pulse durations.

8.1.2 One-dimensional model for multiple memory shape memory alloys

Utilizing a novel combination of normalized transformation strain and effective elastic moduli, a one-dimensional thermodynamic model was developed for monolithic SMAs containing more than one pseudoelastic responses. In this study, material properties were determined through DSC analysis and tensile testing, demonstrating the importance of understanding the material microstructure when attempting to predict the behavior of NiTi instead of curve-fitting data. The most significant findings of this study include:

1. The use of a normalized transformation strain facilitated the expansion of the typical thermodynamic model into one capable of handling multiple pseudoelastic plateaus. For a more accurate stress/strain response in all elastic regions, an effective modulus was used to account for differing elastic responses. The model was shown to be expandable to any number of plateaus, and equally valid for only one plateau.
2. The initial tensile test method gave inaccurate data that portrayed higher transformation strains and residual strains while underestimating the elastic moduli of the materials. The improved contactless visual extensometer method gave much more accurate data with transformation strains correlating closely with those predicted from the DSC analysis. However, due to martensite suppression in the TBM material, full mechanical performance could not be predicted from DSC and required tensile testing to completely characterize the material.
3. The 1-D thermodynamic model of multiple memory SMAs was validated experimentally with custom made NiTi wires that exhibited two different pseudoelastic plateau responses. A good correlation between the model and the experimental data was found for each of the

different length ratios tested. The model was also applied to the SmartArch^{TM} orthodontic arch wires with excellent results. These findings lay the ground work for better modelling capabilities of devices that take advantage of multiple memory technologies.

8.1.3 Two-dimensional deformation of NiTi wires

For this study the 2-D deformation mechanisms were analyzed and compared for different NiTi wires. A good correlation between the texture and the bending curvature was found for all materials. The most important findings of this study were:

1. It was shown that the use of similar triangles can facilitate the prediction of the preferred bending curvature of the transformed material based on the texture and preferred martensite variants found in tension and compression. Additionally, altering the local microstructure can be used to tailor the preferred bending curvature.
2. A new method was developed to determine the maximum tensile and compressive stresses and strains during bending. This method was validated for the as-received materials through comparison with uniaxial tensile data. The microstructure of the as-processed wire most likely underwent internal grain fragmentation and reorientation and plasticity, which resulted in a larger amount of residual strain and an indeterminant maximum tensile and compressive stress.
3. The during the three-point-bend tests, the wires exhibited signs of incompressibility, which was investigated further through torsion testing. It was found that during the phase transformation the material behaves in an incompressible manner. The as-processed material underwent severe plastic deformation during torsion testing.

8.1.4 Designing a self-biasing spring actuator

Novel self-biasing spring actuators were designed, manufactured and demonstrated. Notable findings from this work were:

1. It was shown that the final heat treatment temperature has a significant impact on the phase transformation temperature. Preliminary results indicate a logistic relationship between heat treatment temperature and the phase transformation temperature. A

suitable temperature was chosen that allowed for separation of the phase transformation temperatures from one composition to another.

2. A new method for determining the stroke of a self-biasing spring actuator was developed. This method was validated for two different self-biasing spring actuator designs. Additionally, proof-of-concept self-biasing springs were successfully fabricated and a demonstrated.

8.2 Proposed Future Research

8.2.1 Laser Processing NiTi

The first part of this work was the first comprehensive look into the effect of laser parameters on the Ni vaporization rate for full penetration of NiTi wires. There is still much work to do in this area, including:

1. The effect of the initial bulk composition needs to be investigated. It has been shown that diffusion plays a role even in keyhole vaporization [126], so it is important to better understand complete role of diffusion for NiTi vaporization. Difference in the initial bulk composition will play a role in determining the diffusion rate. Additionally, the effect of surface oxide conditions on the conduction mode vaporization should be investigated. Acid etching procedures can vary [271-274] resulting in different oxide thicknesses and Ti:Ni ratios. This can also have a major effect on the rate of Ni diffusion to the surface for vaporization.
2. The effect of heat build-up in the work material during laser processing should be investigated in-depth before switching from research fabrication methods to industrial production.
    a. Extended continuous laser processing of long sample can result in excessive heat build-up, since the small cross-sectional area of thin NiTi wires limits amount of heat that can be conducted away from the melt pool [207].. This could lead to a change in the microstructure and/or the vaporization rate a long the length of the work material, resulting in undesirable material properties.
    b. The effect of pulse frequency on the heat build-up in the work material should also be investigated. Slowing done the pulse frequency may be a way to mitigate

unwanted heat build-up by allowing the material more time to cool between pulses. However, it will be natural for a manufacturing method to attempt to increase the pulse frequency to decrease the production time. However, increasing the processing speed may result in undesirable heat build-up.

   c. The effect of temperature should also be investigated. By lowering the temperature of the processing environment, it may be possible to prevent excessive heat build-up during laser processing. However, this will alter the cooling rate of the work material and thus the relative vaporization rates of Ni and Ti.

3. The effect of contaminants, both native to the material and introduced during processing, should be investigated. The amount of oxygen present (i.e. thickness of surface oxide layer) may have an effect on the surface micro-eddy formations, bulk mixing, and diffusion rates. Additionally, any oxygen (or other contaminant) introduced during the process, through either the atmosphere or fixturing, can likewise alter the relative vaporization rates by changing the melt pool mixing patterns. This can lead to homogeneity issues if the contaminants are irregularly introduced.
4. The effect of shielding gas flow needs to be investigated. IN this study it was found that in conduction mode vaporization, a saturation point was quickly reach and additional time did not increase the relative Ni loss (see Section). Flow of shielding gas across the surface of the work material could be used to precisely controlled the relative Ni loss by transporting the alloy element vapors away from the surface, alloying for more ions to be vaporized from the melt pool surface. This could result in higher nickel loss with longer pulse durations even that are dependent of shielding gas flow rate.
5. The effect of the laser beam energy density on laser processing also needs to be investigated.
   a. Increasing the spot size and reducing the energy density could help reduce the local heat build-up and allow for a larger range of conduction mode vaporization but may result in melt pools that are too large. If the melt pool grows too large, the surface tension of the molten metal may not be able to maintain wire integrity. This could result in material sagging or drop out occurring [275, 276], which is a major concern when performing full penetration laser processing of thin wires.

b. Decreasing the spot size and increasing the energy density may allow for more controllable vaporization in keyhole mode. The size of the keyhole formation is limited by the laser beam spot size [118], so smaller spot sizes could be used to vaporize smaller volumes during laser processing, refining the compositional change during keyhole vaporization. However, smaller spot sizes would require more pulses per unit length as the melt pool will not be as wide. This could result in a detrimental heat build-up during laser processing, unless the sample could be cooled while it is processed.

6. The effects of sample geometry on vaporization rates.
    a. The most obvious aspect of sample geometry is the surface curvature. The surface curvature plays a role in how much laser energy is absorbed and how much is reflected [118]. Flat sheets will absorb more energy the wires, and tubes will be somewhere in between. Therefore, surface curvature needs to be accounted for when choosing laser parameters.
    b. It is also important to remember that a thin wire has difficulty conducting heat away [207], which results in a build-up of heat during continuous pulsing. A thin sheet or thin-walled tube would be able to conduct heat away more quickly during pulsing, which may require a higher energy input to achieve similar vaporization rates since the vaporization rate is dependent on temperature [127] (see Section 2.3.5 Laser Induced Vaporization).
    c. Another aspect that needs to be considered is the surface area of the melt pool. For full penetration of NiTi wires, the surface area of the melt pool wraps around the entire circumference of the wire. For a sheet or tube, the surface area of the melt pool spreads across the top of the material and can be larger than the surface area of a thin wire. The surface area of the melt pools for a wire and a sheet are given by Equations 7.1 and 7.2, respectively:

$$A_{mp} \approx 2\pi r R_p \qquad \textbf{(Equation 8.1)}$$

$$A_{mp} = \pi {R_p}^2 \qquad \textbf{(Equation 8.2)}$$

where R_p is the radius of the melt pool and *r* is the radius of the wire. It can be seen the surface area of a wire is proportional to the melt pool radius, but for a sheet it

is proportional to the radius square. Therefore, if 2r (or the diameter of the wire) is less than R_p then the melt pool surface area of the wire will be less than on a sheet of similar thickness. The result could be an increased vaporization rate for the sheet since it is proportional to surface area [127] (see Section 2.3.5 Laser Induced Vaporization).

7. An initial study has been performed on partial penetration [22], however, a more comprehensive study is still required. The relationship between the change in Ni composition and laser parameters is more complex for partial penetration, because the melt pool volume needs to be considered. Increases in vaporization rates are counter balanced by increases in melt pool volume. Increases in time grow the melt pool faster than they increase the vaporization rate, causing a reduction in the relative Ni loss per volume [22]. Increases in power raise the vaporization rate faster than they grow the melt pool, resulting in a rise in the relative Ni loss per volume [22]. Melt pool volume was not considered for this full-penetration study that was conduction, since the pulses were consistently overlapped 60 % to ensure full and uniform compositional changes.

8.2.2 Modelling NiTi in Tension

The second part of this work was a novel model capable of predicting the tensile response of multiple memory NiTi loaded past the pseudoelastic plateaus and fully unloaded only once. Future work in this area includes improving the model to account for partial loading/unloading cycles and modelling multiple complete cycles:

1. Partial loading and unloading is an important dynamic that must be implemented into the novel model for multiple memory materials so that use of this material can be expanded to actuation applications. It has already been shown that Preisach models can effectively predict partial loading and unloading of NiTi pseudoelastic plateaus [192-194] and that they can be combined with thermodynamic models for NiTi phase transformation [194]. The obvious next step is to integrate a Preisach model into the multiple memory pseudoelastic model to allow for loading to any point in any plateau and partial unloading to any point in any plateau (not necessarily the same plateau), as depicted in Figure 8.1.

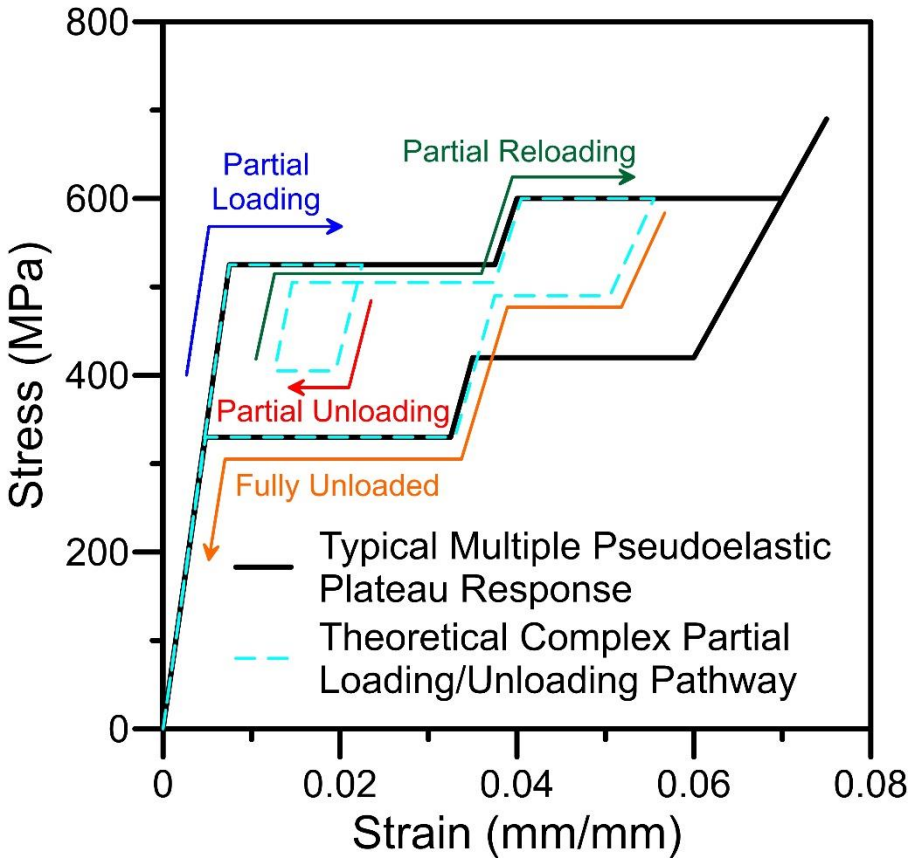

Figure 8.1. Schematic showing various partial loading/unloading conditions for a multiple memory SMA.

2. The wires modeled in this study did not undergo any thermomechanical training, which is typical for commercially available wires. These stabilization techniques involve partial loading and complete unloading of the material at a specific temperature in order to stabilize the mechanical response of the material [277, 278]. These methods have only been established for single plateau materials and have never been applied to multiple memory material. Additionally, the evolution of the pseudoelastic hysteresis during training needs to be developed to facilitate precise actuator design and implementation.

8.2.3 Modelling Complex Deformation

The third part of this work involved a novel model capable of predicting the bending shape of laser processed NiTi and the design of a self-biasing multiple memory NiTi spring. Future work in these areas include improving the understanding of microstructural evolution during bending and torqueing of as-processed NiTi wires and partial loading/unloading cycles, and improving the understanding of the incompressible nature of the austenite to R-phase transformation:

1. To better predict the bending properties of as-processed NiTi wires, microstructural analysis of GR samples before and after bending should be performed. This analysis would shed light on the microstructural changes that occur during the bending process and allow for insights into how the material is accommodating the strain.
2. It was observed that as-processed NiTi wires experienced severe plasticity during torsion testing. This does not bode well for using as-processed wires in applications where a torque will be applied (such as laser processed square orthodontic arch wires). An investigation into torsional training of as-processed wires should be conducted. By cyclically torqueing the wires it may be possible to create a more stable microstructure capable of pseudoelastic recovery without having to wire draw the material.
3. The incompressible nature of the austenite to R-phase transformation poses difficulties in properly modelling complex deformation mechanisms. Some work has already been done in the modelling of this transformation [246, 279-281]. However, that work primarily looked at tension and anisotropy associated with torsion but did not include look closely at the incompressible behavior of mixed austenite/R-phase during bending or compression. More extensive work is still needed in this area.

8.2.4 Designing a Self-Biasing Spring Actuator

The final part of this work involved designing and manufacturing a proof-of-concept self-biasing actuator. Future work in this area includes determining the long-term performance of the self-biasing mechanism and investigating the possibility of increasing the number of imbedded active memories:

1. Work needs to be done to determine if it is possible to create a three-stage self-biasing spring actuator. More specifically, it should investigate the combinations of compositions and heat treatments that can produce four distinct regions that do not overlap their austenite phase transformation temperature with one another and maintain good mechanical properties. Such an actuator would be capable of providing even further functionality over the currently developed NiTi actuators.
2. An improvement to the stroke predictions needs to be done to account for the self-biasing spring acting on another object. Currently, the method is simplified and only accounts for the force of each spring region acting on one another. However, if the actuator were to

move some object from one position to another, then the force balance must account for this.

3. As was mentioned earlier, it is necessary for NiTi linear actuators to undergo thermomechanical training to stabilize the functional properties (see Section 8.2.2 Modelling NiTi in Tension). A stabilization technique has previously been developed for a self-biasing linear actuator [207]. A similar method needs to be developed and applied to the self-biasing spring actuators before they can be used in real applications.

Chapter 9: Contributions to Research and Development

9.1 Articles published and in-press in refereed journals

1. **A. Michael**, Y.N. Zhou, M.I. Khan, Novel method to analyze tensile properties of ultra-fine NiTi wires with a visual extensometer, Materials Letters, 182 (2016) 177-180.
2. **A. Michael**, Y. Zhou, M.I. Khan, Experimental Validation of a One-Dimensional Model for Monolithic Shape Memory Alloys with Multiple Pseudoelastic Plateaus, Journal of Intelligent Systems and Structures, 27 (2016) 2102-2111.

9.2 Articles under review

1. **A. Michael**, Y.N. Zhou, M. Yavuz, M.I. Khan, Modelling the Alloy Element Composition Change in NiTi achieved through Laser Induced Vaporization, Metallurgical and Materials Transactions B (currently under review).
2. **A. Michael**, Y.N. Zhou, M. Yavuz, M.I. Khan, Deconvolution of Overlapping Peaks from Differential Scanning Calorimetry Analysis for Multi-phase NiTi Alloys, Thermochimica Act, (accepted with minor revisions).

9.3 Conference papers and presentations

1. N. Zhou*, **A. Michael**, M.I. Khan, Technology Innovation Built around Vaporization in Laser Welding of NiTi Alloys, American Welding Society Honorary Symposia for Dr. S. David and Prof. T. DebRoy, Chicago, Illinois, November 2017.

2. **A. Michael***, Y.N. Zhou, M. Yavuz, M.I. Khan, Understanding and Modelling Localized Phase Transformation during 2D Bending of NiTi Wires, 14th International Forum of Beihang University for Graduate Students on Micro/Nano Manufacturing Technology, Beihang University (BUAA), Beijing, China, July 2017.

3. **A. Michael***, Y.N. Zhou, M.I. Khan, Precise Control of Pseudoelastic Properties in NiTi, International Conference on Nanojoining and Microjoining 2016 (NMJ2016), Niagara Falls, Ontario, October 2016.

4. **A. Michael***, Y.N. Zhou, M.I. Khan, Modelling of Multiple Memory Pseudoelastic Plateaus in NiTi, International Conference on Nanojoining and Microjoining 2016 (NMJ2016), Niagara Falls, Ontario, October 2016.

Letter of Copyright Permission

The copyright permissions have been obtained for the following figures embedded within this thesis:

- Figure 2.1
- Figure 2.2
- Figure 2.4
- Figure 2.5
- Figure 2.7
- Figure 2.8
- Figure 2.9
- Figure 2.10
- Figure 2.11
- Figure 2.12
- Figure 2.14
- Figure 2.16
- Figure 2.17
- Figure 2.18
- Figure 2.19
- Figure 2.20
- Figure 2.22
- Figure 2.23
- Figure 2.24
- Figure 2.25
- Figure 2.26
- Figure 2.27

The copyright permissions have been obtained for the following chapters of this thesis:

A portion of Chapter 5 has been published by Sage Publishing and as stated by the journal policy, the published paper can be used in this thesis without requesting permission. DOI:

ELSEVIER LICENSE
TERMS AND CONDITIONS
Feb 24, 2018
This Agreement between Mr. Andrew Michael ("You") and Elsevier ("Elsevier") consists of your license details and the terms and conditions provided by Elsevier and Copyright Clearance Center.
License Number 4295450463885
License date Feb 24, 2018
Licensed Content Publisher Elsevier
Licensed Content Publication Progress in Materials Science
Licensed Content Title Physical metallurgy of Ti–Ni-based shape memory alloys
Licensed Content Author K. Otsuka,X. Ren
Licensed Content Date Jul 1, 2005
Licensed Content Volume 50
Licensed Content Issue 5
Licensed Content Pages 168
Start Page 511
End Page 678
Type of Use reuse in a thesis/dissertation
Portion figures/tables/illustrations
Number of figures/tables/illustrations 1
Format both print and electronic
Are you the author of this Elsevier article? No
Will you be translating? No
Original figure numbers Figure 2
Title of your thesis/dissertation Laser Processing and Modelling of Multiple Memory Shape Memory Alloys
Expected completion date Apr 2018
Estimated size (number of pages) 200
Requestor Location Mr. Andrew Michael
256 Louisa St
Kitchener, ON N2H5M9
Canada
Attn: Mr. Andrew Michael
Publisher Tax ID GB 494 6272 12
Total 0.00 USD

INTRODUCTION
1. The publisher for this copyrighted material is Elsevier. By clicking "accept" in connection with completing this licensing transaction, you agree that the following terms and conditions apply to this transaction (along with the Billing and Payment terms and conditions established by Copyright Clearance Center, Inc. ("CCC"), at the time that you opened your Rightslink account and that are available at any time at http://myaccount.copyright.com).
GENERAL TERMS
2. Elsevier hereby grants you permission to reproduce the aforementioned material subject to the terms and conditions indicated.
3. Acknowledgement: If any part of the material to be used (for example, figures) has appeared in our publication with credit or acknowledgement to another source, permission must also be sought from that source. If such permission is not obtained then that material may not be included in your publication/copies. Suitable acknowledgement to the source must be made, either as a footnote or in a reference list at the end of your publication, as follows:
"Reprinted from Publication title, Vol /edition number, Author(s), Title of article / title of chapter, Pages No., Copyright (Year), with permission from Elsevier [OR APPLICABLE SOCIETY COPYRIGHT OWNER]." Also Lancet special credit - "Reprinted from The Lancet, Vol. number, Author(s), Title of article, Pages No., Copyright (Year), with permission from Elsevier."
4. Reproduction of this material is confined to the purpose and/or media for which permission is hereby given.

5. Altering/Modifying Material: Not Permitted. However figures and illustrations may be altered/adapted minimally to serve your work. Any other abbreviations, additions, deletions and/or any other alterations shall be made only with prior written authorization of Elsevier Ltd. (Please contact Elsevier at permissions@elsevier.com). No modifications can be made to any Lancet figures/tables and they must be reproduced in full.
6. If the permission fee for the requested use of our material is waived in this instance, please be advised that your future requests for Elsevier materials may attract a fee.
7. Reservation of Rights: Publisher reserves all rights not specifically granted in the combination of (i) the license details provided by you and accepted in the course of this licensing transaction, (ii) these terms and conditions and (iii) CCC's Billing and Payment terms and conditions.
8. License Contingent Upon Payment: While you may exercise the rights licensed immediately upon issuance of the license at the end of the licensing process for the transaction, provided that you have disclosed complete and accurate details of your proposed use, no license is finally effective unless and until full payment is received from you (either by publisher or by CCC) as provided in CCC's Billing and Payment terms and conditions. If full payment is not received on a timely basis, then any license preliminarily granted shall be deemed automatically revoked and shall be void as if never granted. Further, in the event that you breach any of these terms and conditions or any of CCC's Billing and Payment terms and conditions, the license is automatically revoked and shall be void as if never granted. Use of materials as described in a revoked license, as well as any use of the materials beyond the scope of an unrevoked license, may constitute copyright infringement and publisher reserves the right to take any and all action to protect its copyright in the materials.
9. Warranties: Publisher makes no representations or warranties with respect to the licensed material.
10. Indemnity: You hereby indemnify and agree to hold harmless publisher and CCC, and their respective officers, directors, employees and agents, from and against any and all claims arising out of your use of the licensed material other than as specifically authorized pursuant to this license.
11. No Transfer of License: This license is personal to you and may not be sublicensed, assigned, or transferred by you to any other person without publisher's written permission.
12. No Amendment Except in Writing: This license may not be amended except in a writing signed by both parties (or, in the case of publisher, by CCC on publisher's behalf).
13. Objection to Contrary Terms: Publisher hereby objects to any terms contained in any purchase order, acknowledgment, check endorsement or other writing prepared by you, which terms are inconsistent with these terms and conditions or CCC's Billing and Payment terms and conditions. These terms and conditions, together with CCC's Billing and Payment terms and conditions (which are incorporated herein), comprise the entire agreement between you and publisher (and CCC) concerning this licensing transaction. In the event of any conflict between your obligations established by these terms and conditions and those established by CCC's Billing and Payment terms and conditions, these terms and conditions shall control.
14. Revocation: Elsevier or Copyright Clearance Center may deny the permissions described in this License at their sole discretion, for any reason or no reason, with a full refund payable to you. Notice of such denial will be made using the contact information provided by you. Failure to receive such notice will not alter or invalidate the denial. In no event will Elsevier or Copyright Clearance Center be responsible or liable for any costs, expenses or damage incurred by you as a result of a denial of your permission request, other than a refund of the amount(s) paid by you to Elsevier and/or Copyright Clearance Center for denied permissions.

Brief Overview on Nitinol as Biomaterial
Abdul Wadood
Received 5 September 2016; Accepted 10 October 2016
Academic Editor: Patrice Berthod

SPRINGER NATURE LICENSE
TERMS AND CONDITIONS
Feb 23, 2018
This Agreement between Mr. Andrew Michael ("You") and Springer Nature ("Springer

Nature") consists of your license details and the terms and conditions provided by Springer Nature and Copyright Clearance Center.
License Number 4294931412576
License date Feb 23, 2018
Licensed Content Publisher Springer Nature
Licensed Content Publication Experimental Techniques
Licensed Content Title Tips and tricks for characterizing shape memory alloy wire: Part 1—differential scanning calorimetry and basic phenomena
Licensed Content Author J. A. Shaw, C. B. Churchill, M. A. Iadicola
Licensed Content Date Jan 1, 2008
Licensed Content Volume 32
Licensed Content Issue 5
Type of Use Thesis/Dissertation
Requestor type academic/university or research institute
Format print and electronic
Portion figures/tables/illustrations
Number of figures/tables/illustrations 1
Will you be translating? no
Circulation/distribution <501
Author of this Springer Nature content no
Title Laser Processing and Modelling of Multiple Memory Shape Memory Alloys
Instructor name n/a
Institution name n/a
Expected presentation date Apr 2018
Portions Figure 2
Requestor Location Mr. Andrew Michael
256 Louisa St
Kitchener, ON N2H5M9
Canada
Attn: Mr. Andrew Michael
Billing Type Invoice
Billing Address Mr. Andrew Michael
256 Louisa St
Kitchener, ON N2H5M9
Canada
Attn: Mr. Andrew Michael
Total 0.00 USD

Terms and Conditions

Springer Nature Terms and Conditions for RightsLink Permissions Springer Customer Service Centre GmbH (the Licensor) hereby grants you a nonexclusive, world-wide licence to reproduce the material and for the purpose and requirements specified in the attached copy of your order form, and for no other use, subject to the conditions below:
1.
The Licensor warrants that it has, to the best of its knowledge, the rights to license reuse of this material. However, you should ensure that the material you are requesting is original to the Licensor and does not carry the copyright of another entity (as credited in the published version).
If the credit line on any part of the material you have requested indicates that it was reprinted or adapted with permission from another source, then you should also seek permission from that source to reuse the material.
2.
Where print only permission has been granted for a fee, separate permission must be obtained for any additional electronic re-use.
3.
Permission granted free of charge for material in print is also usually granted for any electronic version of that work, provided that the material is incidental to your work as a whole and that the electronic version is essentially equivalent to, or substitutes for, the print version.

4.
A licence for 'post on a website' is valid for 12 months from the licence date. This licence does not cover use of full text articles on websites.
5.
Where 'reuse in a dissertation/thesis' has been selected the following terms apply: Print rights for up to 100 copies, electronic rights for use only on a personal website or institutional repository as defined by the Sherpa guideline (www.sherpa.ac.uk/romeo/).
6.
Permission granted for books and journals is granted for the lifetime of the first edition and does not apply to second and subsequent editions (except where the first edition permission was granted free of charge or for signatories to the STM Permissions Guidelines http://www.stm-assoc.org/copyright-legal-affairs/permissions/permissions-guidelines/) and does not apply for editions in other languages unless additional translation rights have been granted separately in the licence.
7.
Rights for additional components such as custom editions and derivatives require additional permission and may be subject to an additional fee. Please apply to Journalpermissions@springernature.com/bookpermissions@springernature.com for these rights.
8.
The Licensor's permission must be acknowledged next to the licensed material in print. In electronic form, this acknowledgement must be visible at the same time as the figures/tables/illustrations or abstract, and must be hyperlinked to the journal/book's homepage. Our required acknowledgement format is in the Appendix below.
9.
Use of the material for incidental promotional use, minor editing privileges (this does not include cropping, adapting, omitting material or any other changes that affect the meaning, RightsLink Printable License https://s100.copyright.com/App/PrintableLicenseFrame.jsp?publisherID... intention or moral rights of the author) and copies for the disabled are permitted under this licence.
10.
Minor adaptations of single figures (changes of format, colour and style) do not require the Licensor's approval. However, the adaptation should be credited as shown in Appendix below.

Appendix — Acknowledgements:

For Journal Content:

Reprinted by permission from [the Licensor]: [Journal Publisher (e.g. Nature/Springer/Palgrave)] [JOURNAL NAME] [REFERENCE CITATION (Article name, Author(s) Name), [COPYRIGHT] (year of publication)

For Advance Online Publication papers:

Reprinted by permission from [the Licensor]: [Journal Publisher (e.g. Nature/Springer/Palgrave)] [JOURNAL NAME] [REFERENCE CITATION (Article name, Author(s) Name), [COPYRIGHT] (year of publication), advance online publication, day month year (doi: 10.1038/sj.[JOURNAL ACRONYM].)

For Adaptations/Translations:

Adapted/Translated by permission from [the Licensor]: [Journal Publisher (e.g. Nature/Springer/Palgrave)] [JOURNAL NAME] [REFERENCE CITATION (Article name, Author(s) Name), [COPYRIGHT] (year of publication)

Note: For any republication from the British Journal of Cancer, the following credit line style applies:

Reprinted/adapted/translated by permission from [the Licensor]: on behalf of Cancer Research UK: : [Journal Publisher (e.g. Nature/Springer/Palgrave)] [JOURNAL NAME] [REFERENCE CITATION (Article name, Author(s) Name), [COPYRIGHT] (year of publication)

For Advance Online Publication papers:

Reprinted by permission from The [the Licensor]: on behalf of Cancer Research UK: [Journal Publisher (e.g. Nature/Springer/Palgrave)] [JOURNAL NAME] [REFERENCE CITATION (Article name, Author(s) Name), [COPYRIGHT] (year of publication), advance online publication, day month year (doi: 10.1038/sj.[JOURNAL ACRONYM])

For Book content:

Reprinted/adapted by permission from [the Licensor]: [Book Publisher (e.g. Palgrave Macmillan, Springer etc) [Book Title] by [Book author(s)] [COPYRIGHT] (year of publication)

ELSEVIER LICENSE
TERMS AND CONDITIONS
Feb 23, 2018
This Agreement between Mr. Andrew Michael ("You") and Elsevier ("Elsevier") consists of your license details and the terms and conditions provided by Elsevier and Copyright Clearance Center.
License Number 4294921041948
License date Feb 23, 2018
Licensed Content Publisher Elsevier
Licensed Content Publication Scripta Metallurgica
Licensed Content Title Transformation pseudoelasticity and deformation behavior in a Ti-50.6at%Ni alloy
Licensed Content Author S. Miyazaki,K. Otsuka,Y. Suzuki
Licensed Content Date Mar 1, 1981
Licensed Content Volume 15
Licensed Content Issue 3
Licensed Content Pages 6
Start Page 287
End Page 292
Type of Use reuse in a thesis/dissertation
Intended publisher of new work other
Portion figures/tables/illustrations
Number of figures/tables/illustrations 1
Format both print and electronic
Are you the author of this Elsevier article? No
Will you be translating? No
Original figure numbers Figure 2
Title of your thesis/dissertation Laser Processing and Modelling of Multiple Memory Shape Memory Alloys
Expected completion date Apr 2018
Estimated size (number of pages) 200
Requestor Location Mr. Andrew Michael
256 Louisa St
Kitchener, ON N2H5M9
Canada
Attn: Mr. Andrew Michael
Publisher Tax ID GB 494 6272 12
Total 0.00 USD

Title: Pseudoelasticity and shape memory effects in alloys
Author: K. Otsuka, K. Shimizu
Publication: International Materials Reviews
Publisher: Taylor & Francis
Date: Jan 1, 1986
Rights managed by Taylor & Francis
Logged in as:
Andrew Michael
Thesis/Dissertation Reuse Request
Taylor & Francis is pleased to offer reuses of its content for a thesis or dissertation free of charge contingent on resubmission of permission request if work is published.

SPRINGER NATURE LICENSE
TERMS AND CONDITIONS
Feb 23, 2018
This Agreement between Mr. Andrew Michael ("You") and Springer Nature ("Springer Nature") consists of your license details and the terms and conditions provided by Springer

Nature and Copyright Clearance Center.
License Number 4294940237435
License date Feb 23, 2018
Licensed Content Publisher Springer Nature
Licensed Content Publication Metallurgical and Materials Transactions A
Licensed Content Title Thermodynamic study of the low-temperature phase B19′ and the martensitic transformation in near-equiatomic Ti-Ni shape memory alloys
Licensed Content Author Weijia Tang
Licensed Content Date Jan 1, 1997
Licensed Content Volume 28
Licensed Content Issue 3
Type of Use Thesis/Dissertation
Requestor type academic/university or research institute
Format print and electronic
Portion figures/tables/illustrations
Number of figures/tables/illustrations 1
Will you be translating? no
Circulation/distribution <501
Author of this Springer Nature content no
Title Laser Processing and Modelling of Multiple Memory Shape Memory Alloys
Instructor name n/a
Institution name n/a
Expected presentation date Apr 2018
Portions Figure 5
Requestor Location Mr. Andrew Michael
256 Louisa St
Kitchener, ON N2H5M9
Canada
Attn: Mr. Andrew Michael
Billing Type Invoice
Billing Address Mr. Andrew Michael
256 Louisa St
Kitchener, ON N2H5M9
Canada
Attn: Mr. Andrew Michael
Total 0.00 USD

Title: Optimisation of processing and properties of medical grade Nitinol wire
Author: A. R. Pelton, J. Dicello, S. Miyazaki
Publication: Minimally Invasive Therapy & Allied Technologies
Publisher: Taylor & Francis
Date: Jan 1, 2000
Rights managed by Taylor & Francis
Logged in as:
Andrew Michael
Thesis/Dissertation Reuse Request
Taylor & Francis is pleased to offer reuses of its content for a thesis or dissertation free of charge contingent on resubmission of permission request if work is published.

ELSEVIER LICENSE
TERMS AND CONDITIONS
Feb 23, 2018
This Agreement between Mr. Andrew Michael ("You") and Elsevier ("Elsevier") consists of your license details and the terms and conditions provided by Elsevier and Copyright Clearance Center.

License Number 4294920806524
License date Feb 23, 2018
Licensed Content Publisher Elsevier
Licensed Content Publication Scripta Metallurgica
Licensed Content Title Deformation behavior of shape memory Ti Ni alloy crystals
Licensed Content Author T. Saburi,M. Yoshida,S. Nenno
Licensed Content Date Apr 1, 1984
Licensed Content Volume 18
Licensed Content Issue 4
Licensed Content Pages 4
Start Page 363
End Page 366
Type of Use reuse in a thesis/dissertation
Intended publisher of new work other
Portion figures/tables/illustrations
Number of figures/tables/illustrations 1
Format both print and electronic
Are you the author of this Elsevier article? No
Will you be translating? No
Original figure numbers Figure 3
Title of your thesis/dissertation Laser Processing and Modelling of Multiple Memory Shape Memory Alloys
Expected completion date Apr 2018
Estimated size (number of pages) 200
Requestor Location Mr. Andrew Michael
256 Louisa St
Kitchener, ON N2H5M9
Canada
Attn: Mr. Andrew Michael
Publisher Tax ID GB 494 6272 12
Total 0.00 USD

ELSEVIER LICENSE
TERMS AND CONDITIONS
Feb 23, 2018
This Agreement between Mr. Andrew Michael ("You") and Elsevier ("Elsevier") consists of
your license details and the terms and conditions provided by Elsevier and Copyright
Clearance Center.
License Number 4294920560586
License date Feb 23, 2018
Licensed Content Publisher Elsevier
Licensed Content Publication Acta Materialia
Licensed Content Title Tension–compression asymmetry of the stress–strain response in aged single crystal and polycrystalline NiTi
Licensed Content Author K. Gall,H. Sehitoglu,Y.I. Chumlyakov,I.V. Kireeva
Licensed Content Date Mar 10, 1999
Licensed Content Volume 47
Licensed Content Issue 4
Licensed Content Pages 15
Start Page 1203
End Page 1217
Type of Use reuse in a thesis/dissertation
Intended publisher of new work other
Portion figures/tables/illustrations
Number of figures/tables/illustrations 1
Format both print and electronic
Are you the author of this Elsevier article? No

Will you be translating? No
Original figure numbers Figure 4
Title of your thesis/dissertation Laser Processing and Modelling of Multiple Memory Shape Memory Alloys
Expected completion date Apr 2018
Estimated size (number of pages) 200
Requestor Location Mr. Andrew Michael
256 Louisa St
Kitchener, ON N2H5M9
Canada
Attn: Mr. Andrew Michael
Publisher Tax ID GB 494 6272 12
Total 0.00 USD

SPRINGER NATURE LICENSE
TERMS AND CONDITIONS
Feb 23, 2018
This Agreement between Mr. Andrew Michael ("You") and Springer Nature ("Springer Nature") consists of your license details and the terms and conditions provided by Springer Nature and Copyright Clearance Center.
License Number 4294940723168
License date Feb 23, 2018
Licensed Content Publisher Springer Nature
Licensed Content Publication Metallurgical and Materials Transactions B
Licensed Content Title Alloy element vaporization and weld pool temperature during laser welding of AISI 202 stainless steel
Licensed Content Author P.A.A. Khan, T. Debroy
Licensed Content Date Dec 1, 1984
Licensed Content Volume 15
Licensed Content Issue 4
Type of Use Thesis/Dissertation
Requestor type academic/university or research institute
Format print and electronic
Portion figures/tables/illustrations
Number of figures/tables/illustrations 2
Will you be translating? no
Circulation/distribution <501
Author of this Springer Nature content no
Title Laser Processing and Modelling of Multiple Memory Shape Memory Alloys
Instructor name n/a
Institution name n/a
Expected presentation date Apr 2018
Portions Figure 2, Figure 3
Requestor Location Mr. Andrew Michael
256 Louisa St
Kitchener, ON N2H5M9
Canada
Attn: Mr. Andrew Michael
Billing Type Invoice
RightsLink Printable License https://s100.copyright.com/App/PrintableLicenseFrame.jsp?publisherID...
1 of 4 2/23/2018, 3:32 PM
Billing Address Mr. Andrew Michael
256 Louisa St
Kitchener, ON N2H5M9
Canada

Attn: Mr. Andrew Michael
Total 0.00 USD

SPRINGER NATURE LICENSE
TERMS AND CONDITIONS
Feb 23, 2018
This Agreement between Mr. Andrew Michael ("You") and Springer Nature ("Springer Nature") consists of your license details and the terms and conditions provided by Springer Nature and Copyright Clearance Center.
License Number 4294940649812
License date Feb 23, 2018
Licensed Content Publisher Springer Nature
Licensed Content Publication Metallurgical and Materials Transactions B
Licensed Content Title Effects of oxygen and sulfur on alloying element vaporization rates during laser welding
Licensed Content Author P. Sahoo, M. M. Collur, T. Debroy
Licensed Content Date Dec 1, 1988
Licensed Content Volume 19
Licensed Content Issue 6
Type of Use Thesis/Dissertation
Requestor type academic/university or research institute
Format print and electronic
Portion figures/tables/illustrations
Number of figures/tables/illustrations 1
Will you be translating? no
Circulation/distribution <501
Author of this Springer Nature content no
Title Laser Processing and Modelling of Multiple Memory Shape Memory Alloys
Instructor name n/a
Institution name n/a
Expected presentation date Apr 2018
Portions Figure 6
Requestor Location Mr. Andrew Michael
256 Louisa St
Kitchener, ON N2H5M9
Canada
Attn: Mr. Andrew Michael
Billing Type Invoice
RightsLink Printable License https://s100.copyright.com/App/PrintableLicenseFrame.jsp?publisherID...
1 of 4 2/23/2018, 3:32 PM
Billing Address Mr. Andrew Michael
256 Louisa St
Kitchener, ON N2H5M9
Canada
Attn: Mr. Andrew Michael
Total 0.00 USD

SPRINGER NATURE LICENSE
TERMS AND CONDITIONS
Feb 23, 2018
This Agreement between Mr. Andrew Michael ("You") and Springer Nature ("Springer Nature") consists of your license details and the terms and conditions provided by Springer Nature and Copyright Clearance Center.
License Number 4294940696247
License date Feb 23, 2018

Licensed Content Publisher Springer Nature
Licensed Content Publication Metallurgical and Materials Transactions B
Licensed Content Title Mechanism of alloying element vaporization during laser welding
Licensed Content Author M. M. Collur, A. Paul, T. Debroy
Licensed Content Date Dec 1, 1987
Licensed Content Volume 18
Licensed Content Issue 4
Type of Use Thesis/Dissertation
Requestor type academic/university or research institute
Format print and electronic
Portion figures/tables/illustrations
Number of figures/tables/illustrations 1
Will you be translating? no
Circulation/distribution <501
Author of this Springer Nature content no
Title Laser Processing and Modelling of Multiple Memory Shape Memory Alloys
Instructor name n/a
Institution name n/a
Expected presentation date Apr 2018
Portions Figure 10
Requestor Location Mr. Andrew Michael
256 Louisa St
Kitchener, ON N2H5M9
Canada
Attn: Mr. Andrew Michael
Billing Type Invoice
RightsLink Printable License https://s100.copyright.com/App/PrintableLicenseFrame.jsp?publisherID...
1 of 4 2/23/2018, 3:32 PM
Billing Address Mr. Andrew Michael
256 Louisa St
Kitchener, ON N2H5M9
Canada
Attn: Mr. Andrew Michael
Total 0.00 USD

JOHN WILEY AND SONS LICENSE
TERMS AND CONDITIONS
Feb 23, 2018
This Agreement between Mr. Andrew Michael ("You") and John Wiley and Sons ("John Wiley and Sons") consists of your license details and the terms and conditions provided by John Wiley and Sons and Copyright Clearance Center.
License Number 4294941377192
License date Feb 23, 2018
Licensed Content Publisher John Wiley and Sons
Licensed Content Publication Advanced Engineering Materials
Licensed Content Title Multiple Memory Shape Memory Alloys
Licensed Content Author Mohammad Ibraheem Khan,Andrew Pequegnat,Y. Norman Zhou
Licensed Content Date Feb 15, 2013
Licensed Content Pages 8
Type of use Dissertation/Thesis
Requestor type University/Academic
Format Print and electronic
Portion Figure/table
Number of figures/tables 1

Original Wiley figure/table number(s) Figure 2
Will you be translating? No
Title of your thesis /dissertation Laser Processing and Modelling of Multiple Memory Shape Memory Alloys
Expected completion date Apr 2018
Expected size (number of pages) 200
Requestor Location Mr. Andrew Michael
256 Louisa St
Kitchener, ON N2H5M9
Canada
Attn: Mr. Andrew Michael
Publisher Tax ID EU826007151
Total 0.00 USD

Terms and Conditions

TERMS AND CONDITIONS

This copyrighted material is owned by or exclusively licensed to John Wiley & Sons, Inc. or one of its group companies (each a"Wiley Company") or handled on behalf of a society with which a Wiley Company has exclusive publishing rights in relation to a particular work (collectively "WILEY"). By clicking "accept" in connection with completing this licensing transaction, you agree that the following terms and conditions apply to this transaction (along with the billing and payment terms and conditions established by the Copyright Clearance Center Inc., ("CCC's Billing and Payment terms and conditions"), at the time that you opened your RightsLink account (these are available at any time at http://myaccount.copyright.com).

Terms and Conditions

- The materials you have requested permission to reproduce or reuse (the "Wiley Materials") are protected by copyright.
- You are hereby granted a personal, non-exclusive, non-sub licensable (on a standalone basis), non-transferable, worldwide, limited license to reproduce the Wiley Materials for the purpose specified in the licensing process. This license, and any CONTENT (PDF or image file) purchased as part of your order, is for a one-time use only and limited to any maximum distribution number specified in the license. The first instance of republication or reuse granted by this license must be completed within two years of the date of the grant of this license (although copies prepared before the end date may be distributed thereafter). The Wiley Materials shall not be used in any other manner or for any other purpose, beyond what is granted in the license. Permission is granted subject to an appropriate acknowledgement given to the author, title of the material/book/journal and the publisher. You shall also duplicate the copyright notice that appears in the Wiley publication in your use of the Wiley Material. Permission is also granted on the understanding that nowhere in the text is a previously published source acknowledged for all or part of this Wiley Material. Any third party content is expressly excluded from this permission.
- With respect to the Wiley Materials, all rights are reserved. Except as expressly granted by the terms of the license, no part of the Wiley Materials may be copied, modified, adapted (except for minor reformatting required by the new Publication), translated, reproduced, transferred or distributed, in any form or by any means, and no derivative works may be made based on the Wiley Materials without the prior permission of the respective copyright owner.For STM Signatory Publishers clearing permission under the terms of the STM Permissions Guidelines only, the terms of the license are extended to include subsequent editions and for editions in other languages, provided such editions are for the work as a whole in situ and does not involve the separate exploitation of the permitted figures or extracts, You may not alter, remove or suppress in any manner any copyright, trademark or other notices displayed by the Wiley Materials. You may not license, rent, sell, loan, lease, pledge, offer as security, transfer or assign the Wiley Materials on a stand-alone basis, or any of the rights granted to you hereunder to any other person.
- The Wiley Materials and all of the intellectual property rights therein shall at all times remain the exclusive property of John Wiley & Sons Inc, the Wiley Companies, or their respective licensors, and your interest therein is only that of having possession of and the right to reproduce the Wiley Materials pursuant to Section 2 herein during the continuance of this Agreement. You agree that you own no right, title or interest in or to the Wiley Materials or any of the intellectual property rights therein. You shall have no rights hereunder other than the license as provided for above in Section 2. No right, license or interest to any trademark, trade name, service mark or other branding ("Marks") of WILEY or its licensors is granted hereunder, and you agree that you shall not assert any such right, license or interest with respect thereto

- NEITHER WILEY NOR ITS LICENSORS MAKES ANY WARRANTY OR REPRESENTATION OF ANY KIND TO YOU OR ANY THIRD PARTY, EXPRESS, IMPLIED OR STATUTORY, WITH RESPECT TO THE MATERIALS OR THE ACCURACY OF ANY INFORMATION CONTAINED IN THE MATERIALS, INCLUDING, WITHOUT LIMITATION, ANY IMPLIED WARRANTY OF MERCHANTABILITY, ACCURACY, SATISFACTORY QUALITY, FITNESS FOR A PARTICULAR PURPOSE, USABILITY, INTEGRATION OR NON-INFRINGEMENT AND ALL SUCH WARRANTIES ARE HEREBY EXCLUDED BY WILEY AND ITS LICENSORS AND WAIVED BY YOU.
- WILEY shall have the right to terminate this Agreement immediately upon breach of this Agreement by you.
- You shall indemnify, defend and hold harmless WILEY, its Licensors and their respective directors, officers, agents and employees, from and against any actual or threatened claims, demands, causes of action or proceedings arising from any breach of this Agreement by you.
- IN NO EVENT SHALL WILEY OR ITS LICENSORS BE LIABLE TO YOU OR ANY OTHER PARTY OR ANY OTHER PERSON OR ENTITY FOR ANY SPECIAL, CONSEQUENTIAL, INCIDENTAL, INDIRECT, EXEMPLARY OR PUNITIVE DAMAGES, HOWEVER CAUSED, ARISING OUT OF OR IN CONNECTION WITH THE DOWNLOADING, PROVISIONING, VIEWING OR USE OF THE MATERIALS REGARDLESS OF THE FORM OF ACTION, WHETHER FOR BREACH OF CONTRACT, BREACH OF WARRANTY, TORT, NEGLIGENCE, INFRINGEMENT OR OTHERWISE (INCLUDING, WITHOUT LIMITATION, DAMAGES BASED ON LOSS OF PROFITS, DATA, FILES, USE, BUSINESS OPPORTUNITY OR CLAIMS OF THIRD PARTIES), AND WHETHER OR NOT THE PARTY HAS BEEN ADVISED OF THE POSSIBILITY OF SUCH DAMAGES. THIS LIMITATION SHALL APPLY NOTWITHSTANDING ANY FAILURE OF ESSENTIAL PURPOSE OF ANY LIMITED REMEDY PROVIDED HEREIN.
- Should any provision of this Agreement be held by a court of competent jurisdiction to be illegal, invalid, or unenforceable, that provision shall be deemed amended to achieve as nearly as possible the same economic effect as the original provision, and the legality, validity and enforceability of the remaining provisions of this Agreement shall not be affected or impaired thereby.
- The failure of either party to enforce any term or condition of this Agreement shall not constitute a waiver of either party's right to enforce each and every term and condition of this Agreement. No breach under this agreement shall be deemed waived or excused by either party unless such waiver or consent is in writing signed by the party granting such waiver or consent. The waiver by or consent of a party to a breach of
- any provision of this Agreement shall not operate or be construed as a waiver of or consent to any other or subsequent breach by such other party.
- This Agreement may not be assigned (including by operation of law or otherwise) by you without WILEY's prior written consent.
- Any fee required for this permission shall be non-refundable after thirty (30) days from receipt by the CCC.
- These terms and conditions together with CCC's Billing and Payment terms and conditions (which are incorporated herein) form the entire agreement between you and WILEY concerning this licensing transaction and (in the absence of fraud) supersedes all prior agreements and representations of the parties, oral or written. This Agreement may not be amended except in writing signed by both parties. This Agreement shall be binding upon and inure to the benefit of the parties' successors, legal representatives, and authorized assigns.
- In the event of any conflict between your obligations established by these terms and conditions and those established by CCC's Billing and Payment terms and conditions, these terms and conditions shall prevail.
- WILEY expressly reserves all rights not specifically granted in the combination of (i) the license details provided by you and accepted in the course of this licensing transaction, (ii) these terms and conditions and (iii) CCC's Billing and Payment terms and conditions.
- This Agreement will be void if the Type of Use, Format, Circulation, or Requestor Type was misrepresented during the licensing process.
- This Agreement shall be governed by and construed in accordance with the laws of the State of New York, USA, without regards to such state's conflict of law rules. Any legal action, suit or proceeding arising out of or relating to these Terms and Conditions or the breach thereof shall be instituted in a court of competent jurisdiction in New York County in the State of New York in the United States of America and each party

hereby consents and submits to the personal jurisdiction of such court, waives any objection to venue in such court and consents to service of process by registered or certified mail, return receipt requested, at the last known address of such party.

ELSEVIER LICENSE
TERMS AND CONDITIONS
Feb 23, 2018
This Agreement between Mr. Andrew Michael ("You") and Elsevier ("Elsevier") consists of your license details and the terms and conditions provided by Elsevier and Copyright Clearance Center.
License Number 4294911396654
License date Feb 23, 2018
Licensed Content Publisher Elsevier
Licensed Content Publication Acta Materialia
Licensed Content Title Composition-dependent elastic properties and electronic structures of off-stoichiometric TiNi from first-principles calculations
Licensed Content Author Jian-Min Lu,Qing-Miao Hu,Rui Yang
Licensed Content Date Oct 1, 2008
Licensed Content Volume 56
Licensed Content Issue 17
Licensed Content Pages 8
Start Page 4913
End Page 4920
Type of Use reuse in a thesis/dissertation
Portion figures/tables/illustrations
Number of figures/tables/illustrations 1
Format electronic
Are you the author of this Elsevier article? No
Will you be translating? No
Original figure numbers Figure 3
Title of your thesis/dissertation Laser Processing and Modelling of Multiple Memory Shape Memory Alloys
Expected completion date Apr 2018
Estimated size (number of pages) 200
Requestor Location Mr. Andrew Michael
256 Louisa St
Kitchener, ON N2H5M9
Canada
Attn: Mr. Andrew Michael
Publisher Tax ID GB 494 6272 12

ELSEVIER LICENSE
TERMS AND CONDITIONS
Feb 23, 2018
This Agreement between Mr. Andrew Michael ("You") and Elsevier ("Elsevier") consists of your license details and the terms and conditions provided by Elsevier and Copyright Clearance Center.
License Number 4294921323341
License date Feb 23, 2018
Licensed Content Publisher Elsevier
Licensed Content Publication Materials Science and Engineering: A
Licensed Content Title A comparative study of elastic constants of Ti–Ni-based alloys prior to martensitic transformation
Licensed Content Author X Ren, N Miura, J Zhang, K Otsuka, K Tanaka, M Koiwa, T Suzuki, Yu. I Chumlyakov, M Asai
Licensed Content Date Aug 15, 2001

Licensed Content Volume 312
Licensed Content Issue 1-2
Licensed Content Pages 11
Start Page 196
End Page 206
Type of Use reuse in a thesis/dissertation
Intended publisher of new work other
Portion figures/tables/illustrations
Number of figures/tables /illustrations 1
Format both print and electronic
Are you the author of this Elsevier article? No
Will you be translating? No
Original figure numbers Figure 3
Title of your thesis/dissertation Laser Processing and Modelling of Multiple Memory Shape Memory Alloys
Expected completion date Apr 2018
Estimated size (number of pages) 200
Requestor Location Mr. Andrew Michael
256 Louisa St
Kitchener, ON N2H5M9
Canada
Attn: Mr. Andrew Michael
Publisher Tax ID GB 494 6272 12
Total 0.00 USD

ELSEVIER LICENSE
TERMS AND CONDITIONS
Feb 23, 2018
This Agreement between Mr. Andrew Michael ("You") and Elsevier ("Elsevier") consists of
your license details and the terms and conditions provided by Elsevier and Copyright
Clearance Center.
License Number 4294930000634
License date Feb 23, 2018
Licensed Content Publisher Elsevier
Licensed Content Publication Journal of the Mechanics and Physics of Solids
Licensed Content Title Tension, compression, and bending of superelastic shape memory alloy tubes
Licensed Content Author Benjamin Reedlunn, Christopher B. Churchill, Emily E. Nelson, John A. Shaw, Samantha
H. Daly
Licensed Content Date Feb 1, 2014
Licensed Content Volume 63
Licensed Content Issue n/a
Licensed Content Pages 32
Start Page 506
End Page 537
Type of Use reuse in a thesis/dissertation
Intended publisher of new work other
Portion figures/tables/illustrations
Number of figures/tables /illustrations 1
Format both print and electronic
Are you the author of this Elsevier article? No
Will you be translating? No
Original figure numbers Figure 9
Title of your thesis/dissertation Laser Processing and Modelling of Multiple Memory Shape Memory Alloys
Expected completion date Apr 2018
Estimated size (number of pages) 200
Requestor Location Mr. Andrew Michael
256 Louisa St

Kitchener, ON N2H5M9
Canada
Attn: Mr. Andrew Michael
Publisher Tax ID GB 494 6272 12
Total 0.00 USD

ELSEVIER LICENSE
TERMS AND CONDITIONS
Feb 23, 2018
This Agreement between Mr. Andrew Michael ("You") and Elsevier ("Elsevier") consists of your license details and the terms and conditions provided by Elsevier and Copyright Clearance Center.
License Number 4294930203034
License date Feb 23, 2018
Licensed Content Publisher Elsevier
Licensed Content Publication International Journal of Mechanical Sciences
Licensed Content Title Residual deformation of active structures with SMA actuators
Licensed Content Author Dimitris C. Lagoudas, Steven G. Shu
Licensed Content Date Jun 1, 1999
Licensed Content Volume 41
Licensed Content Issue 6
Licensed Content Pages 25
Start Page 595
End Page 619
Type of Use reuse in a thesis/dissertation
Intended publisher of new work other
Portion figures/tables/illustrations
Number of figures/tables/illustrations 1
Format both print and electronic
Are you the author of this Elsevier article? No
Will you be translating? No
Original figure numbers Figure 1
Title of your thesis/dissertation Laser Processing and Modelling of Multiple Memory Shape Memory Alloys
Expected completion date Apr 2018
Estimated size (number of pages) 200
Requestor Location Mr. Andrew Michael
256 Louisa St
Kitchener, ON N2H5M9
Canada
Attn: Mr. Andrew Michael
Publisher Tax ID GB 494 6272 12
Total 0.00 USD

Smart Materials and Structures
Order detail ID: 71034843
Order License Id: 4294930789333
ISSN: 0964-1726
Publication Type: Journal
Volume:
Issue:
Start page:
Publisher: IOP Publishing
Author/Editor: Society of Photo-optical Instrumentation Engineers ; American Institute of Physics ; Institute of Physics (Great Britain)
Permission Status: Granted

Permission type: Republish or display content
Type of use: Thesis/Dissertation
Requestor type: Academic institution
Format: Print, Electronic
Portion: chart/graph/table/figure
Number of charts/graphs/tables/figures: 2
The requesting person/organization: Andrew Michael
Title or numeric reference of the portion(s): Figure 5, Figure 6
Title of the article or chapter the portion is from: Combining thermodynamic principles with Preisach models for superelastic shape memory alloy wires
Total order items: 1
Order Total: 0.00 USD
Confirmation Number: 11700865

Special Rightsholder Terms & Conditions
The following terms & conditions apply to the specific publication under which they are listed
Smart Materials and Structures
Permission type: Republish or display content
Type of use: Thesis/Dissertation
TERMS AND CONDITIONS
The following terms are individual to this publisher:
These special terms and conditions are in addition to the standard terms and conditions for CCC's Republication Service and, together with those standard terms and conditions, govern the use of the Works.
As the "User" you will make all reasonable efforts to contact the author(s) of the article which the Work is to be reused from, to seek consent for your intended use. Contacting one author who is acting expressly as authorised agent for their co-author(s) is acceptable.
User will reproduce the following wording prominently alongside the Work:

- the source of the Work, including author, article title, title of journal, volume number, issue number (if relevant), page range (or first page if this is the only information available) and date of first publication. This information can be contained in a footnote or reference note; and
- a link back to the article (via DOI); and
- if practicable, and IN ALL CASES for new works published under any of the Creative Commons licences, the words "© IOP Publishing. Reproduced with permission. All rights reserved"

Without the express permission of the author(s) and the Rightsholder of the article from which the Work is to be reused, User shall not use it in any way which, in the opinion of the Rightsholder, could: (i) distort or alter the author(s)' original intention(s) and meaning; (ii) be prejudicial to the honour or reputation of the author(s); and/or (iii) imply endorsement by the author(s) and/or the Rightsholder.
This licence does not apply to any article which is credited to another source and which does not have the copyright line '© IOP Publishing Ltd'. User must check the copyright line of the article from which the Work is to be reused to check that IOP Publishing Ltd has all the necessary rights to be able to grant permission. User is solely responsible for identifying and obtaining separate licences and permissions from the copyright owner for reuse of any such third party material/figures which the Rightsholder is not the copyright owner of. The Rightsholder shall not reimburse any fees which User pays for a republication license for such third party content.
This licence does not apply to any material/figure which is credited to another source in the Rightsholder's publication or has been obtained from a third party. User must check the Version of Record of the article from which the Work is to be reused, to check whether any of the material in the Work is third party material. Third party citations and/or copyright notices and/or permissions statements may not be included in any other version of the article from which the Work is to be reused and so cannot be relied upon by the User. User is solely responsible for identifying and obtaining separate licences and permissions from the copyright owner for reuse of any such third party material/figures where the Rightsholder is not the copyright owner. The Rightsholder shall not reimburse any fees which User pays for a republication license for such third party content.
User and CCC acknowledge that the Rightsholder may, from time to time, make changes or additions to these special terms and conditions without express notification, provided that these shall not apply to permissions already secured and paid for by User prior to such change or addition.
User acknowledges that the Rightsholder (which includes companies within its group and third parties for whom it publishes its titles) may make use of personal data collected through the service in the course of their business.

If User is the author of the Work, User may automatically have the right to reuse it under the rights granted back when User transferred the copyright in the article to the Rightsholder. User should check the copyright form and the relevant author rights policy to check whether permission is required. If User is the author of the Work and does require permission for proposed reuse of the Work, User should select 'Author of requested content' as the Requestor Type. The Rightsholder shall not reimburse any fees which User pays for a republication license.
If User is the author of the article which User wishes to reuse in User's thesis or dissertation, the republication licence covers the right to include the Accepted Manuscript version (not the Version of Record) of the article. User must include citation details and, for online use, a link to the Version of Record of the article on the Rightsholder's website. User may need to obtain separate permission for any third party content included within the article. User must check this with the copyright owner of such third party content. User may not include the article in a thesis or dissertation which is published by ProQuest. Any other commercial use of User's thesis or dissertation containing the article would also need to be expressly notified in writing to the Rightsholder at the time of request and would require separate written permission from the Rightsholder.
User does not need to request permission for Work which has been published under a CC BY licence. User must check the Version of Record of the CC BY article from which the Work is to be reused, to check whether any of the material in the Work is third party material and so not published under the CC BY licence. User is solely responsible for identifying and obtaining separate licences and permissions from the copyright owner for reuse of any such third party material/figures. The Rightsholder shall not reimburse any fees which User pays for such licences and permissions.
As well as CCC, the Rightsholder shall have the right to bring any legal action that it deems necessary to enforce its rights should it consider that the Work infringes those rights in any way.
For STM Signatories ONLY (as agreed as part of the STM Guidelines)
Any licence granted for a particular edition of a Work will apply also to subsequent editions of it and for editions in other languages, provided such editions are for the Work as a whole in situ and do not involve the separate exploitation of the permitted illustrations or excerpts.
Other Terms and Conditions:
STANDARD TERMS AND CONDITIONS
1. Description of Service; Defined Terms. This Republication License enables the User to obtain licenses for republication of one or more copyrighted works as described in detail on the relevant Order Confirmation (the "Work(s)"). Copyright Clearance Center, Inc. ("CCC") grants licenses through the Service on behalf of the rightsholder identified on the Order Confirmation (the "Rightsholder"). "Republication", as used herein, generally means the inclusion of a Work, in whole or in part, in a new work or works, also as described on the Order Confirmation. "User", as used herein, means the person or entity making such republication.
2. The terms set forth in the relevant Order Confirmation, and any terms set by the Rightsholder with respect to a particular Work, govern the terms of use of Works in connection with the Service. By using the Service, the person transacting for a republication license on behalf of the User represents and warrants that he/she/it (a) has been duly authorized by the User to accept, and hereby does accept, all such terms and conditions on behalf of User, and (b) shall inform User of all such terms and conditions. In the event such person is a "freelancer" or other third party independent of User and CCC, such party shall be deemed jointly a "User" for purposes of these terms and conditions. In any event, User shall be deemed to have accepted and agreed to all such terms and conditions if User republishes the Work in any fashion.
3. Scope of License; Limitations and Obligations.
3.1 All Works and all rights therein, including copyright rights, remain the sole and exclusive property of the Rightsholder. The license created by the exchange of an Order Confirmation (and/or any invoice) and payment by User of the full amount set forth on that document includes only those rights expressly set forth in the Order Confirmation and in these terms and conditions, and conveys no other rights in the Work(s) to User. All rights not expressly granted are hereby reserved.
3.2 General Payment Terms: You may pay by credit card or through an account with us payable at the end of the month. If you and we agree that you may establish a standing account with CCC, then the following terms apply: Remit Payment to: Copyright Clearance Center, 29118 Network Place, Chicago, IL 60673-1291. Payments Due: Invoices are payable upon their delivery to you (or upon our notice to you that they are available to you for downloading). After 30 days, outstanding amounts will be subject to a service charge of 1-1/2% per month or, if less, the maximum rate allowed by applicable law. Unless otherwise specifically set forth in the Order Confirmation or in a separate written agreement signed by CCC, invoices are due and payable on "net 30" terms. While User may exercise the rights licensed immediately upon issuance of the Order Confirmation, the license is automatically

unauthorized (but licensable) use of a Work that is terminated immediately upon notice thereof may be liquidated by payment of the Rightsholder's ordinary license price therefor; any unauthorized (and unlicensable) use that is not terminated immediately for any reason (including, for example, because materials containing the Work cannot reasonably be recalled) will be subject to all remedies available at law or in equity, but in no event to a payment of less than three times the Rightsholder's ordinary license price for the most closely analogous licensable use plus Rightsholder's and/or CCC's costs and expenses incurred in collecting such payment.

8. Miscellaneous.

8.1 User acknowledges that CCC may, from time to time, make changes or additions to the Service or to these terms and conditions, and CCC reserves the right to send notice to the User by electronic mail or otherwise for the purposes of notifying User of such changes or additions; provided that any such changes or additions shall not apply to permissions already secured and paid for.

8.2 Use of User-related information collected through the Service is governed by CCC's privacy policy, available online here: http://www.copyright.com/content/cc3/en/tools/footer/privacypolicy.html.

8.3 The licensing transaction described in the Order Confirmation is personal to User. Therefore, User may not assign or transfer to any other person (whether a natural person or an organization of any kind) the license created by the Order Confirmation and these terms and conditions or any rights granted hereunder; provided, however, that User may assign such license in its entirety on written notice to CCC in the event of a transfer of all or substantially all of User's rights in the new material which includes the Work(s) licensed under this Service.

8.4 No amendment or waiver of any terms is binding unless set forth in writing and signed by the parties. The Rightsholder and CCC hereby object to any terms contained in any writing prepared by the User or its principals, employees, agents or affiliates and purporting to govern or otherwise relate to the licensing transaction described in the Order Confirmation, which terms are in any way inconsistent with any terms set forth in the Order Confirmation and/or in these terms and conditions or CCC's standard operating procedures, whether such writing is prepared prior to, simultaneously with or subsequent to the Order Confirmation, and whether such writing appears on a copy of the Order Confirmation or in a separate instrument.

8.5 The licensing transaction described in the Order Confirmation document shall be governed by and construed under the law of the State of New York, USA, without regard to the principles thereof of conflicts of law. Any case, controversy, suit, action, or proceeding arising out of, in connection with, or related to such licensing transaction shall be brought, at CCC's sole discretion, in any federal or state court located in the County of New York, State of New York, USA, or in any federal or state court whose geographical jurisdiction covers the location of the Rightsholder set forth in the Order Confirmation. The parties expressly submit to the personal jurisdiction and venue of each such federal or state court. If you have any comments or questions about the Service or Copyright Clearance Center, please contact us at 978-750-8400 or send an e-mail to info@copyright.com.

References

1. A.C. Keefe, G.P. McKnight, G.A. Herrera, P.A. Bedegi, Development of a shape memory alloy heat engine through experiment and modeling, in: Proceedings of the ASME 2011 Conference on Smart Materials, Adaptive Structures and Intelligent Systems, Phoenix, Arizona, USA, 18-21 September (2011).
2. T. Luchetti, A. Zanella, M. Biasiotto, A. Saccagno, Electrically Actuated Antiglare Rear-View Mirror Based on Shape Memory Alloy Actuator, Journal of Materials Engineering and Performance 18 (2009) 717.
3. C. van der Eijk, J.S. Olsen, Z. Zhang, Applications of NiTi shape memory alloy dampeners in civil structures, in: Proceedings of the First International Conference on Self Healing Materials, Noordwijk aan Zee, Netherlands, 2007.
4. W. Stoeckel, Use of NiTi shape memory alloys for thermal sensor-actuators, in: Proceedings of SPIE, San Diego, CA, 1991, 382-388.
5. A. Pequegnat, M. Daly, J. Wang, Y. Zhou, M.I. Khan, Dynamic actuation of a novel laser-processed NiTi linear actuator, Smart Materials and Structures, 21 (2012) 094004-094011.
6. J.M. Jani, M. Leary, A. Subic, M.A. Gibson, A review of shape memory alloy research, applications and opportunities, Materials and Design 56 (2014) 1078-1113.
7. F. Miura, M. Mogi, Y. Ohura, Japanese NiTi alloy wire: uses of the direct electric resistance heat treatment method, European Journal of Orthodontics, 10 (1988) 187-191.
8. G. Airoldi, G. Riva, Pseudoelasticity of NiTi orthodontic wires modified by current methodologies: A critical comparison, Journal de Physique IV, Colloque C2, supplement au Journal de Physique III, 5 (1995) 397-402.
9. A.S. Mahmud, Y. Liu, T.H. Nam, Gradient annealing of functionally graded NiTi, Smart Materials and Structures, 17 (2008) 015031-015035.
10. Q. Meng, Y. Liu, H. Yang, B.S. Shariat, T.H. Nam, Functionally graded NiTi strips prepared by laser surface anneal, Acta Materialia 60 (2012) 1658-1668.
11. R. Delville, B. Malard, J. Pilch, P. Sittner, D. Schryvers, Transmission electron microscopy investigation of dislocation slip during superelastic cycling of Ni-Ti wires, International Journal of Plasticity, 27 (2011) 282-297.
12. A. Ahadi and Q.P. Sun, Stress-induced nanoscale phase transition in superelastic NiTi by in situ X-ray diffraction, Applied Physics Letters, 103 (2013) 021902-021905.

13. D. Cluff, S. Corbin, R. Gorbet, The influence of reactive sintering process parameters on the martensite to austenite phase transformation of NiTi, in: Proceedings of Cansmart 2009, Montreal, Quebec, Canada, 2009, 273-282.
14. B.V. Krishna, S. Bose, A. Bandyopadhyay, Laser Processing of Net-Shape NiTi Shape Memory Alloy, Metallurgical and Materials Transactions A, 38 (2007) 1096-1103.
15. M. Whitney, S. Corbin, R. Gorbet, Investigation of the mechanisms of reactive sintering and combustion synthesis of NiTi using differential scanning calorimetry and microstructural analysis, Acta Materialia, 56 (2008) 559-570.
16. J.C. Hey, A.P. Jardine, Shape memory NiTi synthesis form elemental powders, Material Science and Engineering A, 188 (1994) 291-300.
17. Y. Wang, X. Ren and K. Otsuka, Shape memory effect and superelasticity in a strain glass, Physical Review Letters, 97 (2206) 225703.
18. P. Sevilla, F. Martorell, C. Libenson, J.A. Planell, F.J. Gil, J. Mater. Sci. Mater. Med. 19 (2008) 525.
19. C.W. Chan, H.C. Man, T.M. Yue, Effects of process parameters upon the shape memory and pseudo-elastic behaviors of laser-welded NiTi Thin Foil, Metallurgical and Materials Transactions A, 42 (2011) 2264-2270.
20. M. Daly, A. Pequegnat, Y. Zhou, M.I. Khan, Fabrication of a novel laser-processed NiTi shape memory microgripper with enhanced thermomechanical functionality, Intelligent Material Systems and Structures 24 (2013) 984-90.
21. M. Daly, A. Pequegnat, Y. Zhou, M.I. Khan, Enhanced thermomechanical functionality of a laser processed hybrid NiTi-NiTiCu shape memory alloy, Smart Materials and Structures, 21 (2012) 045028.
22. M.I. Khan, A. Pequegnat, Y. Zhou, Multiple memory shape memory alloys, Advanced Engineering Materials 15 (2013) 386-93.
23. A. Pequegnat, B. Panton, Y.N. Zhou, M.I. Khan, Local Composition and Microstructure Control for Multiple Pseudoelastic Plateau and Hybrid Self-Biasing Shape Memory Alloys, Materials and Design, 92 (2016) 802-813.
24. K. Tanaka, F. Nishimura, T. Hayashi, H. Tobushi, C. Lexcellent, Phenomenological analysis on subloops and cyclic behavior in shape memory alloys under mechanical and/or thermal loads, Mechanics of Materials 19 (1995) 281–292.

25. C. Liang, C.A. Rogers, A multi-dimensional constitutive model for shape memory alloys, Journal of Engineering Mathematics 26 (1992) 429-443.
26. L.C. Brinson, One-dimensional constitutive behavior of shape memory alloys: Thermomechanical derivation with non-constant material functions and redefined martensite internal variable, Journal of Intelligent Materials Systems and Structures, 4 (1993) 229-242.
27. J.G. Boyd, D.C. Lagoudas, A thermodynamic constitutive model for the shape memory materials. Part 1. The monolithic shape memory alloys, International Journal of Plasticity, 12 (1996) 805-842.
28. B. Raniecki, C.H. Lexcellent, Thermodynamics of isotropic pseudoelasticity in shape memory alloys, European Journal of Mechanics – A/Solids 17 (1998) 185-205.
29. M.A. Qidwai, D.C. Lagoudas, On thermomechanics and transformation surfaces of polycrystalline NiTi shape memory alloy material, International Journal of Plasticity 16 (2000) 1309-1343.
30. C. Lexcellent, A. Vivet, C. Bouvet, S. Calloch, P. Blanc, Experimental and numerical determinations of the initial surface of phase transformation under biaxial loading in some polycrystalline shape-memory alloys, Journal of Mechanics and Physics of Solids 50 (2002) 2717-2735.
31. C.P. Frick, A.M. Ortega, J. Tyber, A.E.M. Maksound, H.J. Maier, Y. Liu, K. Gall, Thermal processing of polycrystalline NiTi shape memory alloys, Materials Science and Engineering A, 405 (2005) 34.
32. P.C. Hall, Resistance welding Ti-rich Nitinol wire, in: Proceedings of the International Conference on Shape Memory and Superelastic Technologies, Pacific Grove, California, USA, 30 April-4 May 2000, SMST-2000, SMST The International Organization on Shape Memory and Superelastic Technology, Fremont, CA, USA (2001) 67.
33. K. Otsuka, X. Ren, Physical metallurgy of Ti-Ni-based shape memory alloys, Progress in Materials Science, 50 (2005) 511-678.
34. A. Wadood, Brief overview on Nitinol as a biomaterial, Advances in Materials Science and Engineering, vol.2016.
35. R.E. Reed-Hill, R. Abbaschian, Physical Metallurgy Principles: Third Edition, PWS Publishing Company, Boston, USA (1994).

36. T.W. Duerig, K.N. Melton, D. Stockel, C.M. Wayman, Engineering Aspects of Shape Memory Alloys, Butterworth-Heinemann Ltd., London (1990).
37. D.C. Lagoudas (Ed), Shape Memory Alloys: Modeling and Engineering Applications, Springer (2008).
38. T.V. Philip, P.A. Beck, CsCl-type ordered structures in binary alloys of transition elements, AIME Transactions 209 (1957) 1269.
39. K. Otsuka, T. Sawamura, K. Shimizu, Crystal structure and internal defects of equiatomic TiNi martensite, Physica Status Solidi A 5 (1971) 457.
40. J.A. Shaw, C.B. Churchill, M.A. Iadicola, Tips and tricks for characterizing shape memory alloy wire: Part 1 – Differential scanning calorimetry and basic phenomena, Experimental Techniques, 32 (2008) 55-62.
41. G.B. Kauffman, I. Mayo, The story of Nitinol: the serendipitous discovery of the memory metal and its applications, The Chemical Educator 2 (1997) 1.
42. G. Fan, W. Chen, S. Yang, J. Zhu, X. Ren, K. Otsuka, Origin of abnormal multi-stage martensitic transformation behavior in aged Ni-rich Ti–Ni shape memory alloys, Acta Materialia, 52 (2004) 4351-4362.
43. Y. Zhou, J. Zhang, G. Fan, X. Ding, J. Sun, X. Ren, K. Otsuka, Origin of 2-stage R-phase transformation in low-temperature aged Ni-rich Ti-Ni alloys, Acta Materialia, 53 (2005) 5365-77.
44. H.C. Ling, K. Roy, Stress-induced shape change and shape memory in the R and martensite transformations in equiatomic NiTi, Metallurgical and Materials Transactions A, 12 (1981) 2101-2111.
45. H. Kimura, O. Izumi, Titanium ’80, Science and Technology: Proceedings of the Fourth International Conference on Titanium, Kyoto, Japan May 19-22, 1980, Metallurgical Society of AIME, Warrendale, PA, USA, 1980.
46. X. Ren, N. Miura, J. Zhang, K. Otsuka, K. Tanaka, M. Koiwa, T. Suzuki, T.I. Chumlyakov, M. Asai, A comparative study of elastic constants of Ti-Ni-based alloys prior to martensitic transformation, Materials Science and Engineering A, 312 (2001) 196-206.
47. A. Dlouhy, J. Khalil-Allafi, G. Eggeler, Multiple-step martensitic transformations in Ni-rich NiTi alloys – an in-situ transmission electron microscopy investigation, Philosophical Magazine, 31 (2003) 339-363.

48. S. Miyazaki, S. Kimura, K. Otsuka, Shape-memory effect and pseudoelasticity associated with the R-phase transition in Ti-50.5 at.% Ni single crystals, Philosophical Magazine A, 57 (1988) 467-478.
49. E.R. Petty, Ed., Martensite: Fundamentals and Technology, Longman, London, U.K. (1970).
50. E. Hornbogen, Surface upheavals, pseudo martensite, and martensite ghosts, Praktische Metallographie 42 (2005) 445.
51. S.P. Gupta, A.A. Johnson, Morphology and crystallography of β' martensite in TiNi alloys, Materials Transactions, The Japan Institute of Metals 14 (1973) 292.
52. T. Onda, Y. Bando, T. Ohba, K. Otsuka, Electron microscopy study of twins in martensite in a Ti-50.0at%Ni alloy, Materials Transactions, The Japan Institute of Metals 33 (1992) 354.
53. K.N. Melton, O. Mercier, Fatigue of NiTi thermoelastic martensites, Acta Metallurgica 27 (1979) 137.
54. American Society for Testing and Materials (ASTM) Standard Terminology for Nickel-Titanium Shape Memory Alloys, Standard F2005, ASTM International, West Conshohocken, PA (2009).
55. S. Zhang, H. Braasch, P. G. McCormick, FEM Simulation of the Martensitic Transformation in NiTi Alloys, Journal of Physics IV, 7 (1997) 537-542.
56. M. H. Elahinia, M. Hashemi, M. Tabesh, S. B. Bhaduri, Manufacturing and processing of NiTi implants: A review, Progress in Materials Science, 57 (2012) 911-946.
57. B. Tam, Micro-Welding of Nitinol Shape Memory Alloy, MASc thesis, University of Waterloo, Ontario, Canada (2010).
58. American Society for Testing and Materials (ASTM) Standard Test Method for Transformation Temperature of Nickel-Titanium by Thermal Analysis, Standard F2004-05, ASTM International, West Conshohocken, PA (2009).
59. A. Pequegnat, Novel Laser Based NiTi Shape Memory Alloy Processing Protocol for Medical Device Applications, PhD Thesis, University of Waterloo, Waterloo, Ontario, Canada (2012).
60. R.F. Hamilton, H. Sehitoglu, Y. Chumlyakov, H.J. Maier, Stress dependence of the hysteresis in single crystal NiTi alloys, Acta Materialia 52 (2004) 3383.

61. T.H. Nam, T. Saburi, K. Shimizu, Cu-content dependence of shape memory characteristics in Ti-Ni-Cu alloys, Materials Transactions, The Japan Institute of Metals 31 (1990) 959.
62. M. Piao, K. Otsuka, S. Miyazaki, H. Horikawa, Mechanism of the As temperature increase by pre-deformation in thermoelastic alloys, Materials Transactions, Japan Institute for Materials 34(1993) 919.
63. K. Bhattacharya, Microstructure of martensite: Why it Forms and how it gives rise to the shape-memory effect, New York: Oxford University Press, 2003.
64. S. Miyazaki, Martensitic transformation in TiNi alloys, in: Thin Film Shape Memory Alloys: Fundamentals and Device Applications, S. Miyazaki, Y.Q. Fu and W.M. Huang, Eds., Cambridge University Press & Science Press, (2009) 73-87.
65. S. Miyazaki, K. Otsuka, Y. Suzuki, Transformation pseudoelasticity and deformation behavior in a Ti-50.5at%Ni alloy, Scripta Metallurgica 15 (1981) 287-292.
66. P. Wollants, M. De Bonte, J.R. Roos, Thermodynamic analysis of the stress-induced martensitic-transformation in a single crystal, Zeitschrift fur Metallkunde 70 (1979) 113-117.
67. A.R. Pelton, J. DiCello, S. Miyazaki, Optimisation of processing and properties of medical grade Nitinol wire, Minimally Invasive Therapy and Allied Technologies 9 (2000) 107.
68. D. Favier, Y. Liu, L. Orgéas, A. Sandel, L. Debove, P. Comte-Gaz, Influence of thermomechanical processing on the superelastic properties of a Ni-rich Nitinol shape memory alloy, Materials Science and Engineering A 429 (2006) 130.
69. K. Otsuka, K. Shimizu, Pseudoelasticity and shape memory effects in alloys, International Metals Reviews 31 (1986) 93-114.
70. S. Miyazaki, Y. Ohmi, K. Otsuka, Y. Suzuki, Characteristics of deformation and transformation pseudoelasticity in Ti-Ni alloys, Journal de Physique Colloques 43 (1982) C4-255-C4-260.
71. D. Hodgson, S. Russell, Nitinol melting, manufacture and fabrication, Minimally Invasive Therapy and Allied Technologies, 9 (2000) 61-66.
72. W. Tang, Thermodynamic study of the low-temperature phase, B19' and martensitic transformation in near equiatomic Ti-Ni shape memory alloys, Metallurgical and Materials Transactions A 28 (1997) 537.

73. A.S. Paula, K. Mahesh and F. Braz Fernandes, Stability in Phase Transformation After Multiple Steps of Marforming in Ti-Rich Ni-Ti Shape Memory Alloy, Journal of Material Engineering and Performance, 20 (2011) 771-775.
74. A.S. Paula, K. Mahesh, C.M.L. dos Santos, F.M. Braz Fernandes, C.S. da Costa Viana, Thermomechanical behavior of Ti-rich NiTi shape memory alloys, Materials Science & Engineering A, 481-482 (2008) 146-150.
75. Y. Motemani, M. Nili-Ahmadabadi, M.J. Tan, M. Bornapour, S. Rayagan, Effect of cooling rate on the phase transformation behavior and mechanical properties of Ni-rich NiTi shape memory alloy, Journal of Alloys and Compounds, 469 (2009) 164-168.
76. H. Morawiec, D. Stroz, D. Chrobak, Effect of deformation and thermal treatment of NiTi alloy on transition sequence, Journal de Physique IV, Colloque C2, 5 (1995) 205-210.
77. L. Bataillard, J.-E. Bidaux, R. Gotthardt, Interaction between microstructure and multiple-step transformation in binary NiTi alloys using in-situ transmission electron microscopy observation, Philosophical Magazine A, 78 (1998) 327.
78. J. Pfetzing-Micklich, R. Ghisleni, T. Simon, C. Somsen, J. Michler, G. Eggeler, Orientation dependence of stress-induced phase transformation and dislocation plasticity in NiTi shape memory alloys on the micro scale, Materials Science & Engineering A, 538 (2012) 265-271.
79. T. Buchheit, J. Wert, Modeling the effects of stress state and crystal orientation on the stress-induced transformation of NiTi single crystals, MMTA, 25 (1994) 2383-2389.
80. T. Saburi, M. Yoshida, S. Nenno, Deformation behavior of shape memory Ti Ni alloy crystals, Scripta Metallurgica, 18 (1984) 363-366.
81. S. Miyazaki, T. Kawai, K. Otsuka, On the origin of intergranular fracture in ß phase shape memory alloys, Scripta Metallurgica, 16 (1982) 431-436.
82. K. Takezawa, T. Izumi, H. Chiba, S. Sato, Coherency of the transformation strain at the grain boundary and fracture in Cu-Zn-Al alloy, Journal of Physics Colloques, 43 (1982) 819-824.
83. S. Miyazaki, K. Otsuka, C. M. Wayman, The shape memory mechanism associated with the martensitic transformation in Ti Ni alloys-I. Self-accommodation, Acta Metallurgica, 37 (1989) 1873-1884.
84. S. Gao, S. Yi, Experimental study on the anisotropic behavior of textured NiTi pseudoelastic shape memory alloys, Materials Science and Engineering: A, 362 (2003) 107-111.

85. Y. Liu, Z.L. Xie, J. Van Humbeeck and L. Delaey, Effect of texture orientation on the martensite deformation of NiTi shape memory alloy sheet, Acta Materialia, 47 (1999) 645-660.
86. N. Ono, A. Sato, Plastic Deformation Governed by the Stress Induced Martensitic Transformation in Polycrystals, Transactions of the Japan Institute of Metals, 29 (1988) 267-273.
87. N. Ono, A. Satoh, H. Ohta, A Discussion on the Mechanical Properties of Shape Memory Alloys Based on a Polycrystal Model, Materials Transactions, 30 (1989) 756-764.
88. K. Gall, H. Sehitoglu, The role of texture in tension–compression asymmetry in polycrystalline NiTi, International Journal of Plasticity, 15 (1999) 69-92.
89. K. Gall, H. Sehitoglu, Y. I. Chumlyakov, I. V. Kireeva, Tension–compression asymmetry of the stress–strain response in aged single crystal and polycrystalline NiTi, Acta Materialia, 47 (1999) 1203-1217.
90. Y. Liu, Z. Xie, J. Van Humbeeck, L. Delaey, Asymmetry of stress–strain curves under tension and compression for NiTi shape memory alloys, Acta Materialia, 46 (1998) 4325-4338.
91. H.C. Lin, S.K. Wu, Y.C. Yen, A study on the wire drawing of TiNi shape memory alloys, Materials Science and Engineering A, 215 (1996) 113-119.
92. R.N. Wright, Physical Conditiona in the Lubricant Layer, Wire Journal International, 30 (1997) 88-92.
93. J. Schaffer, D. Plumley, Fatigue Performance of Nitinol Round Wire with Varying Cold Work Reductions, Journal of Material Engineering and Performance, 18 (2009) 563-568.
94. D.A. Miller, D.C. Lagoudas, Influence of cold work and heat treatment on the shape memory effect and plastic strain development of NiTi, Materials Science & Engineering A, 308 (2001) 161-175.
95. X. Lei, W. Rui, L. Yong, The optimization of annealing and cold-drawing in the manufacture of the Ni–Ti shape memory alloy ultra-thin wire, International Journal of Advanced Manufacturing Technology, 55 (2011) 905-910.
96. C. Grossmann, J. Frenzel, V. Sampath, T. Depka, A. Oppenkowski, C. Somsen, K. Neuking, W. Theisen, G. Eggeler, Processing and property assessment of NiTi and NiTiCu shape

memory actuator springs, Materials Science and Engineering Technology, 39 (2008) 499-510.

97. S.K. Wu, H.C. Lin, Y.C. Yen, J.C. Chen, Wire drawing conducted in the R-phase of TiNi shape memory alloys, Materials Letter, 46 (2000) 175-180.
98. American Society for Testing and Materials (ASTM) Standard Specification for Wrought Nickel-Titanium Shape Memory Alloys for Medical Devices and Surgical Implants, Standard F2063-12, ASTM International, West Conshohocken, PA (2012).
99. K. Yamauchi, M. Nishida, I. Itai, K. Kitamura, A. Chiba, Specimen Preparation for Transmission Electron Microscopy of Twins in B19' Martensite of Ti-Ni Shape Memory Alloys, The Japan Institute of Metals, 37 (1996) 210-217.
100. M. Reinoehl, D. Bradley, R. Bouthot, J. Proft, The influence of melt practice on final fatigue properties of superelastic NiTi wires, in: Proceedings of the International Conference on Shape Memory and Superelastic Technologies, Pacific Grove, CA, USA (2000).
101. N. Morgan A. Wick J. Dicello, R. Graham, Carbon and oxygen levels in nitinol alloys and the implications for medical device manufacture and durability, in: Proceedings of the International Conference on Shape Memory and Superelastic Technologies, Pacific Grove, CA, USA (2006).
102. J. Frenzel, Z. Zhang, K. Neuking, G. Eggeler, High quality vacuum induction melting of small quantities of NiTi shape memory alloys in graphite crucibles, Journal of Alloys and Compounds, 385 (2004) 214-223.
103. Z. Zhang, J. Frenzel, K. Neuking, G. Eggeler, On the reaction between NiTi melts and crucible graphite during vacuum induction melting of NiTi shape memory alloys, Acta Materialia, 53 (2005) 3971-3985.
104. D. Reynaerts, H. Van Brussel, Design aspects of shape memory actuators, Mechatronics, 8 (1998) 635-656.
105. R. Featherstone, Y.H. Teh, Improving the speed of shape memory alloy actuators by faster electrical heating, Ed. M.H. Ang Jr., O. Khatib, Experimental Robotics IX: The 9th International Symposium on Experimental Robotics, Springer, Berlin, 2006, p. 67-76.
106. M.M. Patel, D.L. Plumley, R.J. Bouthot, J.L. Proft, The significance of melt practice on fatigue properties of superelastic NiTi fine diameter wires, in: Proceedings of the

International Conference on Shape Memory and Superelastic Technologies, Pacific Grove, CA, USA (2006).

107. A. Toro, F. Zhou, M. Wu, W. Geertruyden, W. Misiolek, Characterization of Non-metallic inclusions in superelastic NiTi tubes, Journal of Materials Engineering and Performance, 18 (2009) 448-458.
108. J. Otubo, O.D. Rigo, C.M. Neto, M.J. Kaufman, P.R. Mei, Scale up of NiTi shape memory alloy production by EBM, Journal De Physique IV, 112 (2003) 873.
109. J. Otubo, O.D. Rigo, C.M. Neto, M.J. Kaufman, P.R. Mei, Low carbon content NiTi shape memory alloy production by electron beam melting, Materials Research, 7 (2004) 263-267.
110. J. Otubo O.D. Rigo, C.M. Neto, P.R. Mei, The effects of vacuum induction melting and electron beam melting techniques on the purity of NiTi shape memory alloys, Materials Science and Engineering A, 438-440 (2006) 679-682.
111. C.P. Frick, A.M. Ortega, J. Tyber, K. Gall, H.J. Maier, Multiscale structure and properties of cast and deformation processed polycrystalline NiTi shape-memory alloys, Metallurgical and Materials Transactions A, 35 (2004) 2013-2025.
112. S.D. Prokoshkin, I.Y. Khmelevskaya, V. Brailovski, F. Trochu, S. Turenne, V.Y. Turilina, Thermomechanical Treatments and Their Influence on the Microstructure and Stress/Strain Diagrams of NiTi Shape Memory Alloys, Canadian Metallurgical Quarterly., 43 (2004) 95-108.
113. S. Miyazaki, Y. Igo, K. Otsuka, Effect of thermal cycling on the transformation temperatures of Ti-Ni alloys, Acta Metallurgica, 34 (1986) 2045-2051.
114. X. Wang, Y. Bellouard, J.J. Vlassak, Laser annealing of amorphous NiTi shape memory alloy thin films to locally induce shape memory properties, Acta Materialia, 53 (2005) 4955-4961.
115. Y. Bellouard, T. Lehnert, J.E. Bidaux, T. Sidler, R. Cavel, R. Gotthardt, Local annealing of complex mechanical devices: a new approach for developing monolithic micro-devices, Materials Science and Engineering: A 273-275 (1999) 795-798.
116. D. Cluff, S. Corbin, R. Gorbet, Powder metallurgy fabrication of hybrid monolithic SMA actuators, in: Proceedings of Cansmart 2009, International Workshop, Smart Materials and Structures, Montreal, Quebec, Canada, 2009.

117. B. Tam, M.I. Khan, Y. Zhou, Mechanical and functional properties of laser-welded Ti-55.8 Wt Pct Ni Nitinol wires, Metallurgical and Materials Transactions A, 42 (2011) 2166-2175.
118. W.W. Duley, Laser Welding, John Wiley & Sons, Inc. New York, NY (1999).
119. C. Dawes, Laser Welding, McGraw-Hill, New York, NY (1992).
120. R.C. Crafer, P.J. Oakley (Ed), Laser Processing in Manufacturing, Chapman & Hall, New York, NY (1993).
121. S.S. Charschan (Ed), Laser in Industry, Van Nostrand Reinhold Company, New Your, NY (1972).
122. E. Biro, Weldability of Plated thin sheet and Cu by Pulsed Nd:YAG Laser welding, MASc thesis, Univeristy of Waterloo, Ontario, Canada (2001).
123. M.I. Khan, Pulsed Nd:YAG Laser Processing of Nitinol, PhD thesis, University of Waterloo, Ontario, Canada (2011).
124. A. Block-Bolten, T. Eagar, Metal vaporization from weld pools, MTB, 15 (1984) 461-469.
125. M. Collur, A. Paul, T. DebRoy, Mechanism of alloying element vaporization during laser welding, Metallurgical Transactions B, 18 (1987) 733-740.
126. M. Jandaghi, P. Parvin, M.J. Torkamany, J. Sabbaghzadeh, Alloying element losses in pulsed Nd : YAG laser welding of stainless steel 316, Journal of Physics D: Applied Physics, 41 (2008) 235503-235511.
127. P.A.A. Khan, T. Debroy, Alloying element vaporization and weld pool temperature during laser welding of AISI 202 stainless steel, Metallurgical Transactions B, 15 (1984) 641-644.
128. X. He, T. DebRoy, P.W. Fuerschbach, Alloying element vaporization during laser spot welding of stainless steel, Journal of Physics D: Applied Physics 36 (2003) 3079-3088.
129. X. He, T. DebRoy, P.W. Fuerschbach, Composition change of stainless steel during microjoining with short laser pulses, Journal of Applied Physics, 96 (2004) 4547-4555.
130. D.W. Moon, E.A. Metzbower, Laser beam welding of aluminum alloy 5456, Welding Journal, Research Supplement, 62 (1983) 53-58.
131. A. Blake, J. Mazumder, Control of magnesium loss during laser welding of Al-5083 using a plasma suppression technique, Journal of Engineering Industry, 107 (1985) 275-280.
132. C.B. Alcock, V.P. Itkin, M.K. Horrigan, Vapour Pressure Equations for Metallic Elements: 298-2500K, Canadian Metallurgical Quarterly, 23 (1984) 309-313.

133. P. Sahoo, M.M. Collur, T. DebRoy, Effects of Sulfur on Alloying Element Vaporization Rates during Laser Welding, Metallurgical Transactions B, 19 (1988) 967-972.
134. K. Mundra, T. DebRoy, Toward understanding alloying element vaporization during laser beam welding of stainless steel, Welding Journal, Research Supplement, 72 (1993) 1s-9s.
135. T. DebRoy, S. Basu, K. Mundra, Probing laser induced vaporization by gas dynamics and liquid pool transport phenomena, Journal of Applied Physics, 70 (1991) 1313-1319.
136. E.U. Schlunder, V. Gniclinski, Watme- und Stoffubertragung zwischen Gut und aufprallendem Dusenstrhl, Chemie Ingenieur Technik, 39 (1967) 578-584.
137. F.D. Richardson, Physical Chemistry of Melts in Metallurgy, vol. 2, Academic Press, (1974)
138. F.E. Wang, W.J. Beuhler, S.J. Pickart, Crstal structure and a unique "martensitic" transition of TiNi, Journal of Applied Physics, 36 (1965), 3232-3239.
139. D.P. Dautovich, Z. Melkvi, G.R. Purdy, C.V. Stager, Calorimetric study of a diffusionless martensitic transition in TiNi, Journal of Applied Physics, 37 (1966) 2513-2516.
140. S.R. Butler, J.E. Hanlon, R.J. Wasilewski, On martensitic transformation in TiNi, Metal Science Journal, 1 (1967) 104-110.
141. R.J. Wasilewski, S.R. Butler, J.E. Hanlon, D. Wordon, Homogeneity range and the martensitic transformation in TiNi, Metallurgical Transaction, 2 (1971) 229-238.
142. H.C. Man, Z.D. Cui, T.M. Yue, Corrosion properties of laser surface melted NiTi shape memory alloy, Scripta Materialia, 45 (2001) 447-1453.
143. R. Hill, The Elastic Behaviour of a Crystalline Aggregate, Proceedings of the Physical Society, Section A, 65 (1952) 349-354.
144. M. Finnis, Interatomic Forces in Condensed Matter, Oxford University Press, New York, NY (2003).
145. M. Levy, H.E. Bass, R. Stern, Modern Acoustical Techniques for the Measurement of Mechanical Properties, vol. 39, R. Celotta, T. Lucatorto, Experimental Methods in the Physical Sciences, Academic Press, San Diego, CA (2001).
146. P. Sittner, L. Heller, J. Pilch, C. Curfs, T. Alonso, D. Favier, Young's Modulus of Austenite and Martensite Phases in Superelastic NiTi Wires, Journal of Materials Engineering and Performance, 23 (2014) 2303-2314.

147. American Society for Testing and Materials (ASTM) Standard Test Method for Tension Testing of Nickel-Titanium Superelastic Materials, Standard F2516-14, ASTM International, West Conshohocken, PA (2009).
148. B. Reedlunn, S. Daly, L. Hector Jr., P. Zavattieri, J. Shaw, Tips and tricks for characterizing shape memory wire Part 5: full-field strain measurement by digital image correlation, Exp. Tech., 37 (2013) 62-78.
149. W.A. Scrivens, Y. Luo, M.A. Sutton, S.A. Collette, M.L. Myrick, P. Miney, P.E. Colavita, A.P. Reynolds, X. Li, Development of patterns for digital image measurements at reduced length scales, Exp. Mech., 47 (2007) 63-77.
150. J.-M. Lu, Q.-M. Hu, R. Yang, Composition-dependent elastic properties and electronic structures of off-stoichiometric TiNi from first principles calculations, Acta Materialia, 56 (2008) 4913-4920.
151. Y. Zheng, F. Jiang, H. Yang, Y. Liu, Effect of ageing treatment on the transformation behavior of Ti-50.9 at.% Ni alloy, Acta Materialia, 56 (2008) 736-745.
152. Z.-Y. Zeng, C.-E. Hu, L.-C. Cai, X-R. Chen, F.-Q. Jing, First-principles determination of the structure, elastic constant, phase diagram and thermodynamics of NiTi alloy, Physica B, 405 (2010) 3665-3672.
153. K.S. Suresh, D. Hahiri, A. Agarwal, S. Suwas, Microstructure dependent elastic modulus variation in NiTi shape memory alloy, Journal of Alloys and Compounds, 633 (2015) 71-74.
154. T. Alonso, D. Favier, G. Chagnon, P. Sittner, Y. Liu, Dynamic Mechanical Spectroscopy of Nanograined Thin NiTi Wires, in Proceedings SMST, Czech Republic, 2013.
155. D.C. Lagoudas, P.B. Entchev, P. Popov, E. Patoor, L.C. Brinson, X. Gao, Shape memeroy alloys, Part II: Modeling of polycrystals, Mechanics of Materials 38 (2006) 430-462.
156. D.C. Lagoudas, P.B. Entchev, Modelling of transformation-induced plasticity and its effect on the behavior of porous shape memory alloys. Part I: constitutive model for fully dense SMAs, Mechanics of Materials, 36 (2004) 865-892.
157. L. Anand, M. Gurtin, Thermal effects in the superelasticity of crystalline shape-memory materials, Journal of the Mechanics and Physics of Solids 51 (2003) 1015–1058.
158. A.V. Hershey, The elasticity of an isotropic aggregate of anisotropic cubic crystals, Journal of. Applied Mechanics-Transactions of the ASME 21 (1954) 236–240.

159. E. Kroner, Berechnung der elastischen konstanten des vielkristalls aus den konstanten des einkristalls, Zeitschirft fur Physik 151 (1958) 504–518.
160. R. Hill, Continuum micromechanics of elastoplastic polycrystals, Journal of the Mechanics and Physics of Solids 13 (1965) 89–101.
161. T. Mori, K. Tanaka, Average stress in matrix and average energy of materials with misfitting inclusions. Acta Metallurgica 21 (1973) 571–574.
162. R.M. Christensen, Mechanics of Composite Materials, Krieger Publishing Company, Malabar, FL, 1991.
163. S. Nemat-Nasser, M. Hori, Micromechanics: Overall Properties of Heterogeneous Materials, Ed. J.D Achenbach, B. Budiansky, H.A. Lauwerier, P.G. Saffman, L. Van Wijngaarden, J.R. Willis, North-Holland Series in Applied Mathematics and Mechanics, Vol. 37, Elsevier Science Publishers B.V., North-Holland, Amsterdam, Netherlands, 1993.
164. E. Patoor, A. Eberhardt, M. Berveiller, Potentiel pseudoe´lastique et plasticite´ de transformation martensitique dans les mono et polycristaux me´talliques, Acta Metallurgica 35 (1985) 2779–2789.
165. F. Falk, Pseudoelastic stress–strain curves of polycrystalline shape memory alloys calculated from single crystal data, International Journal of Engineering Science 27 (1989) 277–284.
166. E. Patoor, A. Eberhardt, M. Berveiller, Micromechanical modelling of superelasticity in shape memory alloys, Journal de Physique IV 6 (1996) C1-277-C1-292.
167. D.C. Lagoudas, A. Bhattacharya, On the correspondence between micromechanical models for isothermal pseudoelastic response of shape memory alloys and preisach model for hysteresis, Mathematics and Mechanics of Solids 2 (2003) 405–440.
168. Z.K. Lu, G.J. Weng, A self-consistent model for the stress–strain behavior of shape-memory alloy polycrystals, Acta Materialia. 46 (1998), 5423–5433.
169. X. Gao, L.C. Brinson, A simplified multivariant SMA model based on invariant plane nature of martensitic transformation, Journal of Intelligent Material Systems and Structures 13 (2002) 795–810.
170. Y. Benveniste, A new approach to the application of Mori-Tanaka's theory in composite materials, Mechanics of Materials, 6 (1987) 147-157.

171. G.J. Weng, Some elastic properties of reinforced solids, with special reference to isotropic ones containing spherical inclusions, International Journal of Engineering Science, 22 (1984) 845-856.
172. Q.P. Sun, K.C. Hwang, Micromechanics modelling for the constitutive behavior of polycrystalline shape memory alloys – I. derivation of general relations, Journal of Mechanics and Physics of Solids, 41 (1993) 1-17.
173. Q.P. Sun, K.C. Hwang, Micromechanics modelling for the constitutive behavior of polycrystalline shape memory alloys – II. study of the individual phenomena, Journal of Mechanics and Physics of Solids, 41 (1993) 19-33.
174. B. Reedlunn, C.B. Churchill, E.E. Nelson, J.A. Shaw, S.H. Daly, Tension, compression, and bending of superelastic shape memory alloy tubes, Journal of the Mechanics and Physics of Solids, 63 (2014) 506-537.
175. S. De la Flor, C. Urbina, F. Ferrando, Asymmetrical bending model for NiTi shape memory wires: numerical simulations and experimental analysis, Strain, 47 (2011) 255-267.
176. D.C. Lagoudas, S.G. Shu, Residual transformation of active structures with SMA actuators, International Journal of Mechanical Sciences, 41 (1999) 595-619.
177. K.R. Rajagopal, A.R. Srinivasa, On the thermomechanics of shape memory wires, Zeitschrift für angewandte Mathematik und Physik ZAMP, 50 (1999) 459-496.
178. S. Leclercq, C. Lexcellent, A general macroscopic description of the thermomechanical behavior of shape memory alloys, Journal of the Mechanics and Physics of Solids, 44 (1996) 953-957.
179. F. Auricchio, R.L. Taylor, J. Lubliner, Shape-memory alloys: macromodelling and numerical simulations of superelastic behavior, Computer Methods in Applied Mechanics and Engineering, 146 (1997) 281-312.
180. G. Rengarajan, R.K. Kumar, Numerical modeling of stress induced martensitic phase transformations in shape memory alloys, International Journal of Solids and Structures, 35 (1998) 1489-1513.
181. D.C. Lagoudas, P.B. Entchev, Modeling of transformation-induced plasticity and its effect on the behavior of porous shape memory alloys. Part II: porous SMA response, Mechanics of Materials, 36 (2004) 893-913.

182. F.D. Fischer, E.R. Oberaigner, K. Tanaka, F. Nishimura, Transformation induced plasticity revised, an updated formulation, International Journal of Solids and Structures, 35 (1998) 2209-2227.
183. C. Lexcellent, S. Leclerq, B. Gabry, G. Bourbon, The two way shape memory effect of shape memory alloys: an experimental study and phenomenological model, International Journal of Plasticity, 16 (2000) 1155-1168.
184. C. Lexcellent, G. Bourbon, Thermodynamical model of cyclic behaviour of Ti-Ni and Cu-Zn-Al shape memory alloys under isothermal undulated tensile tests, Mechanics of Materials, 24 (1996) 59-73.
185. R. Abeyaratne, S.-J. Kim, Cyclic effect in shape-memory alloys: a one-dimensional continuum model, International Journal of Solids and Structures, 34 (1997) 3273-3289.
186. C. Maletta, F. Furgiuele, 1D Phenomenological Modeling of Shape Memory Pseudoelasticity in NiTi Alloys, in: Smart Actuation and Sensing Systems: Recent Advances and Future Challenges, G. Berselli, R. Vertechy and G. Vassura, Eds., InTech, (2012) 121-144.
187. D. Depriester, A. Maynadier, K. Lavernhe-Taillard, O. Hubert, Thermomechanical modeling of a NiTi SMA sample submitted to displacement-controlled tensile test, International Journal of Solids and Structures 51 (2014) 1901-1922.
188. H. Soul, A. Yawny, Superelastic behavior of NiTi wires under general cycling conditions: Thermomechanical 1-D modelling, Procedia Materials Science 1 (2012) 141-148.
189. Q.P. Sun, Y.J. He, A multiscale continuum model of the grain-size dependence of the stress hysteresis in shape memory alloy polycrystals, International Journal of Solids and Structures 45 (2008) 3868-3896.
190. A. Ahadi, Q. Sun, Stress hysteresis and temperature dependence of phase transition stress in nanostructured NiTi – Effects of grain size, Applied Physics Letters 103 (2013) 021902-1-021902-5.
191. F. Falk, Ginzburg-Landau theory and solitary waves in shape-memory alloys, Zeitschrift für Physik B Condensed Matter, 54 (1984) 159-167.
192. J. Ortin, Preisach modeling of hysteresis for a pseudoelastic Cu-Zn-Al single crystal, Journal of Applied Physics, 71 (1992) 1454.

193. M.M. Khan, D.C. Lagoudas, Modeling of shape memory alloy pseudoelastic spring elements using Preisach model for passive vibration isolation, in Proceedings SPIE, 4693 (2002) 336-347.
194. S. Doraiswamy, A. Rao, A.R. Srinivasa, Combining thermodynamic principles with Preisach models for superelastic shape memory alloy wires, Smart Materials and Structures, 20 (2011) 085032.
195. I.D. Mayergoyz, Mathematical Models of Hysteresis and their Applications: Second Edition, Academic Press, New York, New York (2003).
196. B. Panton, Laser processing, thermomechanical processing, and thermomechanical fatigue of NiTi shape memory alloys, PhD thesis, University of Waterloo, Canada (2016).
197. J.I Kim, Y. Liu, S. Miyazaki, Ageing-induced two-stage R-phase transformation in Ti-50.9at%, Acta Materialia, 52 (2004) 487-499.
198. S.W. Robertson, A. R. Pelton, R. O. Ritchie, Mechanical fatigue and fracture of Nitinol, International Materials Reviews, 57 (2012) 1-37.
199. A. Pelton, Nitinol Fatigue: A Review of Microstructures and Mechanisms, Journal of Materials Engineering and Performance, 20 (2011) 613-617.
200. A. Chakraborty, Design and characterization of self-biasing NiTi spring actuator, Masters thesis, University of Waterloo, Ontario, Canada (2016).
201. M. Follador, M. Cianchetti, A. Arenit, C. Laschi, A general method for the design and fabrication of shape memory active spring actuators, Smart Materials and Structures, 21 (2012) 115029.
202. L. Czarnocki, W. Kim, B. Utter, J. Luntz, D. Brei, Design of SMA helical actuators: an experimental study, in: Proceedings of the ASME 2103 Conference on Smart Materials, Adaptive Structures and Intelligent Systems, Snowbird, Utah, USA (2013).
203. J. Van Humbeeck and L. Delaey, The influence of strain-rate, amplitude and temperature on the hysteresis of pseudoelastic Cu-Zn-Al Single crystal, Journal De physique, 42 (1981) 1007-1011.
204. A. Ahadi and Q.P Sun, Effects of grain size on the rate-dependent thermomechanical response of nanostructured superelastic NiTi, Acta Materialia, 76 (2014) 186-197.
205. M. Carl, B. Zhang, M.L. Young, Texture and strain measurements from bending of NiTi shape memory alloy wires, Shape Memory and Pseudoelasticity, 2 (2016) 254-263.

206. C. Chapman, A. Eshghinejad, Z. Karbaschi, M. Elahinia, Torsional Behavior of NiTi Wires and Tubes: Modeling and Experimentation, Journal of Intelligent Material Systems and Structures, 22 (2011) 1239-1248.
207. B. Panton, A. Michael, Y.N. Zhou, M.I. Khan, Effects of post-processing on the thermomechanical fatigue properties of laser modified NiTi, International Journal of Fatigue, In Press.
208. C. Sandu, R.K. Singh, Modeling differential scanning calorimetry, Thermochimica Acta, 159 (1990) 267-298.
209. X. Shi, L. Cui, D. Jiang, C. Yu, F. Guo, M. Yu, Y. Ren, Y. Liu, Grain size effect on the R-phase transformation of nanocrystalline NiTi shape memory alloys, Journal of Materials Science, 49 (2014) 4643-4647.
210. Y. Monetmani, M. Nili-Ahmadabadi, T.J. Tan, M. Bornapour, S. Rayagan, Effect of cooling rate on the phase transformation behavior and mechanical properties of Ni-rich NiTi shape memory alloy, Journal of Alloys and Compounds 469 (2009) 164-168.
211. J. Frenzel, E.P. George, A. Dlouhy, C. Somsen, M.F.-X. Wagner, G. Eggeler, Influence of Ni on martensitic phase transformations in NiTi shape memory alloys, Acta Materialia, 58 (2010) 3444-3458.
212. N.A. Zarkevich, D.D. Johnson, Shape-memory transformations of NiTi: Minimum-energy pathways between austenite, martensites, and kinetically limited intermediate states, Physical Review Letters, 113 (2014) 256701-1-265701-5.
213. T.W. Duerig, K. Bhattacharya, The influence of the R-phase on the superelastic behavior of NiTi, Shape Memory and Superelasticity, 1 (2015) 153-161.
214. J. Khalil Allafi, X. Ren, G. Eggeler, The mechanism of multistage transformations in aged Ni-rich NiTi shape memory alloys, Acta Materialia, 50 (2002) 793-803.
215. J. Khalil-Allafi, A. Dlouhy, G. Eggeler, Ni_4Ti_3-precipitation during aging of NiTi shape memory alloys and its influence on martensitic phase transformations, Acta Materialia, 50 (2002) 4255-4274.
216. J. Michutta, Ch. Somsen, A. Yawny, A. Dlouhy, G. Eggeler, Elementary martensitic transformation processes in Ni-rich NiTi single crystals with Ni_4Ti_3 precipitates, Acta Materialia, 54 (2006) 325-3542.

217. J.Y. Lee, S.H. Ko, D.F. Farson, C.D. Yoo, Mechanism of keyhole formation and stability in stationary laser welding, Journal of Physics D: Applied Physics, 35 (2002) 1570-1576.
218. J.O. Hirschfielder, C.F. Curtiss, R.B. Bird, Molecular Theory of Gases and Liquids, Wiley, New York, New York, 1964.
219. S.A. Shabalovskaya, Surface, corrosion and biocompatibility aspects of nitinol as an implant material, Bio-Medical Materials and Engineering 12 (2002) 69-109.
220. L. Zhu, J.M. Fino, A.R. Pelton, Oxidation of Nitinol, in: Proceedings of Smart Materials and Superelastic Technologies, California, USA (2003).
221. A. Pequegnat, A. Michael, J. Wang, K. Lian, Y. Zhou, M.I. Khan, Surface characterizations of laser modified biomedical grade NiTi shape memory alloys, Materials Science and Engineering C, 50 (2015) 367-378.
222. A. Coda, S. Zilio, D. Norwich, F. Sczerzenie, Characterization of inclusions in VIM/VAR NiTi Alloys, Journal of Materials Engineering and Performance, 21 (2012) 2575-2577.
223. A. Meyer, The measurement of self-diffusion coefficients in liquid metals with quasielastic neutron scattering, in: Proceedings of 11th International Conference on Quasielastic Neutron Scattering and 6th International Workshop on Inelastic Neutron Spectrometers, Autrans, France (2014).
224. A.K. Roy, R.P. Chhabra, Prediction of solute diffusion coefficients in liquid metals, Metallurgical Transactions A, 19 (1988) 273-279.
225. C.J. Smithells, Metals Reference Book: Volume I, Butterworth's, London, 1967.
226. J. Horbach, R.E. Rozas, T. Unruh, A. Meyer, Improvement of computer simulation models for metallic melts via quasielastic neutron scattering: A case study of liquid titanium, Physical Review B, 80 (2009) 212203-1-212203-4.
227. H. Zhao, T. DebRoy, Weld metal composition change during conduction mode laser welding of aluminum alloy 5182, Metallurgical and Materials Transactions B, 32 (2001) 163-172.
228. F. Thiebaud, M. Collet, E. Foltete, C. Lexcellent, Implementation of a multi-axial pseudoelastic model to predict the dynamic behavior of shape memory alloys, Smart Materials and Structures, 16 (2007) 935-947.
229. C. Maletta, E. Sqambitterra, F. Furgiuele, R. Casati, A. Tuissi, Fatigue of pseudoelastic NiTi within the stress-induced transformation regime: a modified Coffin-Manson approach, Smart Materials and Structures, 21 (2012) 112001-112008.

230. Y. Liu, H. Yang, Strain dependence of the Clasius-Clapeyron relation for thermoelastic martensitic transformation, Smart Materials and Structures, 16 (2007) S22-S27.
231. J.E. Schaffer, Structure-property relationships in conventional and nanocrystalline NiTi intermetallic alloy wire, Journal of Materials Engineering and Performance, 18 (2009) 582-587.
232. M.L. Young, M.F.-X. Wagner, J. Frenzel, W.W. Schmahl, G. Eggeler, Phase volume fractions and strain measurements in an ultrafine-grained NiTi shape-memory alloy during tensile loading, Acta Materialia, 58 (2010) 2344-54.
233. S. Kustov, D. Salas, E. Cesari, R. Santamarta, D. Mari, J. Van Humbeeck, Structural anelasticity, elasticity and broken ergodicity in Ni-Ti shape memory alloys, Acta Materialia 73 (2014) 275-286.
234. A.P. Stebner, D.W. Brown, L.C. Brinson, Young`s modulus evolution and texture-based elastic-inelastic strain partitioning during large uniaxial deformations of monoclinic nickel-titanium, Acta Materialia, 61 (2013) 1944-1956.
235. N.J. Bechle, S. Kyriakides, Localization in NiTi tubes under bending, International Journal of Solids and Structures, 51 (2014) 967-980.
236. D. Jiang, S. Kyriakides, N.J. Bechle, C.M. Landis, Bending of pseudoelastic NiTi tubes, International Journal of Solids and Structures, 124 (2017) 192-234.
237. P. Glaister, Intersecting chords theorem – 30 years on, Mathematics in School, 36 (2007) 22.
238. J.M. Gere, Mechanics of Materials, 6th Edition, Brooks/Cole – Thomas Learning, Belmont, CA (2004).
239. W.D. Callister, D.G. Rethwisch, Materials Science and Engineering, 9th Edition, Wiley, Hoboken, NJ, 2014.
240. American Society for Testing and Materials (ASTM) Standard Test Methods for Bend Testing of Metallic Flat Materials for Spring Applications Involving Static Loading, Standard F855-08, ASTM International, West Conshohocken, PA (2013).
241. A.M. Kenyon, L. Ingold, Trigonometry, The Macmillan Company, New York, NY (1914).
242. L.d.A. Santos, P.D. Resende, M.H.d.A Bahia, V.T.L. Bouno, Effects of R-phase on Mechanical Responses of Nickel-Titanium Endodontic Instrument: Structural Characterization and Finite Element Analysis, The Scientific World Journal, vol.2016 (2016) 11.

243. A. Upadhyay, R. Singh, Prediction of Effective Modulus of Biphasic Composite Materials, Modern Mechanical Engineering, 2 (2012) 6-13.
244. K. Otsuka, X. Ren, Recent developments in the research of shape memory alloys, Intermetallics, 7 (1999) 511-528.
245. K. Taillard, S.A. Chirani, S. Calloch, C. Lexcellent, Equivalent transformation strain and its relation with martensite volume fraction for isotropic and anisotropic shape memory alloys, Mechanics of Materials, 40 (2008) 151.
246. P. Sedlak, M. Frost, B. Benesova, T. Ben Zineb, P. Sittner, Thermomechanical model for NiTi-based shape memory alloys including R-phase and material anisotropy under multi-axial loadings, International Journal of Plasticity, 39 (2012) 132-151.
247. T. Hara, T. Ohba, E. Okunishi, K. Otsuka, Structural study of R-phase in Ti-50.23 at. % Ni and Ti-47.75 at. % Ni-1.50 at. % Fe alloys, Materials Transactions, 38 (1997) 11-17.
248. K. Palinski, M. Parlinska-Wojtan, Lattice dynamics of NiTi austenite, martensite, and R-phase, Physical Review B, 66 (2002) 064307-1-8.
249. J. Khalil-Allafi, W.W. Schmahl, M. Wagner, H. Sitepu, D.M. Toebbens, G. Eggeler, The influence of temperature on the lattice parameters of coexisting phases in NiTi shape memory alloys-a neutron diffraction study, Materials Science and Engineering A, 378 (2004) 161-164.
250. J. Khalil-Allafi, W.W. Schmahl, D.M. Toebbens, Space group and crystal structure of the R-phase in binary NiTi shape memory alloys, Acta Materialia, 54 (2006) 3171-3175.
251. A.R. Abdulghany, Generalization of parallel axis theorem for rotational inertia, American Journal of Physics, 85 (2017), 791-795.
252. M. Frost, P. Sedlak, L. Kaderavek, L. Heller, Numerical and experimental investigation of shape memory alloys subjected to complex mechanical loading: a case study of a NiTi helical spring, in: Proceedings of the 7th Thematic Conference on Smart Structures and Materials, Ponta Delgada, Azores, Portugal, June 2015.
253. J. Zimmermann, M. Strommel, The mechanical behaviour of rubber under hydrostatic compression and the effect on the results of finite element analyses, Archive of Applied Mechanics, 83 (2013) 293.
254. Y. Liu, Z.L. Xie, J. Van Humbeck, L. Delaey, Effect of texture orientation on the martensite deformation of NiTi shape memory alloy sheet, Acta Materialia, 47 (1999) 645-660.

255. J.W. Yoon, F. Barlat, J.J. Gracio, E. Rauch, Anisotropic strain hardening behavior in simple shear for cube textured aluminum alloy sheets, International Journal of Plasticity, 21 (2005) 2426-2447.
256. R.H. Bricknell, K.N. Melton, O. Mercier, The structure of NiTiCu Shape Memory Alloys, Metallurgical Transactions A, 10 (1979) 693-697.
257. J. Bonet, R.D. Wood, Nonlinear Continuum Mechanics for Finite Element Analysis, Cambridge University Press, United Kingdom, 1997.
258. L. de Arruda Santos, P.D. Resende, M.G. de Azevedo Bahia, V.T.L. Buono, Effects of R-phase on mechanical responses of Nickel-Titanium endodontic instrument: structural characterization and finite element analysis, The Scientific World Journal, dx.doi.org/10.1155/2016/7617493.
259. D. Stoeckel, Shape memory actuators for automotive applications, Mater. Design, 11 (6) (1990) 302.
260. S. Kim, E. Hawkes, K. Cho, M. Jolda, J. Foley, R. Wood, Micro artificial muscle fiber using NiTi spring for soft robotics, Proc. of the 2009 IEEE/RSJ Int. Conf. on Intelligent Robots and Systems, October 11-15, 2009, St. Louis, USA.
261. M. Wen, G.F. Tu, Q.Y. Zong, C.X. Xie, A study of NiTi shape memory alloy springs and it's application in a new robotic actuator, Proc. of the IEEE Int. Conf. on Industrial Technology, December 5-9, 1994, Guangzhou, China.
262. G. Costanza, M.E. Tata, C. Calisti, Nitinol one-way shape memory springs: Thermomechanical characterization and actuator design, Sensors and Actuators A: Physical, 157 (2010) 113-117.
263. K. Malukhin, K. Ehmann, Model of a NiTi shape memory alloy actuator, J. Intel. Mat. Syst. Str., 26 (2015) 386-399.
264. J.P. Swensen, A.M. Dollar, Optimization of parallel spring antagonists for Nitinol shape memory alloy actuators, Proc. of the 2014 IEEE Int. Conf. on Robotics and Automation (ICRA), May 31-June 7, 2014, Hong Kong, China.
265. K. Wada, Y. Liu, On the two-way shape memory behavior in NiTi alloy – An experimental analysis, Acta Materialia, 56 (2008) 3266-3277.
266. H. Scherngell, A.C. Kneissl, Generation, development and degradation of the intrinsic two-way shape memory effect in different alloy systems, Acta Materialia, 50 (2002) 327-341.

267. A. Paiva, M. A. Savi, An overview of constitutive models for shape memory alloys, Mathematical Problems in Engineering, vol. 2006 (2006) 30.
268. A. Menciassi, S. Gorini, G. Pernorio, P. Dario, A SMA actuated artificial earthworm, in Robotics and Automation, 2004. Proceedings. ICRA '04. 2004 IEEE International Conference on, 2004, pp. 3282-3287 Vol.4.
269. B. Kim, M. G. Lee, Y. P. Lee, Y. Kim, G. Lee, An earthworm-like micro robot using shape memory alloy actuator, Sensors and Actuators A: Physical, 125 (2006) 429-437.
270. S.M. An, J. Ryu, M. Cho, K.-J. Cho, Engineering design framework for a shape memory alloy coil spring actuator using a static two-state model, Smart Materials and Structures, 21 (2012) 055009.
271. A. Michael, A. Pequegnat, J. Wang, Y.N. Zhou, M.I. Khan, Corrosion performance of medical grade NiTi after laser processing, Surface and Coating Technology, 324 (2017) 478-485.
272. S. Shabalovskaya, J. Anderegg, F. Laab, P.A. Thiel, G. Rondelli, Surface conditions of Nitinol wires, tubing, and as-cast alloys: the effect of chemical etching, aging in boiling water, and heat treatment, Journal of Boimedical Materials Research A: Applied Biomaterials 65 (2003) 193.
273. N. Munroe, C. Pulletikurthi, W. Haider, Enhanced biocompatibility of porous Nitinol, Journal of Materials Engineering and Performance 18 (2009) 765.
274. P. Filip, J. Lausmaa, J. Musialek, K. Mazanec, Structure and surface of NiTi human implants, Biomaterials 22 (2001) 2131.
275. F. Coste, F. Janin, M. Hamadou, R. Fabbro, Deep penetration laser welding with ND:Yag lasers combination up to 11 kW laser power, in Proceedings of SPIE 4831, First International Symposium on High-Power Laser Macroprocessing, Osaka, Japan, March, 2003, 422-427.
276. J. Zhu, L. Li, Z. Liu, CO_2 and diode laser welding of AZ31 magnesium alloy, Applied Surface Science, 247 (2005) 300-306.
277. C. N. Saikrishna, K. V. Ramaiah, S. K. Bhaumik, Effects of thermo-mechanical cycling on the strain response of Ni-Ti-Cu shape memory alloy wire actuator, Materials Science and Engineering A, 428 (2006) 217-224.
278. B. Erbstoeszer, B. Armstrong, M. Taya, K. Inoue, Stabilization of the shape memory effect in NiTi: an experimental investigation, Scripta Materialia, 42 (2000) 1145-1150.

279. M Langelaar, F. van Keulen, A simple R-phase transformation model for engineering purposes, Materials Science and Engineering A, 378 (2004) 507-512.
280. A. Sengupta, P. Papadopoulos, Constitutive modeling and finite element approximation of B2-R-B19' phase transformations in Nitinol polycrystals, Computer Methods in Applied Mechanics and Engineering, 198 (2009) 3214-3227.
281. R. Heinen, S. Miro, Micromechanical modeling of NiTi shape memory alloys including austenite, R-phase, and martensite, Computer Methods in Applied Mechanics and Engineering, 229-232 (2012) 44-55.

Appendix I: Tabulated Transformations Peaks Relative to Ni Concentration

Table A-I.1. List of calculated Mp and Ap values for several Ni concentrations.

C_{Ni} (at.%)	Mp (˚C)	Ap (˚C)		C_{Ni} (at.%)	Mp (˚C)	Ap (˚C)
51	-85.01211071	-57.01211071		**49.45**	38.13995171	87.13995171
50.95	-70.04462671	-41.16962671		**49.4**	38.87140536	87.87140536
50.9	-56.73484087	-26.98484087		**49.35**	39.58845139	88.58845139
50.85	-44.93503952	-14.31003952		**49.3**	40.28660631	89.28660631
50.8	-34.50635529	-3.006355286		**49.25**	40.96069765	89.96069765
50.75	-25.31850767	7.056492329		**49.2**	41.60510111	90.60510111
50.7	-17.24957085	16.00042915		**49.15**	42.21403861	91.21403861
50.65	-10.18567371	23.93932629		**49.1**	42.7818141	91.7818141
50.6	-4.020757675	30.97924232		**49.05**	43.30310535	92.30310535
50.55	1.343694687	37.21869469		**49**	43.77317405	92.77317405
50.5	5.99890995	42.74890995		**48.95**	44.18821859	93.18821859
50.45	10.02911997	47.65411997		**48.9**	44.54553461	93.54553461
50.4	13.51178741	52.01178741		**48.85**	44.84385514	93.84385514
50.35	16.51788664	55.89288664		**48.8**	45.0835743	94.0835743
50.3	19.11217213	59.36217213		**48.75**	45.26702166	94.26702166
50.25	21.35342312	62.47842312		**48.7**	45.39874673	94.39874673
50.2	23.29472971	65.29472971		**48.65**	45.48573589	94.48573589
50.15	24.98374367	67.85874367		**48.6**	45.53771567	94.53771567
50.1	26.46294498	70.21294498		**48.55**	45.5673995	94.5673995
50.05	27.76988888	72.39488888		**48.5**	45.59075975	94.59075975
50	28.93750095	74.43750095		**48.45**	45.62727356	94.62727356
49.95	29.99431562	76.36931562		**48.4**	45.700212	94.700212
49.9	30.96475649	78.21475649		**48.35**	45.83687735	94.83687735
49.85	31.86938477	79.99438477		**48.3**	46.06888223	95.06888223
49.8	32.72515392	81.72515392		**48.25**	46.43241429	95.43241429
49.75	33.54571366	82.54571366		**48.2**	46.96848583	95.96848583
49.7	34.3416245	83.3416245		**48.15**	47.72320557	96.72320557
49.65	35.12065148	84.12065148		**48.1**	48.74805331	97.74805331
49.6	35.88803267	84.88803267		**48.05**	50.10012102	99.10012102
49.55	36.64670873	85.64670873		**48**	51.84239531	100.8423953
49.5	37.39762616	86.39762616				

Appendix II: The Evolution of the Localized Phase Transformation during Bending

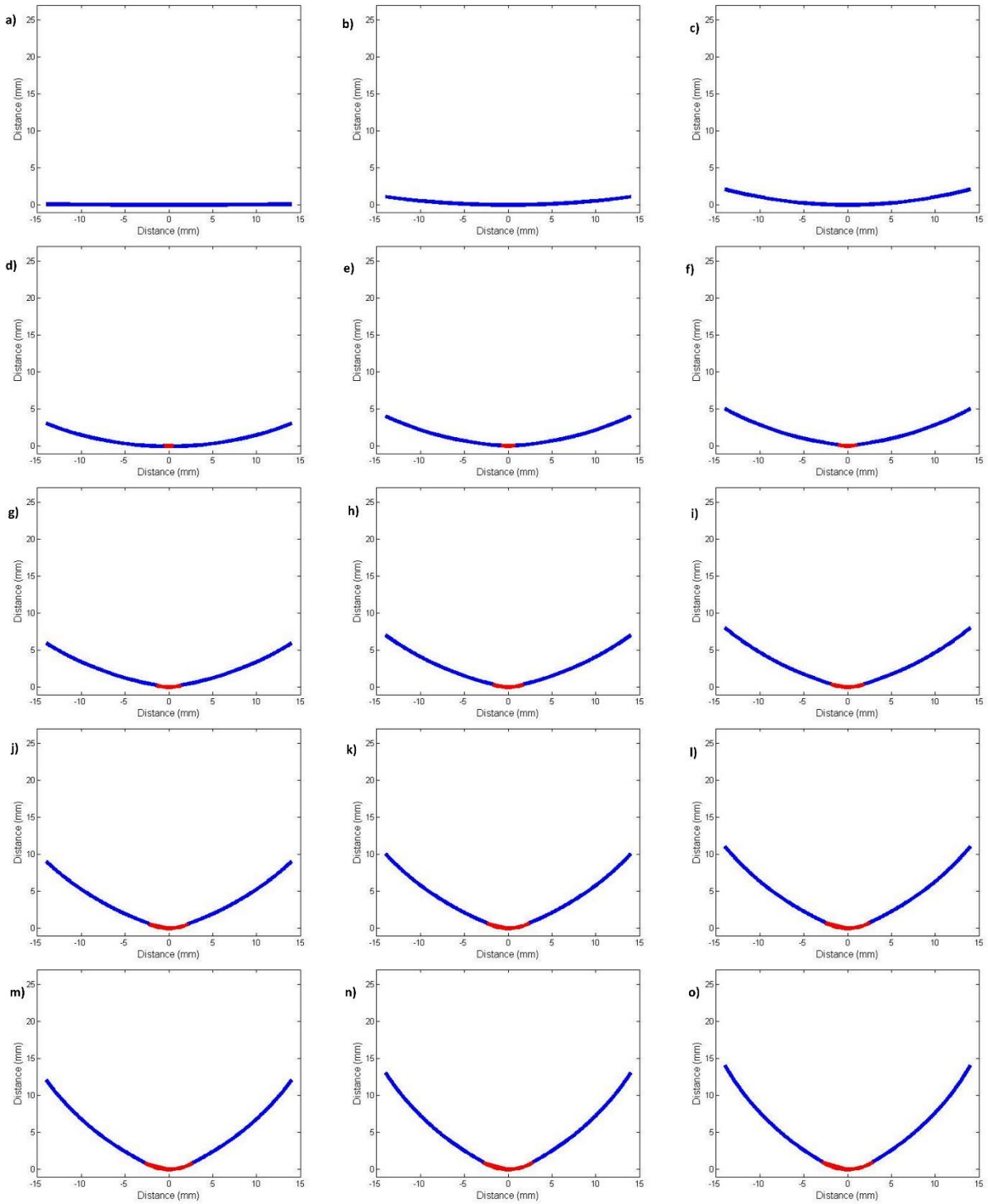

Figure A-II.1: Bending model predictions at a) 0.1, b) 1.0, c) 2.0, d) 3.0, e) 4.0, f) 5.0, g) 6.0, h) 7.0, i) 8.0, j) 9.0, k) 10.0, l) 11.0, m) 12.0, n) 13.0 and o) 14.0 mm displacements for 700 um wire.